

# The role of cosmic voids in galaxy formation and gravitational lensing

Uniwersytet Mikołaja Kopernika  
Wydział Fizyki, Astronomii i Informatyki Stosowanej  
Instytut Astronomii

Marius Peper

*Praca doktorska napisana pod kierunkiem*  
prof. dra hab. Boudewijn Roukema  
(UMK)  
dra hab. Krzysztof Bolejko  
(Uniwersytet Tasmanii)

Toruń 2023

Pracę przyjmuję i akceptuję.

Potwierdzam złożenie pracy doktorskiej.

---

*data i podpis opiekuna pracy*

---

*data i podpis pracownika instytutu*

First I want to thank my supervisors. I want to express my gratitude to Professor Boudewijn Roukema for your great support and your patience. Thank you for your scientific guidance and help with the several projects and challenges that I encountered during my PhD studies, for your deep feedback on my work and this thesis and all the time you invested. I also want to thank you for your support during the challenging time of the global pandemic in which you ensured that everybody in our work group is fine.

I wish to thank my second supervisor Dr. Krzysztof Bolejko. Thank you for joining our discussions and sharing valuable ideas and feedback with us even though our meetings took place in the late evening for you. I am thankful for the great internship with you in which you invested a lot of time for fruitful discussions about our project and about the great hiking trips in which you showed me the beauty of Tasmania.

I want to thank my family for supporting me emotionally during the sometimes challenging times of my PhD studies. Especially, I wish to thank my mother for listening to my problems and helping me to sort out any issue with the authorities while I am abroad.

I am grateful for my colleagues and friends. I wish to thank Matteo Cinus for joining me in this PhD and making this journey together. I am thankful to Dr. Mariana Jaber who constantly encouraged me and gave me a lot of feedback on several proposals, results and this thesis. I thank Dr. Quentin Vigneron for many interesting discussions and your support. Last but not least I wish to thank Dr. Mirko Daumann for being a close friend for all my studies and for your feedback from a non-cosmologist point of view on this thesis.

*Uniwersytet Mikołaja Kopernika zastrzega sobie prawo do licencji niewyłącznej niniejszej pracy doktorskiej w celu udostępniania dla potrzeb działalności naukowo-badawczej lub dydaktycznej*

# Contents

<b>Front matter</b>	<b>vii</b>
List of figures . . . . .	vii
List of tables . . . . .	viii
Abstract (English) . . . . .	ix
Streszczenie (po polsku) . . . . .	x
<b>1 Introduction</b>	<b>1</b>
1.1 Cosmic voids . . . . .	1
1.2 Software pipeline . . . . .	1
1.3 Galaxy formation . . . . .	2
1.4 Void detection via geometric optics . . . . .	2
1.5 Thesis structure . . . . .	2
<b>2 Cosmology</b>	<b>4</b>
2.1 The cosmological standard model . . . . .	4
2.1.1 The isotropic and homogeneous Universe . . . . .	4
2.1.2 Epochs of the Universe . . . . .	10
2.1.3 Distances in Cosmology . . . . .	14
2.2 Structure Formation . . . . .	16
2.2.1 Linear Perturbation Theory . . . . .	16
2.2.2 The cosmic web . . . . .	21
2.3 Gravitational lensing and geometric optics . . . . .	24
2.3.1 Gravitational lensing . . . . .	24
2.3.2 Geometric optics . . . . .	27
<b>3 Method</b>	<b>30</b>
3.1 Initial Conditions – MPGRAFIC . . . . .	30
3.1.1 Single-level simulation . . . . .	30
3.1.2 Zoom simulations . . . . .	32
3.1.3 Fast Fourier Transform . . . . .	33
3.2 $N$ -body problems – RAMSES . . . . .	35
3.2.1 $N$ -body problems . . . . .	35
3.2.2 RAMSES . . . . .	36
3.3 Voids – REVOLVER . . . . .	41
3.3.1 Spherical-expansion tophat heuristic model . . . . .	41
3.3.2 Watershed . . . . .	42
3.3.3 Void centres . . . . .	45
3.4 Halo Finder – ROCKSTAR . . . . .	47
3.4.1 Spherical collapse toy model and dark matter halo properties . . . . .	47

3.4.2	Halo finders . . . . .	48
3.4.3	ROCKSTAR . . . . .	49
3.5	Merger-history tree – CONSISTENT-TREES . . . . .	51
3.6	Semi-analytical galaxy formation – SAGE . . . . .	53
<b>4</b>	<b>The role of the elaphrocentre</b>	<b>58</b>
4.1	Introduction . . . . .	58
4.2	Method . . . . .	61
4.2.1	Software pipeline . . . . .	61
4.2.2	Elaphrocentre and other definitions of void centres . . . . .	64
4.2.3	Analysis . . . . .	65
4.2.4	Reproducibility versus cosmic variance . . . . .	69
4.3	Results . . . . .	70
4.3.1	Simulation pipeline . . . . .	70
4.3.2	Infall rate . . . . .	71
4.3.3	Galaxy Sizes . . . . .	75
4.3.4	Elaphro-acceleration . . . . .	81
4.4	Discussion . . . . .	82
4.4.1	Infall rates . . . . .	82
4.4.2	Galaxy sizes . . . . .	82
4.4.3	Elaphro-acceleration . . . . .	85
4.4.4	Future extensions . . . . .	85
4.5	Conclusion . . . . .	86
<b>5</b>	<b>Hierarchical structure</b>	<b>88</b>
5.1	Method . . . . .	88
5.1.1	Simulation . . . . .	88
5.2	Results . . . . .	91
5.3	Discussion and Conclusion . . . . .	93
<b>6</b>	<b>Cosmic voids in lensing maps</b>	<b>96</b>
6.1	Introduction . . . . .	96
6.2	Method . . . . .	98
6.2.1	Software pipeline . . . . .	98
6.2.2	Simulation geometry . . . . .	99
6.2.3	Void detection . . . . .	100
6.2.4	Matches to intrinsic voids . . . . .	102
6.2.5	Detector variables $\Sigma, \gamma, \theta, \sigma$ . . . . .	104
6.3	Results . . . . .	108
6.3.1	Simulation . . . . .	108
6.3.2	Surface overdensity $\Sigma$ . . . . .	111
6.3.3	Weak-lensing shear $\overline{\gamma}_{\perp}$ . . . . .	114
6.3.4	Optical scalars $\theta$ and $ \sigma $ . . . . .	115
6.4	Discussion . . . . .	115
6.4.1	Void lensing studies when intrinsic voids are known . . . . .	115
6.4.2	Blind (redshift-free) searches for voids . . . . .	120
6.4.3	Projected void centrality and obscuring cosmic web structures . . . . .	120
6.5	Conclusion . . . . .	121

<b>7 Conclusion</b>	<b>123</b>
7.1 Galaxy formation in voids . . . . .	123
7.2 Geometric optics through voids . . . . .	125
<b>References</b>	<b>126</b>

# List of Figures

2.1	Cosmic microwave background observed by COBE DMR . . . . .	6
2.2	Supernovae type Ia distance–redshift relation . . . . .	9
2.3	Structure evolution through inflation. . . . .	13
2.4	The cosmic web . . . . .	21
2.5	Sketch of a lensing plane . . . . .	25
3.1	Particle mesh schematic diagram . . . . .	37
3.2	Schematic Voronoi tessellation . . . . .	42
3.3	Schematic merger-tree . . . . .	51
3.4	Simplified recipe to build a galaxy in a halo . . . . .	53
4.1	Void size distribution in a $128^3$ particle run . . . . .	67
4.2	Relative void size distribution . . . . .	68
4.3	Differential halo number counts in a $128^3$ particle simulation . . . . .	70
4.4	Amplitude of infall rate vs fraction of halo particles in the void $f_{\mathcal{H}\cap\mathcal{V}}$ . . . . .	71
4.5	Decay rate $\tau$ depending on the fraction of halo particles in the void $f_{\mathcal{H}\cap\mathcal{V}}$ . . . . .	72
4.6	Amplitude of the infall rate depending on the relative position in the void . . . . .	73
4.7	Infall decay rate depending on the relative position in the void . . . . .	74
4.8	$r_{\text{disk}}$ in dependence of $f_{\mathcal{H}\cap\mathcal{V}}$ . . . . .	76
4.9	$r_{\text{disk}}$ in dependence of the relative position in a void . . . . .	77
4.10	Spin parameter $\lambda$ in dependence of $f_{\mathcal{H}\cap\mathcal{V}}$ . . . . .	77
4.11	Spin parameter $\lambda$ in dependence of the relative position in a void . . . . .	78
4.12	Virial radius $R_{\text{vir}}$ of haloes in dependence of $f_{\mathcal{H}\cap\mathcal{V}}$ . . . . .	78
4.13	Virial radius $R_{\text{vir}}$ of haloes in dependence of the relative position in a void . . . . .	79
4.14	Hypothetical radial acceleration $\dot{v}_{\parallel}$ around the centre of a void . . . . .	80
4.15	Hypothetical tangential acceleration $\dot{v}_{\perp}$ around the centre of a void . . . . .	81
4.16	$f_{\mathcal{H}\cap\mathcal{V}}$ vs the relative position in a void $r/R_{\text{eff}}$ . . . . .	83
5.1	Comparison of density slices with frozen modes . . . . .	89
5.2	Comparison of halo spin in different environments . . . . .	92
5.3	Comparison of $r_{\text{disk}}$ in different environments . . . . .	93
5.4	Comparison of stellar masses of galaxies in different environments . . . . .	94
5.5	Comparison of formation redshift of central haloes in different environments . . . . .	95
6.1	Sky map and radial profile of the surface overdensity $\Sigma$ . . . . .	109
6.2	Correlation of position and radii of 3D voids and 2D voids identified in $\Sigma$ . . . . .	110
6.3	Radial profile of the averaged tangential weak-lensing shear $\overline{\gamma}_{\perp}$ . . . . .	112
6.4	Correlation of position and radii of 3D voids and 2D voids identified in $\overline{\gamma}_{\perp}$ . . . . .	113
6.5	Sky map and radial profile of the Sachs expansion $\theta$ . . . . .	116

6.6	Correlation of position and radii of 3D voids and 2D voids identified in $\theta$	. . .	117
6.7	Sky map and radial profile of the Sachs expansion $ \sigma $	. . . . .	118
6.8	Correlation of position and radii of 3D voids and 2D voids identified in $ \sigma $	. .	119



# List of Tables

4.1	Fit parameters to the decay rate . . . . .	72
4.2	Median disk scale, $\lambda$ and $R_{\text{eff}}$ of void and non-void galaxies . . . . .	75
4.3	Median elaphro-acceleration estimates . . . . .	80
4.4	Robust best fit parameters for $r_{\text{disk}}$ , $R_{\text{vir}}$ and $\lambda$ vs void-centric distance . . . . .	85
5.1	Volume and galaxy fractions per environment in Bolshoi . . . . .	91
6.1	Parameters used in our two-dimensional void detection algorithm . . . . .	100
6.2	Numbers of detected intrinsic three-dimensional voids and two-dimensional voids	108
6.3	Matching probabilities between three-dimensional and two-dimensional voids .	108

## Abstract

Cosmic voids may play key roles in cosmology, both as an environment for galaxy formation that disfavours the virialisation of dark matter haloes, and as having a gravitational lensing effect of dispersing a light bundle rather than focussing it.

This thesis has two main aims. First, we investigate if the location of a galaxy in the cosmic web has a measurable effect on its properties. We denote the potential hill of a void as the “elaphrocentre”, which should counteract the formation of a matter halo and weaken matter infall. Second, we explore to what degree geometric-optics maps can reveal the underdensities in the intrinsic, non-luminous matter distribution of cosmic voids.

We carry out cosmological  $N$ -body simulations, building merger-history trees for the simulated haloes and populate them with galaxies using semi-analytical recipes. The same tools are employed on the Bolshoi simulation for a significantly increased mass resolution. Voids are identified using watershed algorithms. Based on an  $N$ -body realisation we estimate a surface overdensity map and maps of weak gravitational lensing and geometric-optics scalar variables. We propose a heuristic algorithm with which we identify voids in the projected radial profiles of these detector variables.

While we do not find evidence that an elaphrocentric position weakens matter infall, we do find a significantly later formation epoch of galaxies in voids. We find void galaxies being of lower mass, smaller and having a higher spin parameter. Galaxies modelled in the Bolshoi simulation also yield later formation epochs of haloes in voids and, for halo masses  $M_{\text{vir}} \gtrsim 10^{10} M_{\odot}/h$ , higher spin parameters for galaxies in underdense environments. The differences in the Bolshoi simulation are found for sub-cluster-mass haloes, i.e. masses below  $\sim M_{\text{vir}} = 10^{10} M_{\odot}/h - 10^{11} M_{\odot}/h$ . For a fixed mass, the Bolshoi simulation analysis yields a significantly higher stellar mass in galaxies in the dense regions. Overall, we find that the isolated environment of a void yields quantifiable effects on galaxy formation.

In our geometric-optics work, our heuristic algorithm shows that maps of the weak-lensing tangential shear, the Sachs expansion and the Sachs shear modulus significantly reveal the centres of the underlying three-dimensional watershed-detected voids.

In this thesis, we have shown that the cosmic void environment yields measurable differences in galaxy properties compared to galaxies found in denser regions. Moreover, we have extended the prospects for the observational detection of voids to the use of geometric-optics maps, as we find preliminary evidence that our algorithm provides a viable technique that should provide predictions for spectroscopic survey followups.

## Streszczenie

Kosmiczne pustki mogą odegrać kluczową rolę w kosmologii, zarówno w badaniach wpływu środowiska na powstawanie galaktyk poprzez hamowanie procesu wirializacji hal ciemnej materii, jak i w badaniach efektu soczewkowania grawitacyjnego poprzez rozpraszanie niż skupianie promieni świetlnych.

Niniejsza rozprawa ma dwa główne cele. Po pierwsze, badamy czy położenie galaktyki w ramach kosmicznej struktury ma mierzalny wpływ na jej właściwości. Szczyt potencjału kosmicznej pustki oznaczymy jako “elaphrocentrum”, które powinno przeciwdziałać procesowi skupiania się materia i hamować jego przebieg. Po drugie, badamy w jakim stopniu mapy optyki geometrycznej pozwalają na wyznaczenie rejonów o obniżonej gęstości w rozkładzie ciemnej i nie promieniującej materii obecnie w ramach kosmicznych pustek.

Badania te oparte są na podstawie symulacji  $N$ -ciałowych, z których skonstruowane zostały drzewa historii-połączeń skupisk materia, w których zostały zagnieżdżone galaktyki na podstawie pół-analitycznych procedur. Te same metody zostały zaadoptowane do symulacji Bolshoi w celu poprawienia rozdzielczości masowej. Kosmiczne pustki zostały zidentyfikowane za pomocą algorytmu wododziałowego. Następnie, na podstawie symulacji  $N$ -ciałowej, zostały skonstruowane mapy o podwyższonej gęstości oraz mapy soczewkowania grawitacyjnego, a także odpowiadające im skalary optyki geometrycznej. Na podstawie uzyskanych w ten sposób map, został skonstruowany heurystyczny algorytm do identyfikacji kosmicznych pustek oraz ich radialnych profili w ramach wyżej wymienionej parametryzacji.

Uzyskane wyniki sugerują, iż położenie galaktyk w odniesieniu do elaphrocentrum nie wpływa na osłabienie temp spadku materii, jednakże obserwowany jest znacznie późniejsze tempo formowania się galaktyk znajdujących się we wnętrzu kosmicznych pustek. Galaktyki te, dodatkowo, charakteryzują się mniejszymi masami, mniejszymi rozmiarami oraz, dla masy hal  $M_{\text{vir}} \gtrsim 10^{10} M_{\odot}/h$ , wyższym parametrem rotacji. Galaktyki zidentyfikowane w ramach symulacji Bolshoi, które znajdują się w kosmicznych pustkach także charakteryzują się opóźnionym tempem formowania i wyższym parametrem rotacji. Różnice w ramach symulacji Bolshoi, wskazują na masy z zakresu podgromadowego, tzn. dla mas mniejszych od  $\sim M_{\text{vir}} = 10^{10} M_{\odot}/h - 10^{11} M_{\odot}/h$ . Analiza oparta na symulacji Bolshoi oraz wyróżnionych masach wyraźnie wskazuje na wyższe masy gwiazdowe w ramach rejonów o podwyższonej gęstości. Na podstawie tych wyników wyciągnięty jest wniosek, że kosmiczne pustki jako środowiska wyizolowane wpływają ilościowo na procesy formowania się galaktyk.

Praca oparta na optyce geometrycznej i heurystycznie zdefiniowanym algorytmie wskazuje, że mapy słabego soczewkowanie-grawitacyjnego, ścinania, oraz mapy parametru ekspansji Sachsa i parametru ścinania Sachsa są w stanie jednoznacznie zidentyfikować centra kosmicznych pustek, które zostały wyselekcjonowane za pomocą algorytmu wododziałowego.

Niniejsza rozprawa wykazuje, że galaktyki, które uformowały się w ramach środowisk kosmicznych pustek mają mierzalnie inne własności niż galaktyki które uformowały się w ramach rejonów o podwyższonej gęstości. Co więcej, niniejsza rozprawa także otwiera nowe perspektywy dla identyfikowania kosmicznych pustek w oparciu o mapy optyki geometrycznej. Przedstawione w niej wstępne badania oraz wypracowany algorytm mogą stanowić ważną metodę w detekcji kosmicznych pustek, co z kolei pozwoli na dodatkowe badania oparte na spektroskopijnych przeglądach galaktycznych.

# Chapter 1

## Introduction

### 1.1 Cosmic voids

Thanks to wider and deeper surveys we can probe the processes shaping the distribution of matter on the largest observational scales of the Universe. In this thesis we focus on a prominent component of the large scale structure, namely the cosmic voids, which are a pristine environment to probe cosmological models as well as galaxy formation. Cosmic voids are characterised by being underdense regions; originally, in galaxy surveys these regions were defined as regions devoid of galaxies. They dominate the volume of our Universe, but due to their deficit of luminous matter, their observational inspection faces several challenges.

An idealised void can be thought of as a spherical underdense region that grows in physical size and becomes more underdense over time as it pushes matter to its outer edges. Thus, compared to the surrounding Universe, which in comparison to the void is overdense, a void exerts what is effectively a repulsive gravitational force. A void is a hill in the gravitational potential. Moreover, in contrast to strongly overdense regions, a void should induce a negative spatial curvature. For all these reasons, voids are not only nearly devoid of galaxies, but they also constitute an environment that should disfavour the collapse of dark matter haloes.

The isolated environment of a galaxy forming in a void should also result in the formation and evolution of the galaxy with little external influence. A void galaxy should, in comparison to galaxies that do not form in voids, have fewer merger events throughout its lifetime.

### 1.2 Software pipeline

In this thesis, we start to investigate the effect of the environment on galaxy formation in cosmological  $N$ -body simulations. We implement a fully reproducible pipeline based on established cosmological software to generate a realisation of the matter distribution of the Universe, starting with generating the initial conditions. We identify haloes over the several generated time steps and build a merger-history tree based on these haloes. To model galaxies in the simulation, we use semi-analytical recipes that will generate the right trends over thousands of galaxies. Voids are identified using a watershed void finder. Based on this pipeline we identify void galaxies at redshift  $z = 0$  and compare chosen properties of these galaxies to all galaxies that were not found in a void.

### 1.3 Galaxy formation

In the first main application of this pipeline, we investigate if the environment of a cosmic void is a favourable environment for the formation of large, diffuse galaxies. These galaxies can usually be classified, observationally, as low surface brightness galaxies (LSBGs). We hypothesise that the effect on a galaxy of forming at the gravitational hill of a void should reduce the matter infall, or at least make it more constant over time, yielding a later collapse of the halo. Moreover, LSBGs are suspected to have a higher spin parameter that will naturally increase their disk size (if they are disk galaxies) and make them more diffuse. We thus chose to investigate the matter infall into haloes, the formation epoch, the spin parameter, the disk size of the galaxy and the virial radius of the halo. While we do not find any difference in the infall rates, we find significantly later formation epochs as well as higher spin parameters for void galaxies in comparison to non-void galaxies. This result is promising, as later formation epochs correspond to lower ambient mean matter densities, leading to lower dark matter halo densities, and may imply lower surface densities of disk galaxies.

### 1.4 Void detection via geometric optics

Beside their possible influence on galaxy formation, cosmic voids are used to probe cosmological models by studying the voids' size, growth, abundance, shape and how matter flows out of voids in cosmological simulations. The second part of this thesis presents an analysis of how structures identified in geometric-optics sky maps are related to the real, intrinsic three-dimensional structures. We estimate the effects exerted on light bundles propagating through a dark matter distribution generated in an  $N$ -body simulation that is placed at  $z = 0.5$ . We use the watershed mechanism to identify voids in the three-dimensional galaxy distribution that is generated using semi-analytical tools. These steps use the most of the stages of the pipeline introduced for the first part of the thesis. Independently from the watershed detection of voids, we calculate a projected surface overdensity map as well as maps of weak gravitational lensing and the Sachs geometric-optical scalars based on our simulated matter distribution and gravitational potentials. We propose and implement a novel, heuristically derived algorithm for detecting voids using their expected projected radial profiles derived from the geometric-optics maps.

Given the projected sky-plane centres of the three-dimensional watershed-detected voids, we find significant evidence of correlated void centres in the chosen projected quantities. Conversely, recovering the centres of the three-dimensional voids from the sky-plane information alone is significant using the weak-lensing shear or either of the Sachs optical scalars. This investigation shows preliminary evidence encouraging observational studies of gravitational lensing through individual voids, either blind or with spectroscopic/photometric redshifts. Moreover, our method is sensitive to the underlying dark matter distribution rather than the luminous matter distribution of galaxies. The combination of a few, or all, of the geometric-optics parameters might be developed into a void finder working only on the lensing signal, providing a unique method to trace voids in the dark matter distribution.

### 1.5 Thesis structure

The outline of this thesis is as follows. In chapter 2 we briefly review the standard cosmological model that underlies this work. The chapter is further divided into a discussion of the isotropic and homogeneous background model in Sect. 2.1.1, the different epochs of the background

model in Sect. 2.1.2 and finally how distances are defined in cosmology in Sect. 2.1.3. In Sect. 2.2 we explore the structures that we observe in the Universe. This section is divided into a brief discussion of cosmological linear perturbation theory in Sect. 2.2.1 that describes how matter perturbations evolve in the background Universe and an introduction to the cosmic web in Sect. 2.2.2. Sect. 2.3 discusses gravitational lensing and gives a short introduction to the theory of how an inhomogeneous matter distribution affects light propagation.

In chapter 3 we discuss the many numerical tools that we use and their theoretical justification. The chapter itself is structured to match the individual software packages, starting with the generation of initial conditions in Sect. 3.1. In Sect. 3.2 we explore briefly how to evolve an ensemble of dark matter particles, with the initial velocity perturbations and displacements from a perfectly regular grid, into the cosmic web structure that is observed. We discuss cosmic voids and how they can be detected using a watershed algorithm in Sect. 3.3. Dark matter haloes and how they are detected using a phase-space friends-of-friends algorithm are discussed in Sect. 3.4. Finally, we give a brief overview of semi-analytical galaxy formation recipes in Sect. 3.6.

Chapters 4–6 correspond to the individual publications directly relating to this thesis. In chapter 4 we present our galaxy formation pipeline and our first results investigating the role of the void environment on galaxy properties in cosmological  $N$ -body simulations. This chapter closely follows the published paper (Peper & Roukema, 2021), describing work of which a large majority was by me, implementing the tools and methods described above. Chapter 5 goes one step further and aims to study the link between the inner structures of the cosmic web and the properties of galaxies. This chapter describes the work that was mostly mine, using essentially the same tools as in Peper & Roukema (2021), but using  $N$ -body simulation outputs not generated by me. As of the date of submitting this thesis, this paper is still being finalised for submission (Jaber et al., 2023).

Finally, we present our analysis of light propagation through a matter distribution derived from cosmological  $N$ -body simulations for the detectability of voids in chapter 6. This chapter closely follows the submitted paper (Peper, Roukema, & Bolejko, 2023), describing work of which a large majority was by me, implementing the tools and methods described above.

Our general conclusions and outlook of this work are presented in chapter 7.

# Chapter 2

## Cosmology

### 2.1 The cosmological standard model

#### 2.1.1 The isotropic and homogeneous Universe

Cosmology is the scientific discipline that tries to answer questions such as: what the curvature and topology of the Universe are, how the Universe started, how the structures we observe today were generated, and how the Universe and the structures within will evolve in the future. Tremendous advances have been made in the last century on some of these questions, starting with the presentation of the theory of general relativity by Einstein (1915). Einstein's equations

$$R_{\mu\nu} - \frac{1}{2}g_{\mu\nu}R + \Lambda g_{\mu\nu} = \frac{8\pi G}{c^4}T_{\mu\nu}, \quad (2.1)$$

where  $R_{\mu\nu}$  is the Ricci tensor,  $R$  is the Ricci scalar,  $\Lambda$  is the cosmological constant and  $T_{\mu\nu}$  is the energy momentum tensor, locally link the geometry of the space-time with the energy density and model the trajectories of particles according to the given geometry. This soon was coupled with the cosmological principle, inspired from the Copernican principle. The Copernican principle is given as stating that we are typical observers in the Universe, and that the location of the earth, or, increasing the size of our reference point, the position of the solar system or the location of the Milky Way, is not specially favoured. Soon after the introduction of general relativity, in the 20s and 30s of the XXth century the scientists Alexander Friedmann, Georges Lemaître, Howard P. Robertson and Arthur Geoffrey Walker together are generally credited with finding a general, homogeneous and isotropic solution to the Einstein equations (Friedmann, 1922; Lemaître, 1927; Robertson, 1929; Walker, 1937). The homogeneity and isotropy assumption is the practical implementation of the cosmological principle. This model separates spacetime into a sequence of time snapshots of the spatial section of the Universe. Written in modern notation, the model defines the scale factor  $a(t)$ , with  $a = 1$  at the current time. The snapshots differ only in scale, in proportion to  $a(t)$ , and are given a coordinate system described as comoving, in which  $a(t)$  is ignored. In this sense, the cosmological principle became a pillar of modern cosmology. A more generic version of the principle is closer to the Copernican principle, and states that the Universe is statistically homogeneous and isotropic on large scales and thus any observer in the Universe will statistically make the same observations, rather than making identical observations.

The currently preferred model in this family of solutions has a finite age, which gives a finite-sized observable sphere. The observable sphere has a radius of roughly 14 Gpc (the calculation can be done with the formalism we briefly explain and by using eq. (2.15)). In the context of the

cosmological principle, large scales, above which we assume the cosmological principle to be a good approximation, means scales above  $\sim 100$  Mpc (Mukhanov, 2005).

Lemaître in 1927 (Lemaître (1927)) and Hubble in 1929 (Hubble, 1929) estimated the speed with which galaxies can be described as moving away from us (in the terminology of Newtonian cosmology) in proportion to their distance.

The proportionality factor is the Hubble–Lemaître parameter  $H$ , whose local value is called the Hubble constant  $H_0$ . The Hubble–Lemaître parameter is normally defined as

$$H(t) = \frac{\dot{a}(t)}{a(t)}, \quad (2.2)$$

where the dot denotes a derivative with respect to cosmic time. Lemaître interpreted his estimate in the context of his solution, implying an expanding Universe model.

The following decades showed that the homogeneous, isotropic solutions together with the expansion implied a hot, dense, plasma-dominated early phase of the Universe, where the plasma was in Planckian equilibrium, with a blackbody spectrum, and big bang nucleosynthesis (BBN) took place. The expansion, blackbody radiation and BBN together form the observational basis of the Hot Big Bang model. An early confirmation of this reasoning was found in 1941 by Andrew McKellar, who found blackbody radiation of 2.3K (McKellar, 1941), whose source he considered to be unknown. However, the importance of this measurement was only understood much later. The cosmic microwave background was postdicted (unknowingly, since lack of communication made it appear to be a prediction) in 1948 by Ralph Alpher and Robert Herman (Alpher & Herman, 1948a,b) and was again measured in 1965 by the radio engineers Arno Penzias and Robert Wilson who discovered an unexplainable radio noise in their data (Penzias & Wilson, 1965). The noise was identified to be the cosmic microwave background (CMB). The COBE (1992) observations of the early 90s showed it to be perfect black body radiation with a mean temperature of 2.725 K, see e.g. Fixsen (2009). In the top panel of fig. 2.1 we can see that the signal of the CMB indeed is isotropic. However, the advance in technology made it possible to detect fluctuations in the CMB map, shown in the other panels of fig. 2.1. Nowadays, we know these fluctuations as the CMB dipole (middle panel), which is a measure for our own velocity with respect to the background system of the Universe, and the real fluctuations in the CMB. The later ones are the measurable imprint of density perturbations, which originated in quantum fluctuations, at the time of last scattering, when the CMB photons were emitted (lower panel).

As observed by a sequence of observers at rest in the comoving coordinate system, a photon emitted by a distant galaxy at an epoch  $t$  with scale factor  $a(t)$  has a wavelength in the observers' frames that changes along the path from the galaxy to the observer at the Sun. As shown by Synge (1964) and reviewed by Narlikar (1994), the Minkowski spacetime wavelength in the observer's frame at the Sun is given by

$$1 + z := \frac{\lambda_{\text{obs}}}{\lambda_{\text{em}}} = \frac{a_0}{a} = \frac{1}{a}, \quad (2.3)$$

where  $z$  is called the cosmological redshift,  $\lambda_{\text{obs}}$  and  $\lambda_{\text{em}}$  are the observed and emitted wavelength and  $a_0 := 1$  is the current scale factor.

Based on the version of the cosmological principle in which the Universe is exactly homogeneous and isotropic and using the scale factor  $a(t)$ , the Friedmann–Lemaître–Robertson–Walker (FLRW) line element, in natural units, with spherical coordinates  $r$  (the comoving tangential arc-length for an angle of one radian, also called the “areal radius”, from “area” plus “-al”),  $\theta \in (0, \pi)$  and  $\phi \in (0, 2\pi)$ , is

$$ds^2 = -dt^2 + a^2(t) \left( dr^2 \lim_{r \rightarrow r'} \frac{1}{1 - k r'^2} + r^2 (d\theta^2 + \sin^2 \theta d\phi^2) \right), \quad (2.4)$$



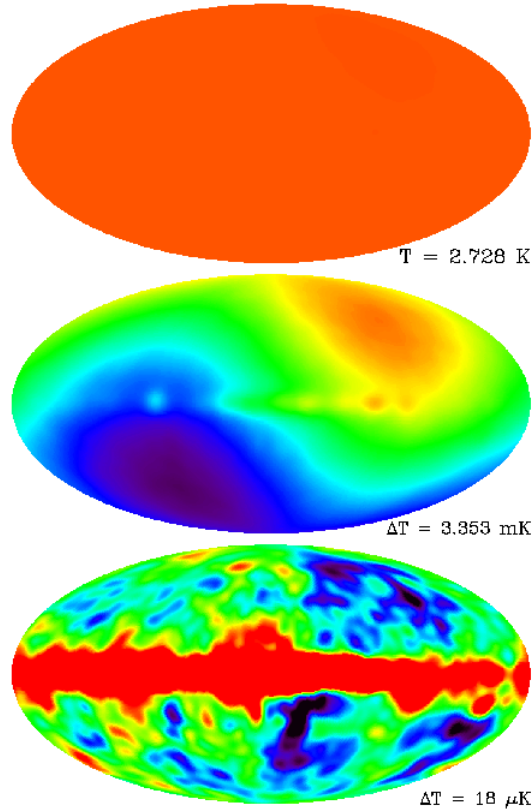



Figure 2.1: Cosmic microwave background constructed from Cosmic Background Explorer (COBE) Differential Microwave Radiometer (DMR) differencing measurements. In the top panel we see the monopole of the CMB as expected by the cosmological principle. In the middle panel the monopole is subtracted and one sees clearly a dipole is dominating. The bottom panel shows the CMB after also subtracting the dipole. In the equator of the bottom panel we see the emissions of the Milky Way dominating the emission and small fluctuations above and below the galactic plane. Image:  public domain, NASA: LAMBDA project/COBE DMR data COBE (1992)

where  $k$  is a constant representing curvature. The limit in the areal radius coordinate is required for the equator in the positive curvature case, because division by zero is undefined. Using the radial comoving distance,  $\chi$ , instead of the areal radius as a radial coordinate, and introducing the conformal time  $\eta$  via the relations  $dt = a(t)d\eta$  and  $\eta(t=0) = 0$ , and rewriting  $a$  as depending on  $\eta$ , the line element can be rewritten as

$$ds^2 = a^2(\eta) \left( -d\eta^2 + d\chi^2 + r^2(\chi) \left( d\theta^2 + \sin^2 \theta d\phi^2 \right) \right) \quad (2.5)$$

where the areal radius  $r(\chi)$  is given by

$$r(\chi) = \begin{cases} \frac{\sinh(\sqrt{-k}\chi)}{\sqrt{-k}}, & k < 0 \\ \chi, & k = 0 \\ \frac{\sin(\sqrt{k}\chi)}{\sqrt{k}}, & k > 0. \end{cases} \quad (2.6)$$

This line element (in either form) needs to be used in Einstein's equations (eq. (2.1)) to find solutions for  $a(t)$ , thus providing the basic equations for the curvature-related components of modern cosmology.

Homogeneity and isotropy of the Universe do not imply a flat ( $k = 0$ ) 3-dimensional spatial section. The other simply connected spaces are a 3-sphere, which is characterised by a positive curvature ( $k > 0$ ) is necessarily finite in volume (closed); and a 3-hyperboloid, which has a negative curvature ( $k < 0$ ), and may be open (infinite) or closed (finite). For each of these curvatures, many different topologies of space are now known to be possible (Luminet & Roukema, 1999, e.g.), well beyond the original multiply connected quotient of the 3-sphere proposed by Lemaître (1927). The relation between the topology of space and local dynamics was discovered theoretically earlier this century (Roukema et al. 2007; for more recent developments, see Vigneron & Roukema 2023 and references therein), but has not yet been detected observationally. A key-result of the era of precise cosmology is that as an observational fit, the spatial curvature is weak and thus a 3-dimensional Euclidean space indeed is a good approximation.

The content of the Universe is generally modelled as an ideal gas for which the energy–momentum tensor usually is written as

$$T_{\mu\nu} = u_\mu u_\nu (\epsilon + p) + g_{\mu\nu} p, \quad (2.7)$$

where  $\epsilon$  is the energy density,  $p$  is the pressure,  $u_\mu$  is the 4-velocity, and  $g_{\mu\nu}$  is the metric (eqs (2.4) or (2.5)). If not stated otherwise in the section, then we note that greek alphabet indices run over (0,1,2,3), where the 0th component is the time component, and latin alphabet indices run over (1,2,3), i.e. only the spatial components.

The spatial flatness of the standard model of the Universe additionally simplifies the areal radius to  $r(\chi) = \chi$  and the metric tensor to

$$g_{\mu\nu} = a^2(\eta) \eta_{\mu\nu}, \quad (2.8)$$

where  $\eta_{\mu\nu}$  is the Minkowski metric ( $\text{diag}(\eta_{\mu\nu}) = (-1, +1, +1, +1)$ ); unrelated to the conformal time  $\eta$ ).

The Friedmann equations, for any sign of curvature, are derived by inserting the FLRW line element, eqs (2.4) or (2.5), into Einstein's equations eq. (2.1), where the time–time component yields the first Friedmann equation (2.9) and the spatial components give the second Friedmann equation (2.10) as

$$H^2 = \frac{8\pi G}{3} \epsilon - \frac{k}{a^2} + \frac{\Lambda}{3} = \frac{8\pi G}{3} (\epsilon_m + \epsilon_r + \epsilon_\Lambda + \epsilon_k), \quad (2.9)$$

$$\dot{H} + H^2 = -\frac{4\pi G}{3} (\epsilon + 3p) + \frac{\Lambda}{3}. \quad (2.10)$$

In the first Friedmann equation we see that the evolution of the Universe is driven by the energy density of the Universe, though we split the energy into three reservoirs, matter  $\epsilon_m$ , radiation  $\epsilon_r$ , and the cosmological constant  $\epsilon_\Lambda$ , and write the curvature dimensionally as energy  $\epsilon_k$ . Originally, the cosmological constant was only introduced by Einstein to get a static solution for the Universe (Einstein, 1917). Starting with the first Friedmann equation we define the critical density  $\epsilon_c \equiv \frac{3}{8\pi G} H_0^2$  and the density parameters  $\Omega_{X0} = \epsilon_{X,0}/\epsilon_c$  where the  $X$  represents the various components in the Universe and the 0 denotes that we refer to the quantity measured today. The critical density is exactly the energy density of a model without spatial curvature and without a cosmological constant. Furthermore it follows from the definition of the critical energy density and eq. (2.9) that

$$\sum_X \Omega_X = 1. \quad (2.11)$$

To model the time evolution we need to model the time dependence of the different energy components. To do so we introduce an effective equation of state

$$p = w\epsilon, \quad (2.12)$$

where  $w$  is a parameter that will depend on the epoch of the Universe, i.e. it depends on which component dominates the energy budget of the Universe at a given epoch. For example for a universe that is matter dominated,  $w = 0$ .

By taking the covariant derivative  $\nabla_\mu T^{\mu\nu}$ , setting it to zero and only taking the  $\nu = 0$  component we recover the conservation law

$$\dot{\epsilon} = -3H(\epsilon + p). \quad (2.13)$$

If we insert eq. (2.12) into eq. (2.13), then we can solve the differential equation in time and get the time dependence of the different energy components. Insertion of the previous result into the first Friedmann equation eq. (2.9) and solving it in terms of the scale factor yields the different scale factor relations for each epoch. The solutions can be characterised as

$$\begin{aligned} \epsilon &\propto a^{-3} \quad \text{and} \quad a \propto \eta^2 \propto t^{2/3}, \quad \text{for } w = 0 \quad (\text{matter dominated}), \\ \epsilon &\propto a^{-4} \quad \text{and} \quad a \propto \eta \propto t^{1/2}, \quad \text{for } w = \frac{1}{3} \quad (\text{radiation dominated}), \\ \epsilon &= \text{const} \quad \text{and} \quad a \propto e^{H_i t}, \quad \text{for } w = -1 \quad (\text{vacuum/dark energy dominated; } H_i = \text{constant}). \end{aligned} \quad (2.14)$$

With this result, and using  $\epsilon_k \propto a^{-2}$  by definition, we can rewrite the implicitly time dependent form of eq. (2.9) as

$$H^2 = H_0^2 \left[ \Omega_{m0}(1+z)^3 + \Omega_{r0}(1+z)^4 + \Omega_{\Lambda 0} + \Omega_{k0}(1+z)^2 \right]. \quad (2.15)$$

However, in contrast to eq. (2.15) which contains the full expression, the standard cosmological model a few decades ago was the Einstein–de Sitter model that assumed a Universe which is completely matter dominated, with no cosmological constant. This model faced several problems. A significant problem was the age crisis. A universe which only consists of matter,  $\Omega_m = 1$ , and has a Hubble constant of roughly  $H_0 = 70 \text{ km}/(\text{Mpc s})$  can be calculated by solving the differential equation eq. (2.15) in time and yields an age of the Universe of roughly 9 Gyr. In the 90s of the previous century, measurements of globular clusters and measurements of radioactive isotopes such as  $^{232}\text{Th}$  in stars (Butcher, 1987; Morell et al., 1992) already yielded a much older Universe. The unexpected solution came with the faint galaxy counts, correlation functions and redshift distribution constraints in the early 90s (Fukugita et al., 1990; Roukema & Yoshii, 1993; Yoshii & Peterson, 1995), and gravitational lensing estimates (Fort et al., 1997) and new data of supernovae Ia in the late 90s that indicated an acceleration of  $a(t)$  (Riess et al., 1998; Schmidt et al., 1998; Perlmutter et al., 1999). Supernovae Ia are empirically standardisable candles that allow for statistically precise distance measurements.

We visualise this trend in fig. 2.2 taking data from the Supernova Cosmology Project ‘‘Union2.1’’ SN Ia compilation, which includes 19 datasets and 580 supernovae Suzuki et al. (2012). For a flat universe, the conclusion to corresponding to an accelerated scale factor is to set the cosmological constant to a positive value. For comparison, we show a curve for a hyperbolic Universe with  $\Omega_{m0} = 0.3$  and  $\Omega_{k0} = 0.7$ , which matches the data less well than a model with a cosmological constant. Today, we denote this energy component more generally as ‘‘dark energy’’; this dominates the total energy budget of the Universe. This discovery led to the success of the  $\Lambda$  Cold Dark Matter ( $\Lambda\text{CDM}$ ) model that matches most of extragalactic

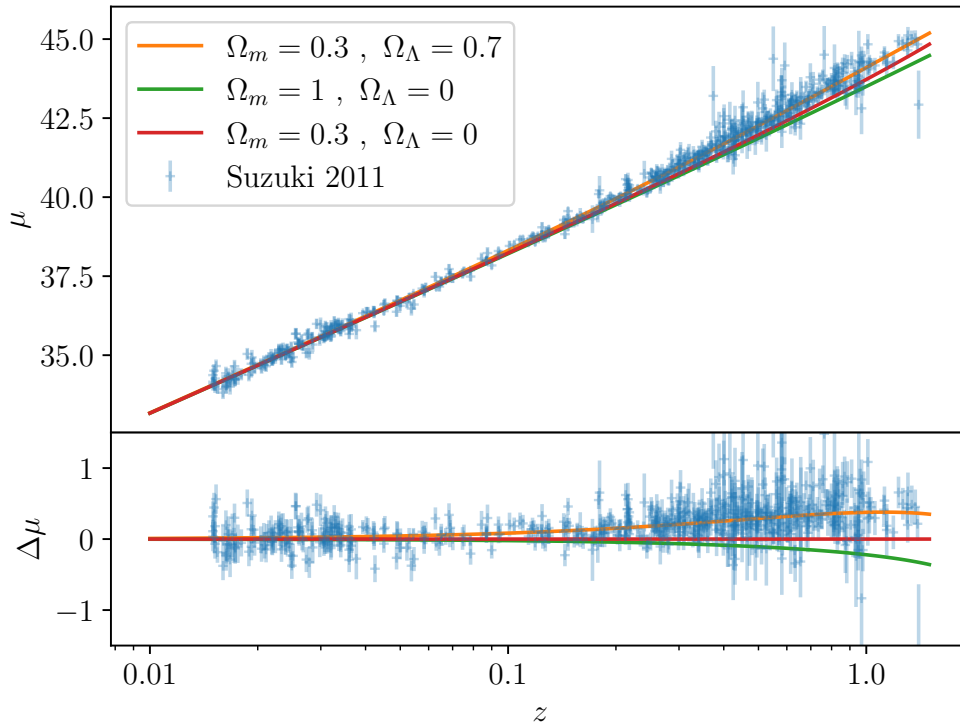


Figure 2.2: Compilation of supernovae distance measurements using the data provided in Suzuki et al. (2012); the style is adapted from e.g. fig. 4 of Riess et al. (1998). The upper panel shows the distance modulus  $\mu$  of supernovae versus their measured redshift. For visualisation we present three different, exact cosmological solutions, an  $\Lambda$ CDM Universe (orange), an Einstein–de Sitter Universe (green) and a hyperbolic Universe with negative curvature (red). The lower panel shows the distance modulus residuals comparing to the hyperbolic model characterised by  $\Omega_{m0} = 0.3$ ,  $\Omega_{\Lambda0} = 0$ . The best fit model for the supernovae data is the  $\Lambda$ CDM model.

observations reasonably well. Recent CMB measurements of the Planck collaboration give the following best-fit parameter for the fundamental cosmological parameters (Planck Collaboration et al., 2020):

$$\begin{aligned} \Omega_{m0} &= 0.315 \pm 0.007, & \Omega_{r0} &\leq 10^{-4},^1 \\ \Omega_{k0} &= 0.001 \pm 0.002, & \Omega_{\Lambda0} &= 0.685 \pm 0.007. \end{aligned} \quad (2.16)$$

<sup>1</sup>This value is taken from Gorbunov & Rubakov (2011).

## 2.1.2 Epochs of the Universe

In the previous section we derived the basic equations that govern the evolution of the background model – the exact solution of Einstein’s equations. The cosmological model also includes density perturbations. These density perturbations will grow and form the observable structures, most prominently the luminous galaxies. Their growth rate depends on the background model, i.e. which component in eq. (2.15) dominates the Universe at a given time. Thus, we first derive an estimate for when each component dominated the Universe. In cosmology, the scale factor, and equivalently via eq. (2.3), the redshift of an object that emitted photons when the scale factor had that value and is observed today, is often used equivalently to the cosmic time. A slice of the Universe today is parametrised this way by  $z = 0$ . The time slicing by redshift approaches infinity if we extend the matter-dominated (or radiation-dominated) to earlier epochs naïvely to  $t \rightarrow 0^+$ . However, a more physical limit is the epoch of last scattering, which is approximately  $z = 1100$ . Moreover, we saw that modern measurements show the Universe’s scale factor is best-approximated as accelerating, whereas in an Einstein–de Sitter model, the Universe’s scale factor would be decelerating. We know that the Universe today is  $\Lambda$  dominated. The transition to a  $\Lambda$  dominated Universe must have happened in the younger history of the Universe, during the epoch of galaxy formation. Hence, we neglect the curvature and the radiation component for the following estimates.

From eq. (2.15) we derive

$$\dot{a}^2 = H_0^2 \left( \Omega_{m0} \frac{a_0^3}{a} + \Omega_{\Lambda 0} a^2 \right). \quad (2.17)$$

Taking another time derivative of this expression yields

$$\ddot{a} = \frac{a}{2} H_0^2 \left( 2\Omega_{\Lambda 0} - \Omega_{m0} \left( \frac{a_0}{a} \right)^3 \right). \quad (2.18)$$

Measurements today indicate that  $2\Omega_{\Lambda 0} > \Omega_{m0}$  and thus that the scale factor is accelerating. However, for sufficiently high redshifts the above equation states that the second derivative of the scale factor becomes negative, thus the transition from deceleration to acceleration occurred in our recent history in the Universe at a redshift of  $z_{m-\Lambda\text{-eq}} = (2\Omega_{\Lambda 0}/\Omega_{m0})^{1/3} - 1 \approx 0.63$  using the values in eq. 2.16.

When we continue to go back in time it becomes clear from eq. (2.15) that in the early Universe there must have been a time when radiation dominated the total energy budget. In cosmology, the term “radiation” is used loosely to refer to all relativistic particles. A relativistic neutrino at the time of last scattering can well be non-relativistic today and hence change the sector to which it contributes energy. The epoch of equilibrium can be inferred from the time dependencies we discovered in eq. (2.14),

$$1 + z_{r-m\text{-eq}} = \frac{a_0}{a_{\text{eq}}} \approx \frac{\Omega_{m0}}{\Omega_{r0}} \sim 10^4. \quad (2.19)$$

The temperature, or energy, decreases over time proportionally to the redshift. Thus we can write

$$T_{\text{eq}} = T_0(1 + z_{r-m\text{-eq}}) \sim 10^4 \text{K} \sim 1\text{eV}. \quad (2.20)$$

This is a simplified approach; for a better estimate we would need to include effect of the three neutrino species. Such a precise calculation yields according to Gorbunov & Rubakov (2011) a temperature of  $T_{\text{eq}} = 0.76 \text{ eV}$  and via eq. (2.20) a redshift of roughly 3265. Before this time the

Universe was very hot and dense. Its dominant physical content was a dense plasma in which photons were not able to propagate freely. The observed CMB can be understood as an echo of this epoch as it contains the information physically encoded during the epoch. We can now explain the term used above, “last scattering”: this means the epoch when the density of the Universe dropped to a level where photons were able to propagate freely; these first photons are now measured as the CMB.

Before that time there were no atoms, and the Universe was too hot for light nuclei to form. We are now considering the epoch of big bang nucleosynthesis (BBN), which will provide crucial insights into the chemical composition of our Universe. We limit ourselves to the formation of light nuclei. The first nucleon that will freeze out of the plasma is the neutron due to its higher mass compared to protons. The fundamental interaction that we consider is



For a particle of type  $X$  the number density can be given as

$$n_X = g_X \left( \frac{m_X T}{2\pi} \right)^{3/2} \exp((\mu_X - m_X)/T), \quad (2.22)$$

where  $g$  is the number of degrees of freedom of the particle,  $m$  is the mass,  $T$  is the temperature and  $\mu$  is the chemical potential. The process eq. (2.21), as long as the energy is sufficiently high, is in equilibrium meaning that the chemical potentials fulfil

$$\mu_p + \mu_e = \mu_n + \mu_\nu. \quad (2.23)$$

The chemical potentials  $\mu_e$  and  $\mu_\nu$  are negligible compared to the others, see e.g. Gorbunov & Rubakov (2011) Chapter 8, which lets us relate the number densities of neutrons and protons by

$$\frac{n_n}{n_p} = \exp(-(m_n - m_p)/T), \quad (2.24)$$

where we set  $m_n/m_p \approx 1$  and used that both particles have the same degrees of freedom for the spin. To estimate the freeze-out time we compare the interaction rate  $\Gamma$  of the proton-to-neutron interaction (eq. (2.21)) to the Hubble time ( $1/H_0$ ). We can express the interaction rate as

$$\Gamma = n_\nu \langle \sigma v \rangle, \quad (2.25)$$

where  $n_\nu = n_{\nu_0} (1+z)^3 = n_{\nu_0} (T/T_0)^3 \propto T^3$  is the neutron number density and  $\langle \sigma v \rangle$  is the averaged cross section for the process. The cross section can be calculated with tools from quantum theory, using effective field theory, which is valid only for low energies. Such a calculation would be out of the scope of this thesis, so we only present the result that  $\langle \sigma v \rangle \propto G_F T^2$ , where  $G_F$  is the Fermi constant. The freeze-out happens when  $\Gamma \approx H$ . In eq. (2.14) we derived how the scale factor scales in a radiation dominated Universe, so we can estimate the Hubble rate at the time as  $H \approx T^2/M_{\text{pl}}$  with  $M_{\text{pl}}$  being the Planck mass. Using the above relations yields the rough estimate for the freeze-out temperature of

$$T_f \approx 1 \text{ MeV}, \quad (2.26)$$

which converts to a neutron to proton fraction of

$$\frac{n_n}{n_p} = \frac{1}{6}. \quad (2.27)$$

With this simple estimate we can conclude how much matter ends up in hydrogen and helium. If we assume that all neutrons end up in helium, then we can write the fraction of helium as

$$Y_p = \frac{4n_{\text{He}}}{n_b} = \frac{4(1/2n_n)}{n_p + n_n} = \frac{2\frac{n_n}{n_p}}{1 + \frac{n_n}{n_p}} \approx \frac{1}{4}, \quad (2.28)$$

where  $n_b$  is the number density of all baryons (protons and neutrons). This very simplistic approach yields that 25% of the protons end up in helium. Isotopes with proton numbers of  $A = 5$  and  $A = 8$  are not stable and will eventually decay again. Three-particle interactions are unlikely. Thus we approximate that no heavier elements are formed at BBN. We conclude that 75% of the mass initially must be in the form of hydrogen, which eventually will form and fuel stars and lead to remnants in planetary disks around the stars that will allow life to form in (at least) one planetary system.

For completeness, we would like to mention cosmic inflation. Inflation is an early epoch of exponential expansion that is hypothesised to solve problems that came up within the  $\Lambda$ CDM model, e.g. the flatness problem and the horizon problem. These problems are the questions of why the curvature is fine tuned to be “extremely close” to zero and why the CMB has a universal, nearly uniform temperature over the whole sky. Within the observable sphere to the limit of last scattering, many areas are not causally connected at the epoch of CMB emission if we limit the early universe model to the radiation dominated behaviour of  $a(t)$ . These areas would not have been able to interact and achieve a uniform temperature through a process tending towards equilibrium. In eq. (2.14) we derived the growth of the scale factor for this epoch which is characterised by a negative effective pressure. This is equal to the assumption that the epoch of inflation is dominated and driven by a scalar field. Small perturbations are stretched during the inflationary period and dependent on their size they may grow larger than the size of the horizon. These modes are considered to be frozen as they cannot evolve and causally interact with the structures in the Universe.

In cosmology we distinguish between subhorizon

$$\lambda_{\text{ph}} \ll \frac{1}{H}, \quad \text{or equivalently } k\eta \gg 1, \quad (2.29)$$

and superhorizon

$$\lambda_{\text{ph}} \gg \frac{1}{H}, \quad \text{or equivalently } k\eta \ll 1, \quad (2.30)$$

Fourier modes of density perturbations. This process is sketched in fig. 2.3 where we sketch how the inverse of the Hubble parameter, named the Hubble length or the particle horizon, evolves over the different epochs of the Universe. As shown in eq. (2.14), the dependence of the Hubble scale  $1/H$  on the scale factor will be different in each different epoch, but the growth in the physical length scale of a fixed comoving scale  $\lambda_{\text{pert}}$  will always, by definition, by proportion to  $a(t)$ . During exponential growth, when the Hubble parameter is a constant, modes can freeze. They can re-enter the horizon during the radiation or matter dominated epoch. The perturbations that enter the horizon or never froze are the seeds of structure formation and eventually led to structure in the observable Universe.

As the  $\Lambda$ CDM model suggests, we are now in the dark energy dominated epoch of the Universe, where the Hubble length is again approaching a constant. Thus, modes above a certain wavelength will never re-enter the horizon. In order to solve the previously mentioned problems of the standard model, we need around 60 e-foldings (factors of e in the growth of  $a(t)$ ). The epoch of inflation was short. The initial time is approximately given by the Planckian time

$t_i = 10^{-43} s$ . For the simplest models it should end at about  $t_f \sim 10^{-34} s - 10^{-36} s$  (Mukhanov, 2005). After the exponential growth of the Universe, the density and thus the temperature should have dropped significantly. To return to the conditions of the standard Hot Big Bang model, we need to reheat the Universe, which is modelled by the decay of the scalar field that caused inflation.

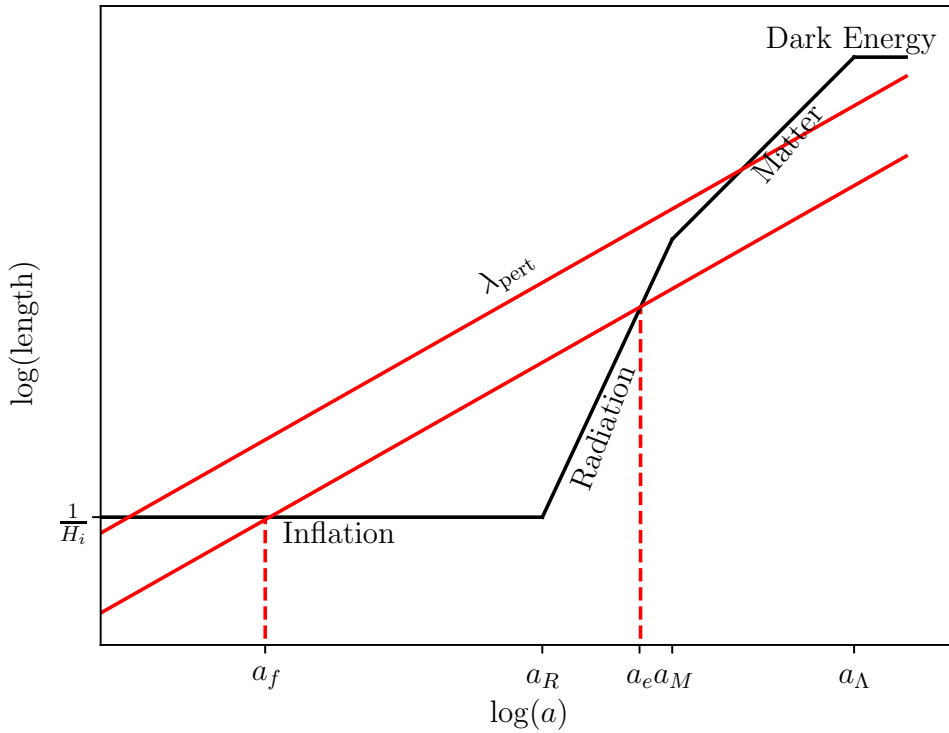


Figure 2.3: This figure sketches the behaviour of the Hubble length  $\frac{1}{H}$  and the wavelength of two perturbations over time following the solutions of the background model presented in eq. (2.14). While the horizon stays constant during inflation the perturbations grow and, given an initial size, eventually a certain range of perturbations will freeze out during inflation, sketched at the time  $a_f$ . During the radiation and matter dominated epochs of the Universe these modes can re-enter the horizon, visualised by the event  $a_e$ . Once these initial perturbations have entered the horizon again, they can evolve and will grow into the structures we see in the Universe. The figure is adapted from Kolb & Turner (1990).



### 2.1.3 Distances in Cosmology

Measurements of the distance to astronomical objects are not trivial. For close objects, we can use the parallax method, which compares the apparent movement of nearby objects with the quasi static celestial position of faraway stars. The first reliable measurements of distances using the parallax method goes back to Friedrich Bessel in the early 19th century. The second step of the ladder uses the Hertzsprung–Russell diagram, in which Antonia Maury’s stellar classification (Maury & Pickering, 1897) played a key role (Hoffleit, 1994). This diagram relates the luminosity (the energy emitted per second in the rest frame) of stars – obtained thanks to parallaxes – to their colour. Since colour only changes weakly with distances to stars in the Galaxy, this step extends the distance to which stellar distances can be estimated. The third step uses cepheids, which can be understood as pulsating stars. The period of the pulses is very stable for this special class of stars. The relation between the frequency of the pulse strongly correlates to the luminosity of a cepheid. Hence, it was possible to expand the distance ladder by another step. Another step in the distance ladder uses supernovae of type Ia, which, as mentioned before, are standardisable candles, for which luminosities can be estimated to within a few tenths in the absolute magnitude. Since the late nineteenth century, the measurement of the spectra of stars has been a key element of observational astronomy. In these spectra we can identify characteristic absorption lines at a sharply defined energy level. As mentioned above, the energy in the reference frames of a sequence of fundamental observers scales with the expansion as  $\nu_o = \nu_e / (1 + z)$ . Thus, we can measure the redshift of an object by measuring the shift in the redward direction (towards lower frequencies) using its spectroscopic data.

We now consider the question, above left hidden, of how to define distance in a relativistic cosmological model. Photons travel along null geodesics, with a zero invariant interval from their emission to absorption, so there is no physically intrinsic distance travelled by a photon. Instead, “the distance a photon travels” is only defined after choosing a method of projecting a photon’s trajectory into spatial sections of a universe model.

For a light ray we can set the condition  $ds^2 = 0$  in eq. (2.5) and derive the expression, for any of the curvatures of an FLRW model, relating conformal time to the lookback distance,

$$d_{\text{lookback}} = \int_{\chi}^0 a(\chi') d\chi' = \int_{\eta}^{\eta_0} a(\eta) d\eta' = \int_t^{t_0} dt' = t_0 - t, \quad (2.31)$$

where  $\chi$  is the comoving distance, as above, with values  $\chi$  at the distance of an observed galaxy and zero at the observer;  $\eta$  is the conformal time, as above, with values  $\eta$  at the epoch of an observed galaxy and  $\eta_0$  at the observer; and  $t$  is the cosmic time, as above, with values  $t$  at the epoch of an observed galaxy and  $t_0$  at the observer.

The radial comoving distance  $\chi$  is sometimes also called the “coordinate distance”:

$$d_C := a_0 \chi := \chi. \quad (2.32)$$

The path of the light can be projected to the current time, making the path length  $\chi$ .

Alternatively, a small interval in the radial direction can be projected to the spatial slice at the epoch, giving what is called a “physical distance”, i.e. the radial comoving distance interval times the scale factor,

$$d_{\text{phys}} := \int_{\chi_1}^{\chi_2} a(t) d\chi' \approx a(t_{\text{mid}}) \int_{\chi_1}^{\chi_2} d\chi' = a(t_{\text{mid}}) (\chi_2 - \chi_1) = (1 + z_{\text{mid}}) (\chi_2 - \chi_1), \quad (2.33)$$

where  $t_{\text{mid}}$  is an average of  $t_1$  and  $t_2$ . This physical distance grows with the expansion of the Universe, which was already seen in the Hubble–Lemaître law (which itself can be used to infer

naïve Hubble–Lemaître distances, that differ from the relativistically justified distances discussed here). This physical distance is appropriate for the study of the local physics of galaxies and the cosmic web over a short enough distance interval, in the radial direction from the observer.

Via the condition derived from the line element  $-dt = a(t)d\chi$  and with the derivation of the cosmological redshift we can find the relation for the comoving distance to  $a(t)$  or  $H(t)$ , with

$$d_C(z) = \int_0^z \frac{dz'}{H(z')}. \quad (2.34)$$

The next “distance” needed is the areal radius  $r(\chi)$  given in eq. (2.6) above for the three signs of curvature. This is the comoving length of an arc of one radian in angular size. An observationally useful distance measure derived from the areal radius is the angular diameter “distance”, which is the physical length of an arc of one radian in angular size, i.e.

$$D_A = a(\chi) r(\chi). \quad (2.35)$$

The reason for the name is that it is the distance at which an object would be placed if its physical size  $x_{\text{obj}}$  and its measured angular size  $\theta$  were interpreted in a static Euclidean space, ignoring the relativistic derivation. The physical size  $x_{\text{obj}}$  is  $\theta$  times the physical arc length, so  $x_{\text{obj}} = \theta a(\chi) r(\chi)$ , giving this static-Euclidean-interpreted distance as

$$\frac{x_{\text{obj}}}{\theta} = a(\chi) r(\chi) = D_A. \quad (2.36)$$

Yet another useful distance measure is the luminosity distance, which relates the luminosity  $L$  of an object to its emitted photon flux  $F$ . It is defined as

$$d_L = \sqrt{\frac{L}{4\pi F}}, \quad (2.37)$$

where  $F$  is the bolometric flux of photons (e.g. in erg/s), motivated by analogy with the inverse square laws of static Euclidean space.

The comoving area of a sphere crossed by photons, emitted by a source at the centre of the sphere, can be calculated using the areal radius (hence the name “areal”) as

$$A(z) = 4\pi r^2(\chi). \quad (2.38)$$

Let us heuristically motivate an expression for the flux  $F$ . The photon flux is defined as the energy of photons crossing through the area  $A$  per unit time. Classically imagining particles being emitted from a point source, it is clear that that the summed energy of photons, equivalently the number of photons, crossing a fixed number of square cm, for example, is inversely proportional to  $A$ . Additionally, the flux will be proportional to  $(1+z)^{-2}$  due to two projection effects – the redshifting of a photon and time dilation – so that the full expression for the flux, measured on Earth, can be written as

$$F = \frac{L}{(1+z)^2 A(z)} = \frac{L}{4\pi(1+z)^2 r^2}. \quad (2.39)$$

Inserting this relation into eq. (2.37) we find the relation between the areal distance (comoving one-radian arc length), the angular diameter distance and the luminosity distance is

$$d_L = (1+z) r = (1+z)^2 D_A. \quad (2.40)$$

By introducing the distance modulus, for  $d_L$  given in Mpc,

$$\mu = m - \mathcal{M} = 5 \log(d_L) + 25, \quad (2.41)$$

where  $m$  is the measured bolometric apparent magnitude and  $\mathcal{M}$  is the absolute bolometric magnitude, we can derive the model curves in fig. 2.2.

## 2.2 Structure Formation

In fact, the assumption of a homogeneous and isotropic Universe is a strong simplification. Measurements of the spatial distribution of galaxies show instead a highly inhomogeneous distribution. Matter clumps into clusters of high density connected by dense filaments and walls. Between these overdense regions we measure large underdense regions that we call cosmic voids. Sloan Digital Sky Survey (SDSS) observations suggest that voids fill up to 70% of spatial volume (Mao et al., 2017). These structures form the cosmic web, which is well observed and can be reproduced very well by simulations.

### 2.2.1 Linear Perturbation Theory

In this section we discover a short approach to investigate the evolution of matter perturbations without going into the details of cosmological perturbation theory. For the first part of this section we follow the excellent description of Mukhanov (2005). We assume small perturbations, keeping only linear order perturbations, and thus the perturbed components of the Einstein equations, the metric and the energy momentum tensor, will be written as

$$g_{\mu\nu} = g_{\mu\nu}^{(0)} + \delta g_{\mu\nu} \quad \text{and} \quad T_{\mu\nu} = T_{\mu\nu}^{(0)} + \delta T_{\mu\nu}. \quad (2.42)$$

In the leading order of perturbation theory, scalar, vector and tensor perturbations decouple and we can decompose the metric into these different parts. Using Helmholtz–Hodge decomposition, we can rewrite  $\delta g$  explicitly as

$$\delta g = a^2 \begin{pmatrix} -2\phi & -(B_{,i} + B_i) \\ -(B_{,i} + B_i) & 2\psi\delta_{ij} + 2E_{,ij} + F_{i,j} + F_{j,i} + h_{ij} \end{pmatrix}. \quad (2.43)$$

The scalar perturbations  $\phi$ ,  $\psi$ ,  $B$ , and  $E$  exhibit gravitational instability and thus lead to structure formation. They are induced by inhomogeneities in the energy density. The vector perturbations are described by the vectors  $F_i$  and  $S_i$  and are related to the rotational motion in fluids. They decay very quickly and thus are less important than the other perturbations. The tensor perturbations  $h_{ij}$  are related to gravitational waves.

This section aims to give a rough overview about structure formation and the growth of perturbations, which eventually lead to the formation of the structures we observe in the Universe. As matter perturbations are described by scalar perturbations, the discussion here is mostly restricted to scalar perturbations alone. However, before we can investigate the time dependence of scalar perturbations, we need to fix all degrees of freedom in eq. (2.43). The necessity of fixing the degrees of freedom becomes clear when we consider that there is a transformation

$$g_{\mu\nu}^{(0)}(x^\alpha) + \delta g_{\mu\nu}(x^\alpha) = g_{\mu\nu}^{(0)}(y^\alpha), \quad (2.44)$$

in which the perturbations are only an artifact of transforming from coordinate system  $x^\alpha$  to system  $y^\alpha$ . By fixing the degrees of freedom we only consider physical perturbations of the metric. The following calculation will be carried out in conformal coordinates. Let us consider the coordinate transformation

$$x^\alpha \rightarrow \tilde{x}^\alpha = x^\alpha + \xi^\alpha, \quad (2.45)$$

where  $\xi^\alpha$  are infinitesimally small functions of space and time. Under such a transformation the metric tensor will take the form

$$\tilde{g}_{\mu\nu}(\tilde{x}^\rho) = \frac{\partial x^\gamma}{\partial \tilde{x}^\mu} \frac{\partial x^\delta}{\partial \tilde{x}^\nu} g_{\gamma\delta}(x^\rho) = g_{\mu\nu}^{(0)}(x^\rho) + \delta g_{\mu\nu} - g_{\gamma\nu}^{(0)} \xi_{,\mu}^\gamma - g_{\mu\delta}^{(0)} \xi_{,\nu}^\delta + \mathcal{O}(\xi^2), \quad (2.46)$$

where we ignore higher orders of  $\xi$ . With this expression we directly see that the perturbed part of the metric tensor consists of

$$\delta\tilde{g}_{\mu\nu} = \delta g_{\mu\nu} - g_{\mu\nu,\delta}^{(0)}\xi^\delta - g_{\delta\nu}^{(0)}\xi_{,\nu}^\delta - g_{\mu\gamma}^{(0)}\xi_{,\mu}^\gamma. \quad (2.47)$$

Together with eq. (2.43) we now can write down the perturbations in the new coordinate system and find

$$\begin{aligned} \tilde{\phi} &= \phi - \frac{a'}{a}\xi^0 - \xi^{0'}, & \tilde{\psi} &= \psi - \frac{a'}{a}\xi^0, & \tilde{B} &= B + \zeta' - \xi^0 \\ \tilde{B}_i &= B_i + \xi'_{\perp i}, & \tilde{E} &= E - \zeta, & \tilde{F}_i &= F_i - \xi_{\perp i}, \end{aligned} \quad (2.48)$$

where we again used the Helmholtz decomposition  $\xi^i = \xi_{\perp}^i + \zeta^i$ . The line element for scalar perturbation, only including  $\phi$ ,  $\psi$ ,  $B$ , and  $E$  now can be expressed as

$$ds^2 = a^2 \left[ -(1 + 2\phi) d\eta^2 - 2B_{,i} d\eta dx^i + [(1 + 2\psi)\delta_{ij} + 2E_{,ij}] dx^i dx^j \right]. \quad (2.49)$$

Moreover, we see in eq. (2.48) that only  $\xi^0$  and  $\zeta$  occur in the scalar perturbations which means that we have two degrees of freedom. Gauge freedom now can be used to make any of the variables vanish. The simplest gauge invariant – linear combinations of these functions – are the Bardeen potentials

$$\Phi = \phi - \frac{1}{a} [a(B + E')] \quad \text{and} \quad \Psi = \psi - \frac{a'}{a} (B - E'). \quad (2.50)$$

Probably the most famous, and most used, gauges are the conformal gauge and the synchronous gauge. The conformal-Newtonian gauge is defined by fixing

$$B_N = E_N = 0. \quad (2.51)$$

It is therefore also called longitudinal gauge or shear-free gauge since, as we can see in the line element, there is no shear in an expanding volume element in this gauge. The line element takes the form

$$ds^2 = a^2 \left[ -(1 + 2\Phi) d\eta^2 + (1 + 2\Psi)\delta_{ij} dx^i dx^j \right], \quad (2.52)$$

which we use again in section 6. We see later that in a universe without anisotropic stress we have  $\Phi = -\Psi$ . Conformal-Newtonian gauge is popular due to its very simple form as it only has a diagonal component. The name is inspired by the physical understanding of the role of  $\Phi$  and  $\Psi$ . As we will see  $\Phi$  fulfils a Poisson-like equation and is thus the generalization of the Newtonian potential that describes the volume expansion, whereas  $\Psi$  describes the spatial curvature.

In chapter 2.3 & 6 we work in conformal-Newtonian gauge. However, as we aim to give a rather complete overview, synchronous gauge will also be mentioned. As the name suggests, all clocks in all points of space are synchronized in this gauge (Landau & E.M.Lifschitz, 2009). This can be achieved by a vanishing  $\delta g_{0\alpha}$  component. Additionally, we need the condition  $g_{00} = -1$ , which in our notation means  $\phi_S = B_S = 0$ . The line element thus takes the form

$$ds^2 = a^2 \left[ -d\eta^2 + [(1 + 2\psi_s)\delta_{ij} + 2E_{,ij_s}] dx^i dx^j \right]. \quad (2.53)$$

A disadvantage of this gauge, in contrast to the conformal-Newtonian gauge, is that it is not uniquely fixed. There exists a whole class of synchronous coordinate systems. However, the importance of this gauge is nevertheless crucial as it is used in many numerical codes, e.g. in CLASS (Blas et al. 2011; this code is public, but currently distributed under a non-free licence).

With the metric fully defined we can derive the Christoffel symbols of the second kind (symmetric definition)

$$\Gamma_{\mu\nu}^{\rho} = \frac{1}{2}g^{\rho\sigma} (g_{\sigma\nu,\mu} + g_{\mu\sigma,\nu} - g_{\mu\nu,\sigma}), \quad (2.54)$$

and the Riemann tensor

$$R_{\sigma\mu\nu}^{\rho} = \Gamma_{\nu\sigma,\mu}^{\rho} - \Gamma_{\mu\sigma,\nu}^{\rho} + \Gamma_{\mu\alpha}^{\rho}\Gamma_{\nu\sigma}^{\alpha} - \Gamma_{\nu\alpha}^{\rho}\Gamma_{\mu\sigma}^{\alpha}. \quad (2.55)$$

By contracting the first and third index of the Riemann tensor we derive the Ricci tensor  $R_{\mu\nu}$  and hence have the full left-hand side of the Einstein equations (eq. (2.1)). For the sake of brevity we do not derive the explicit expressions of the above relations. The right-hand side consists of the energy–momentum tensor for which we assume a perfect fluid yielding

$$T_{\nu}^{\mu} = (\epsilon + p)u^{\mu}u_{\nu} + p\delta_{\nu}^{\mu}. \quad (2.56)$$

We decompose the energy density and the pressure into a background and a perturbation as  $\epsilon = \bar{\epsilon} + \delta\epsilon$  and  $p = \bar{p} + \delta p$ . For the 4-velocity, we use the same decomposition, thus

$$\bar{u}^{\mu} = \begin{pmatrix} u^0 \\ \vec{0} \end{pmatrix} \quad \text{and} \quad \delta u^{\mu} = \begin{pmatrix} \delta u^0 \\ \vec{v} \end{pmatrix}. \quad (2.57)$$

The velocity is a time-like vector that, with our sign convention, will always fulfil  $u_{\mu}u^{\mu} = -1$  and therefore we can show that the velocity decays as

$$u^{\mu} = \frac{1}{a} \begin{pmatrix} 1 - \Phi \\ \vec{v} \end{pmatrix}. \quad (2.58)$$

Finally, we use the Helmholtz theorem again to decompose the velocity perturbation into a scalar and a vector field  $v_i = v_{,i} + v_{\perp i}$  and derive an expression for the energy–momentum tensor in first order perturbation theory

$$\delta T_{\nu}^{\mu} = \begin{pmatrix} -\delta\epsilon & (\bar{\epsilon} + \bar{p})v^{,i} \\ -(\bar{\epsilon} + \bar{p})v_{,j} & \delta p \delta_j^i \end{pmatrix}. \quad (2.59)$$

Having also the right-hand side expression of the Einstein equations we now can express these equations including the perturbations yielding

$$\Delta\Phi - 3\mathcal{H}(\Phi' + \mathcal{H}\Phi) = 4\pi G a^2 \delta\epsilon, \quad (2.60)$$

$$(\Phi' + \mathcal{H}\Phi)_{,i} = 4\pi G a^2 (\bar{\epsilon} + \bar{p})v_{,i}, \quad (2.61)$$

$$[-\Psi'' + \mathcal{H}(-2\Psi + \Phi)' + (2\mathcal{H}' + \mathcal{H}^2)\Phi + \frac{1}{2}\Delta(\Phi + \Psi)]\delta_{ij} - \frac{1}{2}(\Phi + \Psi)_{,ij} = 4\pi G a^2 \delta p \delta_{ij}, \quad (2.62)$$

where  $\Delta := \nabla \cdot \nabla$  in these equations is the Laplacian and  $' := d/d\eta$ , a derivative with respect to conformal time  $\eta$ . Equation (2.60) makes clear why we call  $\Phi$  the generalised Newtonian potential, as this equation has the form of the Poisson equation. Based on eq. (2.62) it also becomes clear that  $\Phi = -\Psi$ . Taking the off-diagonal entries the equation simplifies to  $(\Phi + \Psi)_{,ij} = 0$ . Given that this has to hold globally for all perturbations we must conclude that  $\Phi = -\Psi$ . Hence, we rewrite eq. (2.62) as

$$\Phi'' + 3\mathcal{H}\Phi' + (2\mathcal{H}' + \mathcal{H}^2)\Phi = 4\pi G a^2 \delta p, \quad (2.63)$$

which now gives us the full Einstein equations in linear perturbation theory.

This set of equations also allows us to study the time evolution of scalar perturbations and thus how matter perturbations grow during the different epochs of the Universe. We follow Schwarz (2008) and start this estimate by defining the relativistic density contrast for each fluid ( $a$  defines the fluid, typically cold dark matter or baryons)

$$\Delta_a \equiv \frac{\delta\epsilon_a}{(\bar{\epsilon} + \bar{p})_a}, \quad \Delta \equiv \sum_a \frac{(\bar{\epsilon} + \bar{p})_a}{\epsilon + p} \Delta_a, \quad (2.64)$$

where  $\Delta$  now denotes a perturbative quantity. The peculiar velocity (a velocity with respect to the background FLRW model) can be expressed as

$$v = \sum_a \frac{(\bar{\epsilon} + \bar{p})_a}{\epsilon + p} v_a. \quad (2.65)$$

Similarly to eq. (2.13), we can take the derivative of eq. (2.59) and recover the conservation law, resolved into Fourier modes (since we assume a flat spatial hypersurface; see eq. (2.78) below), which for a mode with wave number  $k$  is

$$\Delta'_a = kv_a + 3\Phi'. \quad (2.66)$$

The Euler equation – differential equations derived from fluid dynamics – for this problem is given by

$$v'_a + (1 - 3c_a^2)\mathcal{H}v_a = -c_a^2 k\Delta_a - k\Phi. \quad (2.67)$$

The last thing we need to introduce is a hypersurface-invariant variable

$$\zeta = \frac{\delta\epsilon}{3(\bar{\epsilon} + \bar{p})} + \Phi, \quad (2.68)$$

which can either be interpreted as the perturbation of spatial curvature on a constant density hypersurface or as the relativistic density contrast on a uniform curvature hypersurface. The variable is constant for superhorizon modes for every different epoch. Inserting  $\zeta$  into eq. (2.66) yields  $\zeta'_a = 3kv_a$ . For superhorizon modes, with  $k\eta \ll 1$ ,  $\zeta_a$  is approximately constant, since the mode is frozen.

Rewriting eq. (2.60) in Fourier space yields

$$-k^2\Phi - 3\mathcal{H}\Phi' - 3\mathcal{H}^2\Phi = -(\mathcal{H}' - \mathcal{H}^2)\Delta. \quad (2.69)$$

Let us consider superhorizon modes ( $k \ll \mathcal{H}$ ) first. In this case we can neglect  $\Delta\Phi$  and  $\Phi'$  in the 00-component of the Einstein equation eq. (2.60). If we insert the Hubble parameter  $\mathcal{H}^2 = \frac{8\pi G}{3}a^2\epsilon$ , then we derive

$$\frac{\delta\epsilon}{\bar{\epsilon}} = \frac{2}{\Phi}, \quad (2.70)$$

and then inserting this in the definition of the hypersurface variable eq. (2.68), using  $p = \epsilon w$ , yields

$$\zeta = \frac{2}{3} \frac{\Phi}{3(1+w)} + \Phi. \quad (2.71)$$

Thus  $\zeta$  stays constant during the different epochs, so we can compare the initial potential during radiation domination ( $w = 1/3$ ) with the final potential during matter domination ( $w = 0$ ), obtaining

$$\Phi_f = \frac{9}{10}\Phi_i. \quad (2.72)$$

As  $\zeta$  stays constant also for  $w = -1$  the potential  $\Phi$  needs approach zero at early times.

For subhorizon modes ( $k \gg \mathcal{H}$ ) we combine the continuity equation eq. (2.66), its derivative, the Poisson equation in Fourier space (eq. (2.69)) and eq. (2.67). We drop all terms with  $\Phi$  and  $\Phi'$  as they are negligible compared to  $k^2\Phi$  in this regime, obtaining

$$\Delta_m'' + \mathcal{H}\Delta_m' = \frac{3}{2}(1+w)\mathcal{H}^2\Delta, \quad (2.73)$$

using  $c_m^2 = 0$  and  $\mathcal{H}' = -\frac{1}{2}\mathcal{H}^2(1+w)$ . Now it is easy to see how matter evolves over time. First we look at the radiation dominated epoch, in which  $w = \frac{1}{3}$  and  $\mathcal{H} = \frac{1}{\eta}$ . Furthermore it is clear, since it is radiation dominated, that  $\Delta = \Delta_r$ . Substituting this in eq. (2.73) leads to

$$\Delta_m'' + \frac{\Delta_m'}{\eta} - \frac{2}{\eta^2}\Delta_r = 0. \quad (2.74)$$

The solution of this differential equations has the form

$$\Delta_m \propto b_1 + b_2 \ln(\eta), \quad (2.75)$$

where  $b_1$  and  $b_2$  are constants. This is only the homogeneous solution. During the matter dominated epoch  $w = 0$ ,  $\mathcal{H} = \frac{2}{\eta}$  and again it should be clear that  $\Delta = \Delta_m$ . Again this is inserted in eq. (2.73) and the solution to the differential equations yields

$$\Delta_m \propto \eta^2 \propto a. \quad (2.76)$$

Lastly, we study the perturbations during  $\Lambda$  domination, so  $w = -1$  and  $\mathcal{H} = \text{const}$ . This leads to

$$\Delta_m = \text{const}. \quad (2.77)$$

We have the interesting result that matter perturbations cannot grow in a  $\Lambda$  dominated Universe.

As already mentioned above, the matter perturbations  $\Delta(\vec{k}, z)$  are characterised by their power spectrum

$$\langle \Delta(\vec{k}, z)\Delta(\vec{k}', z) \rangle \equiv \frac{P(k, z)}{(2\pi)^3} \delta(\vec{k} + \vec{k}') \quad (2.78)$$

since we assume a flat spatial hypersurface (the topology restricts which modes are allowed; a trivial topology allows a continuous range of modes).  $P(k, z)$  is the power spectrum which gives a measure for how many perturbation of which length, equivalently characterised by the wave vector  $\vec{k}$ , exist. The power spectrum can be measured from observations, thus yielding a direct probe of cosmological perturbation theory. The challenging tasks that are beyond the scope of the background review in this thesis include how to model the power spectrum and relate matter perturbations to it in the radiation dominated epoch, and how to model their transition through to the matter dominated epoch. Instead, in section 3.1 we accept the standard approach for use in generating the initial conditions describing matter-epoch perturbations appropriate for an  $N$ -body simulation.

### 2.2.2 The cosmic web

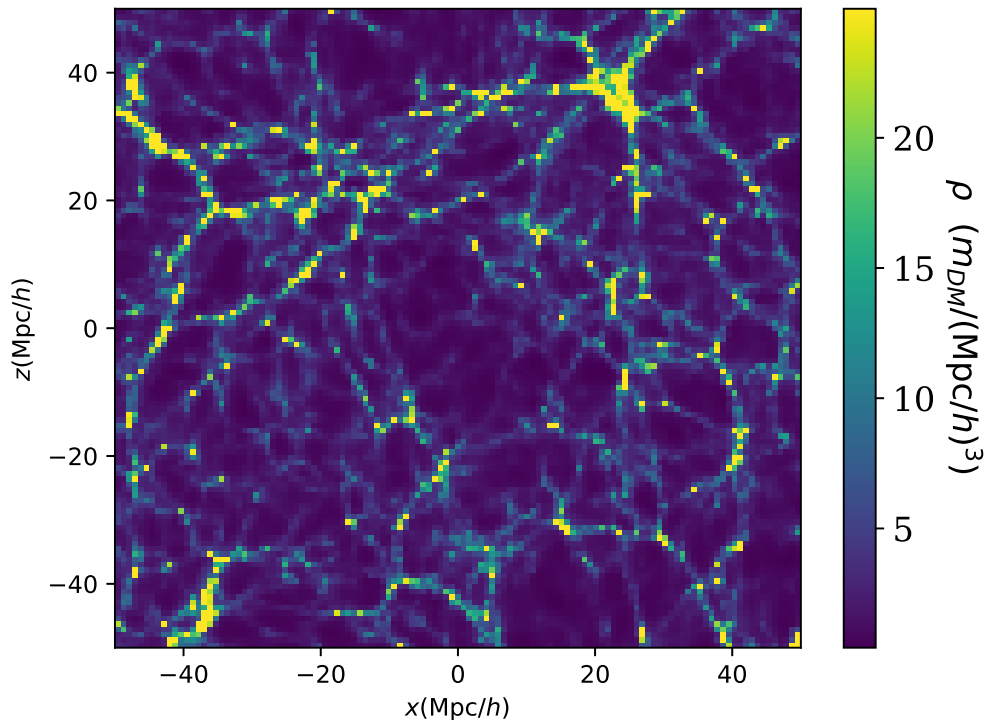


Figure 2.4: The cosmic web derived from a pure dark matter  $N$ -body simulation. The figure displays the density distribution of a slice of a realisation of the Universe. The brighter yellow parts visualise regions of higher density while blue regions are underdense. We clearly see a web-like structure spanning the simulation and smaller scale structures of lower density contrast within the voids. Most galaxies will form in the overdensities, or close by, while a few galaxies will form in the rather underdense areas of the web.

We learned about the homogeneous, isotropic background model of the Universe and how the background Universe evolves in the  $\Lambda$ CDM model according to the Hot Big Bang model. Moreover, we studied density perturbations, which are normally thought to start as quantum fluctuations that were spread out by cosmic inflation and then grow in size and amplitude to form the structures that we observe today. This section will explain what cosmologists call large-scale structure or the cosmic web.

A visualisation of the cosmic web can be seen in fig. 2.4, which shows the density distribution of a slice of an  $N$ -body simulation. We clearly see that there is a web-like structure of overdensities that spreads through the space. These overdensities can be characterised as clusters (nodes in the cosmic web) which are the most massive structures, followed by filaments and walls which connect the different clusters. In between we see huge underdense regions which are known as cosmic voids that dominate the volume budget of the Universe. Unfortunately, in contrast to most other disciplines of physics, we cannot create small test labs to study, for example, structure formation or galaxy evolution. We thus rely on cosmological  $N$ -body simulations and fine-tune these to represent what is seen observationally. We can also extrapolate results based on simulated data to estimate what we expect to see in observations.

Historically, the overdense regions such as clusters are much better studied because they contain more luminous matter and hence they are easier to detect. However, the first measurements of underdense regions go well back over 40 years (Gregory & Thompson, 1978; J oeveer et al.,



1978; de Lapparent et al., 1986). In these first galaxy catalogues the authors noted that there are regions which are devoid by galaxies. From these measurements it is known that a high volume fraction of the Universe consists of large underdense regions. More recent measurements have increased our knowledge about these underdense regions, now known as cosmic voids or voids in the cosmic web. Sloan Digital Sky Survey (SDSS) measurements show that cosmic voids dominate the volume of our Universe, constituting 60% of the volume in Pan et al. (2012)'s analysis and 70% of the volume in Mao et al. (2017)'s analysis. Several more SDSS-related analyses have shown that void sizes span about an order of magnitude, ranging from 10 to  $200 \text{ Mpc}/h^{-1}$ , with higher numbers of smaller voids (Hoyle & Vogeley, 2002, 2004; Pan et al., 2012; Nadathur & Hotchkiss, 2014; Sutter et al., 2014; Pisani et al., 2014, 2015a,b; Mao et al., 2017).

Even though most galaxies will form in more dense regions, namely the filaments and the clusters, some galaxies will form in cosmic voids. Simulations show that inside voids, there is a hierarchical substructure of over- and under-densities that is similar to the larger scale structures found in the cosmic web, i.e. nodes, filaments and walls (Gottlöber et al., 2003), but traced by dark matter haloes of much lower mass.

Depending on the chosen catalogue and void detection algorithm, a modest fraction of galaxies can be considered as being located in voids. For example, Pan et al. (2012) estimate that about 7% of galaxies are located in voids. The true volume that is occupied by voids is hard to assess and generally depends on the method used, but since the fraction of volume may be as high as 80% (for theoretical estimates, see e.g. Colberg et al., 2008; Cautun et al., 2015), they are suspected to play a key role in relation to dark energy (e.g. Buchert et al., 2016).

Furthermore, voids themselves are fascinating objects to study as they can yield important insights about the nature of the Universe and their size, abundance, shape and density profile can be used to probe the cosmological standard model. The way that matter clumps in voids and how it is pushed outside is studied to derive the matter density and dark energy parameters  $\Omega_{m0}$  and  $\Omega_{\Lambda0}$ . For example, Dekel & Rees (1994) use the radial peculiar velocities of galaxies in order to estimate the matter content of the Universe, arguing that a low matter Universe will result in lower velocities. Bernardeau et al. (1997) argue that since accelerations exerted by gravity will account for luminous and dark matter, the velocity field can be used to re-model the underlying mass distribution and thus can be used to estimate the matter content of the Universe. Fliche & Triay (2010) investigate how the cosmological constant  $\Lambda$  influences the growth of an isolated, spherical void.

Using  $N$ -body simulations, we can also use voids to test other aspects of cosmological models. Li et al. (2012) study  $f(R)$  gravity by adding a fifth force, acting in the very dense regions of clusters, to an  $N$ -body simulation and study the size of voids in the model. They find that the Universe in such a modified gravity scenario hosts significantly more voids of larger sizes compared to the standard  $\Lambda$ CDM model. The shape of voids is used by Bos et al. (2012) in five cosmological simulations, each using a different dark energy model. The authors conclude that the differences between the models are significant and should be measurable, and thus the shape of voids can be used to test and falsify specific dark energy models. Defining and detecting voids in observational and simulated data is therefore a crucial task and will be explained in section 3.3.

A void will grow in size over time and become more empty as matter is pushed towards its edges. The void acts against the clumping of matter in its interior. A galaxy forming in a cosmic void, especially at the centre of a cosmic void, should have difficulties to form due to the lowest densities and the trend against clumping. This trend is twofold. Naïvely we expect that the effective force that pushes matter out of the void would act against structure formation. We also

expect a comparably undisturbed formation and evolution of the galaxies as there are fewer other massive structures that might interact gravitationally with the galaxies via tidal effects or collide (merge) with them. Moreover, it is shown that in order to turn around prior to collapse, a dark matter halo needs to undergo a phase of positive spatial curvature (Roukema & Ostrowski, 2019; Vigneron & Buchert, 2019; Ostrowski, 2020). A void, on the contrary, will induce a negative spatial curvature and thus counteract the formation process of dark matter haloes. These effects will be stronger the deeper a galaxy resides in a void.

Observational void galaxies are measured to have lower masses, being bluer, smaller and having a higher specific star formation rate (Hoyle et al., 2005; Patiri et al., 2006; Kreckel et al., 2011). Some studies that probe the properties of void galaxies while fixing their stellar mass do not find any substantial difference between void galaxies and non-void galaxies. Beygu et al. (2016) find that the measured differences are mostly caused by the statistically lower mass of void galaxies. However, other studies find that void galaxies have an enhanced star formation rate for a fixed mass (Florez et al., 2021). Further studies are needed to resolve this apparent contradiction.

Recent studies investigate the molecular gas content of void galaxies. Whereas Florez et al. (2021) find higher gas masses for void galaxies, Domínguez-Gómez et al. (2022) do not find any significant difference between void galaxies and galaxies in filaments and clusters. It remains an open question if galaxy formation is heavily influenced by the large-scale environment of the void or rather by the small scale environment.

In chapter 3 we explore the steps that are needed to generate a realistic density distribution derived from initial conditions. We explain the tools that are used to identify structures – dark matter haloes and voids – in the resulting density distributions. With these tools in place, we are able to probe the above assumptions in a controlled way and study the statistical effects on void galaxies.

## 2.3 Gravitational lensing and geometric optics

Einstein's theory of gravity is, up to the present day, a very successful and powerful tool that describes the measured Universe. A consequence of the theory is that light rays travel on straight lines in the space-time. A perturbation in the density field thus will influence the path that a light ray will take. Even in Newtonian gravity we can explain that matter will have a measurable effect on light propagation e.g. by connecting the energy of a photon to a mass using the analogy between waves and mass that was proposed by de Broglie 1924. However, predicting the measured deflection was a great success for GR and increased the acceptance of the theory. In this section we introduce a simple approach to estimate the lensing signal following Bartelmann & Schneider (2001), and continue to the geometric-optics approach following Sasaki (1993) and Clarkson et al. (2012).

### 2.3.1 Gravitational lensing

If an object with a high gravitational mass, the lens object, lies between a galaxy and an observer, then the light bundle emitted by the galaxy will be deflected and deformed while propagating. This effect can be so strong that a single galaxy can have multiple visible images as multiple light bundles reach the observer. For the rare setup that the emitting source, the lens and the observer are well aligned it is possible to measure Einstein rings, which means that the source appears as a ring around the lens. As galaxies are usually not perfectly spherical or the disk is not observed face-on, estimating the real deflection and the shear that the light bundle experiences can be difficult. However, a unique feature of lensing observations is that the light ray sees all the matter, not just baryonic matter. By extracting the lensing signal it is thus possible to probe the underlying matter distribution of the Universe.

An illustration of the lens effect can be seen in fig. 2.5. If we consider a single mass as the source of lensing, then we can write the deflection angle, as long as the impact parameter  $\xi$  is much larger as than the Schwarzschild radius of the source, i.e. the light bundle passes the lens object with a sufficient distance, as

$$\hat{\alpha} = \frac{4GM}{c^2\xi}, \quad (2.79)$$

where  $M$  is the mass of the lens object. That is however only valid if the light bundle only sees one lens object which, in general, will not be the case. As we have seen in section 2.2.2 and fig. 2.4 there are several structures within the cosmic web that will have an impact on a light bundle, thus the more realistic case is that a light ray travels through the Universe seeing a matter distribution with multiple effective lensing objects. As long as the deflection caused by the gravitational field is small the problem can be linearised, which means that the total effect on the light ray is the vectorial sum of the deflections each lensing object will cause.

Let us divide the Universe into cells of size  $dV$  and mass  $dm = \rho dV$ . A light ray, far away from the lensing source will travel along the unperturbed path  $r_3$ . In this approximation the deflection angle is small, therefore the path of the light can be approximated as a straight line close to the lensing source, the source acts as one effective potential. This is possible as the energy of the light ray is negligible compared to the energy of the mass that causes the deflection which is similar to the Born approximation from quantum physics, meaning that we can solve the equation for the path of the light without taking the motion of the lens object into account. Thus, the impact vector  $\vec{\xi} = (\xi_1, \xi_2)$  is independent of the affine parameter  $\lambda$  that characterises the light ray's trajectory.

We characterise the light ray by  $(\xi_1, \xi_2, r_3)$ , i.e. its path far away from the lensing source

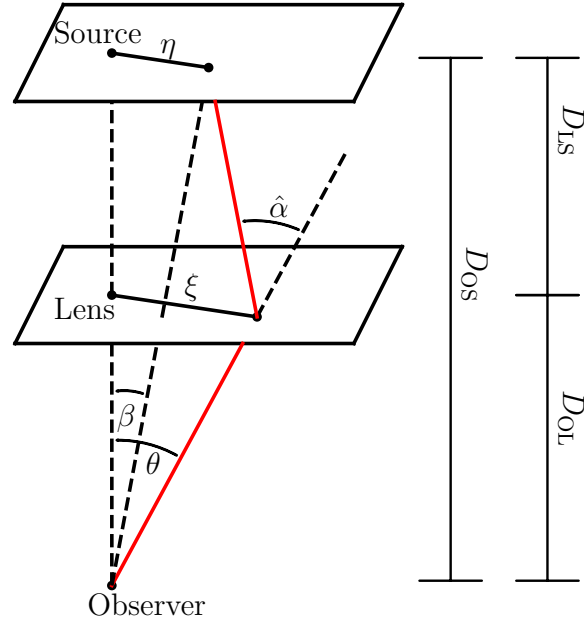


Figure 2.5: A simplified sketch for a light bundle that experiences a deflection for a single lens. Image adapted from Bartelmann & Schneider (2001)

and the impact vector caused by the mass of the lens object. The total (effective) impact vector is therefore given by the difference  $\vec{\xi} - \vec{\xi}'$ , taking into account that there are multiple lensing objects influencing the light bundle, acting on a light ray at position  $\vec{r} = (\xi'_1, \xi'_2, r'_3)$ . The total deflection angle, the sum of several lensing objects, with the qualitative arguments above, now can be written as

$$\begin{aligned} \hat{\alpha}(\vec{\xi}) &= \frac{4G}{c^2} \sum dm(\xi'_1, \xi'_2, r'_3) \frac{\vec{\xi} - \vec{\xi}'}{|\vec{\xi} - \vec{\xi}'|^2} \\ &= \frac{4G}{c^2} \int d^2\xi' \int dr'_3 \rho(\xi'_1, \xi'_2, r'_3) \frac{\vec{\xi} - \vec{\xi}'}{|\vec{\xi} - \vec{\xi}'|^2} \\ &= \frac{4G}{c^2} \int d^2\xi' \Sigma(\vec{\xi}') \frac{\vec{\xi} - \vec{\xi}'}{|\vec{\xi} - \vec{\xi}'|^2}, \end{aligned} \quad (2.80)$$

where we introduced the surface mass density  $\Sigma(\vec{\xi}') \equiv \int dr'_3 \rho(\xi'_1, \xi'_2, r'_3)$  in the last step. This approximation for the deflection angle is valid as long as the deviation from an undeflected light ray is small on the scale on which the mass distribution changes, which is the case for almost all astrophysical cases.

We now aim to get an analytical expression for the deflected position on the sky  $\vec{\eta}$ . In fig. 2.5 we can read that  $\vec{\eta} = D_{OS}\vec{\beta}$  and  $\vec{\xi} = D_{OL}\vec{\theta}$ . Moreover, by using the angular diameter distance (eq. (2.36)) and assuming that  $\alpha$  is very small, we can read  $D_{OS} = \frac{\vec{\eta} + D_{LS}\vec{\alpha}}{\vec{\theta}}$  and hence

$$\vec{\eta} = \frac{D_{OS}}{D_{OL}}\vec{\xi} - D_{LS}\hat{\alpha}(\vec{\xi}) \quad (2.81)$$

and by inserting  $\vec{\eta}$  and  $\vec{\xi}$  rewrite it as

$$\vec{\beta} = \vec{\theta} - \frac{D_{\text{LS}}}{D_{\text{OS}}} \hat{\alpha}(D_{\text{OL}}\vec{\theta}) \equiv \vec{\theta} - \vec{\alpha}(\vec{\theta}), \quad (2.82)$$

where we define the scaled deflection angle  $\vec{\alpha}(\vec{\theta}) \equiv \frac{D_{\text{LS}}}{D_{\text{OS}}} \hat{\alpha}(D_{\text{OL}}\vec{\theta})$ . According to fig. 2.5 an observer will see an object at position  $\vec{\theta}$  while its true position is  $\vec{\beta}$ . It can occur that the equation has more than one solution, meaning that the object is visible at several different positions in the sky. Such a lens is called "strong". It is common to introduce the dimensionless quantities

$$\kappa(\vec{\theta}) = \frac{\Sigma}{\Sigma_{\text{crit}}}, \quad (2.83)$$

where  $\Sigma_{\text{crit}} = \frac{c^2}{4\pi G} \frac{D_{\text{OS}}}{D_{\text{OL}}D_{\text{LS}}}$  is the critical surface mass density.  $\Sigma_{\text{crit}}$  can be used to distinguish between "strong" and "weak" lensing. If  $\Sigma > \Sigma_{\text{crit}}$ , then  $\kappa > 1$  which results in multiple images for a single object. Rewriting the scaled deflection angle with  $\kappa$  we find

$$\vec{\alpha}(\vec{\theta}) = \frac{1}{\pi} \int d^2\theta' \kappa(\vec{\theta}') \frac{\vec{\theta} - \vec{\theta}'}{|\vec{\theta} - \vec{\theta}'|^2}. \quad (2.84)$$

We can now formulate a lensing potential by noticing that we can write  $\vec{\alpha} = \nabla\Psi$  and therefore

$$\Psi(\vec{\theta}) = \frac{1}{\pi} \int d^2\theta' \kappa(\vec{\theta}') \ln(|\vec{\theta} - \vec{\theta}'|). \quad (2.85)$$

$\Psi$  is the equivalent of a gravitational Newtonian potential. Using  $\frac{d}{d\vec{\theta} \ln|\vec{\theta} - \vec{\theta}'|} = \delta(\vec{\theta} - \vec{\theta}')$  we can show that  $\kappa$  and  $\Psi$  satisfy the Poisson equation  $\Delta\Psi(\vec{\theta}) = 2\kappa(\vec{\theta})$ .

With these equations we can now find the deflection on the sky via solutions of the equations. As light of extended bundles gets deflected differentially the shape of the image will deviate from the original image of the source. Probably the most famous observations of this deflection are the previously mentioned Einstein rings, though this deformation of the image will generally produce bright arcs that do not have to be rings. We can connect the observed image with the image of the source via the amplification matrix

$$\Theta_{\text{S}}^a = A_b^a \Theta_{\text{O}}^b. \quad (2.86)$$

As there is no emission nor absorption of light, using Liouville's theorem we can conclude that the surface brightness of the image must be preserved. The measured surface brightness thus can be expressed as

$$I^{\text{O}}(\vec{\theta}) = I^{\text{S}}\vec{b}(\vec{\theta}). \quad (2.87)$$

If the source is much smaller than the scale on which the lensing properties change, then we can linearise the mapping and write an explicit form for the amplification matrix as the Jacobian of the potential

$$A = \frac{\partial\vec{\beta}}{\partial\vec{\theta}} = \delta_{ij} - \frac{\partial^2\Psi(\vec{\theta})}{\partial\theta_i\partial\theta_j} = \begin{pmatrix} 1 - \kappa - \gamma_1 & \gamma_2 - \omega \\ \gamma_2 + \omega & 1 - \kappa + \gamma_1 \end{pmatrix}. \quad (2.88)$$

The convergence  $\kappa$  is defined over the Poisson equation,  $\gamma$  is the shear and  $\omega$  the rotation, which will be dropped for simplicity. The shear is thus given by

$$\gamma_1 = \frac{1}{2}(\Psi_{,11} - \Psi_{,22}) = \frac{1}{\pi} \int d^2\theta' \kappa(\vec{\theta}') \frac{(\theta_2 - \theta'_2)^2 - (\theta_1 - \theta'_1)^2}{\left((\theta_1 - \theta'_1)^2 + (\theta_2 - \theta'_2)^2\right)^2} \quad (2.89)$$

and

$$\gamma_2 = \Psi_{,12} = \Psi_{,21} = \frac{1}{\pi} \int d^2\vec{\theta}' \kappa(\vec{\theta}') \frac{-2(\theta_1 - \theta'_1)(\theta_2 - \theta'_2)}{\left((\theta_1 - \theta'_1)^2 + (\theta_2 - \theta'_2)^2\right)^2}. \quad (2.90)$$

If the weak lensing convergence  $\kappa$  is azimuthally symmetric, similarly this has to hold true for  $\Sigma$  based on eq. (2.83), then it can be shown that

$$\gamma = \gamma_1 + i\gamma_2 = \bar{\Sigma}(< \theta) - \Sigma(\theta) = \frac{2}{\theta^2} \int_0^\theta \theta' \Sigma(\theta') d\theta' - \Sigma(\theta), \quad (2.91)$$

where we wrote  $\vec{\theta}$  in polar coordinates. Assuming the deflection is small we can use a Taylor expansion and write

$$I^O(\vec{\theta}) = I^S \left( \vec{b}_0 + A(\vec{\theta}_0)(\vec{\theta} - \vec{\theta}_0) \right). \quad (2.92)$$

Let us assume the image of the source is a perfect sphere. It is then clear that the image seen by an observer becomes an ellipse. The ratio of the semi-axes compared to the radius of the original image are given by the content of the amplification matrix. The ratio is given by the inverse of the eigenvalues which are  $1 - \kappa \pm |\gamma|$ . The ratio of the solid angles is given by the inverse of the determinant of  $A$ . The fluxes are the integrals over  $I^S$  and respectively  $I^O$ . Their ratio is given by the magnification

$$\mu = \frac{1}{\det(A)} = \frac{1}{(1 - \kappa)^2 - |\gamma|^2}. \quad (2.93)$$

With this set of equations we have heuristically derived the fundamental equations and concepts for weak lensing.

### 2.3.2 Geometric optics

While weak lensing only holds true assuming an FLRW background, the optical scalars, first derived by Sachs (1961), hold true for any background. A light ray propagating through a matter distribution will be deflected according to the inhomogeneities which in the context of linear order perturbation theory are characterised by  $\Phi$ , see eq. (2.52). A description can be found in Sasaki (1993) and Clarkson et al. (2012).

Clarkson et al. (2012) formalise the propagation of a bundle of light rays  $x^\mu(\nu_s)$ , where  $\nu$  is the affine parameter and  $s$  labels the geodesic. Let us assume a monochromatic light bundle with propagation vector  $k^\mu$  and using the geometric optics approximation meaning that the wavelength of the light is much smaller than the structures in the Universe. In this approximation we can assume that the phase of the light ray is constant and thus there is no deformation due to any rotation of the image. Such a light bundle is described as irrotational null geodesics such that

$$k_\mu k^\mu = 0, \quad k^\mu_{;\nu} k^\nu = 0, \quad k_{\mu;\nu} - k_{\nu;\mu} = 0. \quad (2.94)$$

The connection vector  $\eta^\nu = dx^\nu/ds$  connects neighbouring geodesics of the bundle, with a tangent vector  $k^\mu = dx^\mu/d\nu$ . Describing the change of  $\eta^\nu$  while the light bundle propagates along the affine parameter  $\nu$  therefore gives full information about the shape of the light bundle. The connection vector can at each point be chosen to be orthogonal to  $k^\mu$ . We span the space orthogonal to the affine parameter by introducing the dyad basis  $e_\mu^A$ , where  $A = (1,2)$  such that  $g^{\mu\nu} e_\mu^A e_\nu^B = \delta^{AB}$  and  $\eta_a^\mu k_\mu = 0$ . We can construct the orthogonal space spanned by the dyad basis such that the connection vector in the dyad basis can be written as

$$\eta^\mu = \eta_1 e_1^\mu + \eta_2 e_2^\mu, \quad (2.95)$$

and vice versa

$$\eta^A = e^A_\mu \eta^\mu. \quad (2.96)$$

The geodesic deviation equation is given by

$$k^\alpha k^\beta \nabla_\alpha \nabla_\beta \eta^\gamma = R^\mu_{\nu\alpha\beta} k^\nu k^\alpha \eta^\beta. \quad (2.97)$$

We rewrite this equation in the dyad basis using  $\frac{d}{dv} = k^\mu \nabla_\mu$  and that the dyad basis is parallel transported as  $\frac{d}{dv} e^\nu_A = 0$  as

$$\frac{d^2}{dv^2} \eta_A = R_{\mu\nu\sigma\rho} k^\nu k^\sigma e^\mu_A e^\rho_B \eta^B \equiv R_{AB} \eta^B, \quad (2.98)$$

where  $R_{AB}$  is defined over the equation above. According to Clarkson et al. (2012) the linearity of this equation implies

$$\eta^A(v) = D^A_B(v) \left. \frac{d\eta^B}{dv} \right|_{v=0}, \quad (2.99)$$

where  $D^A_B$  is a Jacobian matrix. Inserting the solution back into the geodesic deviation equation eq. (2.98) yields

$$\frac{d^2}{dv^2} D^A_B = R^A_C D^C_B, \quad \eta_A(0) = 0, \quad \frac{dD^A_B}{dv}(0) = \delta^A_B. \quad (2.100)$$

The latter two expressions can be thought of boundary conditions.

Clarkson et al. (2012) then defines the deformation matrix  $S$  as

$$\frac{dD^A_B}{dv} = D^A_C S^C_B \quad (2.101)$$

and we rewrite the geodesic deviation equation, which is a second order differential equation, as a first-order differential equation in  $S$  as

$$\frac{dS^A_B}{dv} + S^A_C S^C_B = R^A_B. \quad (2.102)$$

Via its connection to the Riemann tensor the deformation matrix contains all information about the energy distribution seen by the light bundle. The deformation matrix usually is decomposed as

$$S = \begin{pmatrix} \frac{1}{2}\hat{\theta} & 0 \\ 0 & \frac{1}{2}\hat{\theta} \end{pmatrix} + \begin{pmatrix} \hat{\sigma}_1 & \hat{\sigma}_2 \\ \hat{\sigma}_2 & -\hat{\sigma}_1 \end{pmatrix}. \quad (2.103)$$

$\hat{\theta}$  and  $\hat{\sigma}$  are the optical scalars; here we use the decomposition according to eq. (3.12) of Sasaki (1993) with an additional factor of  $\frac{1}{2}$  in front of  $\hat{\theta}$  compared to Clarkson et al. (2012). If we insert this expression for the deformation matrix back into eq. (2.102), then we can derive the expression for the optical scalars

$$\frac{d\hat{\theta}}{dv} + \frac{1}{2}\hat{\theta}^2 + 2|\sigma|^2 = R^A_A \quad (2.104)$$

$$\frac{d\hat{\sigma}}{dv} + \hat{\theta}\hat{\sigma} = R^0_0 - R^1_1 + i(R^0_1 + R^1_0). \quad (2.105)$$

Sasaki (1993) argues that in linear order perturbation theory we can find approximations relating the optical scalars to the perturbations and rewrite the optical scalars as

$$\frac{d\hat{\theta}}{dv} + \frac{1}{2}\hat{\theta}^2 + 2|\sigma|^2 = 8\pi G\rho\omega^2 \quad (2.106)$$

$$\frac{d\hat{\sigma}}{dv} + \hat{\theta}\hat{\sigma} = C_{A0B0} \approx (2\Phi_{,AB} - \delta_{AB}\Phi_{,C}^C)\omega^2, \quad (2.107)$$

where  $\omega$  is the energy of the light ray.

The weak lensing formalism and the Sachs optical scalars both measure the deflection of a light bundle. It is straightforward that these two measures of deflection thus can be related. Clarkson et al. (2012) find that the two Jacobian matrices are related over the angular diameter distance  $\bar{D}_A$  in a FLRW Universe by

$$A_B^A(\nu) = \frac{D_B^A(\nu)}{\bar{D}_A(\nu)}. \quad (2.108)$$

If we insert this relation into eq. (2.101), then we can find the relation between the weak lensing parameters and the optical scalars via

$$(A^{-1})_C^A \frac{d}{d\nu} (A_B^C) + \delta_B^A \frac{d}{d\nu} (\bar{D}_A) \frac{1}{\bar{D}_A} = S_B^A. \quad (2.109)$$

Inserting eqs. (2.103) and (2.88) will yield the analytical expression between  $(\hat{\theta}, \hat{\sigma})$  and  $(\kappa, \gamma)$  (see eqs (41)–(43) in Clarkson et al. (2012)). As the optical scalars are more general such a relation can be useful in some cases.



# Chapter 3

## Method

This pipeline used for this thesis aims to build a realistic galaxy population starting from initial conditions that are modelled by generating a realisation of the initial perturbation power spectrum, evolving this into the spatial density distribution of the cosmic web using  $N$ -body simulations, classifying the large-scale structure – voids and haloes – in the cosmic web, and populating the haloes with galaxies using semi-analytical recipes based on the halo’s merger-history trees.

The work presented in chapter 4 and 6 will be fully reproducible. We follow the Manage scheme of reproducibility (Akhlaghi et al., 2021). The software presented below is embedded in the Manage template, meaning that we create an independent directory on the used machine in which all necessary software will be installed. Software packages are indicated by their version numbers and SHA512 checksums for the upstream versions of software used in our pipeline. This method avoids problems such as software not compiling or giving substantially different results due to the versions of software installed on the parent system. Reproducibility of the method, together with the free licence of the code, allow users to quickly check and validate the presented results and the used tools. We present a heavily numerical approach where the individual steps will be briefly discussed in the following sections.

### 3.1 Initial Conditions – MPGRAFIC

We have learned about the evolution of our Universe and density perturbations. The initial perturbations are believed to be quantum fluctuations which are stretched during inflation. In this analysis initial conditions for the density and velocity perturbations are generated with MPGRAFIC (Prunet et al., 2008). This software package was designed to enable easy, correct generation of the initial conditions for a multiscale “zoom” simulation. Moreover, MPGRAFIC is published under a free-software licence, the GNU General Public License version 2 or later,<sup>1</sup> which satisfies one of the Akhlaghi et al. (2021) criteria (criterion 8) for high-quality scientific reproducibility (Rougier et al., 2017).

#### 3.1.1 Single-level simulation

For the derivation of the mathematical basics we follow the description of (Bertschinger, 2001). Let us assume a density distribution  $\delta(x)$  in real, flat space. Using the Fourier transform it can

---

<sup>1</sup><https://www.gnu.org/licenses/old-licenses/gpl-2.0.html>

be written as

$$\delta(\vec{x}) = \int d^3k \exp(i\vec{k}\vec{x})\tilde{\delta}(\vec{k}), \quad (3.1)$$

where  $\tilde{\delta}(\vec{k})$  is the same distribution in Fourier space. The Fourier distribution is then split into Gaussian white noise  $\xi(\vec{k})$  and an evolution/transfer function  $T(k)$  as  $\tilde{\delta}(\vec{k}) = T(k)\xi(\vec{k})$ . The white noise has to satisfy

$$\langle \xi(\vec{k}_1)\xi(\vec{k}_2) \rangle = \delta^3(\vec{k}_1 + \vec{k}_2), \quad (3.2)$$

which implies that the power spectrum is normalized and the modes are independent.

The transfer function is defined here specifically for this type of numerical generation of initial conditions. It differs from the usual transfer function that describes the transition from a primordial Harrison–Zel’dovich-like spectrum through to a post-recombination spectrum. The transfer function in this context contains all the information about both the pre-recombination spectrum and the evolution of the modes through this epoch, and is defined

$$T(k) := \sqrt{P(k)}. \quad (3.3)$$

By using the Fourier transformation on infinite, simply connected flat space,  $T(|x|) = \int \frac{d^3k}{(2\pi)^3} \exp(i\vec{k}\vec{x})T(k)$  and  $\xi(x) = (2\pi)^3 \int d^3k \exp(i\vec{k}\vec{x})\xi(\vec{k})$ , it is easy to check that we can represent the density perturbation as

$$\delta(x) = \int d^3x' \xi(\vec{x}')T(|\vec{x} - \vec{x}'|). \quad (3.4)$$

In other words, we see that a Gaussian density perturbation can be constructed by the convolution of white noise and the transfer function.

The main task of `MPGRAFIC` is the discretisation of these equations on the 3-torus. First we investigate the case for a single-scale simulation. To do this let us assume a box (fundamental domain of the 3-torus) of length  $L$  with  $M$  grid points in each direction. The grid position consequently can be written as  $\vec{x}(\vec{m}) = (L/M)\vec{m}$  where  $m_i \in [0, 1, \dots, M]$  (i.e.  $\vec{m}$  is a vector in  $\mathbb{N}^M$ , where  $\mathbb{N}$  is the set of natural numbers including zero). The sum is the discretised version of an integral. Thus, using the adimensional wavenumber  $\vec{k} = \vec{k}L/(2\pi)$ , we can rewrite 3.1 as

$$\delta(\vec{m}) = \sum_{\vec{k}} \exp\left(\frac{i2\pi}{M}\vec{k} \cdot \vec{m}\right) T(k)\xi(\vec{k}). \quad (3.5)$$

The correlation function (which is adimensional) can be written as

$$\xi(\vec{k}) = M^{-3} \sum_m \exp\left(-\frac{i2\pi}{M}\vec{k} \cdot \vec{m}\right) \xi(\vec{m}). \quad (3.6)$$

The discrete form of the Dirac delta is the Kronecker delta and eq. (3.2) becomes

$$\langle \xi(\vec{m}_1)\xi(\vec{m}_2) \rangle = M^3 \delta_K^3(\vec{m}_1, \vec{m}_2) \quad (3.7)$$

The algorithm now consists of the following steps

1. Generating independent  $\xi(\vec{m})$  at every grid point
2. Calculate eq. (3.6) with a Fast Fourier Transform algorithm
3. Multiply  $\xi(\vec{k})$  with the discrete power spectrum
4. Calculate eq. (3.5) with a Fast Fourier Transform algorithm

The outputs of `MPGRAFIC` can then be used according to the Zel’dovich approximation (Zeldovich & Grishchuk, 1984) to generate both an initial peculiar velocity field and proportional particle displacements as initial conditions of an  $N$ -body simulation.

### 3.1.2 Zoom simulations

Understanding zoom simulations helps to understand the history of the development of the MPGRAFIC code, although we did not run zoom simulations for this thesis.

The challenging task in the early 2000s was to generate a high resolution grid beyond the limitation of available computer memory (RAM). The solution chosen was to generate a high resolution grid nested into a coarser grid. Today, current computer hardware allows us to generate a high-resolution grid over the full volume which is sufficient for many purposes.

We are nevertheless interested in understanding the technique behind zoom simulations as this technique is still frequently used. Therefore we derive the formalism here. A recent example of a high-powered zoom simulation is the Cosmic-Zoom project (Liu et al., 2023).

Let us assume a two-level grid with different resolutions. The coarse grid again has  $M$  grid positions. The subgrid is laid over the coarse grid. It lies on  $M_s$  points of the coarse grid and additionally is characterised by the refinement factor  $r$  which specifies how many points the subgrid contains per position of the coarse grid (see fig. 1 Bertschinger (2001)). Each cell of the original coarse grid is therefore split into  $r^3$  subcells which themselves form the subgrid. The position now obviously is dependent on two integers because we can move on both grids at the same time. The position can be written as

$$x(\vec{m}, \vec{n}) = \vec{x}_0 + \left(\frac{L}{M}\right) \left(\vec{m} + \frac{1}{r}\vec{n}\right). \quad (3.8)$$

Conventionally we introduce an offset,  $\vec{x}_0 = (1-r)L/(2rM)(1,1,1)$  here to set the origin in the centre. The first step now is again to generate the density perturbations on the coarse grid as before, additionally there is a refined white noise  $\xi(\vec{m}, \vec{n})$  generated. The white noise  $\xi(\vec{m}, \vec{n})$  is then convolved with a high resolution transfer function. The code has to ensure that  $\xi(\vec{m}, \vec{n})$  has the same large-scale structure (long wavelength) as  $\xi(\vec{m})$ . To do this the code has to generate uncorrelated white noise  $\xi_1(\vec{m}, \vec{n})$  with variance  $(rM)^3$  and model the following relation

$$\xi(\vec{m}, \vec{n}) = \xi(\vec{m}) + (\xi_1(\vec{m}, \vec{n}) - \xi_1(\vec{m})) \quad (3.9)$$

with

$$\xi_1(\vec{m}) \equiv r^{-3} \sum_n \xi_1(\vec{m}, \vec{n}). \quad (3.10)$$

We can understand this method as follows. First the subgrid takes coarse-grained white noise and then small corrections  $\xi_1(\vec{m}, \vec{n}) - \xi_1(\vec{m})$  are added. By constructing it like this we enforce the white noise to fulfil

$$\sum_n \xi(\vec{m}, \vec{n}) = r^3 \xi(\vec{m}). \quad (3.11)$$

Moreover, the refined white noise has to preserve the low-frequency structure of the coarse grid. That is ensured by the above construction, the sum of all white noise grid positions equals the white noise of the coarse grid. The covariance of this white noise is

$$\langle \xi(\vec{m}_1, \vec{n}_1) \xi(\vec{m}_2, \vec{n}_2) \rangle = (rM)^3 \delta_K(\vec{m}_1, \vec{m}_2) \delta_K(\vec{n}_1, \vec{n}_2). \quad (3.12)$$

The method consists of many convolutions of the subgrid. Analogous to 3.5 we set the density perturbation as

$$\delta(\vec{m}, \vec{n}) = \sum_{\vec{k}} \exp(i\vec{k} \cdot \vec{x}(\vec{m}, \vec{n})) T(k) \xi(\vec{k}), \quad (3.13)$$

where the sum runs over  $\vec{k} = \frac{2\pi}{L} (\vec{k} + M\vec{b})$  and thus over all points of both grids. The technical challenge is to convolve 3.13 without summing over the whole Fourier space. Using the Fourier transforms for  $\xi(\vec{m}, \vec{n})$ ,  $T(\vec{m}, \vec{n})$  and the linearity of  $x(\vec{m} - \vec{m}', \vec{n} - \vec{n}')$  it is possible to show that we can rewrite 3.13 as

$$\delta(\vec{m}, \vec{n}) = \sum_{\vec{m}', \vec{n}'} \xi(\vec{m}', \vec{n}') T(\vec{m} - \vec{m}', \vec{n} - \vec{n}'). \quad (3.14)$$

We note down

$$\xi(\vec{m}, \vec{n}) = \sum_{\vec{k}} \exp \left[ i\vec{k} \cdot \vec{x}(\vec{m}, \vec{n}) \right] \xi(\vec{k}) \quad (3.15)$$

and

$$T(\vec{m}, \vec{n}) = (rM)^{-3} \sum_{\vec{k}} \exp \left[ i\vec{k} \cdot \vec{x}(\vec{m}, \vec{n}) \right] T(k). \quad (3.16)$$

By rewriting 3.13 like above we do not need to sum over the whole grid anymore. It is now possible to calculate the density perturbations only over the subgrid.  $\xi(\vec{m}, \vec{n})$  can be drawn from independent Gaussian random distributions with mean 0 and variance  $(rM)^3$  fulfilling eq. (3.10); outside the subgrid  $\xi(\vec{m}, \vec{n}) = 0$ . The transfer function can be estimated as above though this requires  $\mathcal{O}(r^6 M_s^3 M^3)$  operations. Bertschinger (2001) suggests more efficient methods to estimate the transfer function on the subgrid that will not be considered further in this thesis. Assuming a cubic box for our subgrid we want to compute the Fourier transforms

$$\xi(\vec{k}') = 1/N_s \sum_{\vec{x}} \exp(i\vec{k}' \cdot \vec{x}(\vec{m}, \vec{n})) \xi(\vec{k}'), \quad (3.17)$$

where  $N_s = (2rM_s)^3$  is the total number of grid points in the subgrid and

$$T(\vec{k}') = \sum_{\vec{x}} \exp(i\vec{k}' \cdot \vec{x}(\vec{m}, \vec{n})) T(\vec{k}'). \quad (3.18)$$

The sum runs over all positions in the subgrid. The Fourier space is a different one than before, note the  $\vec{k}'$  since we change the Volume from  $V = L^3$  to  $V' = ((2M_s/M)L)^3$ . The final step is to perform the convolution 3.4 in  $k$ -space and then Fourier-transform it. We refer the reader to Bertschinger (2001) and (Prunet et al., 2008) for the implementation of the mathematical description presented above.

### 3.1.3 Fast Fourier Transform

In computational science the technique of Fast Fourier Transforms (FFT) has become very important. One of many examples is described above: the generation of initial conditions requires to perform several FFTs during one run. FFTs are commonly used in many different disciplines, where frequencies of a signal have to be analysed (e.g. telecommunication, maths and physics). There exist many different algorithms for the FFT, but the general idea is to have a fast algorithm to perform the discrete Fourier Transform of a given function. An example was introduced in Cooley & Tuckey (1965). This abstract work can be used to explain the Discrete Fast Fourier Transform as shown in Mkleine & other Wikipedia contributors (2023). Assume we want to make the Fourier Transform of a vector  $\vec{x} = (x_0, x_1, \dots, x_n)$ . The Fourier Transform then is given by

$$f_m = \sum_{k=0}^{2n-1} x_k \exp\left(-\frac{2\pi i}{2n} mk\right), \quad (3.19)$$

with  $m = 0, 1, \dots, 2n - 1$ . Let us split the Fourier Transform in a sum over all even indices and a sum over all odd indices, i.e.  $x'_k = x_{2k}$  and its Fourier Transform will be  $f'_k$  and  $x''_k = x_{2k+1}$  with the Fourier Transform (FT)  $f''_k$ . It immediately follows that we can write the FT as

$$f_m = \sum_{k=0}^{n-1} x_{2k} \exp\left(-\frac{2\pi i}{2n} m 2k\right) + \sum_{k=0}^{n-1} x_{2k+1} \exp\left(-\frac{2\pi i}{2n} m(2k+1)\right) \quad (3.20)$$

$$= \sum_{k=0}^{n-1} x'_k \exp\left(-\frac{2\pi i}{n} m k\right) + \sum_{k=0}^{n-1} x''_k \exp\left(-\frac{2\pi i}{n} m k\right) \quad (3.21)$$

$$= f'_m + \exp\left(-\frac{\pi i}{n} m k\right) f''_m \quad \text{for } m < n \quad (3.22)$$

$$= f'_{m-n} + \exp\left(-\frac{\pi i}{n} (m-n)k\right) f''_{m-n} \quad \text{for } m \geq n \quad (3.23)$$

Calculating  $f'_m$  and  $f''_m$  for  $m = 0, \dots, n - 1$  is sufficient to calculate all FTs, the calculation time thus nearly halved.

A widely used FFT is FFTW, the ‘‘Fatest Fourier Transform in the West’’ (Frigo & Johnson, 2012), licensed under the GNU General Public License version 2 or later.<sup>2</sup> The MPGRAFIC software currently uses FFTW2.

---

<sup>2</sup><https://www.gnu.org/licenses/old-licenses/gpl-2.0.html>

## 3.2 $N$ -body problems – RAMSES

### 3.2.1 $N$ -body problems

In physics we often come across a rather simple problem that is easily solvable for two particles but becomes unsolvable (in an exact analytical sense) for  $N$ -body systems. The maybe most famous example, or at least the first problem we encounter during our studies, is the elastic collision of two bodies which is an easy task and fully deterministic. The elastic collision of three particles is analytically solvable by calculating it in the centre-of-mass frame, which effectively decreases the dimension of the problem by one and leads to a continuous spectrum. The  $N$ -body collision is not solvable analytically. The same holds true for many problems, like the Coulomb forces on the electrons in an atom. While the hydrogen atom is analytically completely solvable, we fail to find an exact, generic analytical solution for the helium atom. Usually we use approximations to solve these problems, especially when continuing to quantum mechanical models, e.g. we can treat the electron–electron interaction as a perturbative term and calculate the energy corrections by solving the Schrödinger equation.

However, every problem eventually will become analytically unsolvable when we take too many bodies into account. A challenging problem arises in the context of cosmology. We cannot create little laboratory sized universes to test our cosmological model. If we want to test our cosmological and gravity models, we have to test them with large  $N$ -body simulation. The challenging task is to perform a large simulation of millions (modern simulations easily use billions) of particles.

Gravity has a unique role when we look at the four fundamental physical forces. The coupling constant of gravity is, when compared to the other forces, rather weak. We experience this in our daily lives, as ordinary household magnets exert a stronger force on an object than the Earth’s gravitational attraction does. On the other hand, the weak and strong interaction have a limited length and electromagnetic forces are shielded by a conjugate charged particle. The gravitational force is not shielded as we do not know any particle that carries a negative mass; its action length – in its Newtonian model – is infinite, though its strength decreases over large distances. In Newtonian physics we can express the force between two objects of masses  $m_1$  and  $m_2$  and with a spatial separation  $r$  as

$$F = -G \frac{m_1 m_2}{r^2}. \quad (3.24)$$

We see that the strength of the force drops rapidly but nonetheless every object feels every other particle exerting a gravitational force on it. These small forces are especially important in cosmology as there is no other, stronger, force working on a particle. Thus, reasonable approximations are needed to perform  $N$ -body simulations. In the following we explore some of the basics of an  $N$ -body simulation. Nearly all  $N$ -body problems can be summarized by the equation

$$U(\vec{x}_0) = \sum_{i=0}^N F(\vec{x}_i, \vec{x}_0), \quad (3.25)$$

where  $i$  is a summation over all particles. This formula means that a given variable  $U$  at position  $\vec{x}_0$  is the summed up interactions  $F$  of all particles at positions  $\vec{x}_i$ . Using this scheme for gravitational force on a particle of mass  $m$  we find, similarly to eq. (3.24) but in vector form,

$$\vec{F}(\vec{x}_0) = \sum_{i=0}^N -Gm \frac{m_i}{r_i^2} \hat{r}_i, \quad (3.26)$$

where  $\hat{r}_i$  is the unit vector in the direction of particle  $i$  and  $r_i$  is the spatial distance.

### 3.2.2 RAMSES

In this thesis, we use the RAMSES code Teyssier (2002) to perform  $N$ -body simulations, aimed at approximating the standard cosmological model (chapter 2) and generate a realisation of the density distribution. RAMSES is published under a free-software licence, CeCILL,<sup>3</sup>, which satisfies Akhlaghi et al. (2021) reproducibility criterion 8.

We follow Teyssier (2002) and add information about the numerical tools from Hockney & Eastwood (1988) together with Lindholm (1999). In Newtonian physics the motion of a particle is fully described by the Vlasov-Poisson equations given by

$$\frac{dv_i}{dt} = -\nabla_x \phi \quad \text{and} \quad \Delta_x \phi = 4\pi G \rho, \quad (3.27)$$

where  $\phi$  is the gravitational potential and  $\rho$  is the matter density. To discuss how RAMSES is solving these equations and how it evolves particles over time we first have to understand how RAMSES is organizing its data.

#### Cosmological $N$ -body methods

There are different methods to solve the Poisson equation. A few will be explored in this section.

**Particle–particle (PP)** Calculating the force exerted by every particle in the simulation on every other particle is not practical since its computation time scales as  $\sim N^2$  for  $N$  particles. Moreover, for a standard 3-torus simulation, the covering space is infinite, so a first-principles calculation would require an infinite number of pairwise force calculations. Even worse, in the Newtonian, instantaneous particle–particle attraction model, the net vector values  $\vec{F}$  in eq. (3.26) are divergent sums, i.e. they are undefined. A simply connected infinite Newtonian model has the same problem if it is statistically approaches homogeneity on successively larger scales. Switching to a model of potentials (eq. (3.27)) bypasses these divergences.

The naïvest of these approaches, calculating direct particle–particle attractions for a single copy of each particle in the covering space, is called the particle–particle method (PP) method and is conceptually the easiest solution to the problem, as it only requires calculating the sum in eq. (3.26).

**Particle–Mesh (PM)** The Particle–Mesh algorithm (PM) bypasses the above issues of Newtonian approaches by representing the field equations, e.g. the density estimation in the Poisson equation, on a mesh, changing from a continuous derivative for the Laplacian to finite differences. Doing so means that the algorithm is only sensitive to fluctuations that have a larger wavelength than the mesh grid size. The algorithm then interpolates the (density) field on the particle position and performs force calculations based on the interpolation. In the context of a cosmological  $N$ -body simulation we can visualise the particle–mesh algorithm by placing every particle in a mesh-cell, see fig. 3.1.

Based on such a mesh definition we derive the matter density around a particle and we solve eq. (3.27). A naïve and easy approach to assign a mass to each cell is the nearest gridpoint method (NGP). The mass  $m_i$  of a particle  $i$  is assigned to the cell of volume  $V$  with the closest mesh point to the particle. The density is then  $m_i/V$ . RAMSES instead uses the cloud-in-cell (CiC) method to estimate the matter density, which, in general, should give a more realistic estimate. The mass of the cell is assigned corresponding to the intersection of the “cloud” of a particle

<sup>3</sup><http://www.cecill.info>

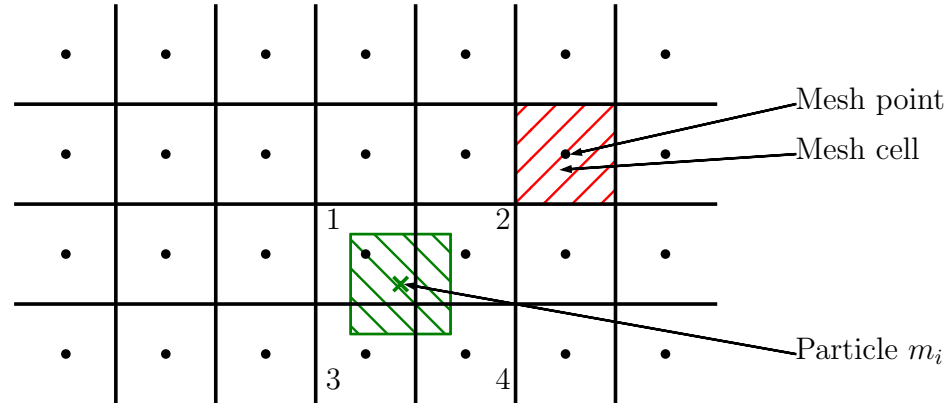


Figure 3.1: An illustration of an example particle mesh adapted from Lindholm (1999). The particles are laying in a cell of the mesh, the code knows about the neighbours of every cell and of the displacement of the particle.

and the cell. In fig 3.1 the cloud is shown by the green sketched box around the particle. In this case most of the mass is assigned to cell 1. Cells 2 and 3 are getting nearly the same amount of mass assigned to them and only a small fraction is assigned to cell 4. The limitation of mesh codes is that the precision relates to how fine the mesh grid spacing is defined. The particle mesh code is faster than calculating the force contribution of every single particle in a single copy of the fundamental domain, but it is imprecise when it comes to close interactions. Hockney & Eastwood (1988) state that a correlated system with interacting particles would require so many mesh points that the PM method would even exceed the computational time of the PP method.

**Particle-particle-particle-mesh (P3M)** A significant improvement can be done by including particle-particle interactions of nearby particles; the method becomes a particle-particle-particle-mesh code (P3M). The P3M method splits the problem into a smooth, slowly varying large scale interaction and a rapidly changing short range interaction. In such a method we assume a length  $r_e$  to quantify the problem. Every particle closer to the particle of interest than  $r_e$  has to be taken into account by particle-particle interactions. Doing so combines the speed of the PM code for the far away perturbations while keeping a correct treatment of the close environment. It is obvious that this algorithm gets very expensive once the particles have clustered in the simulation. A solution was proposed by Couchman (1991) by using an adaptive version of the P3M method. The idea is to search for mesh cells (starting or joining a mesh-cell chain) with a high operation count. The algorithm counts the particles in a chain cell and if the number of particles is above a set threshold, then it will refine the chain cell into smaller cells. The order of refinement is crucial for obtaining better results. The algorithm approximates the amount of computational savings as a function of a parameter  $L$ , the number of refined cells,



and chooses  $L$  to maximize the savings.

**Tree code** Another method is that of tree codes, e.g. Barnes & Hut (1986) created one of the first tree-code algorithms. When a distribution of particles is sufficiently far away we can model this distribution by a single, heavier particle that is located at the centre of mass of the particle distribution. The particles get divided into boxes, each of these boxes has 8 children in a three-dimensional case (in 2D the box would have 4 children). This is called a octree structure. The boxes are successively subdivided until every child box contains a maximum of one particle. Following the tree analogy, these children are called leaves. To quantify if a particle is sufficiently far away from a target particle, we can establish a rough check by introducing

$$\theta = \frac{D}{r}, \quad (3.28)$$

where  $D$  is the length of a side of the box of the current target particle and  $r$  is the distance between the target particle and the centre of mass of a different box. We have to set a threshold for  $\theta$  to decide if a node is sufficiently far away to use the approximation of using a single higher mass particle or if the code needs to go to the next level of the tree hierarchy and use child boxes.

It is clear that this algorithm will use the highest order (coarse) grid boxes for far particles while successively including more children boxes when getting closer to the particle of interest. If  $\theta = 0$ , the algorithm reverts to the PP method. The code traverses the nodes starting from the root and then decides if a node is sufficiently far away and calculates the net force. Even though this algorithm seems to be faster than the standard PP codes, it needs significantly more memory to store the additional data, as it is necessary to connect all children with their parents and vice versa.

**Adaptive mesh refinement (AMR)** RAMSES makes use of a combination of all the above mentioned methods. It uses adaptive mesh refinement (AMR) (Teyssier, 2002). This method defines the mesh on a recursively refined, spatial tree. The approach combines the advantages of the speed of fast Poisson-solvers from PM and the high dynamical resolution of tree codes.

The basic structure of RAMSES is a fully threaded tree (Khokhlov, 1998). The basic element is not a single cell but eight sibling cells (3D, four siblings in 2D) analog to the octree structure. These eight sibling cells are called an oct. The refinement level is denoted by  $l$ . Every oct in level  $l$  is linked to its neighbouring octs, its parent cell in a higher refinement level  $l - 1$  and to its children octs at  $l + 1$ . If an oct has no children, then it is called a leaf. On the highest order level  $l = 0$  a uniform Cartesian grid of a user-defined resolution (specified by the number of particles) builds the base of the tree structure. When updating the properties of the particles the time integration can be performed in two different ways, with a constant timestep  $\Delta t$  for all levels or using a timestep adapted at each level. In the latter case, the equations of motion are solved for  $\Delta t$  on the  $l = 0$  level and in adaptive smaller timesteps on the lower levels. At  $l = 1$  we have to solve the equations in two timesteps, at  $l = 2$  for four timesteps and so on.

To cope with the evolution of the dark matter distribution from an almost uniform grid with small initial perturbations up to the complex structure of the cosmic web the code needs to generate a refinement map deciding where the density gets too high so that further resolution is needed. In RAMSES the user has to define a refinement criterion; a common refinement criterion is the gradient of a flow variable exceeding a threshold. The code runs through 3 phases, starting from  $l_{max}$  and ending at  $l = 0$ , to mark the cells that need refinement.

- 1 If a cell has a marked or an already refined children, then mark it.

- 2 Mark the neighbouring cells.
- 3 If the cell matches the refinement criteria, then mark it.

After the cells have been marked for refinement the code needs to update the tree structure accordingly. RAMSES starts to go through all cells starting at the coarse grid,  $l = 0$ , level. The code will create the cell's child-oct when a leaf cell, a cell that previously had no child, is marked for refinement. The code destroys the child-oct of a cell when it is not marked for refinement. RAMSES does not need to build up the complete refinement-map at every timestep from scratch. Typically, only a few octs are created and destroyed as the  $N$ -body simulation evolves over time. New octs are included into the existing tree structure or existing octs are deleted from it.

The core component of the RAMSES  $N$ -body simulation is to solve the Vlasov-Poisson-equation, eq. (3.27). As stated above, RAMSES does this similarly to a PM code.

- 1 Approximate the matter density  $\rho$  by using CIC.
- 2 Solving the Poisson equation on the mesh to obtain the potential  $\phi$ .
- 3 Compute the acceleration of the mesh by using the gradient of the potential.
- 4 Compute the acceleration of each particle using an inverse CIC scheme.
- 5 Update the particle velocity by using the acceleration.
- 6 Update the particle position by using the velocity.

When computing the density field the algorithm first takes particles on level  $l$  into account. After that the algorithm will take the neighbouring particles into account when their cloud overlaps with the volume of interest. Once RAMSES has derived the matter density it can start to solve the Poisson equation. The coarse grid solutions are unaffected by any effect of the fine grids while the boundary conditions of the coarse grid solutions are passed to the finer grids via linear interpolation. The Poisson equation at the uniform grid at  $l = 0$  is solved with a Fast Fourier Transform, the higher order grids are solved with a relaxation method that we describe now.

RAMSES uses the conjugate gradient algorithm (CGA) to solve the Poisson equation. The algorithm was designed to search for the minimum of a function and can also be used to solve a set of differential equations. This section follows the description presented in Hockney & Eastwood (1988). Assume a function of the shape

$$A\phi = b, \quad (3.29)$$

which has the same shape as the Poisson equation and will be solved. Define the quadratic function

$$V(\phi) = \frac{1}{2}\phi^T A\phi - b^T \phi, \quad (3.30)$$

where  $b$  is a vector containing all matter density values at each charge point of the mesh.  $\phi$  is as suggested the potential vector. The matrix  $A$  can be computed using a mesh relaxation method, RAMSES uses the Gauss–Seidel method, yielding

$$\phi_{i,j}^{n+1} = \frac{1}{4} \left( \phi_{i+1,j}^n + \phi_{i-1,j}^n + \phi_{i,j+1}^n + \phi_{i,j-1}^n \right) - \frac{1}{4}\rho_{i,j}, \quad (3.31)$$

where  $i$  and  $j$  are the indices for the cells. With this formula we can compute the entries for the matrix. The CGA can only be used when  $A$  is positive definite and symmetric, which is ensured by using the finite difference approximation for  $-\nabla^2$ , i.e.

$$\frac{d^2\phi}{dt^2} = \frac{\phi(t - \Delta t) - 2\phi(t) + \phi(t + \Delta t)}{\Delta t^2} + O(\Delta t). \quad (3.32)$$

Differentiating eq. (3.29) we obtain the gradient vector  $r$

$$r = A\phi - q = \frac{\partial V}{\partial \phi} \quad (3.33)$$

and the second derivative shows us that  $A$  is determined by

$$\frac{\partial^2 V}{\partial \phi_i \partial \phi_j} = A_{ij}. \quad (3.34)$$

From the latter two equations we can conclude that all first derivatives are zero at a solution to eq. (3.29) ( $A\phi - b = 0$ ) and that, if  $A$  is positive definite, then this is a minimum.

The algorithm now calculates the gradient  $r_0$  at the initial position for an initial value  $\phi_0$ . It then searches for the minimum along the direction  $\hat{s} = -\hat{r}_0$ . By construction this direction has the steepest slope. Assume the algorithm finds a minimum at  $\phi_1$ . The next direction to search for a minimum is chosen to be a superposition of  $s_0$  and the next steepest-descent direction (see fig. 6-4 in Hockney & Eastwood (1988))

$$s_1 = -r_1 + \beta s_0 \quad \text{with} \quad \beta = \frac{r_1 \times r_1}{r_0 \times r_0}. \quad (3.35)$$

After a few steps the algorithm will eventually find the global minimum and the iterative scheme stops.

### 3.3 Voids – REVOLVER

#### 3.3.1 Spherical-expansion tophat heuristic model

The simplest approach to model a void is to model it with an isolated upside-down tophat profile in a homogeneous, isotropic FLRW background. This is a reasonable toy model. Even if the void initially does not possess a perfect tophat structure, the density profile will naturally evolve towards it. This tophat model was first developed for a spherically symmetric, tophat, overdensity profile to describe matter infall into a cluster (Gunn & Gott, 1972; Lilje & Lahav, 1991), though it was noticed that there is a closely related solution for underdensities (Sheth & van de Weygaert, 2004).

The underdense density perturbation of a cosmic void will, in contrast to overdensities such as clusters, expand faster than the background. Hence, voids grow in size over time and will become more empty as the matter is stretched more and more thinly over time. Such an idealised structure can be thought of as a conjunction of concentric matter shells that will each evolve based on the scale factor behaviour of an FLRW  $a(t)$  solution as a spatially bounded patch (a thick spherical shell) of an FLRW hypersurface.

Details of this toy model are given in App. A of Sheth & van de Weygaert (2004) in a self-contained compact form. Based on this model, Sheth & van de Weygaert (2004) characterise void formation by the following processes:

- Voids expand faster compared to the background model and in contrast to the overdense regions, which collapse. This faster expansion is approximately spatially constant within the void, so the expression “super-Hubble bubble” can be used to describe the void as a bubble that expands faster than the background Hubble–Lemaître expansion rate.
- As the void expands the density will decrease, which is called evacuation. To first order the effect is only due to the higher volume of the void, while at second order the void loses matter to the surroundings.
- The expansion will drive the void to become more spherical.
- The density profile will tend towards the shape of an upside-down tophat.
- As the density inside a void becomes more homogeneous in this toy model, structure formation is damped and eventually will completely stop.
- As the matter shells are pushed outwards, they will form a ridge at the edge of the void.
- The expansion is not completely Hubble-like: some of the inner shells will pass the outermost shells, due to their higher velocity, and the process becomes non-linear. We denote this process as shell-crossing.

This very simplistic model was first used to generate simulations of hierarchical void formations that were able to generate the well observed cosmic web. Walls, filaments and clusters in this approach are not directly modelled but a direct consequence of matter being pushed to the edge of the voids.

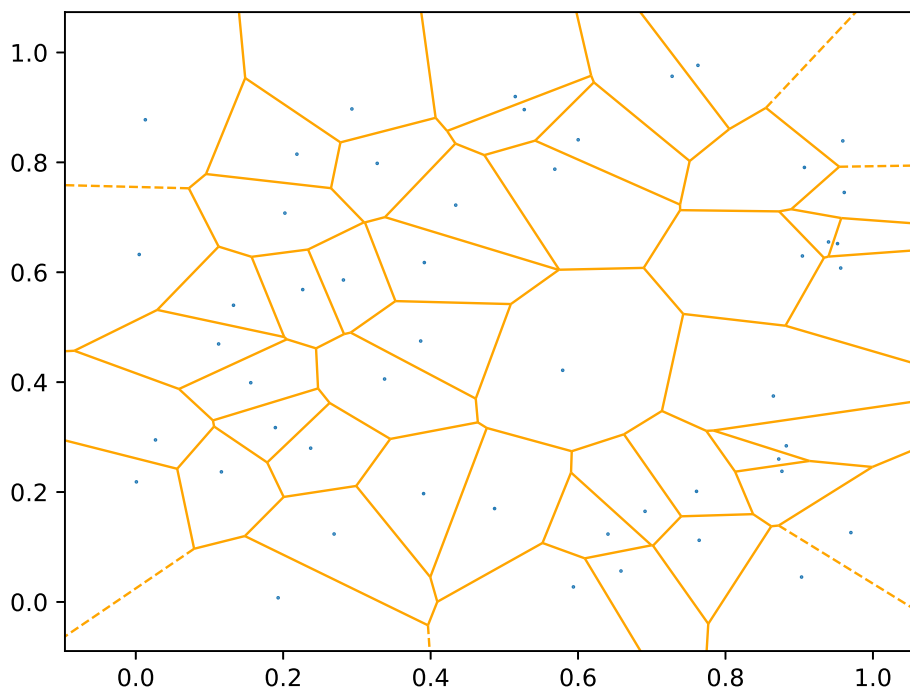


Figure 3.2: A schematic example, in two dimensions, of the Voronoi tessellation where blue dots represent the tracers and orange lines indicate the borders of the Voronoi cells.

### 3.3.2 Watershed

We have now learned about a simplistic, theoretical description of voids being perfectly spherical underdensities. As mentioned in section 2.2.2, voids yield a pristine environment to probe cosmological models such as dark energy models. One major goal of this work will be to investigate whether this special environment has a measurable influence on the formation and evolution of galaxies. Galaxies located in voids will be much more isolated than those in dense environments. Thus their evolution should not be influenced by disturbances like mergers as much as in the case of galaxies forming in other environments. We do this study based on numerical data, although the tool described in this section is also designed for and used to identify voids in observational catalogues.

In our pipeline we use the watershed void finder `REVOLVER` to identify voids (Nadathur et al., 2019). `REVOLVER` includes its own void finding technique, but for this work we only focus on it as a wrapper for `ZOBOV` (**Z**Ones **B**ordering **O**n **V**oidness) (Neyrinck, 2008). Thus we first introduce the watershed method underlying `ZOBOV`. `REVOLVER` is published under a free-software licence, the GNU General Public License version 3,<sup>4</sup> satisfying Akhlaghi et al. (2021) reproducibility criterion 8.

A straightforward and easy definition of a void is a sphere; in fact there exist void finders that build upon this simplified model by defining voids as spheres or merged spheres, e.g. Kauffmann & Fairall (1991a); Müller et al. (2000). However, this still is a strong simplification that in general will not hold true for an observationally detected void. Voids tend to become more spherical as they grow, yet do not become exactly spherical – in particular because they have to coexist with

<sup>4</sup><https://www.gnu.org/licenses/gpl-3.0.html>

surrounding structures of the cosmic web.

Since we aim to identify void galaxies – galaxies that are “in” voids, the question of how we define the borders of a void is significant. Differences in deciding on the boundary of a void will give different consequences for classifying galaxies as void galaxies or as belonging to another environment.

Watershed finders as ZOBOV do not assume any shape of the void. In fact, they aim to find voids with as few model dependent input parameters as possible and are close to being parameter-free. We outline the key steps of the watershed method in the following:

### 1st

First the code estimates the density using the Voronoi Tessellation Field Estimator (VTFE). See fig. 3.2. The tessellation technique is another way to estimate the local density in discrete data (we recall the CiC method introduced in Sec. 3.2). The VTFE divides the space into cells, where each cell contains the space around a particle which is closest to this particle. The density of a particle  $i$  is now defined as  $\rho_i = 1/V_i$ , where  $V_i$  is the volume of the cell. The volume on the contrary is the convex hull of the Voronoi cell. Moreover, it is straightforward to define the neighbouring particles with this method. An alternative estimator could be the Delaunay Tessellation Field Estimator (DTFE). In fact, the two methods are closely related as they are inverse to each other. Voronoi cells isolate one particle per cell, while Delaunay tessellations join particles in triangles (in two dimensional flat space) or tetrahedra (in three dimensional flat space). The points of the triangle or tetrahedron for the Delaunay tessellation are chosen so that the circumscribing circle does not include any of the other data points. A more detailed discussion of the DTFE method can be found in Schaap (2007). Given a Delaunay tessellation, the Voronoi cells can be constructed by taking the centres of the circumscribing circles as the vertices for the faces of the polyhedron (in three dimensions) of each Voronoi cell. ZOBOV uses the QHULL library to first construct the Voronoi cells of the tracer distribution.

### 2nd

The next step is called zoning. In this step, ZOBOV associates each particle with a local density minimum. A local minimum is defined as a cell which has a density less than or equal to all of its neighbouring cells. To find the minimum cell to which a particle in cell  $i_0$  should be associated, if the particle is not already in a cell that is a local minimum, then the particle is associated with its neighbouring cell  $i_1$  of lowest density. If cell  $i_1$  is not a local minimum, then the search continues successively to the lowest density cell  $i_2$  that neighbours cell  $i_1$ , and then to cell  $i_3$  that neighbours cell  $i_2$  if necessary, until a local minimum  $i_n$  is found for the particle whose actual location is in cell  $i_0$ . This can be loosely visualised as water iteratively flowing down each local neighbourhood of maximum steepness until it reaches a local minimum. The cells of the set of particles associated with a given locally minimal cell is defined as a zone.

### 3rd

Based on this definition of zones, the code continues with the watershed step. Imagine the density field as a mountainous area with valleys, peaks and saddle-shaped ridges, where heights represent densities. The method begins with setting a “water” level in the lowest density cell of a zone. This starts off the definition of a void. The water level is then gradually raised in the zone, covering neighbouring cells and adding them to the void. If water reaches a saddle point (or void boundary for a perfectly symmetric void), then the water leaks into the neighbouring

zone. If the central particle of the zone, in which the water leaks into, has a lower density than the lowest density cell of the starting zone, then the process stops. This void cannot grow any further. Otherwise, the zone will be added to the void and the process continues to increase the water level. By construction, the original minimum of the zone, where water was first added, corresponds to the minimum density of the void. This process is repeated for all identified zones. This method leads to one parent void (the deepest) that fills the whole volume. All other voids are subvoids of the parent void. We consider the growth of voids and subvoids further in the 5th step.

#### 4th

The next task is to find a way to state the statistical significance of the part of a zone identified as a (sub)void, i.e. whether the object is really a void. To do so we introduce  $\rho_l$ , the density at which water flows across a saddle point or void boundary into a neighbouring zone (“l” stands for linking). We define the linking-density contrast as  $r(v) \equiv \frac{\rho_l(v)}{\rho_{\min}}$  (where “v” is an identifier for a void), where  $\rho_{\min}$  is the minimal density of the void. The linking-density contrast  $r$  is converted to a probability based on the assumption of a Poisson distribution of the particles. Neyrinck (2008) models the cumulative probability  $P(r)$  that a void with linking-density contrast  $r$  arises from a Poisson particle distribution based on two numerically generated distributions (one with  $128^3$  particles and one with  $256^3$  particles) and finds a best-fit approximation

$$P(r) \approx \exp\left(-5.12(r-1) - 0.8(r-1)^{2.8}\right). \quad (3.36)$$

$P(r)$  now gives an estimate of the probability that the detected void arises from Poisson noise thus that it is not real.

Additionally, we can use a theoretical, physical rule-of-thumb, arguing that the natural dark matter density of a top-hat void that has undergone expansion is  $\rho_{\text{void}} \approx 0.2\rho_{\text{mean}}$ . Neyrinck (2008) suggests that this criterion be used as sanity check on the void population. He found that all voids detected satisfied this requirement, so none were eliminated by this extra criterion.

#### 5th

As mentioned above, the watershed method leads to one dominating void. There are three different ways to deal with this.

The first option is to accept it. This requires no parametric choices, but is inconvenient if “isolated” voids are to be studied, and not their subvoids.

The second option is to specify a significance level and to cut all voids below a fixed significance level derived from the Poissonian probability  $P(r)$  (eq. (3.36)). This is equivalent to a restriction setting a minimum for the linking-density contrast  $r(v)$ . If a subvoid is excluded via this criterion, then all zones that joined the parent void due to the accretion of the subvoid are removed.

The third option is to determine the most probable extent of voids by comparing the probability that the particle distribution of a void could arise from a Poisson particle distribution before and after adding a zone to the void. The estimate is based on the linking-density contrast  $r$ . Following (Neyrinck, 2008) we define the significance  $S_i$  for each zone-adding event. The significance of zero zone additions is defined as  $S_0 \equiv P(r(z))$ , where  $P$  is the probability that the particle distribution of the first zone of the void, indicated as  $z$ , arises from a Poisson particle distribution. The union of  $z$  and a void after the  $i$ th adding event to the zone  $z$  will be called  $v_i$ , with  $v_0 = z$ . Assume that  $j$  zones are added in the  $(i+1)$ th zone-adding event; we call the

set of these  $j$  zones  $Z_{i+1} = \{z_{i+1,j}\}$ . ZOBOV now compares the probability that  $v_i$  and all of the zones in  $Z_{i+1}$  are individually a Poissonian chance event to the probability that their union,  $v_{i+1} = v_i + Z_{i+1}$ , is a chance event. Based on these two probabilities, the code decides if the extension of the void makes sense; we can recursively define  $S_{i+1}$ , knowing  $S_i$ , as

$$S_{i+1} = S_i \frac{P(r(v_{i+1}))}{P(r(v_i)) \prod_j P(r(z_{i+1,j}))}, \quad (3.37)$$

where  $r(v_{i+1}) = \rho_l(v_i)/\rho_{\min}(z)$ , with  $\rho_l(v_i)$  being the lowest density of the subsample of particles at the ridge separating the zones of void  $v_i$  to the newly added zones in the event  $Z_{i+1}$ . If the significance of the union is lower than the significance of the single zones, then their union is statistically favoured. Additionally, to prevent voids from growing into haloes, we can set a maximal linking density can be set, such as  $\rho_{l,\max} = 0.2\rho_{\text{mean}}$ .

In contrast to the early theoretical descriptions of voids, a watershed void has no information regarding shell crossings, so the work of connecting spherical-expansion model voids with numerically detected watershed voids is not yet completed (Nadathur & Hotchkiss, 2015a,b).

### 3.3.3 Void centres

As a first step we are interested in the formation history of galaxies near the centre of a void. We stated in section 2.2.2 that the evolution of galaxies that formed in voids might differ from galaxies evolving in more dense environments. It is a fair assumption that the most significant difference will be found in the centre of the void. Our hypothesis is that galaxies near the centre of a void will naturally tend to be large and underdense. It seems to be natural that a large, underdense galaxy will evolve in an area that shares the same properties. Moreover, a void centre is a special place in the cosmic web, since the evolution of a galaxy will be undisturbed by other galaxies coming close by or merging with it.

How do we define the centre of a void? An obvious choice of the centre could arise from the watershed mechanism, by defining the centre of the void as a central position in the cell of lowest density in the void. REVOLVER provides us with two different approaches. It returns what it calls a “volume averaged barycentre” and calculates it via

$$\vec{c} = \sum_i \frac{\vec{x}_i}{V_i}, \quad (3.38)$$

where  $\vec{x}_i$  are the position vectors of all particles in the void and  $V_i$  is the corresponding volume of the Voronoi cell. In fact, this definition gives the geometrical centroid, not the barycentre (the barycentre is, by definition, mass-weighted).

The second centre returned by REVOLVER is the circumcentre, which indicates the lowest density cell and the three lowest density neighbours. The centre returned by the code is the circumcentre of a sphere that goes through all four particles of the lowest density cell and the three neighbours. This should approximately mark the location of lowest density in the void.

A third approach is to use the gravitational potentials that are accessible from cosmological simulations. While the void is a minimum in density, it is a maximum in potential. We use the routine in REVOLVER to estimate the maximum potential in a void based on the particle with the highest potential and its three highest-potential neighbours. By searching for the maximum of the potential, we find the spatial position in a void that is a gravitational equilibrium point – within the Poissonian gravitational model of the simulation, the gravitational forces exerted by the matter in surrounding walls and clusters cancel each other. This equilibrium point is, of



course, unstable. We refer to this location in a void as the void's "elaphrocentre". Due to the correlation between density and potential in the Poisson equation, we expect the circumcentre and elaphrocentre to not differ significantly.

Nadathur, Hotchkiss, & Crittenden (2017) investigate if they can trace the gravitational potential using the voids properties in their simulations. They find that they can trace the gravitational potential by introducing a new void observable, which is a combination of the average galaxy density and the size of the voids.

## 3.4 Halo Finder – ROCKSTAR

### 3.4.1 Spherical collapse toy model and dark matter halo properties

The growth of matter perturbations eventually leads to the structures we observe today. Gravitational attraction will create massive structures, including galaxies and clusters of galaxies. The underlying dark matter distribution clumps first, creating haloes of various sizes. The extended process in which dark matter collapses to an overdense structure is ended by virialisation. Galaxies will form in dark matter haloes, so in order to have a cohesive descriptive chain, from initial perturbations up to galaxies, we briefly describe the formation of dark matter haloes following Cooray & Sheth (2002).

The evolutionary history of dark matter haloes is in general very difficult and not linear. Thus it is not possible to solve it completely analytically. A simplified approach is provided in the spherical collapse model that assumes that a halo can be modelled as a spherical top-hat perturbation.

In comoving distance units, an overdensity perturbation shrinks since the early universe, e.g. per the Zel’dovich approximation (Zeldovich & Grishchuk, 1984). However, in physical distance units, the perturbation initially expands, just slightly slower than the expanding background Universe. The “turnaround” epoch is the epoch when the perturbation has sufficiently slowed down its expansion in physical distance units that it starts collapsing. In this simplified approach of the spherical collapse model, presented here in the Einstein–de Sitter case, the turnaround epoch of a perturbation is characterised by a parameter called the development angle reaching the value  $\Theta = \pi$ , and the collapse epoch by  $\Theta = 2\pi$ . However, a real halo is not perfectly homogeneous and spherical, nor is the process linear.

Instead of collapsing, the halo structure rather reaches virial equilibrium. Let us denote the initial comoving size of the perturbation as  $R_0$  and the initial density of the perturbation as  $\delta_i$ . As the Universe evolves over time also the comoving size  $R$  of the perturbed region changes over time. We define the density in the region as  $(1 + \delta) = (R_0/R)^3$ . The growth of the perturbation with respect to the background in this model is given by (eq. 51 of Cooray & Sheth 2002)

$$\frac{R_0}{R(z)} = \frac{6^{2/3}}{2} \frac{(\Theta - \sin \Theta)^{2/3}}{(1 - \cos \Theta)}. \quad (3.39)$$

With this equation, we can estimate the density at turnaround,  $\Theta = \pi$ , which is  $(6\pi)^2/4^3 \approx 5.55$  times the mean density. If a halo collapses, then we can also infer that the density would diverge to infinity according to this model. In reality, particles will bypass the halo’s centre, and those that are bound may gradually reach a virialised equilibrium. In order to estimate the overdensity at which the halo virialises, it is common to assume that the halo virialises at half the turnaround radius. The background universe expands during the time between turnaround and collapse by the factor  $(1 + z_{\text{ta}})/(1 + z_{\text{col}}) = 2^{2/3}$ . Thus, the background density at collapse is four times as low as at the time of turnaround. As the spatial size of the perturbation is half the turnaround radius, the density of the perturbation is eight times higher. Thus, in total, the mean density of the virialised object is 32 times  $(6\pi)^2/4^3 = 18\pi^2 \approx 178$  times that of the background density of the Universe at the time of virialisation.

The above description is a simplified toy model presented for the Einstein–de Sitter case (with similar calculations for other FLRW cases, e.g. Lacey & Cole 1993, Appendix A for the hyperbolic,  $\Lambda$ -free case). A real halo is not a perfectly spherical, isolated object with a homogeneous density distribution. Today, it is common to define a virialised object by using an overdensity constant  $\Delta_c$ , which most commonly is set to 200, even in models that are not

Einstein–de Sitter. By introducing this constant, it is straightforward to define the virial radius of a gravitationally bound structure as the radius at which the density of the object fulfils  $\rho(R_{\text{vir}}) = \Delta_c \rho_c$ , with  $\rho_c$  being the critical density of the background universe. This popular definition aids comparisons among models and between models and observations. The virial mass is then defined as the mass contained inside this radius, with  $M_{\text{vir}} = \frac{4}{3}\pi R_{\text{vir}}^3 \Delta_c \rho_c$ . In early simulations it was shown that the density profile of a dark matter halo can be approximately modelled by a Navarro–Frenk–White profile

$$\rho(r) = \frac{\rho_0}{\frac{r}{R_s} \left(1 + \frac{r}{R_s}\right)^2}, \quad (3.40)$$

where  $\rho_0$  and the scale radius  $R_s$  have to be found for each halo.

Another interesting property to study, which we just mention briefly here, is the halo mass distribution, which roughly follows a Press–Schechter distribution (Press & Schechter, 1974), which inspired the Schechter (1976) form, widely used to represent the observational galaxy luminosity function.

### 3.4.2 Halo finders

There are several different halo finder algorithms and codes available. The identification of haloes, though, is not trivial. An intuitively understandable problem is the identification of substructures. Usually, in the scenario of hierarchical structure formation, we observe a central structure that is surrounded by several smaller structures. For halo identification it can be difficult to identify the edges of these structures precisely and to distinguish between the central object and the smaller objects.

One popular routine to identify haloes is the friends-of-friends (FoF) algorithm, which groups nearby particles together in a gravitationally bound structure (a bottom-up approach). Another approach is spherical-overdensity methods, where the code first identifies local overdensities as the centres of haloes and then grows a shell around the centres, until the density of the shell falls below a predefined density threshold (derived from the spherical collapse formalism), binding particles in the shell to the halo, until a certain criterion is fulfilled (a top-down approach). It is not surprising that the choice of the halo finder influences the characteristics of the identified structures. A comparison of different routines was done in Knebe et al. (2011).

In this work we use an FoF algorithm and thus focus on this subclass of halo identification routines. The first FoF halo finder was proposed by Davis et al. (1985) where the authors used  $N$ -body simulations of different cosmological models and compared the structures that they found with theoretical predictions. Roughly speaking, an FoF finder will identify groups of particles using a fixed linking length. An FoF algorithm that only uses the positions of the particles, a 3D FoF algorithm, will have problems to distinguish between different structures. More advanced routines identify haloes in 6D phase space, i.e. they additionally use the peculiar velocities of the particles to distinguish between different structures. In general, substructures will have a different velocity distributions to each other, making it possible to distinguish between several substructures in the same group. However, defining a metric in phase space allows several choices. One can either define two separate metrics in spatial and velocity space separately, or a combined metric.

### 3.4.3 ROCKSTAR

We use the ROCKSTAR halo finder (Behroozi et al., 2013a). ROCKSTAR is published under the GNU General Public License version 3,<sup>5</sup> satisfying Akhlaghi et al. (2021) reproducibility criterion 8.

ROCKSTAR initially groups the particles in FoF groups by using the spatial (three-dimensional) information. These groups are only generated for efficiency purposes given the large amount of data. The code next identifies hierarchical substructures by using the full phase-space data of the particles in each FoF group. The phase-space metric used is

$$d(\vec{x}_1, \vec{x}_2, \vec{v}_1, \vec{v}_2) = \left( \frac{|\vec{x}_1 - \vec{x}_2|^2}{\sigma_x^2} + \frac{|\vec{v}_1 - \vec{v}_2|^2}{\sigma_v^2} \right)^{1/2}, \quad (3.41)$$

where  $\vec{x}_i$  are the spatial coordinates of a particle,  $\vec{v}_i$  is the velocity and  $\sigma$  is the dispersion for a given FoF group. Further iterative checks are also made to improve the physical and numerical justification of identifying groups of particles as haloes.

The linking length of the initial position-based FoF groups is chosen as a fraction of the mean interparticle distance. For subsequent steps in a hierarchical analysis, the linking length is refined such that an approximately constant fraction of particles are linked to at least one other particle at each step. The input parameters for ROCKSTAR have to be chosen carefully, since an initial linking length that is too high will find not significant subgroups, whereas an initial linking length that is too low will not resolve small substructures.

For each subgroup, the code recalculates the phase-space distances between particles in the subgroup, and can continue to identifying sub-subgroups until the minimal number of particles per group is reached. The minimal number of particles is a parameter that has to be chosen by the user.

Each subgroup in the largest-scale level of the hierarchy will host a seed halo. If these haloes' positions satisfy  $\sqrt{(\vec{x}_1 - \vec{x}_2)^2 (\sqrt{n}/\sigma_x)^2 + (\vec{v}_1 - \vec{v}_2)^2 (\sqrt{n}/\sigma_v)^2} < 10\sqrt{2}$ , i.e. if they are too close to each other, then they will be merged by ROCKSTAR into a single halo. Particles in the FoF group are initially considered to belong to the halo to which they have the smallest phase-space distance, where the metric  $d$  in eq. (3.41) is modified by replacing  $\sigma_x$  by the dynamical virial radius

$$r_{\text{dyn,vir}} = \frac{v_{\text{max}}}{\sqrt{4/3\pi G \rho_{\text{vir}}}}, \quad (3.42)$$

where  $v_{\text{max}}$  is the maximal circular velocity. This favours assigning particles to the correct haloes to which they are dynamically bound.

Subhaloes are identified as smaller structures within the virial radius of the most massive object. During merger events it is possible that particles change their membership from one halo to another. This can lead to ambiguity when defining the masses of haloes. ROCKSTAR takes care of this by additionally comparing the haloes to their progenitors if several snapshots are available. In this sense, ROCKSTAR can be described as a 7D halo finder. However, to have a consistent mass measure for haloes, even if a major merger happens, the definition of the central object might be changed when masses change. All particles within the dynamical virial radius are considered to contribute to the central object, while particles that are only within the virial radii of the subhaloes are considered to contribute to the masses of the subhaloes.

Halo properties that are interesting to study are their mass distribution, their abundance and their spatial distribution (spatial two-point autocorrelation function). Moreover,  $v_{\text{max}}$  and the radius  $R_{\text{max}}$  where the maximal circular velocity is reached are useful quantities, though they

<sup>5</sup><https://www.gnu.org/licenses/gpl-3.0.html>

depend on the position of the centre of the halo. The edge of a halo and its centre depend on the method chosen, while other properties are more robust. Knebe et al. (2011) uses these quantities, among others, to compare the haloes of several different halo finders.

Generally, spherical-overdensity halo finders perform better when identifying the spatial centre of a halo, as they place the halo at the density peak instead of taking the average over all particles contained in the bound structure. In particular, the particles at the boundary tend to add noise for finding a halo centre, since (by definition) they have a high dispersion in position. ROCKSTAR addresses this problem by minimising  $\sigma_x/\sqrt{N}$ , which reduces the influence of particles that statistically have a high positional dispersion in relation to the halo centre. Thus, the code reconstructs the centres of haloes well.

### 3.5 Merger-history tree – CONSISTENT-TREES

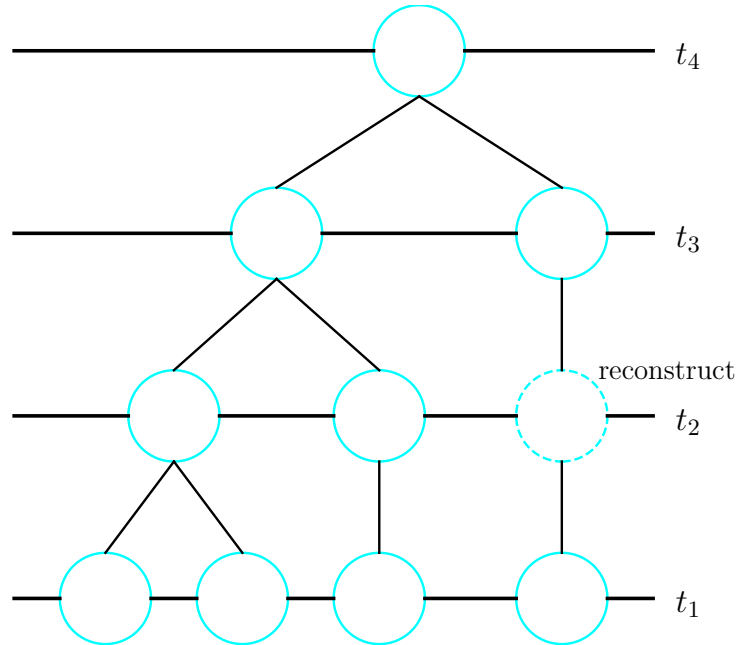


Figure 3.3: A scheme of a possible merger-tree over 4 snapshots. The different haloes merge along the time axis into one final halo whose properties are determined by its progenitors. One halo is only drawn with a sketched circle, indicating that this halo fell below the identification threshold of the halo finder but can be reconstructed using halo properties of its descendant and progenitor.

To populate our haloes with galaxies it remains necessary to construct a merger-history tree based on the haloes that are identified over several snapshots. Deriving dark matter halo merger-history trees from  $N$ -body simulations was first presented briefly in Roukema & Yoshii (1993), and in more depth in Roukema et al. (1997). A visualisation of a strongly simplified merger-history tree can be seen in fig. 3.3. Fig. 2 of Roukema & Yoshii (1993) shows the first merger-history tree derived from an  $N$ -body simulation and plotted, illustrating the much greater merger rates at earlier epochs.

The original criterion for deciding on when a halo at an earlier time step merges into a halo at the following time step was a 50% criterion (Roukema & Yoshii 1993, §3; Roukema et al. 1997, §2.1.3). If strictly more than 50% of the particles in a halo at one time step are present in a halo at the following time step, then a halo relation across the two time steps is established between the two haloes, representing either an identity (same halo, no merger) or progenitor–successor (multiple progenitors for one successor) relation. This criterion allows mergers, and by definition, excludes the possibility of complicated merger-trees in which a halo may split up and re-merge later. Kauffmann, Colberg, Diaferio, & White (1999a, §3) kept the same criterion, but added a second criterion by defining the ‘central particle’ of each halo (the most bound particle) and requiring that the central particle of a successor halo be present in the progenitor halo.

Several alternative sets of criteria for defining halo relations between  $N$ -body simulation time

snapshots have been developed since the original 50% and central particle criteria. In particular, Behroozi et al. (2013b) presented a method to construct merger-trees based on halo properties – the halo mass, position, and maximal circular velocity  $v_{\max}$ , and the bulk velocity, aiming at ensuring consistent halo properties over several snapshots. The bulk velocity for FoF haloes usually refers to an average of all particle velocities that constitute the haloes. The authors argue that particle based merger-trees suffer from the inconsistencies when haloes (usually a subhalo to its central halo) are too close to each other so that particles will falsely identified to belong to the wrong object. These cases will lead to haloes that in one snapshot are falsely represented as a single halo, but due to not being gravitationally bound reappear later as two separate successors, in an apparent split of a halo into two if a particle-based merger criterion with a lower than 50% is used. In the case of the original 50% criterion, at least one of the two successors would have no progenitor and appear to be new. Accounting particles to the wrong halo will additionally yield false halo properties and will occur regardless of how well developed a halo finder might be.

The code presented in Behroozi et al. (2013b), `CONSISTENT-TREES`, aims to solve this problem by checking the consistency between halo properties over several time steps. `CONSISTENT-TREES` is published under the GNU General Public License version 3,<sup>6</sup> satisfying Akhlaghi et al. (2021) reproducibility criterion 8. The code calculates, by using Newtonian gravity and inertia, the properties that the haloes should have in the previous time step and can thus evaluate if there might be an inconsistency. If a halo location does not match with the locations of estimated potential descendants, then the code will check if this halo is a temporal artifact of this snapshot or if the halo merges into a larger halo. To do so the code estimates the spatial derivative of the acceleration field to check if a merger might be feasible. The authors suggest that a simple threshold on the derivative is sufficient to distinguish between haloes that could have merged into another halo and those that could not. The code does this for all time steps filling up missing haloes and removing haloes that are just temporary fluctuations. If a halo has no direct progenitor but reappears after a few time steps, then the halo is reconstructed for the time steps in which it was missing. It is expected that halo properties only change slowly. Under the assumption that  $M_{\text{vir}}$  and  $R_{\text{vir}}$  are strongly correlated to  $v_{\max}$ , the authors define the metric

$$d(e,c) = \sqrt{\frac{|\vec{x}_e - \vec{x}_c|^2}{2\tau_x^2} + \frac{|\vec{v}_e - \vec{v}_c|^2}{2\tau_v^2} + \frac{\log\left(\frac{v_{\max,e}}{v_{\max,c}}\right)^2}{2\tau_{v_{\max}}^2}}, \quad (3.43)$$

where  $x$  are the halo positions and  $v$  the velocities, to quantify how reasonable the match between an expected progenitor (subscript  $e$ ) and a candidate progenitor (subscript  $c$ ) is. The parameter  $\tau$  refers to the characteristic errors in predicting the respective quantities. The code returns a cleaned merger-history tree with all spurious haloes removed, missing haloes added and properly linked haloes to their progenitors. Based on this merger-history tree, we populate the haloes with galaxies.

---

<sup>6</sup><https://www.gnu.org/licenses/gpl-3.0.html>

### 3.6 Semi-analytical galaxy formation – SAGE

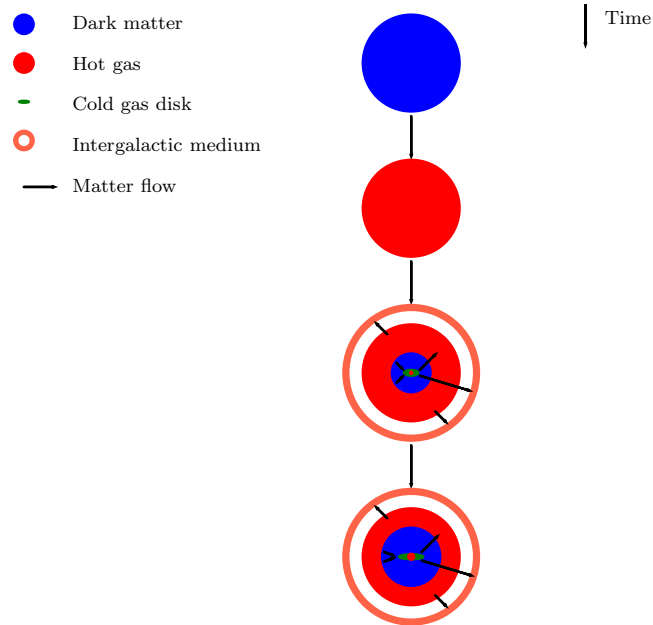


Figure 3.4: This scheme visualises the basic concepts of a semi-analytical model to build a galaxy in a dark matter halo. Semi-analytical models are build upon merger-trees – either semi-analytical themselves, or derived from  $N$ -body simulations. Thus the model starts with an empty dark matter halo. Baryonic matter proportional to a halo’s mass will fall into the halo being heated in this process (2nd timestep). The hot gas content starts to cool and form a rotationally supported disk with a supermassive black hole in the middle that will heat up nearby cold gas due to feedback processes (3rd timestep). Due to these internal processes and supernovae in the galaxy cold gas can be heated again again or hot gas can even be ejected from the halo. The figure was inspired by Baugh (2006) and is adapted to the modification that SAGE (Croton et al., 2016) did to the model.

Gravitationally bound structures – dark matter haloes – are necessary, but not sufficient, for galaxies to form. Baryonic matter, mostly hydrogen as we have seen in section 2.1.2, can only cool down in the potential wells of a dark matter halo. In the hierarchical structure formation model there cannot be a galaxy without a dark matter halo.

For initial work in combining semi-analytical halo merger-trees with semi-analytical formulae for gas cooling and the formation of galaxy disks, see Lacey & Cole (1993); Kauffmann et al. (1993). For the use of semi-analytical star-formation recipes (merger-induced starbursts) and stellar evolution population synthesis applied to  $N$ -body simulation derived merger-trees, see Roukema et al. (1993, 1997).

This chapter will generally follow Baugh (2006) with a few additions related to the software package that we use, SAGE (Croton et al., 2016), and will explore some details that will eventually lead to a representative galaxy population built upon the merger-trees. SAGE is published under the Expat License, also called the MIT 3-clause licence,<sup>7</sup>. This is a “permissive” free-software licence, satisfying Akhlaghi et al. (2021) reproducibility criterion 8. As the licence is permissive,

<sup>7</sup><https://directory.fsf.org/wiki/License:Expat>



redistribution of modified copies of software under non-free (proprietary) licences is allowed. We chose to distribute our modified version of SAGE under the same Expat License.

Semi-analytical models need at least three pieces of information about the dark matter haloes: their abundance, their merger-history and their internal properties such as their radial density profile and their angular momentum. Semi-analytical models aim to generate galaxy populations on top of  $N$ -body simulations (or semi-analytically generated merger trees, though we don't consider these further in this brief review) by carefully reproducing the statistically measured trends. Free input parameters are fine-tuned to reproduce measured properties. We visualise a simplified scheme of the semi-analytical model that will be used in this work in fig. 3.4. We explain in the following how the dark matter halo is modelled to accrete baryonic gas and how the gas can cool down to form a galaxy. Our model starts with a pure dark matter halo without baryonic matter (step 1 in fig. 3.4). This scheme should help support some of the basic concepts of semi-analytical models and does not claim to model the full set of processes contributing to galaxy formation.

A first conclusion was drawn based on a simple toy model which assumes a constant mass to light ratio over all halo masses and will result in a wrong luminosity function of groups. Compared to observations, e.g. Eke et al. (2004a,b), such a toy model produces too many faint groups and too many bright groups, see fig. 6 of Baugh (2006). To match observational data, star formation has to be suppressed for low mass haloes as well as for the highest mass haloes. Luminous matter is best produced in haloes of roughly  $10^{12}M_{\odot}/h$ . The crucial step to form luminous matter is that baryonic gas has to cool down. In our model, we assume that gas that falls into the dark halo is initially hot, heated up by shocks when falling into the gravitational well (step 2 of fig. 3.4). Only cooled-down gas will be able to collapse further into stars as hot gas is not collapsing any further due to the pressure (kinetic energy) of the gas. The process of cooling itself is dependent on the mass of the hot gas in the system; the initial temperature of the hot gas will be the temperature of the virial object

$$T_{\text{vir}} = \frac{1}{2} \frac{\mu m_H}{k} V_{\text{vir}}^2, \quad (3.44)$$

where  $\mu$  is the mean molecular mass of the gas,  $m_H$  is the mass of hydrogen and  $k$  is the Boltzmann constant. Here,  $V_{\text{vir}} = \sqrt{GM_{\text{vir}}/r_{\text{vir}}}$  can be thought of as a circular velocity at the virial radius (thermalised velocities prevent the halo from further gravitational collapse).

As the gas cools down it will fall into the centre of the dark matter halo and form a rotationally supported disk (step 3 fig. 3.4). To model this process, the radius of a sphere of gas that has had sufficient time to cool is defined, the cooling radius. The cooling radius grows with time. The gas contained within the cooling radius sphere is assumed to form the disk and will be compressed during its collapse. This results in a small gap between the disk and the hot gas halo, as the mass that was initially covering the volume is now collapsed. We assume that the angular momentum of the halo is preserved. The size of the disk can be estimated by the virial radius of the dark matter halo and the dimensionless spin parameter, generally attributed to Peebles (1969, eqs (35), (37)), using the definition introduced in Bullock et al. (2001)

$$\lambda = \frac{J|E|^{(1/2)}}{GM^{(5/2)}}, \quad (3.45)$$

where  $J$  is the angular momentum of the host halo,  $E$  is the total energy of the halo,  $G$  is the gravitational constant and  $M$  is the mass of the system. The spin parameter thus is basically a measure for the rotation of the halo. It is straightforward to imagine that a higher spin parameter will push matter out, enlarging the disk, along with the model proposed in Mo et al. (1998) we

thus define the disk radius as

$$r_{\text{disk}} = \frac{\lambda}{\sqrt{2}r_{\text{vir}}}. \quad (3.46)$$

This size is an important result of semi-analytical models as it can be compared against observations while we cannot measure the size of the dark matter halo easily.

For the hot gas in dark matter haloes to cool down the most important channels are emissions of photons and bremsstrahlung. The first is the result of collisions of partially excited atoms and electrons. These interactions will excite the electrons of the atoms to higher levels and they will emit this energy as photons when they fall back into the more stable lower states. This process is important for haloes with virial temperatures of  $10^4 K < T_{\text{vir}} < 10^6 K$ . Bremsstrahlung is, as the name suggests, emitted by electrons accelerating (or decelerating) in a magnetic field. Such a magnetic field is generated, in the context of galaxies, by the ionised plasma. The channel is important for massive dark matter haloes with  $T_{\text{vir}} \approx 10^7 K$ . Other channels are inverse Compton scattering, which is not efficient enough to cool down galaxies in the age of the Universe and thus is only important at the earliest time scales; and the excitation rotational or vibrational energy levels in molecular hydrogen due to collisions in small mass haloes.

The cooling time can be approximated by

$$t_{\text{cool}}(r) = \frac{3}{2} \frac{\mu m_H k T_{\text{vir}}}{\rho_g(r) \Lambda(T_{\text{vir}}, Z)}, \quad (3.47)$$

which is the ratio of the specific thermal energy to the cooling rate per unit volume. The gas density  $\rho_g(r)$  depends on the radial position in the halo and  $\Lambda(T_{\text{vir}}, Z)$  is the cooling function, which itself depends on the temperature of the hot gas and the metallicity  $Z$  of the gas. By ‘‘metals’’, we refer to elements other than hydrogen and helium. Significant quantities of these elements are released to the baryonic gas content of a galaxy at late stages of stellar evolution through stellar winds and supernova explosions. The authors model metal enrichment by returning a proportional amount of metals for every solar mass of stars formed in a galaxy. The metals are placed in the cold disk of the galaxy. SAGE uses the cooling functions computed in Sutherland & Dopita (1993).

Additionally to the processes that cause the gas to cool we can think of factors that will heat up the gas again. For low mass haloes the background of far ultraviolet photons, emitted by quasars or massive stars in other galaxies, heats the intergalactic medium up to roughly 4 K. This leads to a reduced gas infall into haloes that are below  $T_{\text{vir}} < 4 K$  as it increases the pressure of the baryons. Feedback of stars of the host galaxy are taken into account in processes discussed later; the feedback of far ultraviolet photons reduces matter infall and gas cooling in low mass haloes and thus disturbs star formation in these haloes. In addition to the lower mass accretion of small haloes, the radiation ionises the gas content of low mass haloes and dampens the channels where atoms and ions cool down due to excitement from collisions. With this simple treatment we are able to explain the reduced luminosity in low mass haloes. SAGE models photoionisation by defining a filtering mass  $M_F$ . If a halo has a lower mass than  $M_F$ , then the fraction of baryons per unit dark matter  $f_b$  is reduced. Croton et al. (2016) show that this modelling not only reduces the number of faint galaxies but also increases the number of bright galaxies.

High mass haloes also face several problems when cooling gas. First of all supernovae that form in massive haloes will, once they explode, add energy to the gas content of the galaxies. The amount of reheated gas is proportional to the rate at which new stars form. In SAGE, Croton et al. (2016) furthermore compare the energy added by supernovae  $\dot{E}_{\text{SN}}$  to the hot gas reservoir to the change of the kinetic energy of the reheated gas in the halo  $\dot{E}_{\text{hot}}$ . The authors conclude that if  $\dot{E}_{\text{hot}} > \dot{E}_{\text{SN}}$ , then the supernovae have added enough energy into the hot halo to unbind some

of the hot gas (suggested by the matter flow arrows in steps 3 and 4 in fig. 3.4). This modelling has the advantage that due to the lower kinetic energy of small mass haloes this feedback process can destroy the disk and all gas will be released into an external reservoir. More massive haloes, on the other hand, develop a stable shell of hot gas. The ejected gas is able to fall back into the hot gas halo in later snapshots. The authors model a  $V_{\text{vir}}$  dependent infall law that will boost the infall into high mass haloes while the lowest mass haloes will never reincorporate the ejected gas.

A second mechanism is the feedback of active galactic nuclei (AGN) which is split up into the radio mode and the quasar mode in *SAGE*. While the central supermassive black hole is accreting mass it will emit energy into the gas content of the galaxy. The feedback of the central black hole is the radio mode and will have a significant effect to the gas content and it is assumed that the sheer amount of energy an AGN emits will have a lasting impact on the gas content. To treat this phenomenon, we can assume that the inner gas, around the central black hole, is heated up and will never cool down (see the inner hot gas sphere in steps 3 and 4 in fig. 3.4). This effectively reduces the area in which gas can cool down. With this simple model the authors of *SAGE* try to mimic the rather complicated processes in a galaxy, in which cooling and infall of gas is coupled with the reheating by the energy emitted from the radio mode. The quasar mode is triggered by disk instabilities, i.e. its rotational energy is not sufficient to preserve a disk of a given mass, or a merger with another galaxy occurs.

*SAGE* requires an inequality to hold true to check if a disk remains stable after an episode of star formation, e.g. due to a merger represented in the merger-history tree. If the inequality is not met, then the disk is assumed to be unstable. In that case, *SAGE* transfers stellar and cold gas to the bulge of the disk to retain stability.

If the quasar mode is triggered, then the central black hole will accrete a lot of the cold gas that is transferred to the bulge. This is the main channel for the central black hole to grow and usually these events are also causing a burst in the star formation. The code again estimates the amount of infalling matter and calculates an ejected energy proportional to the matter. This energy is compared to the total thermal energy of the cold gas disk and hot gas halo. If the energy exceeds the energy in the cold gas disk but not the total thermal energy, then an equivalent fraction of the cold gas gets immediately blown out into the external gas reservoir. If the energy exceeds the total thermal energy, i.e. the sum of the energy stored in the cold gas disk and hot gas halo, then the quasar wind will eject the cold and hot gas from the halo.

Modelling star formation is a challenging task as it depends on several factors such as the positions of the stars in the galaxy, the metallicity of the galactic gas and magnetic fields. In a semi-analytical approach this complicated and chaotic process is only tackled statistically again. Only gas that is cooled down can form stars. Thus, it is a fair assumption that the star formation rate is proportional to the available cold gas. The approach used in *SAGE* is designed to model the star formation history over a large range of redshifts. The star formation rate is modelled as

$$\dot{M}_{\star} = \alpha \frac{m_{\text{cold}} - m_{\text{crit}}}{\tau_{\text{dyn}}}, \quad (3.48)$$

where  $\tau_{\text{dyn}}$  is a dynamical timescale characteristic to the system. In the case of *SAGE*, this is defined  $\tau_{\text{dyn}} = r_{\text{disk}}/V_{\text{vir}}$ . The star formation rate  $\alpha$  is a factor that specifies how efficient the conversion between cold gas a stellar mass is, and is an input parameter. A critical mass,  $m_{\text{crit}}$ , unique to each system, is used. The authors of *SAGE* assume that star formation is only possible for matter above a critical threshold in surface density and thus too diffuse systems will not be able to form stars in *SAGE*.

Modelling the metallicity of a galaxy in general is a complicated process as it depends on the initial mass function with which stars are formed. Heavier stars tend to create and release different

elements in supernovae explosions than smaller stars. The metallicity itself is important as it influences the rate at which hot gas can cool, and the chemical composition of stars influences the colour and luminosity of the stars. In the context of *SAGE* we assume a yield, which specifies the fraction of matter that is transformed into heavier elements. If new stars are formed, matter is reheated or ejected, then a fraction of the metals will be affected as well. As the investigation of luminosities and possibly metallicities will constitute followup work beyond the scope of this thesis itself, we leave a more detailed discussion of the model to Croton et al. (2006, 2016).

# Chapter 4

## The role of the elaphrocentre in void galaxy formation

### 4.1 Introduction

We outlined the structure of the cosmic web with an emphasis on cosmic voids in Sect. 2.2.2. To what degree does the void environment, and the elaphrocentre in particular, have on galaxy formation?

In this section we will present our work published in Peper & Roukema (2021), of which a large majority was by me, implementing the tools and methods described above to seek answers to this question, and analysing the results. A significant part of the work was compilation of a complete software pipeline to simulate galaxy formation, starting from initial perturbations modelling a power spectrum and evolving these perturbations using an  $N$ -body simulation through to extracting merger-history trees of haloes, identifying voids and use semi-analytical galaxy formation recipes to produce synthetic galaxies. See chapter 3 for a more detailed discussion of the tools we selected. The pipeline is built from well-established, free-licensed cosmological software packages, and aims at highly portable long-term reproducibility.

As pointed out before, voids may influence galaxy evolution due to their underdense nature. In this work we investigated if voids may affect galaxy formation via weakening mass infall or increasing disk sizes, which could potentially play a role in the formation of giant low surface brightness galaxies (LSBGs). The formation mechanisms of LSBGs (Sandage & Binggeli 1984; Bothun, Impey, Malin, & Mould 1987) with high masses and low star formation rates remain unclear. Hoffman, Silk, & Wyse (1992) presented a peaks-in-peaks structure-formation calculation arguing that voids are likely to play a major role in the formation of giant low surface brightness galaxies. While the previous discussion was rather general we will now outline why voids could have a major influence on galaxies that form inside them with special emphasis on the elaphrocentre introduced in Sect. 3.3.

In the cosmological galaxy formation context, we denote the gravitational potential hill corresponding to a cosmic void on megaparsec scales as an “elaphrocentre” in order to emphasise its gravitational role in opposition to that of a barycentre<sup>1</sup>. Whereas galaxies in clusters and the walls of the cosmic web typically undergo a gravitationally very active evolution with many mergers, void galaxies tend to have few mergers. Galaxy mergers usually lead to bursts of star formation, making galaxies briefly much brighter. It is typical in modelling the formation of a galaxy in a gravitational barycentre – a knot of the cosmic web – to approximate the surrounding universe via the Newtonian iron-spheres theorem. Relativistically, the conditions of Birkhoff’s

---

<sup>1</sup>From ancient Greek: *ελαφρος* (light) and *βαρυσ* (heavy), respectively.

theorem, for spherical symmetry and an asymptotically 4-Ricci flat universe (Birkhoff & Langer, 1923), are not satisfied for a flat Friedmann–Lemaître–Robertson–Walker (FLRW) model, but nevertheless provide heuristic motivation for applying the iron-spheres theorem. However, the situation in a void is different: the density contrast is much weaker, and there is a mass deficit below the mean density, rather than a mass excess above the mean density. Approximating a strong overdensity as being embedded in a surrounding empty universe that is Newtonian is likely to be less inaccurate than approximating a modest (in terms of linear mean density) underdensity in the same way, since gravity is attractive. What is effectively antigravity in voids – in comparison to the surroundings – is unlikely to be well modelled by a Newtonian approximation. Indeed, relativistically, to reach turnaround, an overdensity has to pass through a strongly positive spatial curvature phase (Roukema & Ostrowski, 2019; Ostrowski, 2020; Vigneron & Buchert, 2019), after which it virialises at an overdensity of a few hundred times the mean density (e.g. Lacey & Cole, 1993). Since a void tends to have negative spatial curvature (for a flow-orthogonal spacetime foliation), an overdensity inside a void will have difficulty forming. If it forms nevertheless, the negative spatial curvature environment will tend to weaken matter infall, weakening the star formation rate. A void can also be thought of as approximated by a spatially compact domain in a relativistic Milne model – empty of matter and spatially hyperbolic (often called “open”) – in which structure forms more slowly than in the idealised background FLRW model.

A pseudo-Newtonian way of thinking about this is that compared to a background FLRW model, a galaxy in the emptiest parts of a void – the “elaphrocentre” – feels a weak antigravitational environmental force around it, since the void is underdense compared to idealised average regions of space. Another toy model way of thinking about the elaphrocentric effect is as follows. Let the core of a dark matter halo be modelled as forming via linear theory followed by the standard pseudo-Newtonian spherical collapse approximation in a background FLRW model, and then by slow uniform mass infall induced by the elaphrocentric environment. This would appear as a history of mass infall that is spread out in time and gradual, rather than fast and sudden. If slow gradual infall is interpreted as the late collapse of the outer parts of the halo, then this corresponds to collapse at late epochs, when the FLRW critical density has dropped, implying a greater virial radius for a fixed total halo mass.

Based on these heuristic arguments we assume that if a dark matter halo forms at or near an elaphrocentre, then the merger rate of small haloes into that halo and the overall infall rate of dark matter and gas into the halo should be weaker than the usual infall rates towards a halo of similar mass at a barycentre. This effect should tend to create lower mass dark matter haloes at elaphrocentres compared to barycentres, which is generally the case: the most massive haloes form at the knots of the cosmic web. For a high-mass dark matter halo at the present epoch of a fixed mass, this elaphrocentric effect should tend to increase the probability of the halo having grown in mass after its initial collapse by weak infall and a weak merger rate over a long period, rather than by an initial short burst of mass accumulation. These effects on the host haloes could lead, for a fixed mass and a fixed efficiency factor for converting available baryons into stars, to galaxies closer to the elaphrocentre preferentially forming with weak star formation rates over long time scales.

While Hoffman et al. (1992) proposed that voids play a major role in LSBG formation, here we briefly present a broader overview of LSBG formation scenarios. LSBGs were discovered more than three decades ago (Sandage & Binggeli, 1984; Bothun et al., 1987), leading to the question of their formation mechanisms (Schombert, Maciel, & McGaugh, 2011; Schombert, McGaugh, & Maciel, 2013; Schombert & McGaugh, 2014b,a). Interest in LSBGs was recently reignited by van Dokkum et al. (2015), who found a high abundance of large LSBGs in the Coma cluster,

that they called ultra diffuse galaxies (UDGs), to distinguish them from traditional LSBGs. It is not yet clear whether LSBGs and UDGs share the same formation scenario, especially since this is dependent on their definitions. A common scenario is that UDGs form in high-spin haloes. Rong et al. (2017) find from simulations that UDGs form naturally in high-spin haloes within the  $\Lambda$ CDM model; Kim (2015) has started investigating this observationally. Chan et al. (2018) show that they can reproduce the observed quantities of red UDGs by imposing quenching, without assuming high spin haloes. Di Cintio et al. (2017) showed that UDGs can be produced in isolated dwarf galaxy haloes with stellar feedback and episodes of gas outflow. Jiang et al. (2019) extended this work by investigating field UDGs. Compared to other galaxies, LSBGs tend to be more spatially isolated, i.e. they tend to be somewhat elaphrocentric. Rosenbaum et al. (2009) quantified this on a 2–5 Mpc scale, finding that LSBGs are located in regions with lower galaxy number densities than those in which high surface brightness galaxies are located. LSBGs typically have low HI surface densities, below around  $5M_{\odot}\text{pc}^{-2}$ , yielding weak star formation, with star formation rates that are approximately constant with cosmological time, rather than the exponentially declining star formation rates typically associated with high surface brightness galaxies (Di Paolo & Salucci, 2020, Sect. 7.1, 7.2).

Here, we focus on the degree to which the elaphrocentric location may contribute to low surface brightness of void galaxies for a given host halo mass, via (i) a total-matter infall rate closer to being constant rather than being exponentially declining, and (ii) an enlarged disk size of a galaxy due to high spin (Rong et al., 2017) and/or an increase in the typical virial radius. (iii) We estimate the magnitude of elaphrocentric acceleration as a basis for more detailed studies.

To study this hypothesis, we present a highly reproducible (Akhlaghi et al., 2021) galaxy formation simulation and analysis pipeline (Peper, Roukema, & Bolejko, 2019). The packages in the pipeline are free-licensed packages, and should only require a POSIX-compatible operating system with sufficient memory and disk space for reproducing the full calculations, tables and figures, generating values that are statistically equivalent to those published here. We present the software packages and the pipeline in Sect. 4.2.1.

In Sect. 4.2.2 we propose a Voronoi-cell based definition of the “elaphrocentre” and discuss alternative definitions of the “centre” of a void from the literature. We present two different parameters characterising void membership and propose a criterion for use in global population comparisons between void and non-void galaxies in Sect. 4.2.3. We describe how we study the dependence of the infall of matter into galaxies (Sect. 4.2.3) and the dependence of galaxy sizes (Sect. 4.2.3) on these parameters and on the global void membership criterion. The elaphrocentres themselves are the places that are the most difficult to study via particle distributions, so in Sect. 4.2.3 we describe how we investigate accelerations near the elaphrocentres in preparation for future studies of elaphrocentric effects that might help form LSBGs.

We present our results in Sect. 4.3, discussion in Sect. 4.4 and conclude in Sect. 4.5. The reproducibility package for the results presented in this chapter is available at zenodo.4699702 and in live<sup>2</sup> and archived<sup>3</sup> GRT repositories. The commit hash of the version of the source package used to produce the results of this chapter is 027ad20. The package was configured, compiled and run on a Little Endian x86\_64 architecture.

---

<sup>2</sup><https://codeberg.org/boud/elaphrocentre>

<sup>3</sup>swh:1:dir:54f00113661ea30c800b406eee55ea7a7ea35279

## 4.2 Method

### 4.2.1 Software pipeline

We provide a highly reproducible software pipeline for generating a realisation of galaxies with merger-history-tree based galaxy disk formation histories (and star formation histories, though we do not analyse these in this work) starting from early universe initial conditions. This approach not only combines existing community tools, but can also help in improving those existing tools by embedding them in a controlled software environment. Our pipeline is intended to be modular, so that the well established cosmological software tools currently chosen, can, in principle, be replaced in a modular way, provided that the user manages the input and output formats correctly. Our results are intended to be statistically reproducible. Parallelisation in several steps of the computational pipeline currently prevents byte-for-byte reproducibility.

We follow the steps introduced in chapter 3 to build up the pipeline. In the following we give the key parameters used in these models. URLs and SHA512 checksums for the upstream versions of software used to produce this work are listed in the reproducibility package. (An SHA512 checksum is a 512-bit integer computed from the bytes in a file using the SHA512 algorithm, aiming to provide a data integrity check on the file contents that is sensitive to small changes in the file.)

The reproducibility structure is based on the Maneage template that aims for a high level of reproducibility (Akhlaghi et al., 2021). We follow Rougier et al. (2017) for the definitions of the “reproducibility” of a research paper – in which independent authors attempt to use the same input data and the same source code and analysis pipeline to obtain the paper’s claimed results – versus the paper’s “replicability” – in which independent authors attempt to use different but similar input data and/or a different but equivalent analysis to obtain the claimed results. Using these definitions, we believe that it should be straightforward for the reader to verify the reproducibility of our results. We expect that our results will also be replicable. Version identities of the software packages in the text below include git commit hashes. Modifications that we have made to upstream versions of codes are included as patch files in the reproducibility source package (zenodo.4699702).

### Initial conditions

We use `MPGRAFIC-0.3.19-4b78328` (Prunet et al. 2008; see Sect. 3.1) to generate a set of standard initial conditions for a flat-space  $N$ -body simulation with the standard 3-torus topology (often called “periodic boundary conditions”). At this step we already set the cosmological background model for our simulation. We generate a simulation with  $N = 128^3$  particles. The comoving fundamental domain size, often called the “box size”, is  $L_{\text{box}} = 80 \text{ Mpc}/h$ . These parameters give a dark matter particle mass of  $2.03 \times 10^{10} M_{\odot}$ , which is a reasonable mass resolution for modest RAM and CPU resources. Together with the minimum number of particles per halo (Sect. 4.2.1), this sets a minimum halo mass and indirectly a minimum galaxy mass in the simulation. We do not expect to detect dwarf galaxies in the results presented here. We use the  $\Lambda$ CDM model, discussed in Sect. 2.1.1 as a proxy model that fits many observations. The FLRW cosmological parameter settings include the current values of the matter density parameter  $\Omega_{\text{m}0} = 0.3$ , the dark energy parameter  $\Omega_{\Lambda 0} = 0.7$  and the Hubble–Lemaître constant  $H_0 = 70.0 \text{ km/s/Mpc}$ .



## Simulations

For our  $N$ -body simulation, we chose `RAMSES-SCALAV-0.0-482f90f`, a fork of the widely used adaptive mesh code `RAMSES-3.0` (Teyssier, 2002). The `RAMSES-SCALAV` fork has modifications to comply with the MPI 3.0 recommended standards for inclusion of the MPI header file<sup>4</sup> and optional extensions related to scalar averaging (Roukema, 2018). The adaptive mesh structure of `RAMSES` (see Sect. 3.2), is designed to allow fast calculations that can resolve detailed gravitational behaviour in high density regions. The maximum `RAMSES` resolution, which effectively corresponds to a softening length, is set at `levelmax = 12`. We produce snapshots starting at  $t_i = 10$  Myr with an equally spaced time step of  $\Delta t = 100$  Myr, and convert to scale factor values using `COSMDIST-0.3.8.2`.

## Halo detection

For detecting dark matter haloes, we use `ROCKSTAR-0.99.9-RC3+-6d16969` (Behroozi et al. 2013a; see Sect. 3.4). We run `ROCKSTAR` using a linking length of 0.28 and a minimum of 5 particles per halo. We set the virial radius criterion for `ROCKSTAR` detection to "200c", i.e., 200 times the critical density.

## Merger history trees

We construct halo merger trees (see Sect. 3.5) from the simulations (Roukema et al., 1993; Roukema, 1993; Roukema et al., 1997; Roukema & Yoshii, 1993; Kauffmann et al., 1999a; Okamoto & Nagashima, 2001, and references thereof). In this work, instead of using the original Fortran77 routines from 1992, we use a more modern package, `CTREES-1.01-e49cbf0` (Behroozi et al., 2013b), which was designed to perform on outputs from `ROCKSTAR`. In order to use these merger history trees for simulating galaxy evolution using `SAGE`, which was developed for following up simulations such as the Millenium simulation, we need to convert the trees to the `LHALOTREE` format. We do the conversion with `CONVERTCTREES-0.0-522dac5`.

## Galaxy formation and matter infall

To form galaxies within our dark matter haloes, we use semi-analytical galaxy formation recipes (Roukema et al., 1993; Kauffmann et al., 1993; Roukema et al., 1997; Kauffmann et al., 1999a,b). Again, rather than using the original code from 1992, we use `SAGE` (Croton et al., 2016), see Sect. 3.6. We use the built-in functions of `SAGE` for estimating the "size" and the infall rate history of each galaxy at the final output time. Under the hypothesis that voids are a favourable environment for large, diffuse galaxies we investigate the disk size (3.46), which is dependent on two other key variables of interest: the virial radius  $R_{\text{vir}}$  set in `ROCKSTAR` at "200c" and the dimensionless spin parameter (3.45).

The infalling mass is defined at a given time step by

$$\Delta M_{\text{infall}}(t_i) := f_{\text{reion}} f_{\text{b}} M_{\text{vir}} - M_{\text{tot}}, \quad (4.1)$$

where  $f_{\text{reion}}$  is the reionisation factor, which estimates the effect of ionisation of the intergalactic medium from early stars; the baryon fraction  $f_{\text{b}} = 0.20$  determines what fraction of total matter is baryonic (assumed to be the same for any dark matter halo/galaxy pair);  $M_{\text{vir}}$  is the virial (total matter) mass of the halo; and  $M_{\text{tot}}$  is the sum of all reservoirs of baryonic matter from

<sup>4</sup><https://mpi-forum.org/docs/mpi-3.0/mpi30-report.pdf>

the previous timestep (except at the initial timestep, when it is zero). Cases where  $M_{\text{infall}} < 0$  are interpreted to mean that baryonic mass is ejected from the galaxy. We extended `SAGE` in order to estimate infall rate, star formation rate (SFR) and outflow rate histories. The history of any of these parameters for a given galaxy at a given time, traced backwards in cosmological time, is assumed to be the sum of the histories of all the separate pre-merger progenitors of the galaxy, appropriately matched by cosmological time. At each merger event, this physically corresponds to the components (dark matter, hot gas, cold gas, stars) of the progenitors being conserved in the merger. The summed star formation rate traced back for a given galaxy is what was originally used together with evolutionary stellar population synthesis to calculate galaxy spectral energy distributions and absolute magnitudes (Roukema et al., 1993, 1997); we do not carry out evolutionary stellar population synthesis in this work. To evaluate these sums, we identify all galaxies present at the present epoch,  $a(t) = 1$ , and trace their progenitors' history back in time along the merger tree. For example, if a progenitor is itself the result of a merger at an earlier timestep, then its own history is the sum of its own progenitors. This procedure is continued recursively back in time in the merger tree for a given present-epoch galaxy. As in the original implementation (Roukema et al., 1993), other effects from mergers than conservation of mass, such as merger-induced starbursts, are also assumed in `SAGE`, but with a power law dependence on the satellite mass rather than direct proportionality (Croton et al., 2016, eq. (27)).

## Voids

We identify the void environment of galaxies using the `REVOLVER` watershed void finder based on `ZOBOV` (Neyrinck, 2008; Nadathur et al., 2019), which provides a nearly parameter-free void finder that does not require assumptions about void shapes (see Sect. 3.3). In contrast to other works, we use the full dark matter (DM) particle distribution as tracers. Nadathur & Hotchkiss (2015b) showed that the voids identified using the galaxy distribution as tracers differ from those traced using a randomly subsampled particle distribution. The authors recommend using the galaxy distribution as tracers in order to match observations. However, since our priority here is gravitational effects, we use the DM particle distribution rather than the galaxy distribution. It is likely that we will detect voids that are smaller and more numerous than those observed in the galaxy distribution (e.g. Mao et al., 2017), since the full DM particle distribution will show positive fluctuations in the density field that may be too weak to form DM haloes and galaxies, but will be detected by the watershed void finder and interpreted as boundaries of voids.

We introduce several small changes into `REVOLVER`. In addition to Nadathur & Hotchkiss (2015a)'s definition of the circumcentre, we calculate the position of the elaphrocentre, as defined below in Sect. 4.2.2. We add a routine to read in simulation data in `GADGET-2` format (Springel, 2005), the default output format that we chose for the `RAMSES`  $N$ -body simulation. We output lists of particle identities of the DM particles that constitute each void. This information is needed to decide the extent to which a galaxy's host halo is located in a void.

We adopt the `REVOLVER` definition of the effective radius of a void,  $R_{\text{eff}}$ , which is not directly related to the choice of a definition of the void centre. The effective radius  $R_{\text{eff}}$  is defined by `REVOLVER` as the radius of a hypothetical sphere that has the same volume as the total volume of all the Voronoi cells that constitute the void, i.e.  $R_{\text{eff}} := \frac{3}{4\pi} (\sum_i V_i)^{1/3}$  where  $V_i$  are the volumes of the Voronoi cells that determine the void.

## 4.2.2 Elaphrocentre and other definitions of void centres

To investigate if a galaxy’s position in a void – its elaphrocentric location – has a significant effect on the formation and evolution of the galaxy, we first need to clarify earlier terminology regarding void centres from the literature, and we need to define the elaphrocentre.

Nadathur & Hotchkiss (2015a, Sect. 2.3) define the “*circumcentre*” for a given void using the Voronoi cell with the lowest density and the three lowest density adjacent Voronoi cells. The intersection of these four Voronoi cells determines the circumcentre. By construction, the circumcentre is the centre of the largest sphere that can be inscribed in the tetrahedron determined by the particles in these four (neighbouring) Voronoi cells, and the centre of the largest empty sphere that can be inscribed in the void. Nadathur et al. (2017, Sect. 2.3 (ii)) rename this the “*void centre*” and show that it correlates strongly with the local maxima of the gravitational potential with respect to the background FLRW model.

We define the *elaphrocentre* similarly. In a void identified by the watershed algorithm, we identify the particle at which the potential is highest, using the potentials estimated by RAMSES (Sect. 4.2.1). We then identify the three adjacent Voronoi cells whose particles have the highest potentials. Together with the cell of the highest potential particle, we again form a tetrahedron between the four particles that respectively define the four cells. The centre of this tetrahedron is the elaphrocentre. While we expect a strong spatial correlation between elaphrocentres and circumcentres, they will differ in general, in particular for small, highly non-spherical voids. By definition, elaphrocentres are appropriate for studying elaphrocentric effects on galaxy formation. A group of test particles at an elaphrocentre will, in the Newtonian sense, be accelerated away from the elaphrocentre, and disperse rather than cluster together. Thus, the elaphrocentre would seem to be a good environment to form a large, diffuse galaxy, provided that the mass that forms the future galaxy is low compared to the mass deficit determining the gravitational properties of the void as a whole.

A third centre commonly defined in void studies is the “macrocentre” or “volume-weighted barycentre”. This is defined (Sutter et al. 2015, Sect. 3, eq. (4); Nadathur & Hotchkiss 2015a, Sect. 2.3, eq. (2)) as the volume-weighted mean of the position vectors  $\vec{x}_i$  of all DM particles identified as being in the void, i.e.,  $\vec{c}_{\text{vwb}} := (\sum_i V_i \vec{x}_i) / \sum_i V_i$ , where  $V_i$  is the Voronoi cell volume associated with the  $i$ -th particle. Since the position is not mass-weighted, it is unrelated to the normal Newtonian definition of a barycentre for a particle distribution,  $\vec{c}_m := (\sum_i m_i \vec{x}_i) / \sum_i m_i$ , where  $m_i$  is the mass of the  $i$ -th particle. In the continuous limit to arbitrarily high particle resolution (assuming a continuous fluid), the volume-weighted barycentre approaches  $\vec{c}_{\text{vwb}} = \int_{\mathcal{D}} \vec{x} dV / \int_{\mathcal{D}} dV$  over a spatial domain  $\mathcal{D}$ . Clearly, in the continuous limit,  $\vec{c}_{\text{vwb}}$  is the geometrical centroid of the domain  $\mathcal{D}$ , which in geometry is often termed the “barycentre”. In general, this corresponds to the astronomical barycentre only if the density distribution in the domain  $\mathcal{D}$  is uniform. In other words, the volume-weighted barycentre contains no information about the density distribution within  $\mathcal{D}$  apart from numerical noise.

By definition, apart from discretisation and numerical effects,  $\vec{c}_{\text{vwb}}$  only determines the geometrical mean position (the centroid) of the overall shape of the void, as defined by the outermost particles of the void. Adding a few particles with big Voronoi cells adjacent to a single side of a void would significantly modify the global shape (union of Voronoi cells) of the void. This would shift the volume-weighted barycentre – the centroid – significantly. Thus, Nadathur & Hotchkiss (2015a) are correct that  $\vec{c}_{\text{vwb}}$  depends on the presence rather than the absence of tracers. However, the fundamental problem with using  $\vec{c}_{\text{vwb}}$  in the context of cosmological voids is that it indicates a void centre that (apart from numerical effects) has no dependence on the density variations in the interior of the polyhedron (union of all Voronoi cells) that defines the void; only the void boundary affects  $\vec{c}_{\text{vwb}}$ . Since there is no reason for

the centroid of the polyhedron bounding a void to have any tight relation with the position of minimal density if the void is even mildly asymmetrical, it is unsurprising that Nadathur & Hotchkiss (2015a) found the density at  $\vec{c}_{\text{vwb}}$  to be higher than at the circumcentre. Thus, in the context of cosmological voids, the physical relevance of  $\vec{c}_{\text{vwb}}$  is unclear, and if used, we recommend that it be described by the term “geometrical centroid” (or “boundary centroid”) rather than “macrocentre” or “volume-weighted barycentre”.

### 4.2.3 Analysis

To study our hypothesis that the elaphrocentric location of galaxies in voids plays a significant role in their evolution, we analyse the simulated haloes, galaxies and voids produced by our pipeline in relation to the voids’ elaphrocentres as follows.

#### Void membership and elaphrocentric distance

Identifying which galaxies are located in a void is non-trivial. For a given galaxy, we could find the void that gives the shortest elaphrocentric or circumcentric distance, and consider the galaxy to be a member of the void if the circumcentric or elaphrocentric distance is below a given fraction of the void effective radius. A distance between two positions in this work is calculated using the shortest of the multiple 3-torus ( $\mathbb{R}^3/\mathbb{Z} \times \mathbb{Z} \times \mathbb{Z} \equiv \mathbb{S}^1 \times \mathbb{S}^1 \times \mathbb{S}^1$ ) spatial geodesic comoving distances. This is often described more loosely as “the comoving distance with periodic boundary conditions”.

However, identifying galaxy membership in a void by the elaphrocentric or circumcentric distance would only be accurate for voids that are spherically symmetric. Although voids tend to evolve to become more spherical, as shown analytically by Icke (1984) by reverting a simple toy model for collapsing density perturbations and numerically by Sheth & van de Weygaert (2004) in  $N$ -body simulations, a void will in general be non-spherical. Moreover, the elaphrocentre will not, in general, coincide exactly with the circumcentre. Thus, a more accurate way of deciding on void membership should, in principle, be possible by using knowledge of the particle positions.

The void membership criterion proposed here, as with the  $> 50\%$  merging identity criterion initially published in 1993 for merger history trees (Roukema & Yoshii 1993, Sect. 3; Roukema et al. 1997, Sect. 2.2.1), is a simple proposal that we expect to be improved upon later. Our voids are detected as a union of Voronoi cells – each containing a DM particle – by REVOLVER. Thus, for any given void, we have a list of particles that approximately define the void. Since we know from ROCKSTAR which particles are members of a halo in which a given galaxy forms, we can check which of these halo particles are present in the list of void member particles for any given void. We restrict the list of void particles to those that are within  $r \leq 2.eps R_{\text{eff}}$  from the elaphrocentre, where  $R_{\text{eff}}$  is the void effective radius calculated by REVOLVER (the radius of the hypothetical sphere having the same volume as the void’s Voronoi cells; see Sect. 4.2.1). The  $r \leq 2.eps R_{\text{eff}}$  restriction should remove some of the sharpest regions adjacent to the knots of the cosmic web and exclude the outermost regions of voids of high ellipticity. In this sense, it will counteract the space-filling nature inherent to any watershed voidfinder to some degree.

Our void membership criterion is that we require that a fraction  $f_{\mathcal{H} \cap \mathcal{V}}$  strictly greater than  $f_{\mathcal{H} \cap \mathcal{V}}^{\text{min}} = 0.50$  of the particles in a halo  $\mathcal{H}$  be members of a void  $\mathcal{V}$  for a galaxy in that halo to be considered a member of the void. As in the case of the  $> 50\%$  merging identity criterion, which prevents a halo from having multiple descendants, this void membership criterion is strong enough to prevent a galaxy in a halo that lies on a wall, filament or knot from being allocated to more than one void. This criterion could be strengthened to force a selection of galaxies that are

placed further in the interior of the voids, at the cost of reducing the total number of galaxies recognised as being members of voids. A galaxy that does not satisfy this criterion is considered to be a non-void galaxy.

### Infall dependence on environment

We wish to see if infall rates – of dark and baryonic matter in general – are affected by the host halo’s location in a void. The infall history should affect the star formation rate, which requires baryonic matter to first collapse into the centre of its host dark matter halo’s potential well. We consider the infall rate traced backwards in time for any halo at the final output time. This infall rate is the sum of the mass accumulation histories of the component haloes of the final halo’s merger tree. We can write this backtraced history, over predecessor haloes destined to merge together, as the mass evolution assigned to the final halo,  $M(t)$ , so that  $dM/dt \approx \Delta M/\Delta t(t)$  is the infall rate – of small haloes and diffuse matter together.

The hypothesis that the elaphrocentre of a void (corresponding to a spatially compact part of a hyperbolic, super-Friedmannian expanding region) would weaken the infall rate can now be formalised. For a given mass  $M$ , the average (mean) infall rate is, by definition, independent of location. To distinguish the archetypal case of a typical disk galaxy, with an initial burst of star formation followed by an exponential decay, from that of an archetypal LSBG, with an approximately flat star formation rate, we attempt to fit  $dM/dt$  by an exponential, of the form

$$\frac{dM}{dt}(t) = A \exp(-t/\tau), \quad (4.2)$$

where  $A$  is the infall amplitude and  $\tau$  is a decay time scale.

Typical disk galaxies should have low time scales  $\tau$ , while we hypothesise that void galaxies should on average have higher  $\tau$ , corresponding to approximately flat infall rates.

The exponential form of the fit for the matter infall rate is a heuristic choice inspired by the traditionally used declining exponential for modelling the star formation rate (Bruzual A., 1983). In reality, merger histories are more complex than these simplified extremes, so we expect a fair fraction of automated fits to fail, especially since we apply this to all timesteps defined in Sect. 4.2.1, starting from the first time step in which a galaxy is modelled to form in a dark matter halo. Nevertheless, this automated fit procedure should be able to distinguish whether the infall of matter is closer to a brief, quickly weakening series of early events or rather a more steady infall extended over a long period. We expect that a flat infall rate would correspond to a roughly constant star formation rate over time. The early, brief, burst scenario of the infall of matter would allow a high star formation rate immediately after the infall, whereas a constant rate of matter infall should yield an approximately constant star formation rate. Long cooling times would modify this relation, especially for galaxies in high-mass haloes in voids (Hoffman et al., 1992, Einstein–de Sitter case).

We first compare  $A$  and  $\tau$  for galaxies depending on their classification as void or non-void galaxies. The infall histories are calculated using our modification of `SAGE`. The prediction for creating LSBGs is that void galaxies should tend to have low amplitude  $A$  and a high (slow) decay rate  $\tau$ , and vice versa for non-void galaxies.

### Galaxy size dependence on environment

The other parameter that may indicate an elaphrocentric contribution to a disk galaxy becoming an LSBG is the disk scale length  $r_{\text{disk}}$  (for a density profile  $\rho \propto \exp(-r/r_{\text{disk}})$ ). This can be converted to a disk half-mass radius using the relation  $r_{1/2} = \nu r_{\text{disk}}$ , where  $\nu$  solves  $(\nu +$

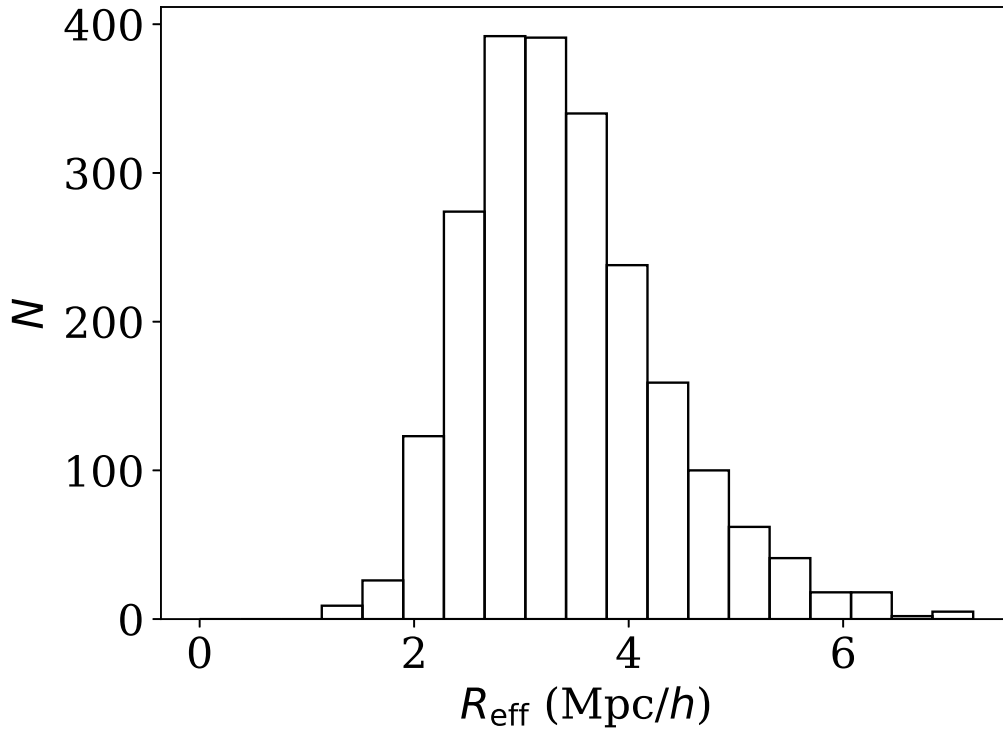


Figure 4.1: Histogram of void effective radii  $R_{\text{eff}}$  (Sect. 4.2.1), using the full dark matter particle distribution, which leads to voids much smaller than typically observed or found in simulations when traced by galaxies.

1)  $\exp(-\nu) = 1/2$  (e.g. Kravtsov, 2013,  $\nu = 1.678$ ). As stated above (Sect. 4.2.1; Eq. (3.46)), SAGE calculates  $r_{\text{disk}}$ . Since voids are underdensities, dark matter haloes forming in voids will tend to collapse somewhat later than in overdensities (e.g. Lacey & Cole, 1993, App. A). In an expanding FLRW universe, the critical density  $\rho_{\text{crit}}$  decreases, so for a fixed virialisation overdensity threshold and fixed mass,  $R_{\text{vir}}$  increases with time. Thus, modelling galaxy disk scale lengths as being proportional to the halo virial radius (Eq. (3.46)), it would be reasonable to expect void galaxies to have greater  $r_{\text{disk}}$  than non-void galaxies, for a fixed value of the spin parameter  $\lambda$ . Elaphrocentric galaxies will typically undergo a more isolated evolution than barycentric galaxies, with fewer merger events. D’Onghia (2008) found, based on  $N$ -body simulations, that the spin parameter of haloes in equilibrium is not influenced by merger events. If the role of the spin parameter is indeed weak, then void galaxies should be marginally larger than non-void galaxies. We consider both  $r_{\text{disk}}$  directly, and  $R_{\text{vir}}$  and  $\lambda$  individually.

### Elaphro-acceleration

As a complement to the direct analyses of simulated galaxies via SAGE, we also investigate accelerations near the elaphrocentres, as preparation for future studies of elaphrocentric effects that might have an effect on galaxy formation in voids and might help form giant LSBGs. We estimate the acceleration (compared to the FLRW reference model) of test particles directed away from the elaphrocentre, in the direction of the boundaries of the void. This acceleration can be thought of as counteracting the self-gravity of an overdensity that is destined to collapse into a dark matter halo and allow the formation of a galaxy within the halo. This acceleration is the effective antigravity that we have assumed could enlarge the size of a galaxy and decrease its infall rate, provided that the simulation has a detectable galaxy near the elaphrocentre.

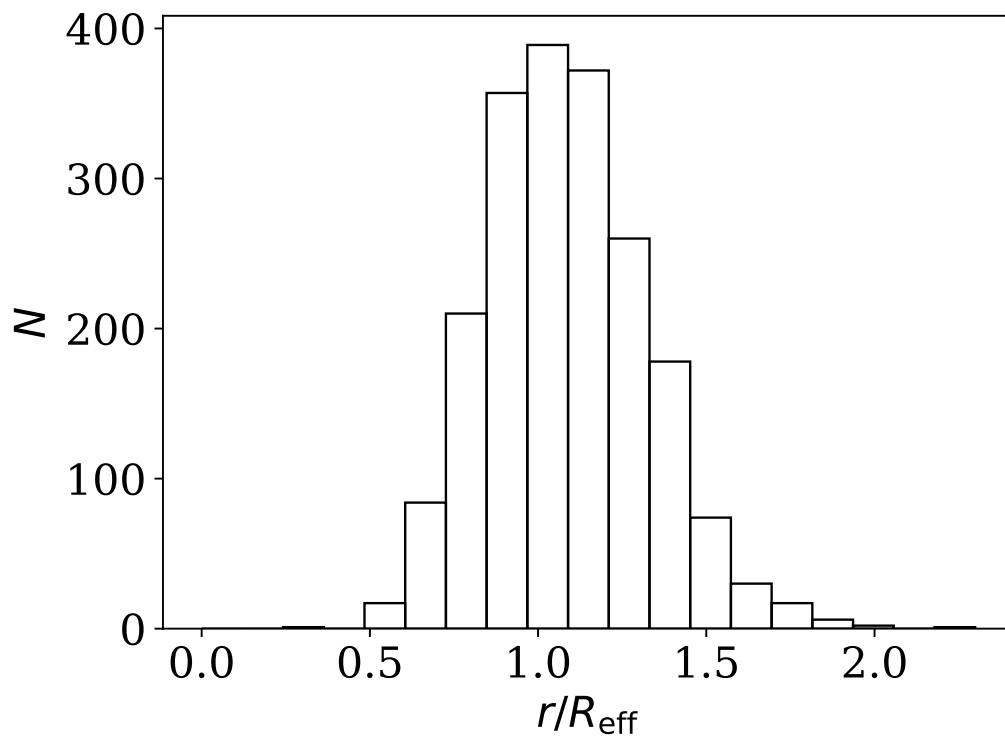


Figure 4.2: Histogram of elaphrocentric distance of galaxies identified as being located in voids. The distribution at  $r/R_{\text{eff}} < 1$  is typical of observational and simulated void profiles, with most galaxies located near the effective radius. The distribution at  $r/R_{\text{eff}} \geq 1$  can be interpreted as showing galaxies in the outer parts of voids that are generally quite asymmetrical. A perfectly symmetrical void would have all its member galaxies at  $r/R_{\text{eff}} < 1$ .

Here, we describe how we estimate this “elaphro-acceleration” without requiring the presence of a halo or galaxy. We will compare our results with the Newtonian estimate for the gravitational pull towards the centre of a halo of a Malin-1–like galaxy (Bothun et al., 1987). In this simplified model, we assume a high-mass test halo at the elaphrocentre of a void identified in the simulation, without modifying the underlying DM distribution. In the real Universe and in simulations, it is rather unlikely for a galaxy to form exactly at an elaphrocentre. Nevertheless, we feel that this calculation will be a useful guide, since the elaphro-acceleration should be maximal in amplitude at the elaphrocentre. For our canonical high-mass test halo we adopt parameters that are motivated by observations of Malin 1 (Seigar, 2008; Junais et al., 2020). For an order of magnitude estimate, we adopt  $M^{\text{test}} = 10^{12}M_{\odot}$  for the mass of the halo and  $r^{\text{test}} = 1.20$  Mpc for the region from which dark matter originated.

For any given void, we interpolate the potential  $\phi$  linearly, and calculate the acceleration as the gradient of the potential,  $\dot{v} \propto -\nabla\phi$ . We use the full dark matter particle distribution, since gravitationally this should be more accurate than that of collapsed haloes (or galaxies) alone. We use the gravitational potential estimates calculated by RAMSES (Sect. 4.2.1). Since RAMSES only provides potential estimates at particle positions, the resolution limit implied by using these is determined by the particle number density. By definition, the number density is very low inside a void, so there are very few particle positions available for interpolating the potential. We sample the elaphro-acceleration at six positions which lie on the sphere with radius  $r^{\text{test}}$ , i.e. at  $((\pm r^{\text{test}}, 0, 0), (0, \pm r^{\text{test}}, 0), (0, 0, \pm r^{\text{test}}))$ , where the elaphrocentre is the origin of the coordinate system. For a given void, we calculate the radial (signed) and tangential (amplitude) components of the velocity vector  $\vec{v}$  for each of the six positions, and find the mean values  $\dot{v}_{\parallel}$  and  $\dot{v}_{\perp}$ , respectively. As stated in Sect. 4.2.1, some of the six positions may fall outside of a void when the void is too small; we ignore the void in such cases.

#### 4.2.4 Reproducibility versus cosmic variance

We present results below (Sect. 4.3) with a preference for reproducibility over cosmic variance. Our pipeline, using the Maneage template (Akhlaghi et al., 2021), includes a step for verification, in the sense of verifying that when the reader recalculates our complete pipeline, s/he should obtain statistically equivalent results to our original results, within some tolerances. Estimation of these tolerances effectively requires an approximate estimate of cosmic variance in the parameters of interest. In principle, we could use these repeated full runs of the pipeline to obtain mean or median estimates of our main parameters of interest, rather than presenting the values from a single simulation, and the random uncertainties derived from that simulation. However, that would reduce the reproducibility of our results, in the sense that readers wishing to run our pipeline would also have to perform multiple full runs.

Thus, here we favour reproducibility over cosmic variance, using the latter only for reproducibility purposes, not for obtaining results of the work. We first run a fixed version of our full package 10 times, for different random seeds and with physical randomisation induced by parallel computation. We obtain a full set of the results presented in this work from each run. For any given parameter, we calculate the standard deviation  $\sigma_{\text{cv}}$  of the values of the parameter, where the subscript “CV” refers to “cosmic variance”. The particular version of the source package used for these verification runs has the string e93569c as its GIT commit identity (commit hash). We use these repeat runs only for verification in the reproducibility sense, not for results. A given parameter in a fresh realisation that aims to reproduce our results can then be verified for consistency by requiring that it agree with our published value to within  $5.0\sqrt{2}$  times the stated random error  $\sigma_{\text{ran}}$ , where the  $\sqrt{2}$  factor represents the assumption that both have independent



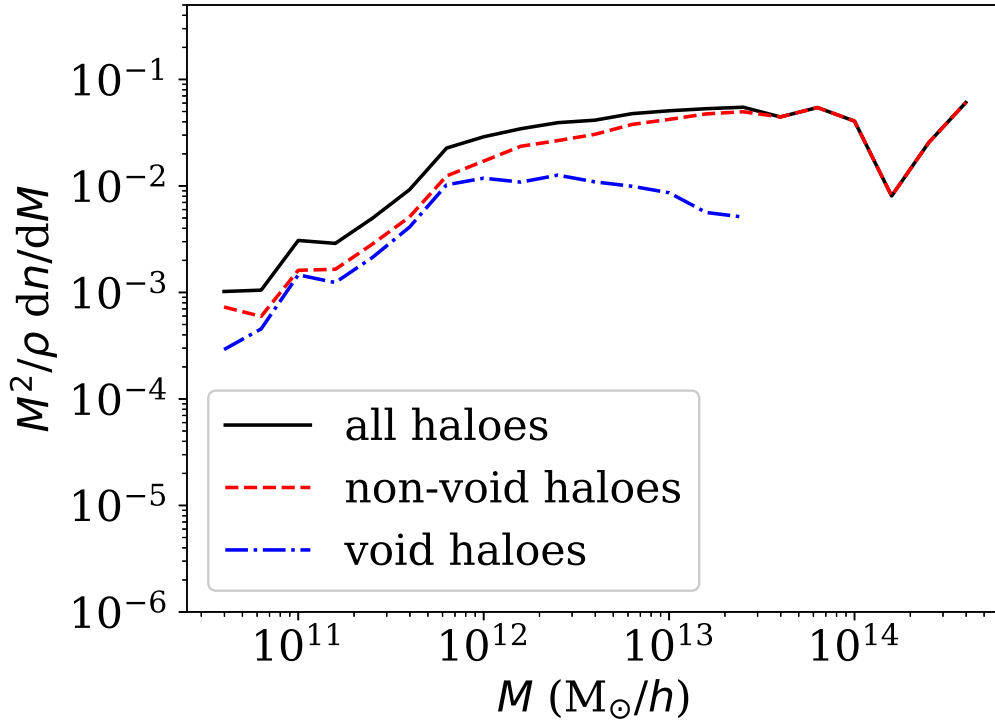


Figure 4.3: Differential halo number counts  $M^2/\rho dn/dM$  versus halo mass  $M$  for the haloes that host galaxies in the simulation, where  $n$  is the number density of haloes in a given mass interval and  $\rho$  is the mean mass density of the simulation. The solid, black (top) curve represents all haloes; the dashed, red (middle) curve is for haloes that are not in a void; and the dash-dotted, blue (bottom) curve is for haloes that are identified as being located in a void. The gradual decline in the numbers of haloes towards the lower mass scales and the sharp cut at the lowest mass scale are artefacts of the limited resolution of our simulation.

Gaussian errors drawn from the same distribution. For parameters with high  $\sigma_{\text{cv}}$  (i.e., those known to fail this verification), we require agreement between the fresh value and the mean from the ensemble of runs within 5.0 times  $\sigma_{\text{cv}}$ , and we state  $\sigma_{\text{cv}}$  as an additional uncertainty, using the notation “ $\pm_{\text{cv}}$ ”. We use this formalised verification procedure for the parameters that we judge to be the more physically relevant.

The simulation presented below was chosen randomly.

## 4.3 Results

### 4.3.1 Simulation pipeline

In the final time step of our  $N = 128^3$ -particle simulation, we detected 5329 haloes, with 4817 galaxies evolved along the merger history trees for these haloes. Among these galaxies, 3848 have virial mass  $M$  in the range  $10^{11}$ – $10^{13}M_{\odot}/h$ , which we study with the aim of seeking a factor in the formation of high-mass galaxies. Applying the  $f_{\text{H}\cap\text{V}} > 0.50\%$  definition in Sect. 4.2.3, we identify 1998 galaxies in voids, among which 1588 of these galaxies have a mass in the selected range. This fraction of galaxies identified as void galaxies is larger than the 7% estimated by Pan et al. (2012). A more detailed analysis of the galaxies that are identified to be in voids is given below. We investigate key quantities dependent on the fraction of their host haloes

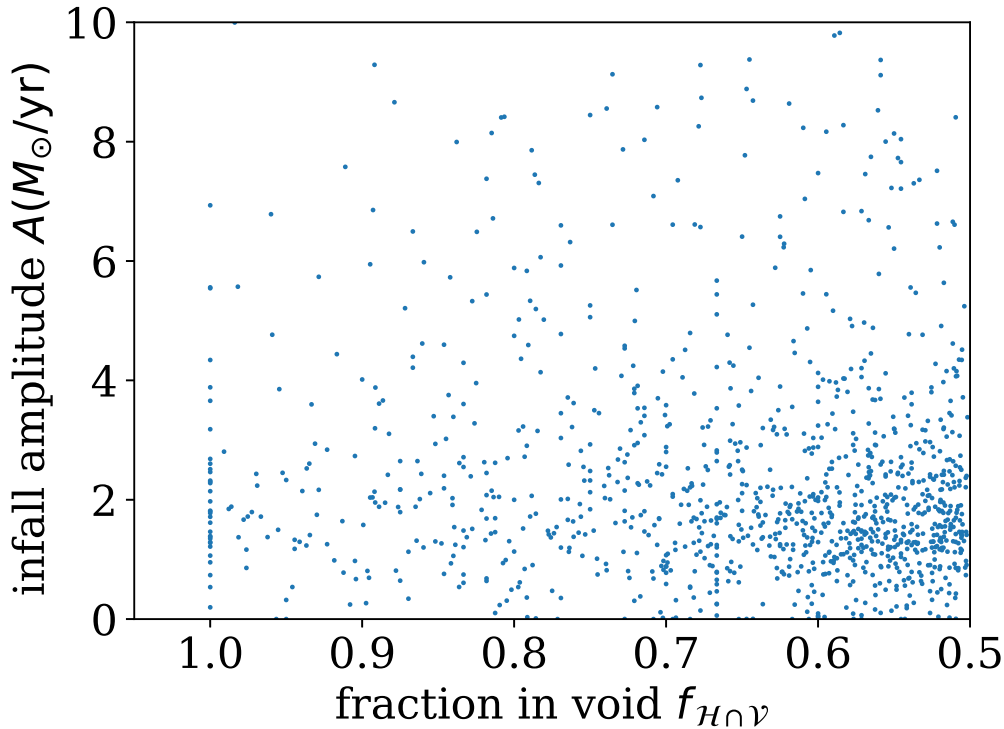


Figure 4.4: Amplitude of infall rate  $A$  versus fraction  $f_{H \cap V}$  of a galaxy’s host halo composed of void particles. A Theil–Sen robust linear fit to the relation gives  $A = [(1.25 \pm 0.30) + (1.24 \pm 0.51 \pm_{\text{cv}} 0.40)f_{H \cap V}] M_{\odot}/\text{yr}$ . Galaxies towards the left ( $f_{H \cap V} = 1$ ) are those best identified as being in voids. Fits are made for this figure through to Fig. 4.16. These are robust best fits for studying statistical relations; they are not predictive models. We display the fits in almost all these scatter plots, quantifying them and their uncertainties in the captions (fits are not displayed in this figure, nor in Figs. 4.6, 4.8, 4.15 and 4.16). See the text for discussion of which relations have significantly non-zero slopes. Plain text table for this figure through to Fig. 4.7: zenodo.4699702/voidgals\_infall.dat.

particles in a void  $f_{H \cap V}$  and dependent on their relative distance to the voids centre  $r/R_{\text{eff}}$ . We use Theil–Sen robust linear fits (Theil, 1950; Sen, 1968) on each key quantity to see if it has a statistically significant dependence on either of the two void location parameters. There are 2198 voids in the final time step. The void size distribution is shown in Fig. 4.1. Since we detect voids physically, following the dark matter particular distribution, as described in Sect. 4.2.1, it is unsurprising that the void population is dominated by voids a few  $\text{Mpc}/h$  in size, with a correspondingly higher number density than that typically seen in void catalogues calculated using galaxies as tracers. The distribution of void galaxy elaphrocentric distances is shown in Fig. 4.2.

### 4.3.2 Infall rate

As described in Sect. 4.2.3, we first compared infall rates for galaxies as separate void and non-void populations. For each galaxy mass infall history  $dM/dt(t)$ , we first find a linear least-squares best fit to  $\log_{10}(dM/dt)$  versus  $t$  for time steps where  $dM/dt(t) > 0$ . The optimal parameters of this fit are used to find a non-linear least-squares best fit of  $dM/dt(t)$  to a decaying exponential (Eq. (4.2)), starting from the first time step with  $dM/dt(t) > 0$  and no longer excluding time steps with  $dM/dt = 0$ . As stated above, merger histories are complex, and many

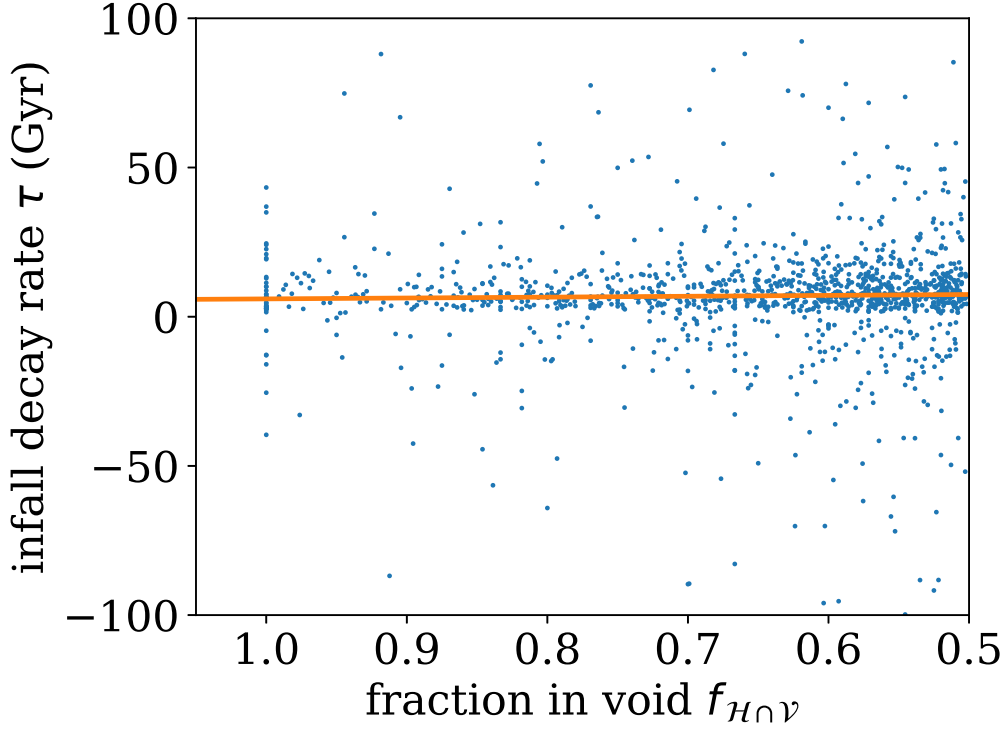


Figure 4.5: Infall decay rate  $\tau$  versus fraction  $f_{\mathcal{H} \cap \mathcal{V}}$  of a galaxy’s host halo composed of void particles, as in Fig. 4.4, with a Theil–Sen robust linear fit  $\tau = [(8.91 \pm 1.05) + (-2.94 \pm 1.63 \pm_{cv} 1.15)f_{\mathcal{H} \cap \mathcal{V}}]$  Gyr, is shown.

Table 4.1: Exponential decaying fit parameters (medians and standard error in the median) for infall rates for void and non-void galaxies. A large standard error in the time scale, of the order of the age of the Universe, indicates that many fits represent nearly constant infall rates.

	in voids	not in voids
$\log_{10}(A) (M_{\odot}/\text{yr})$	$0.31 \pm 0.02$	$0.29 \pm 0.02$
$\tau$ (Gyr)	$3.67 \pm 25.40$	$3.35 \pm 5.18$

galaxies’ infall histories are poorly fit by this procedure. This applies both to void and non-void galaxies, and we do not attempt to analyse these cases. The limitations of this simplified approach should similarly affect both populations and should not affect our comparison of the successfully fit subsets of the two populations.

We find  $m_v = 1263$  valid fits for the void galaxies, and  $m_v^- = 325$  fits that are rejected either as failed fits ( $m_{vf}^- = 1$ ) or as having an unreasonably high amplitude,  $A > 1000 M_{\odot}/\text{yr}$ , indicating a physically unrealistic fit ( $m_{vu}^- = 324$  cases). For non-void galaxies we find  $m_v = 1877$  valid fits and  $m_v^- = 525$  fits rejected either as failed fits ( $m_{vf}^- = 1$ ) or as having unphysically high amplitudes ( $m_{vu}^- = 524$  cases). For galaxies in host haloes with virial masses in the range  $10^{11} - 10^{13} M_{\odot}/h$ , we find the medians listed in Table 4.1, where the uncertainties are standard errors in the median. Throughout this work, uncertainties in the median are given as the standard error in the median, unless otherwise stated. The median host halo mass for the void galaxies is  $(4.1 \pm 0.4) \times 10^{11} M_{\odot}$ , lower than that of the non-void galaxies,  $(5.7 \pm 2.6) \times 10^{11} M_{\odot}$ . Figure 4.3 shows the differential mass function of the haloes in the form of the halo multiplicity function. We show the differential halo masses for all haloes, for haloes that are classified as being associated with a void and for haloes that not associated with any void. As stated in Sect. 4.2.1, we cannot

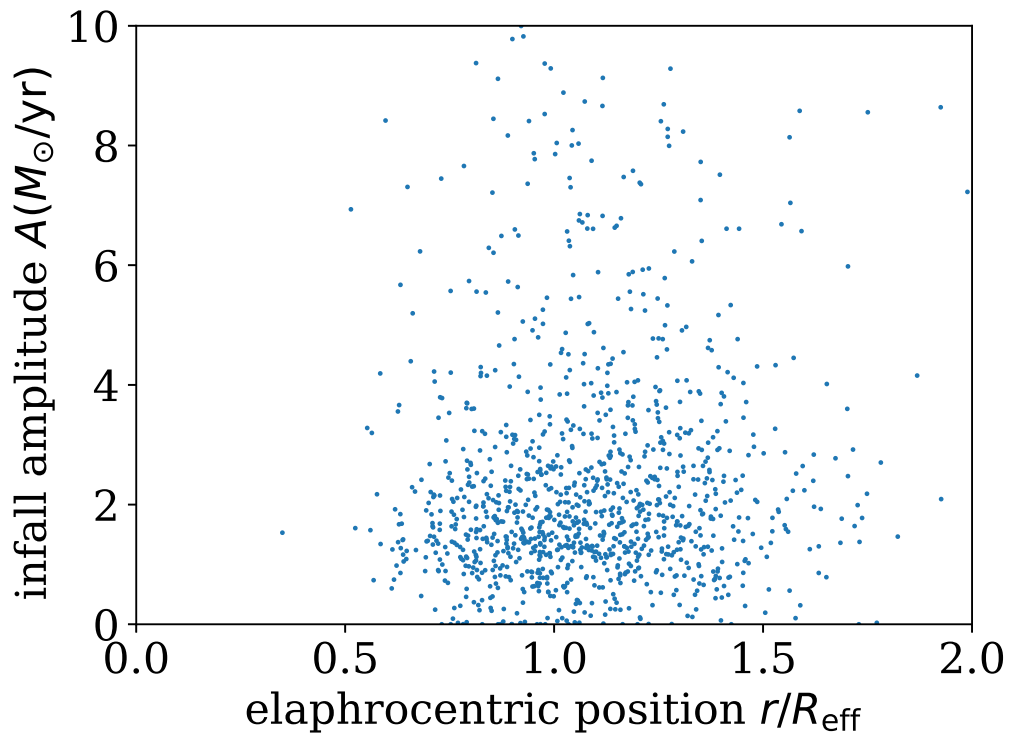


Figure 4.6: Amplitude of infall rate  $A$  versus elaphrocentric location  $r/R_{\text{eff}}$  of a galaxy's host halo. The fit is  $A = [(1.47 \pm 0.21) + (0.54 \pm 0.15 \pm_{\text{cv}} 0.30) r/R_{\text{eff}}] M_{\odot}/\text{yr}$ . As in Fig. 4.4, galaxies towards the left are those best identified as being in voids, but voidness is characterised in this plot by a lower elaphrocentric distance  $r/R_{\text{eff}}$ , instead of by a higher void fraction  $f_{\mathcal{H} \cap \mathcal{V}}$ .

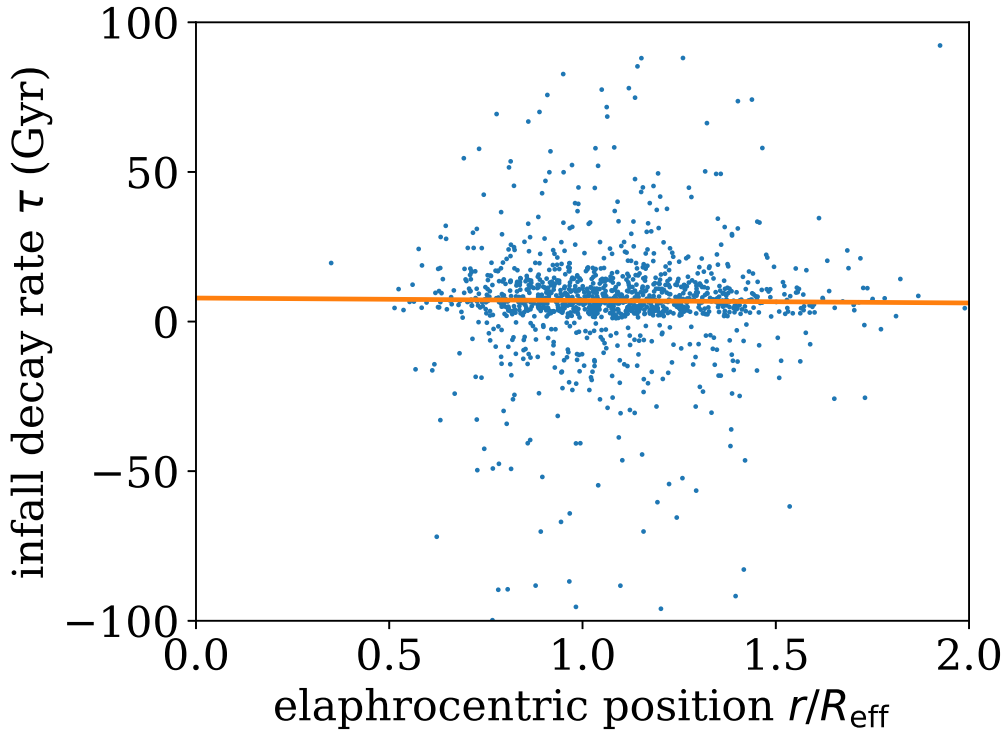


Figure 4.7: Infall decay rate  $\tau$  versus versus elaphrocentric location  $r/R_{\text{eff}}$  of a galaxy’s host halo, as in Fig. 4.6, with robust fit  $\tau = [(7.86 \pm 1.33) + (-0.82 \pm 1.14) r/R_{\text{eff}}]$  Gyr.

resolve dwarf galaxies; this is seen in the sharp cut at the lowest masses. The gradual decline in low-mass haloes and the sharp cut are both consistent with the use of the ROCKSTAR halo finder (Sect. 4.2.1). The void and non-void halo mass functions clearly differ in the higher mass ranges. The most massive haloes form in voids very rarely, while among the lowest mass haloes, the probabilities of forming in a void or not are of similar magnitude.

We find (Table 4.1) no significant difference in either the amplitude  $A$  or the time scale  $\tau$  of infall between the void and non-void galaxy populations. The dispersion in infall patterns within each population is as great as both  $A$  and  $\tau$  themselves. We found that, to very high significance, void galaxies typically form later than non-void galaxies, as expected, since they form in underdensities. We find median collapse epochs (in standard FLRW cosmological time) of  $t_{\text{v}}^{\text{f}} = 4.1 \pm 0.1$  Gyr and  $t_{\text{nv}}^{\text{f}} = 3.3 \pm 0.1$  Gyr for the void and non-void galaxies, respectively. By the collapse epoch of a galaxy, we mean the first epoch at which the mass infall rate calculated by SAGE for the galaxy is non-zero.

We investigate the results for  $A$  and  $\tau$  more closely by checking if either  $A$  or  $\tau$  has a dependence on either the fraction of a host halo’s particles that are identified as void particles,  $f_{\mathcal{H} \cap \mathcal{V}}$ , or on the host halo’s elaphrocentric distance  $r/R_{\text{eff}}$ . Figures 4.4–4.7 show the dependence of  $A$  and  $\tau$  on  $f_{\mathcal{H} \cap \mathcal{V}}$  and  $r/R_{\text{eff}}$  for all void galaxies. The  $f_{\mathcal{H} \cap \mathcal{V}}$  axis is shown with  $f_{\mathcal{H} \cap \mathcal{V}}$  decreasing from left to right, so that the galaxies that are best qualified as void galaxies are shown towards the left in all four figures. There is no visually obvious dependence of the infall parameters on  $f_{\mathcal{H} \cap \mathcal{V}}$ . However, Fig. 4.4 does show a modestly significant non-zero slope, i.e., the median of the infall amplitudes  $A$  is somewhat higher for galaxies better identified as void galaxies (having a higher value of  $f_{\mathcal{H} \cap \mathcal{V}}$ ). This would tend to oppose the hypothesis of a general tendency to form LSBGs in voids. The other slopes of the best fit linear relations, using robust

Table 4.2: Median disk galaxy scale length, spin parameter and virial radius for void and non-void galaxies in the mass interval  $10^{11}$ – $10^{13}M_{\odot}/h$  and on all mass scales. Two parameters are known to have high cosmic variance, as given in the table (see Sect. 4.2.4).

	in voids	not in voids
restricted mass interval		
$r_{\text{disk}}(\text{kpc}/h)$	$3.77 \pm 0.08$	$4.21 \pm 0.07$
$\lambda$	$0.0421 \pm 0.0008$	$0.0413 \pm 0.0007$
$R_{\text{vir}}(\text{kpc}/h)$	$134.8 \pm 1.3$	$150.5 \pm 1.4$
all mass scales		
$r_{\text{disk}}(\text{kpc}/h)$	$3.37 \pm 0.08 \pm_{\text{cv}} 0.05$	$4.19 \pm 0.09$
$\lambda$	$0.0420 \pm 0.0009$	$0.0414 \pm 0.0008$
$R_{\text{vir}}(\text{kpc}/h)$	$120.5 \pm 1.4 \pm_{\text{cv}} 1.73$	$145.2 \pm 2.2$

statistics as above, indicated numerically in the figure captions, are not significantly non-zero.

### 4.3.3 Galaxy Sizes

While we do not detect significant elaphrocentric effects on infall rates, effects on galaxy sizes could play an important role in forming large diffuse galaxies. As stated above (Sect. 4.2.3), to check the size of a galaxy at the final output time step, we use the disk scale length  $r_{\text{disk}}$  provided by SAGE. The results for the galaxies divided into void and non-void populations are shown in Table 4.2, where we list the disk exponential scale length  $r_{\text{disk}}$ , the spin parameter  $\lambda$  and the virial radius  $R_{\text{vir}}$ . Table 4.2 shows a significant difference for the overall scale length  $r_{\text{disk}}$ . Our results show that, as a population, void galaxies form significantly smaller disks, both for our selected mass interval and for the full sample. Although this might seem to support van de Weygaert et al. (2011, fig. 2, left)’s finding that, for a given absolute magnitude, void galaxies tend to be smaller than the general galaxy population, we do not (yet) model stellar populations and estimate absolute magnitudes, so this qualitative agreement is promising but not conclusive.

A likely explanation for the smaller sizes of void galaxies is shown by the other rows in Table 4.2: the void galaxy population has a much smaller median virial radius  $R_{\text{vir}}$  than the non-void population, but an insignificantly higher spin parameter  $\lambda$ . The slightly greater spin parameter appears insufficient to compensate or override the lower  $R_{\text{vir}}$  of the void galaxies. The values of the spin parameter are reasonable in relation to standard values in the literature. Our non-void host halo values of  $\lambda$  listed in Table 4.2 are consistent with the friends-of-friends halo estimate of Zjupa & Springel (2017, Sect. 2.4, para. 8),  $\lambda_{\text{B,FOF}} = 0.0414$ , while our void host halo values of  $\lambda$  are slightly higher.

As stated above, the void galaxy host haloes are typically somewhat less massive than the non-void haloes and the collapse epochs of void galaxies are significantly later. These two parameters should have opposite effects on the halo virial radii. In Table 4.2, we see that  $R_{\text{vir}}$  is significantly larger for non-void galaxies, showing that the higher mass of non-void galaxies plays the dominant role.

To see if a general trend of  $r_{\text{disk}}$  also exists as a function of a galaxy’s void location, Figs 4.8 and 4.9 examine the dependence of  $r_{\text{disk}}$  on  $f_{\mathcal{H} \cap \mathcal{V}}$  and elaphrocentric distance for void galaxies. The slope of the best fit in Fig. 4.8,  $dr_{\text{disk}}/df_{\mathcal{H} \cap \mathcal{V}} = -1.44 \pm 0.46 \pm_{\text{cv}} 0.42 \text{ kpc}/h$ , is not significantly non-zero when we take into account cosmic variance (the distribution of  $dr_{\text{disk}}/df_{\mathcal{H} \cap \mathcal{V}}$  over repeated runs includes a strong tail of values that are not significantly non-zero). The dependence on elaphrocentric position (Fig. 4.9) is not significant either.

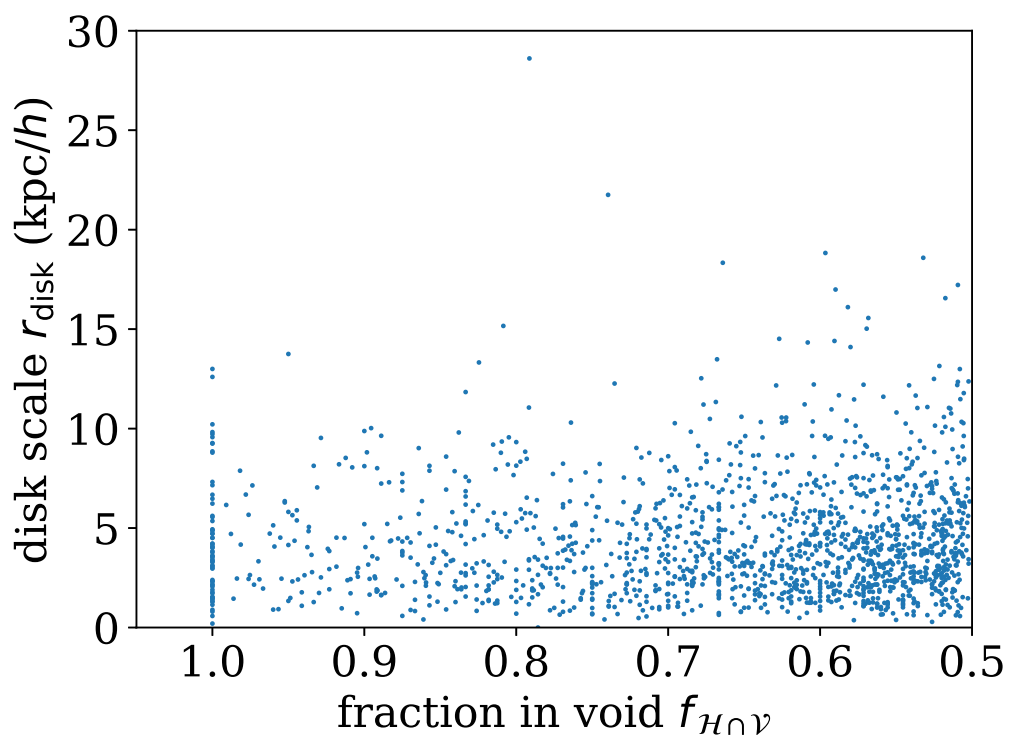


Figure 4.8: Galaxy disk scale length  $r_{\text{disk}}$  versus fraction  $f_{\mathcal{H} \cap \mathcal{V}}$  of a galaxy's host halo composed of void particles. The fit is  $r_{\text{disk}} = [(4.72 \pm 0.33) + (-1.44 \pm 0.46 \pm_{\text{cv}} 0.42)f_{\mathcal{H} \cap \mathcal{V}}]$  kpc/h. Plain text table for this figure through to Fig. 4.13: zenodo.4699702/voidgals\_infall.dat.

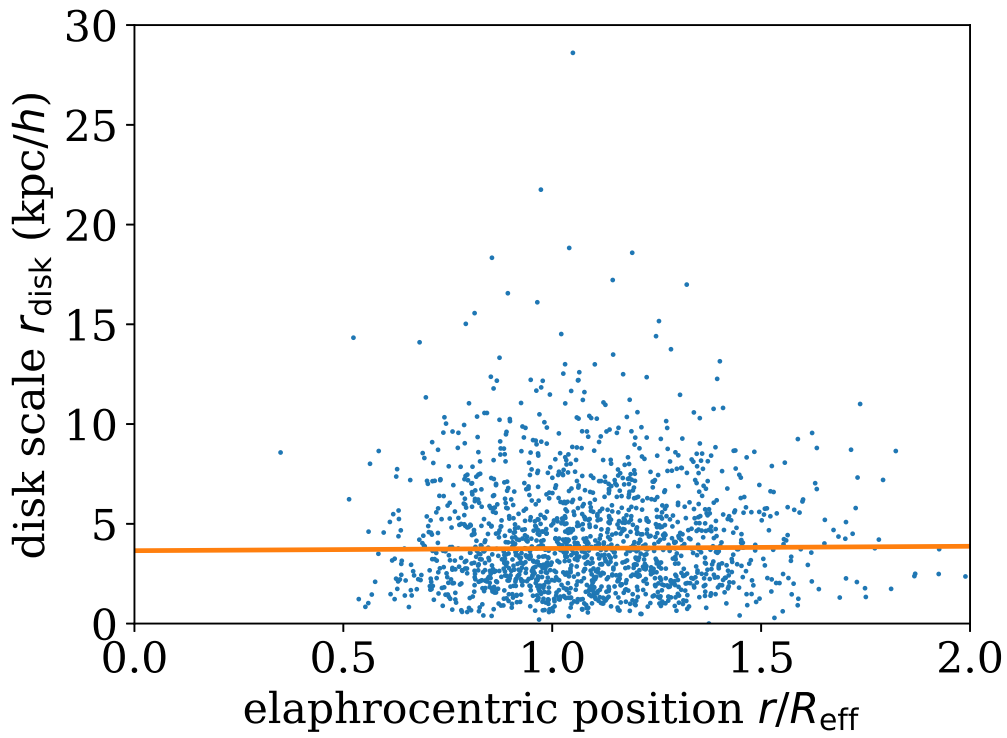


Figure 4.9: Disk scale length  $r_{\text{disk}}$  versus elaphrocentric location  $r/R_{\text{eff}}$ , as in Fig. 4.8. The fit is  $r_{\text{disk}} = [(3.65 \pm 0.26) + (0.11 \pm 0.22) r/R_{\text{eff}}]$  kpc/h.

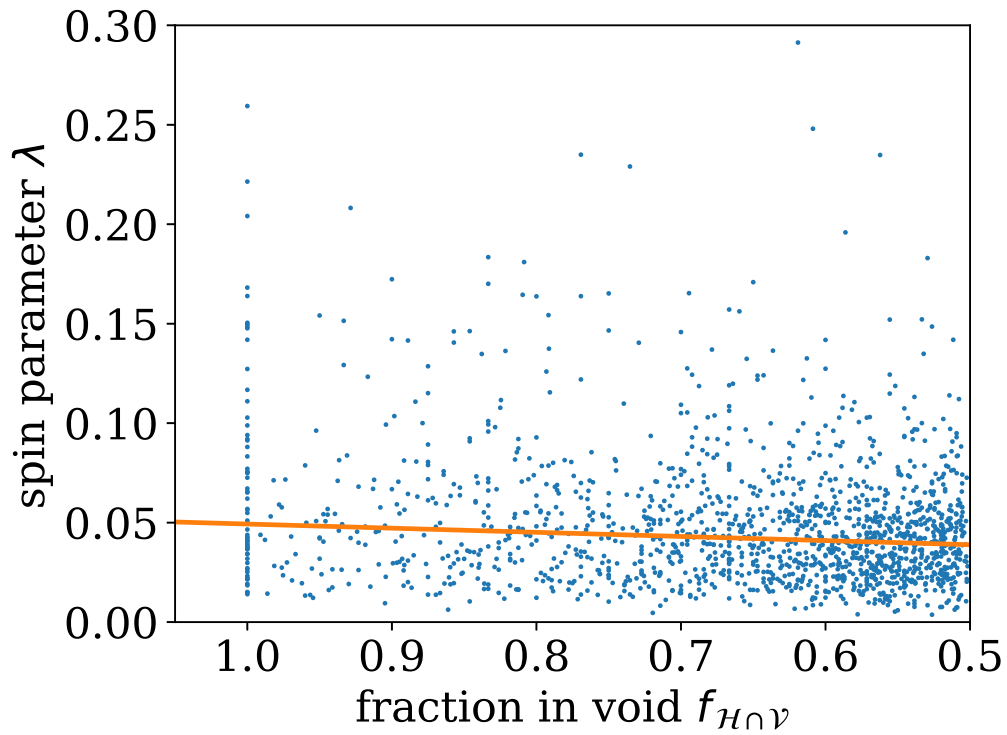


Figure 4.10: Dimensionless spin parameter  $\lambda$  (Eq. (3.45)) versus  $f_{\mathcal{H} \cap \mathcal{V}}$ . The fit is  $\lambda = (0.028 \pm 0.003) + (0.021 \pm 0.004 \pm_{\text{cv}} 0.005) f_{\mathcal{H} \cap \mathcal{V}}$ .



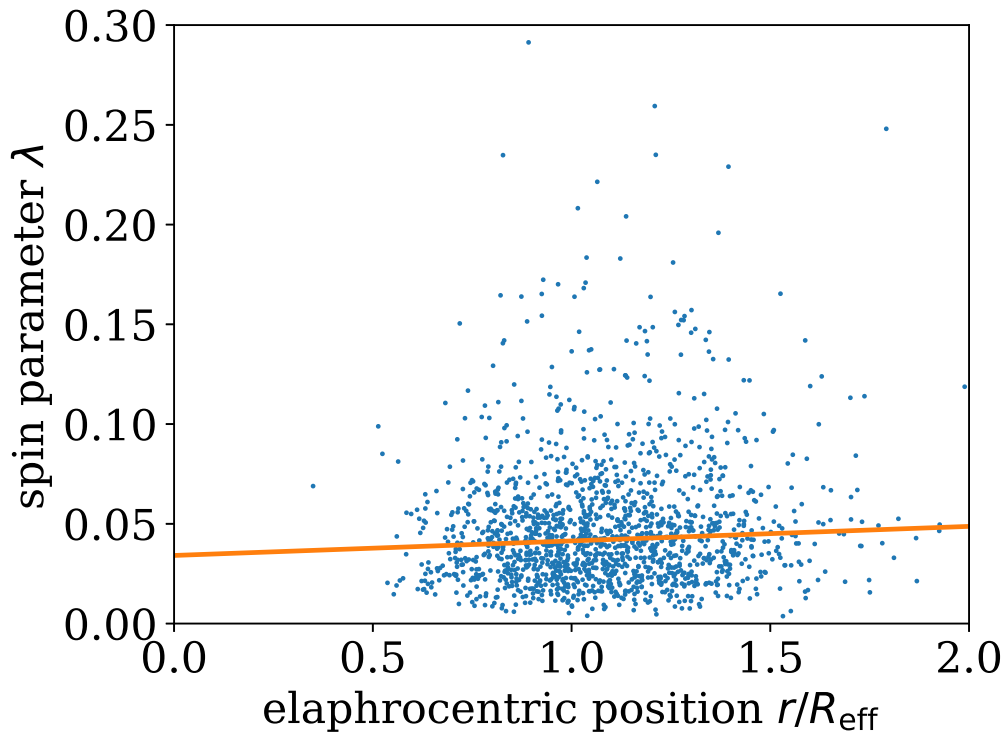


Figure 4.11: Dimensionless spin parameter  $\lambda$  (Eq. (3.45)) versus elaphrocentric location  $r/R_{\text{eff}}$ , as in Fig. 4.10. The fit is  $\lambda = (0.034 \pm 0.003) + (0.007 \pm 0.002 \pm_{\text{cv}} 0.002) r/R_{\text{eff}}$ .

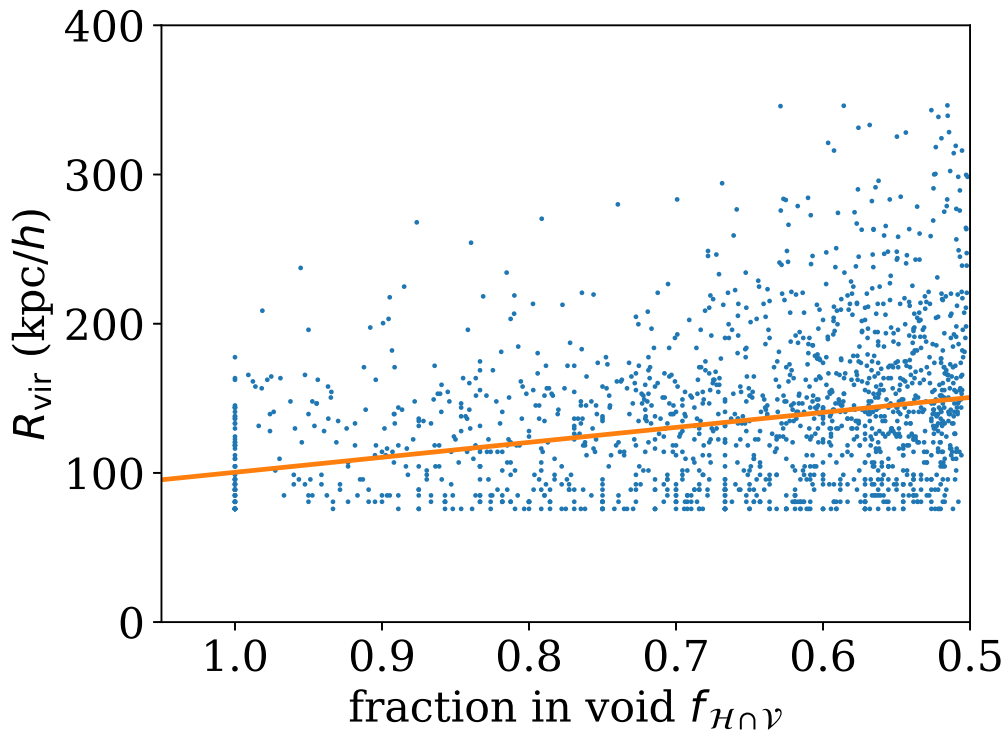


Figure 4.12: Virial radius  $R_{\text{vir}}$  (Eq. (3.45)) versus  $f_{\mathcal{H} \cap \mathcal{V}}$ . The fit is  $R_{\text{vir}} = [(201 \pm 6) + (-100 \pm 9)f_{\mathcal{H} \cap \mathcal{V}}]$  kpc/h. The sharp lower limit in  $R_{\text{vir}}$  follows from the minimum detectable halo mass in the  $N$ -body simulation.

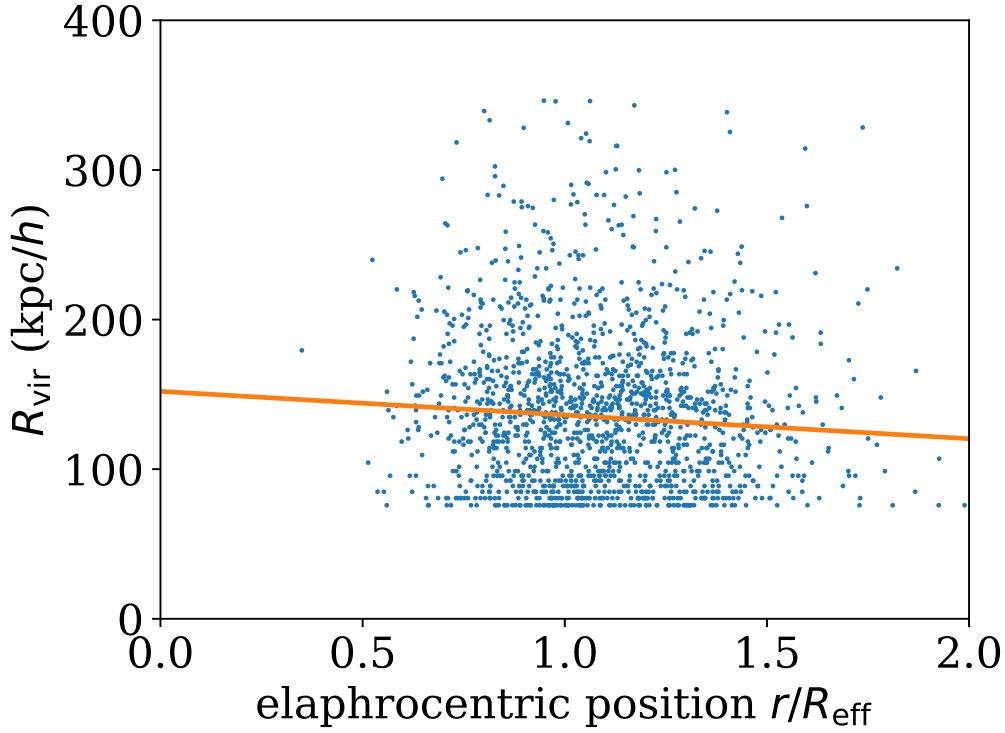


Figure 4.13: Virial radius  $R_{\text{vir}}$  versus elaphrocentric location  $r/R_{\text{eff}}$ , as in Fig. 4.12. The fit is  $R_{\text{vir}} = [(152 \pm 7) + (-15.8 \pm 5.9 \pm_{\text{cv}} 6.7) r/R_{\text{eff}}]$  kpc/h.

In Figs 4.10–4.13, we investigate whether the spin parameter  $\lambda$  or the virial radius  $R_{\text{vir}}$  is more responsible for the modest reduction in the disk scale length of void galaxies as indicated in Table 4.2. The sharp lower limit in Figs 4.12 and 4.13 is an artefact of the detection threshold of dark matter haloes in the  $N$ -body simulation. The virial radius is calculated by SAGE from the halo mass. Out of the four figures (Figs 4.10–4.13), two show highly significant slopes: Figs 4.10 and 4.12. The slopes in Figs 4.11 and 4.13 are not significantly different from zero.

The slopes in Figs 4.10 and 4.12,  $d\lambda/df_{\mathcal{H}\cap\mathcal{V}} = 0.021 \pm 0.004 \pm_{\text{cv}} 0.005$  and  $dR_{\text{vir}}/df_{\mathcal{H}\cap\mathcal{V}} = -100 \pm 9$  kpc/h, respectively, are both very strong, but opposed. Galaxies better identified as void galaxies have higher spins, but also lower virial radii and lower masses. The overall effect, as shown in Fig. 4.8, is that the two effects more or less cancel, in contrast to the full-population results shown in Table 4.2.

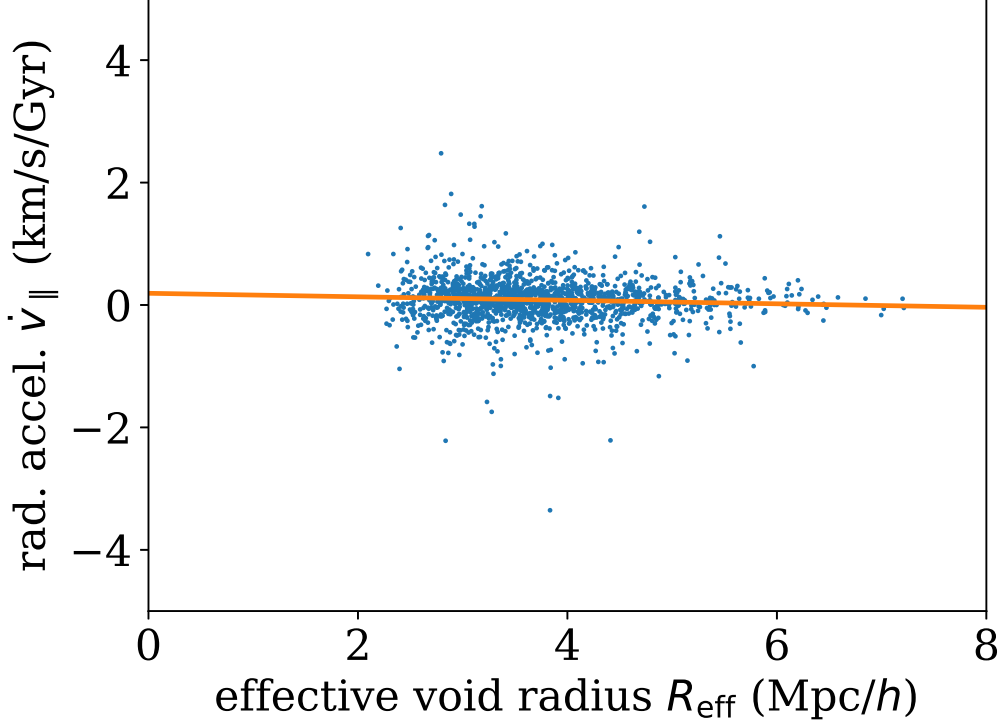
Figure 4.9 and its fit show that overall, the elaphrocentric distance  $r/R_{\text{eff}}$  has only a weak effect on galaxy disk scale lengths  $r_{\text{disk}}$ . The halo size and spin parameter both have weak, though apparently again opposite, dependences on  $r_{\text{disk}}$ , with  $d\lambda/d(r/R_{\text{eff}}) = 0.007 \pm 0.002 \pm_{\text{cv}} 0.002$  in Fig. 4.11 and  $dR_{\text{vir}}/d(r/R_{\text{eff}}) = -15.8 \pm 5.9 \pm_{\text{cv}} 6.7$  kpc/h in Fig. 4.13.

In summary, the trends for  $r_{\text{disk}}$ ,  $\lambda$ , and  $R_{\text{vir}}$  found in Table 4.2 are similar, but strengthened, when void location of a galaxy is quantified by  $f_{\mathcal{H}\cap\mathcal{V}}$ , and insignificant when void location is quantified by  $r/R_{\text{eff}}$ . The lack of a significant dependence of these parameters on the elaphrocentric distance,  $r/R_{\text{eff}}$ , is somewhat surprising, since one might expect  $f_{\mathcal{H}\cap\mathcal{V}}$  and  $r/R_{\text{eff}}$  to be proxies for one another, equally valid for defining how high a galaxy is on the potential hill of a void. We discuss this counterintuitive result further in Sect. 4.4.2.

Since  $R_{\text{vir}}$  is obtained from  $M_{\text{vir}}$  by SAGE on the assumption of a detection threshold of 200 times the critical density, Fig. 4.12 can be qualitatively compared with observational estimates

Table 4.3: Median radial  $\dot{v}_{\parallel}$  and tangential  $\dot{v}_{\perp}$  accelerations at  $r^{\text{test}} = 1.20 \text{ Mpc}/h$  from the elaphrocentre.

median acceleration	
$\dot{v}_{\parallel}$	$0.09 \pm 0.01 \text{ km/s/Gyr}$
$\dot{v}_{\perp}$	$1.90 \pm 0.04 \pm_{\text{cv}} 0.29 \text{ km/s/Gyr}$

Figure 4.14: Dependence of the radial elaphro-acceleration  $\dot{v}_{\parallel}$  as a function of effective void radius  $R_{\text{eff}}$ , together with a robust linear fit. The fit is  $\dot{v}_{\parallel} = [(0.191 \pm 0.040) + (-0.029 \pm 0.010 \pm_{\text{cv}} 0.006) h/\text{Mpc} R_{\text{eff}}] \text{ km/s/Gyr}$ .

of the masses of void galaxies. Keeping in mind the fixed lower limit in mass resolution, the robust best fit relation can be used to describe the galaxies best located in a void ( $f_{\mathcal{H} \cap \mathcal{V}} = 1$ ) as having host haloes with  $R_{\text{vir}} \sim 100 \text{ kpc}/h$ , and those best located in walls ( $f_{\mathcal{H} \cap \mathcal{V}} = 0$ ) as having higher mass host haloes, with  $R_{\text{vir}} \sim 200 \text{ kpc}/h$ . Thus, the masses of galaxies' host haloes located in the walls should be typically eight times those of galaxies located in voids. Weistrop et al. (1995) found that 12  $H\alpha$ -emitting galaxies in the Boötes void were mostly quite luminous, and Szomoru et al. (1996) found that a sample of 16 targetted Boötes void galaxies (along with 21 companion galaxies) appeared to be similar to corresponding late-type, gas-rich field galaxies and of similar masses. These Boötes void surveys would appear to be inconsistent with the mass difference found here. However, the more recent and bigger survey of 60 void galaxies in the Sloan Digital Sky Survey (SDSS) by Kreckel et al. (2012) found that these have moderately low stellar masses, mostly around  $10^9 - 10^{10} M_{\odot}$ . The SDSS void galaxy survey would appear more likely to be consistent with our results. Future work, in which the remaining steps in galaxy formation and evolution modelling are added to the pipeline presented here, should enable quantitative comparisons to see if the Boötes and SDSS void galaxies (see also Pan et al., 2012; Nadathur & Hotchkiss, 2015a; Sutter et al., 2015) are consistent with those modelled here.

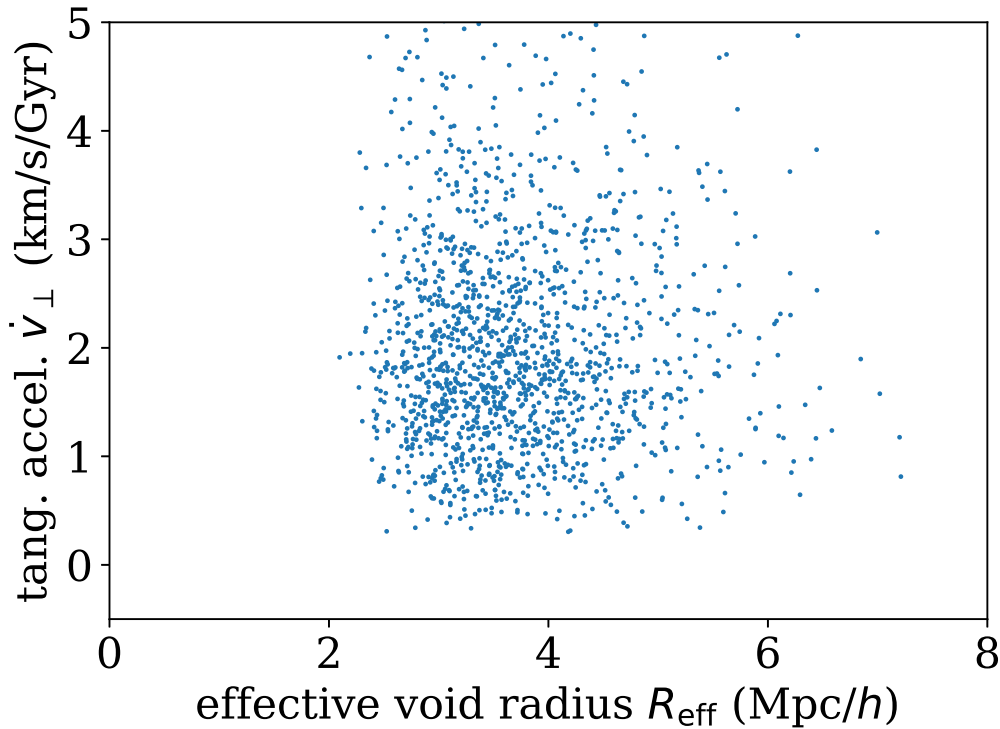


Figure 4.15: Dependence of the tangential elaphro-acceleration  $\dot{v}_\perp$  as a function of  $R_{\text{eff}}$ . The best robust linear fit is  $\dot{v}_\perp = [(1.841 \pm 0.122) + (0.012 \pm 0.031 \pm_{\text{cv}} 0.036) h/\text{Mpc} R_{\text{eff}}] \text{ km/s/Gyr}$ .

#### 4.3.4 Elaphro-acceleration

Elaphro-accelerations were calculated as described in Sect. 4.2.3, at elaphrocentric distances of  $r^{\text{test}} = 1.20 \text{ Mpc}$ . We found 1570 voids that allowed valid estimates. The median radial acceleration for a test particle at these positions is given in Table 4.3. The amplitudes of these two values are not directly comparable, because  $\dot{v}_\parallel$  is the median of signed values, while  $\dot{v}_\perp$  is non-negative by construction. The Newtonian estimate for the gravitational pull at  $r^{\text{test}}$  away from the centre of the canonical high-mass test halo of mass  $M^{\text{test}}$ , a barycentre, is an inward-pointing acceleration, i.e.  $\dot{v}_\parallel^{\text{test-halo}} = -3.05 \text{ km/s/Gyr}$ .

The median estimate of  $\dot{v}_\parallel$  given in Table 4.3 is an outward-pointing elaphro-acceleration to high statistical significance. This is consistent with what could be expected of the elaphrocentre, defined as the location of the global maximum in the potential of a void, with mass typically moving away from the elaphrocentre. The amplitude is more than an order of magnitude weaker than that of the barycentric acceleration towards our canonical high-mass halo. Figure 4.14 shows that the full spread of radial elaphro-accelerations is wide, including many negative values, and that dependence on the void effective radius  $R_{\text{eff}}$  is weak. Together, these properties imply that, at least with the numerical techniques and simulation parameters adopted in this work, a systematic antigravitational effect at the elaphrocentre helping to oppose infall is likely to be modest. This is consistent with our infall results above.

The median tangential acceleration  $\dot{v}_\perp$  is given in Table 4.3 and the individual estimates and fit are shown in Fig. 4.15. These values are about an order of magnitude higher in amplitude than those of  $\dot{v}_\parallel$ , and similar to that for our canonical high-mass halo. This supports the argument that rotational properties of the fluid flow such as shear and vorticity are likely to be significant in understanding voids. Figures 4.14 and 4.15 do not show significant dependence of  $\dot{v}_\parallel$  and  $\dot{v}_\perp$

on the size of a void.

## 4.4 Discussion

### 4.4.1 Infall rates

We generally found a lack of statistically significant trends in the two infall parameters on  $f_{\mathcal{H} \cap \mathcal{V}}$  and  $r/R_{\text{eff}}$  (Table 4.1, Figs 4.4–4.7), for those galaxies whose host haloes’ infall rates could be fit with an exponential best fit. A moderately significant non-zero dependence is that of  $A$  on  $f_{\mathcal{H} \cap \mathcal{V}}$ , shown in Figure 4.4, opposite to that expected: void galaxies have slightly higher amplitudes of their best fit infall rate histories. The simplest interpretation is that in a halo destined to collapse with a given final mass, the infall history of matter into that halo is nearly independent of the environment. The modest amplitude of the median acceleration outwards from the elaphrocentre – the *elaphro-acceleration*  $\dot{v}_{\parallel}$  (Table 4.3) – is probably the main reason for this. This is something like a Newtonian numerical equivalent of Birkhoff-like (Birkhoff & Langer, 1923) or “finite infinity” (Ellis, 1984; Wiltshire, 2007) arguments for modelling galaxies in isolation from their environment. Our hypothesis that the void environment helps to form giant LSBGs by providing slow, weak infall is not supported by our numerical results.

Although the parameters of our simplified infall fit are not affected by the position of a galaxy, we found a significant difference in the median galaxy collapse epoch (the first time step with a non-zero, non-negative infall rate) between void galaxies and non-void galaxies. While we did not expect this to play a major role in galaxy formation, it should. The median collapse epochs (in standard FLRW cosmological time) that we found were  $t_{\text{v}}^{\text{f}} = 4.1 \pm 0.1$  Gyr and  $t_{\text{nv}}^{\text{f}} = 3.3 \pm 0.1$  Gyr for the void and non-void galaxies, respectively (Sect. 4.3.2). Thus, to very high significance, void galaxies typically form later than non-void galaxies. We interpret this as a result of their formation in underdensities. Haloes that collapse later should, according to the standard spherical collapse model, have a lower matter density. Galaxies should thus form with lower dark matter and baryonic matter densities ( $M_{\odot}/\text{kpc}^3$ ), which may lead to lower surface densities ( $M_{\odot}/\text{kpc}^2$ ) of galaxy disks and lower surface brightnesses ( $L_{\odot}/\text{kpc}^2$ ) induced by star formation.

This characteristic of void galaxies agrees with Rong et al. (2017), in the sense that these authors found that UDGs have a later formation time than typical dwarfs, and assuming that we associate UDGs as being located in voids. Rong et al. (2017) found that UDGs at the current epoch have a median age of 7.1 Gyr compared to typical dwarfs with a median age of 9.6 Gyr. For the current epoch estimated at  $t_0 \sim 13.8$  Gyr, these correspond to median UDG and ordinary dwarf formation epochs of 6.7 Gyr and 4.2 Gyr, respectively. Since (i) we consider high-mass host haloes and correspondingly high-mass galaxies, rather than the more typical UDGs and dwarfs, and (ii) we separate populations by their location in voids rather than by continuing through to stellar population synthesis, more precise correspondence with Rong et al. (2017)’s results would be unlikely with our current pipeline. The qualitative agreement that void galaxies typically form later than non-void galaxies by about a Gigayear (our result) and that UDGs form about three Gigayears later than ordinary dwarf galaxies (Rong et al., 2017) is a promising sign of progress towards a cohesive theory of LSBG formation.

### 4.4.2 Galaxy sizes

The most massive galaxies and their host haloes (with the largest virial radii  $R_{\text{vir}}$ ) form in the tight knots of the cosmic web. Although we found that galaxies in voids tend to be smaller when

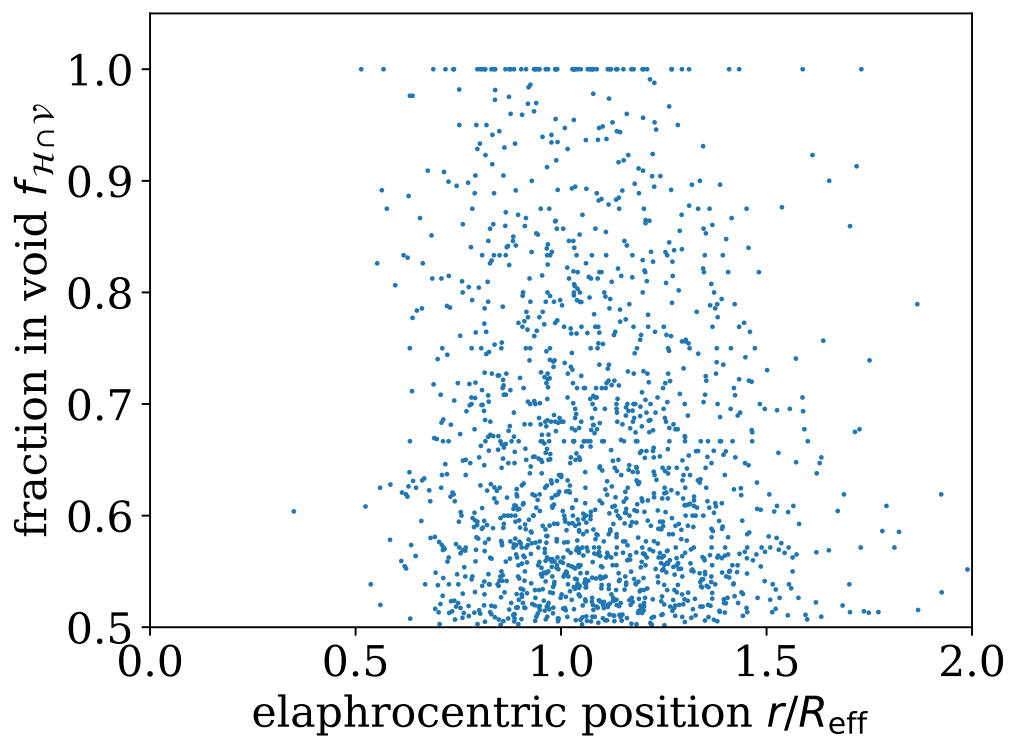


Figure 4.16: Relation between fraction in void  $f_{H \cap V}$  and elaphrocentric position  $r/R_{\text{eff}}$ . The best robust linear (Theil–Sen) fit is  $\lambda = (0.667 \pm 0.015) + (-0.041 \pm 0.011 \pm_{\text{cv}} 0.012) r/R_{\text{eff}}$ . Plain text table for this figure: [zenodo.4699702/voidgals\\_infall.dat](https://zenodo.org/record/4699702/files/voidgals_infall.dat).

comparing the overall void to non-void populations (Table 4.2), this was not detected in the dependence of the galaxy disk scale length  $r_{\text{disk}}$  on  $f_{\mathcal{H}\cap\mathcal{V}}$ , nor on  $r/R_{\text{eff}}$ . In contrast, we did find significant dependences of the two contributing parameters to  $r_{\text{disk}}$ , the spin parameter  $\lambda$  and the virial radius  $R_{\text{vir}}$ , on  $f_{\mathcal{H}\cap\mathcal{V}}$ , but insignificant dependence on  $r/R_{\text{eff}}$ . While the dependence on  $R_{\text{vir}}$  is clearly the dominant effect, we find that the spin parameter considered alone, which tends to form large galaxy disks, is higher for void galaxies. This is seen most significantly in Fig. 4.10, via the dependence of  $\lambda$  on  $f_{\mathcal{H}\cap\mathcal{V}}$ . The higher spin parameter effect could be interpreted as the result of either fewer merger events weakening the spin parameter, or of gravitational effects inside the void. A likely candidate for the latter is the tangential acceleration  $\dot{v}_{\perp}$  (Table 4.3). This is typically of the same order of magnitude as the gravitational pull of the source region of the high-mass test halo that is, in its properties, inspired by Malin 1. However, in this work we have focussed on overall population properties and reproducibility of the pipeline. Continuation through to disk surface densities, for comparison with Di Paolo & Salucci (2020, Sect. 7.1, 7.2), and to stellar population evolution, remains a task for future work. Moreover, the rare high-mass galaxies that are well identified as void galaxies may require high numbers of simulations, if realised randomly, since, by definition, they are rare. Alternatively, a small number of big simulations may provide qualitative clues, as in the Malin 1 analogue found in the IllustrisTNG simulation by Zhu et al. (2018).

It may seem somewhat surprising that these significant dependences on  $f_{\mathcal{H}\cap\mathcal{V}}$  do not translate into significant dependences on  $r/R_{\text{eff}}$ . The explanation most likely lies in the fact that REVOLVER traces voids using Voronoi tessellation and the watershed algorithm, and voids are in general aspherical. Galaxies can lie in fairly empty parts of a void, with high  $f_{\mathcal{H}\cap\mathcal{V}}$ , while lying, for example, in the far ends of a prolate void, where  $r/R_{\text{eff}} > 1$ . It would be useful to quantify the relation between  $f_{\mathcal{H}\cap\mathcal{V}}$  and  $r/R_{\text{eff}}$ .

Figure 4.16 shows visually that there is no obvious relation between  $f_{\mathcal{H}\cap\mathcal{V}}$  and  $r/R_{\text{eff}}$ . As indicated in the caption, the best robust fit indicates no statistically significant non-zero linear slope relating the two parameters. The fact that most of the void galaxies lie at  $r/R_{\text{eff}} \gtrsim 1$  is consistent with the explanation suggested above. This can also be thought of as follows. Voids are defined by the absence of particles. Galaxies are generally not found in the interior of voids, because then the void shapes would be defined differently, shifting those galaxies' host haloes from void status to near-boundary status in the redefined voids. A halo located at approximately  $r/R_{\text{eff}} \gtrsim 1$  in a highly aspherical void is not necessarily located in a locally low density region, so it is not constrained to contain a high number of particles identified as void particles.

Thus,  $f_{\mathcal{H}\cap\mathcal{V}}$  and  $r/R_{\text{eff}}$  appear to be statistically independent parameters. The significant trend of  $r_{\text{disk}}$  on  $f_{\mathcal{H}\cap\mathcal{V}}$ , and the fact that  $f_{\mathcal{H}\cap\mathcal{V}}$  has a more local physical meaning than  $r/R_{\text{eff}}$ , suggest that  $f_{\mathcal{H}\cap\mathcal{V}}$  is the more physically useful parameter to choose. Numerical and observational studies that measure the local number density around a given density will tend to correspond to the use of  $f_{\mathcal{H}\cap\mathcal{V}}$  as a parameter for characterising the void nature of a galaxy.

To see if earlier definitions of void centres, as discussed in Sect. 4.2.2, could have more significant effects on galaxy sizes, we repeated our calculations for distances from the circumcentre and from the geometrical centroid instead of the elaphrocentre. Table 4.4 shows the robust best fits to the dependence of  $r_{\text{disk}}$ ,  $R_{\text{vir}}$  and  $\lambda$  on void-centric distance for the three definitions. The full scatter plots (not shown) are visually indistinguishable from Figs 4.9, 4.11 and 4.13. The differences between the three cases are statistically negligible. Given that the geometrical centroid (macrocentre or volume-weighted barycentre) only encodes information about the void's periphery, with no information from its interior, it may seem surprising that this gives similar results to the other two centres. However, this is probably explained by the near-total absence of galaxies located within the central half-radius of the void; the detected galaxies' radial distances from

Table 4.4: Robust best fit parameters for  $r_{\text{disk}}$ ,  $R_{\text{vir}}$  and  $\lambda$  with respect to the void-centric distance for the three different centre definitions discussed in Sect. 4.2.2.

elaphrocentre	
$r_{\text{disk}}$	$(3.65 \pm 0.26) + (0.11 \pm 0.22) r/R_{\text{eff}}$
$R_{\text{vir}}$	$(152 \pm 7) + (-15.8 \pm 5.9) r/R_{\text{eff}}$
$\lambda$	$(0.034 \pm 0.003) + (0.007 \pm 0.002) r/R_{\text{eff}}$
circumcentre	
$r_{\text{disk}}$	$(3.65 \pm 0.31) + (0.12 \pm 0.28) r/R_{\text{eff}}$
$R_{\text{vir}}$	$(152 \pm 6) + (-15.6 \pm 5.7) r/R_{\text{eff}}$
$\lambda$	$(0.034 \pm 0.003) + (0.007 \pm 0.002) r/R_{\text{eff}}$
geometrical centroid	
$r_{\text{disk}}$	$(3.66 \pm 0.30) + (0.11 \pm 0.27) r/R_{\text{eff}}$
$R_{\text{vir}}$	$(152 \pm 6) + (-15.6 \pm 6.1) r/R_{\text{eff}}$
$\lambda$	$(0.034 \pm 0.003) + (0.007 \pm 0.002) r/R_{\text{eff}}$

the centre only vary mildly with different definitions of the centre.

### 4.4.3 Elaphro-acceleration

We found a significantly non-zero positive median acceleration towards the edges of a void. However, this median outwards acceleration,  $\dot{v}_{\parallel}$  (Table 4.3), is of the order of only a few percent of the inward gravitational pull at  $r^{\text{test}} = 1.20$  Mpc that the source mass excess for our canonical high-mass host halo would create,  $\dot{v}_{\parallel}^{\text{test}} = -3.05$  km/s/Gyr. Moreover, Fig. 4.14 shows a wide scatter between outward and inward accelerations from the elaphrocentre. Thus, while a modest average effect in opposing infall could be expected for galaxies that are close to the elaphrocentre of a void, the effect would be sensitive to the wide distribution in values and to relations between the elaphrocentric acceleration and other dynamical parameters.

Future work in placing a test halo near an elaphrocentre, with the assumption that the test halo has no dynamical effect on the underlying void properties, may use these results as a guide to judging the likely strength of the effect. For example, the probability that a test halo of a given mass placed at the elaphrocentre of a random void has its infall rate weakened sufficiently to make it a candidate LSBG could be estimated. This could be compared with the infall rate behaviour from haloes from the  $N$ -body realisation itself, as we presented in Sect. 4.3.2, at elaphrocentric positions far from the elaphrocentre.

The median tangential acceleration  $\dot{v}_{\perp}$  is much higher than the radial acceleration, and might be used to study the higher spin parameter  $\lambda$  found for void galaxies when identified by  $f_{\mathcal{H} \cap \mathcal{V}}$ , as shown in Fig. 4.10. Since this is of the same order of magnitude as our canonical radial acceleration,  $\dot{v}_{\parallel}^{\text{test}}$ , it is likely that  $\dot{v}_{\perp}$  could play an important role for galaxies forming in voids.

### 4.4.4 Future extensions

An obvious further development, not yet included in the present work, would be to analyse the star formation rate histories and to extend the pipeline with evolutionary stellar population synthesis methods. This would allow us to identify LSBGs in our galaxy population in a way more closely comparable to observational results, while continuing to benefit from the reproducibility and modularity of the pipeline presented in this work. The inclusion of metallicity evolution, in



particular that of O/H, would allow comparison with the populations of extremely metal-poor gas-rich, dwarf galaxies that seem to characterise a difference between void and non-void galaxy formation (Pustilnik et al., 2020).

Another extension would be to extend or replace the gravitational simulation. Using a relativistic simulation, rather than a standard (Newtonian) simulation, would provide a major theoretical improvement towards more realistic results. The scalar averaging extensions provided by INHOMOG through the RAMSES/RAMES-SCALAV front end to check background-independent dynamical properties (Roukema, 2018), using the relativistic Zel’dovich approximation Buchert & Ostermann (2012); Buchert, Nayet, & Wiegand (2013), could easily be added. Other options could include using either GEVOLUTION (Adamek et al., 2016) or the fully relativistic EINSTEIN TOOLKIT (Bentivegna & Bruni, 2016; Macpherson, Lasky, & Price, 2017). Hydrodynamical simulations would also be useful for comparison. Given the aims of this project in providing a reproducible pipeline with modular, free-licensed components, it should, in principle, be straightforward to replace any of the pipeline steps or to start the pipeline at an intermediate step, such as analysing pre-calculated  $N$ -body simulation outputs. The present form of the pipeline assumes GADGET2 format for the  $N$ -body simulation output snapshots.

Alternatives in the statistical analysis of infall rate histories would also be useful to explore. Here, we chose to fit the infall rate history with decaying exponentials, which include nearly constant rates as a special case with very long time scales  $\tau$ , but the reality of the mass infall rate history, and the corresponding star formation rate history, is in generally much more complex, depending especially on merger events. A more general quantitative way of characterising the global population of mass infall or star formation rate histories would bring this pipeline closer to physical reality.

## 4.5 Conclusion

We have presented a complete, *ab initio*, reproducible galaxy formation pipeline starting from a standard post-recombination-epoch spectrum of initial perturbations, aiming to identify key factors in void galaxy formation that might contribute to the formation of giant low surface brightness galaxies in voids (Sect. 4.2.1). We introduced the term *elaphrocentre* to clarify its opposite physical nature to the barycentre and we clarified the confusing use of the latter term in void studies (Sect. 4.2.2).

We did not find statistically significant numerical evidence that the elaphrocentre, or the void location of a galaxy more generally, plays a key role in forming major populations of large diffuse galaxies – LSBGs – via the parameters that we considered as the most likely to play a strong role –  $A$  and  $\tau$  (Figs 4.4–4.7). Since gravity is attractive, there is an asymmetry between the sharp nature of barycentres (potential wells) and the wide spread of elaphrocentres (potential hills), which could explain the lack of a strong effect.

We found that the fractional elaphrocentric distance of a void galaxy  $r/R_{\text{eff}}$  is, statistically, a less useful independent variable than  $f_{\mathcal{H}\cap\mathcal{V}}$ , the fraction of a galaxy’s host halo particles that are identified as being in a single void. This is important for observational studies of void galaxies. The characterisation of galaxies as void galaxies by  $f_{\mathcal{H}\cap\mathcal{V}}$ , which should roughly correspond to a low local dark matter density, or by relative elaphrocentric radius  $r/R_{\text{eff}}$ , which would require identification of voids in a catalogue, will in general give uncorrelated results; the two parameters show no significant linear correlation (Fig. 4.16).

A serendipitous result is that void galaxies were found to be significantly smaller in virial radius (host halo mass) than non-void galaxies (Table 4.2, Figs 4.8–4.13). This complicates the question of giant LSBG formation, because the disk scale length  $r_{\text{disk}}$ , as calculated in Eq. (3.45),

is dominated by the virial radius. We did find that galaxies better identified in voids have a higher spin parameter. This finding of a higher spin parameter for high  $f_{\mathcal{H} \cap \mathcal{V}}$  is qualitatively consistent with Rong et al. (2017)'s result that a higher spin is a key feature of UDGs and thus indirectly supports the hypothesis of void location constituting a significant factor in LSBG formation. Higher resolution simulations, extending to lower mass galaxies, would be needed to see if the higher spin of UDGs is quantitatively explained as a consequence of void location.

We also found that the median galaxy collapse epoch differs to very high statistical significance between void and non-void populations ( $t_v^f = 4.1 \pm 0.1$  Gyr and  $t_{nv}^f = 3.3 \pm 0.1$  Gyr for void and non-void galaxies, respectively; Sect. 4.3.2). For a standard spherical collapse model, the later collapse of void galaxies should lead to these galaxies being less dense, quite likely resulting in lower surface densities and star formation rates.

In summary, despite not finding direct numerical evidence for LSBG formation in our overall populations, the higher spin parameter  $\lambda$  for the overall population of void galaxies, especially when characterised by  $f_{\mathcal{H} \cap \mathcal{V}}$ , and the later formation epoch of void galaxies, are qualitatively consistent with Rong et al. (2017)'s findings for UDGs, assuming that the extension to lower masses remains valid. Together with these two key features that contribute to the formation of diffuse galaxies, the smaller size of void galaxies suggests that, in contrary to our hypothesis of giant LSBG formation in voids, the role of voids is to preferentially form diffuse, somewhat smaller galaxies. Moreover, we hope that by providing our complete software pipeline<sup>5</sup> using the Maneage template that aims at full reproducibility (Rougier et al., 2017; Akhlaghi et al., 2021), rather than only giving the names and URLs of cosmological software packages, our work will encourage the community to avoid unnecessary effort spent in guessing the precise details of the computational software used in this and other extragalactic research.

---

<sup>5</sup>DOI-stamped record: zenodo.4699702; live git repository: <https://codeberg.org/boud/elaphrocentre>

# Chapter 5

## Hierarchical structure of the cosmic web and galaxy properties

The previous chapter investigates what role voids play in galaxy formation yielding higher spin parameter, smaller halo sizes and significantly later formation epochs. This chapter is based on Jaber, Peper, Hellwing, Aragon-Calvo, & Valenzuela (2023), describing my main contributions to the paper, and their relation to the rest of this thesis. Jaber et al. (2023) aims to investigate the influence that the cosmic web environment of a galaxy has on the galaxy's properties, with special emphasis on the effects of the internal filamentary structure of voids, and continues the work of (Aragon-Calvo & Szalay, 2013). To analyse the filamentary structure in cosmic voids we need a high-resolution simulation, to provide sufficient detail in examining the inner composition of cosmic voids, a way of selecting such internal structures of voids and a method to calculate the density field that is accurate in the under-dense regions.

We use the Bolshoi simulation (Klypin et al., 2011), which provides a significantly improved mass resolution that not only allows analysing the internal structure of a void, it also extends the mass resolution of resolved galaxies presented in chapter 4. We use the same tools to model galaxies as presented in Peper & Roukema (2021) and point out key differences between our previously established pipeline and the work done within this project. We do not make this chapter computationally reproducible in the sense of chapters 4 or 6.

### 5.1 Method

#### 5.1.1 Simulation

As stated this work is based on the Bolshoi simulation (Klypin et al., 2011) that uses  $2048^3$  dark matter particles and a fundamental domain size of  $L_{\text{box}} = 250 \text{ Mpc}/h$ . The resolved galaxies cover a significant larger range of scales than presented in chapter 4. The Bolshoi simulation assumes the  $\Lambda$ CDM model with the values for the cosmological parameters  $\Omega_{\text{m}0} = 0.27$ ,  $\Omega_{\Lambda 0} = 0.73$  and a Hubble parameter of  $H = 70 \frac{\text{km}}{\text{Mpc s}}$ . This choice of parameters yields a particle mass of  $1.35 \times 10^8 M_{\odot}/h$  and is thus able to resolve dwarf galaxies. Similarly to our software pipeline presented in Peper & Roukema (2021), the tree data was generated by the Bolshoi collaboration using the ROCKSTAR halo finder Behroozi et al. (2013a) and CTREES Behroozi et al. (2013b) and is available online.<sup>1</sup>

The core of the hierarchical analysis includes three  $512^3$  particle runs whose initial conditions

---

<sup>1</sup>[https://www.slac.stanford.edu/~behroozi/Bolshoi\\_Trees/](https://www.slac.stanford.edu/~behroozi/Bolshoi_Trees/)

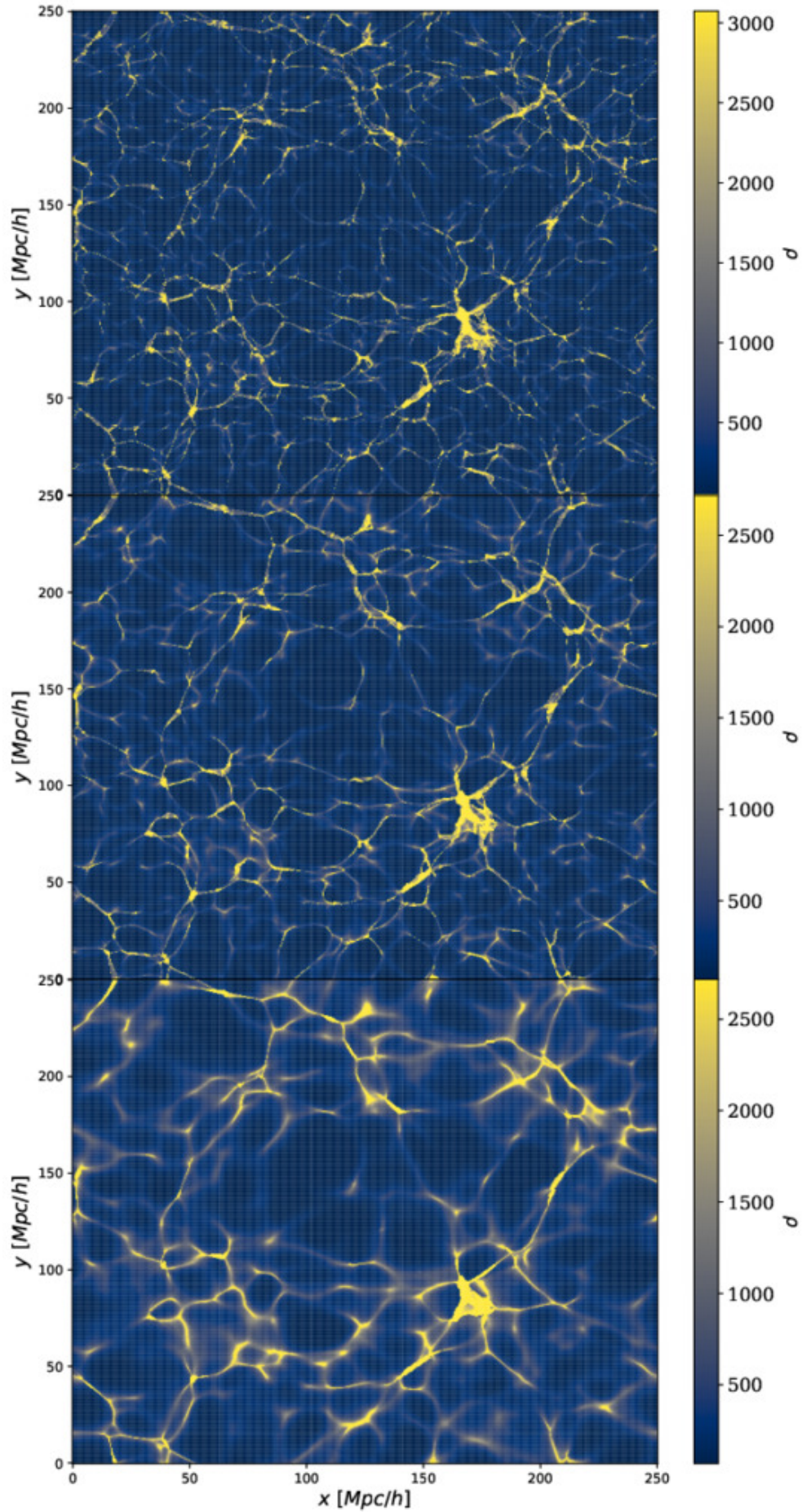


Figure 5.1: A slice of the three simulations at  $z = 100 \text{ Mpc}/h$ . The effect of the filter ( $\beta_s = 1, 2, 4 \text{ Mpc}/h$ ) is visible as we go from top to bottom, showing successively less small-scale structure.

were the Bolshoi initial conditions re-sampled on the  $512^3$  grid. The three realisations will thus have the same structure as the Bolshoi simulation. We employ a sharp  $k$ -filter ( $k$  being the wavevector) to remove specific modes from the power spectrum and thus prevent them from evolving. This filter is applied in the linear regime, at the start of the simulation, where the Fourier modes are independent. Thus, the filter does not introduce artifacts (Sheth & van de Weygaert, 2004; van de Weygaert & Sheth, 2004; Einasto et al., 2011a,b). To dissect the hierarchical nature of voids we set a filter on the lowest wavelength of perturbations for the simulations of  $\beta_s = 4, 2, 1 \text{ Mpc}/h$ . Excluding smaller wavelengths in the power spectrum will prevent these modes from growing, allowing the unfiltered modes of the matter distribution to evolve through to the full non-linear regime, without interference from the filtered modes.

We visualise the three resulting density distributions in fig. 5.1. We clearly see that the large-scale features are present in all three panels, while lower order structures are respectively less present from the top to bottom panels. In contrast to chapter 4, densities are not calculated with the VTFE, but instead use the Lagrangian Sheet Density Estimator (LSDE) method<sup>2</sup>, which recovers the density field extremely well in the underdense regions, originally proposed in Shandarin (2011); Abel et al. (2012).

### Structure Identification

The structures in the cosmic web, especially voids, are identified using the SPINWEB method (Aragón-Calvo et al., 2010a). In general, this void finder uses the watershed method introduced in section 3.3, starting to find local minima in the density field, assigning every voxel (volume pixel) to one of the minima and using a flooding algorithm to detect voids. The SPINWEB method has been designed to capture and analyse the complex, interconnected structure of the cosmic web. It requires that the density field is provided on a regular three-dimensional grid; the uniform cells around each of these grid points are the voxels.

A key feature lies in the assignment of morphological labels to each voxel. By identifying all the voxels lying on the void’s boundaries, identified during the watershed step, a morphological label can be attached to discriminate between voxels belonging to a void, a wall, a filament, or a cluster (node) in the cosmic web. This is done by taking advantage of the fact that every voxel is assigned an index numbering the different watershed regions. By counting the number of neighbouring voids  $N_v$ , i.e. the number of neighbouring voxels with a differing void identifier, we classify to what component of the cosmic web a voxel is assigned. If there are no other voids than the current one (i.e.  $N_v = 1$ ), then the current voxel is classified as being inside a void. A voxel with  $N_v = 2$ , meaning that the voxel’s adjacent voxels belong to two different voids, is classified as belonging to a wall. Voxels with  $N_v = 3$  are classified as being in the filaments of the cosmic web and those with  $N_v \geq 4$  are classified as clusters. We assign every voxel to a watershed region, so the case  $N_v = 0$  (no voids found) is excluded.

We use the SPINWEB method on all three hierarchical scales, giving us the density fields segmented into voxels, which are accordingly labelled as voids, walls, filaments and clusters. We use the three hierarchical levels to extract information on the cosmic web, following fig. 5.1 and calling them the top, middle and bottom levels, as in the figure. We use the term “spine-in-void” to refer to voxels that are classified as being part of a void ( $N_v = 1$ ) in the bottom hierarchical realisation,  $\beta_4 = 4 \text{ Mpc}/h$ , while being part of a dense structure ( $N_v > 1$ ) in the top hierarchy,  $\beta_1 = 1 \text{ Mpc}/h$ .

We populate the haloes in the merger trees as before, using SAGE (Croton et al., 2016). The SAGE code was originally tested using the Bolshoi simulation. Thus we adopt the parameters

<sup>2</sup><https://github.com/miguel-aragon/Lagrangian-Sheet-Density-Estimator>

Table 5.1: The volume filling fraction for the different environments as well as the galaxy fractions found in these environments. We present the fractions in all three hierarchical levels. We find, as expected, that filtering all modes below  $\beta_4 = 4 \text{ Mpc}/h$  yields the largest fraction of the volume being allocated to voids and consequently having the highest fraction of galaxies in voids.

<b>Filter</b>	$\beta_1 = 1 \text{ Mpc}/h$	$\beta_2 = 2 \text{ Mpc}/h$	$\beta_4 = 4 \text{ Mpc}/h$
<b>Voids</b>			
Vol. frac.	77.03%	81.71%	86.97%
Frac. gal.	(44.5%)	(48.7%)	(58.6%)
<b>Walls</b>			
Vol. frac.	20.31%	16.62%	12.23%
Frac. gal.	(43.4%)	(42.0%)	(35.9%)
<b>Filaments</b>			
Vol. frac.	2.19%	1.37%	0.61%
Frac. gal.	(10.0%)	(7.7%)	(4.5%)
<b>Nodes</b>			
Vol. frac.	0.46%	0.31%	0.21%
Frac. gal.	(2.01%)	(1.52%)	(0.89%)

advised by the authors for `SAGE` for the Bolshoi simulation. We then classify the galaxies as belonging to the different environments by using the information from the voxels in the highest resolution simulation (the top level), which uses the wavelength filter  $\beta_1 = 1 \text{ Mpc}/h$  and thus contains the most modes. Additionally, to study the internal structures of voids, we analyse galaxies that are in the spine-in-void voxels, meaning the galaxies that are in the web-like dense substructures within voids.

For this thesis, we present the parts of the project that relate to the previously discussed questions on the role of voids on galaxy formation. We again investigate the dimensionless spin parameter  $\lambda$ , the disk scale length and the formation epoch of these galaxies. Additionally, we investigate the stellar mass of the galaxies at redshift  $z = 0$ .

## 5.2 Results

We show dependence of the characteristics of the galaxies and their host haloes on their environment in the large-scale structure. At  $z = 0$  we detect a total of 7909721 galaxies over all environments; how they distribute themselves into the different environments for the different levels of hierarchy can be seen in Table 5.1. We also show the occupied volume, as a fraction of the total volume, and confirm that the watershed void finder `SPINWEB` is volume filling (the total volume fraction is 100% to within numerical uncertainty in each case). Following our classification we find that spine-in-void galaxies constitute 22.8% of the galaxies. The spine-in-void galaxies are found in the walls, filaments and clusters in the top hierarchy level with  $\beta_1 = 1 \text{ Mpc}/h$ .

We bin our data for the galaxies as a function of the virial mass of their host halo, in 20 bins for masses between  $10^9 M_\odot/h$  and  $10^{15} M_\odot/h$ . Errors are estimated using the bootstrap method with 200 randomly generated test sets. The errors show the 95% central percentile of the distribution of the medians. Consistently with the result we reported in Peper & Roukema (2021), we find in fig. 5.2 a higher spin parameter  $\lambda$  (see eq. (3.45)) for void galaxies compared

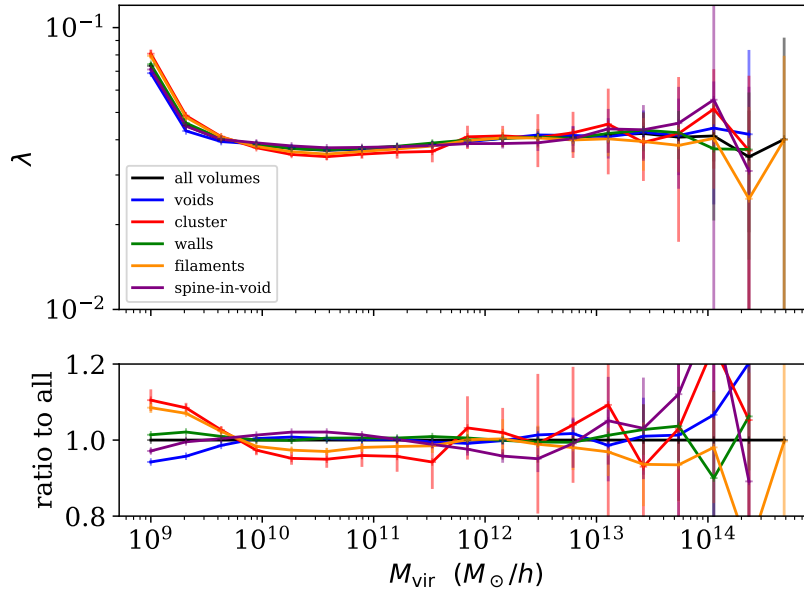


Figure 5.2: The dimensionless spin parameter of galaxies identified in the Bolshoi simulation characterised by their environment in the large scale structure. The upper panel shows the mean of the full population divided in several bins in the virial mass while errors are estimated using the bootstrap method. The lower panel shows the quotient compared to all galaxies in the simulation.

to galaxies in dense environments, namely filaments and clusters, for  $M_{\text{vir}} \gtrsim 10^{10} M_{\odot}/h$ , where the error bars are small enough to suggest significant differences. For the lowest masses, with  $M_{\text{vir}} \lesssim 10^{10} M_{\odot}/h$ , below the halo mass range in our own simulation, the trend of  $\lambda$  is inverted and  $\lambda$  is statistically lower for void galaxies than for the full set of galaxies, while galaxies in dense environments have a higher spin parameter.

A possible interpretation of the inversion at low masses is the fact that halo properties can vary strongly for haloes with too few particles, as Behroozi et al. (2013a) state; they recommend 20 particles as a minimum for consistent halo properties. The high mass end of galaxies has no statistically significant difference in the trend of the spin parameter for the galaxies as a function of environment. Galaxies in the spine-in-voids environment seem to have spin parameters in between those found for void galaxies and those for galaxies in dense environments.

Figure 5.3 does not show any significant trend in  $r_{\text{disk}}$  as a function of galaxy environment. Deviations from the trend of all galaxies at the low and high mass end are not significant due to the fewer numbers of galaxies that populate these mass bins.

The stellar to halo mass ratio will yield information in how efficient galaxies of different masses are in producing stars. As explained in Sect. 3.6, SAGE assigns baryonic mass to a dark matter halo, and forms stars in proportion to the available cooled gas (see eq. (3.48)). Figure 5.4 shows that for low and intermediate mass haloes,  $M_{\text{vir}} \lesssim 10^{11} M_{\odot}/h$ , there are significant differences in stellar masses as a function of environment. The stellar mass in galaxies identified in high density environments yield roughly twice the stellar mass as the global median, while the production of stellar mass in low density environments is slightly suppressed.

Finally, we analyse the formation epoch of the galaxies. In contrast to our smaller simulation of  $128^3$  dark matter particles, we cannot trace back the full tree of all galaxies in the Bolshoi simulation. Tracing back the history of a galaxy as described in chapter 4 for 8 million galaxies, each one having many progenitors and merger events in the available 180 snapshots, is a computationally unreasonable task. SAGE handles all haloes of linked merger-trees at once,

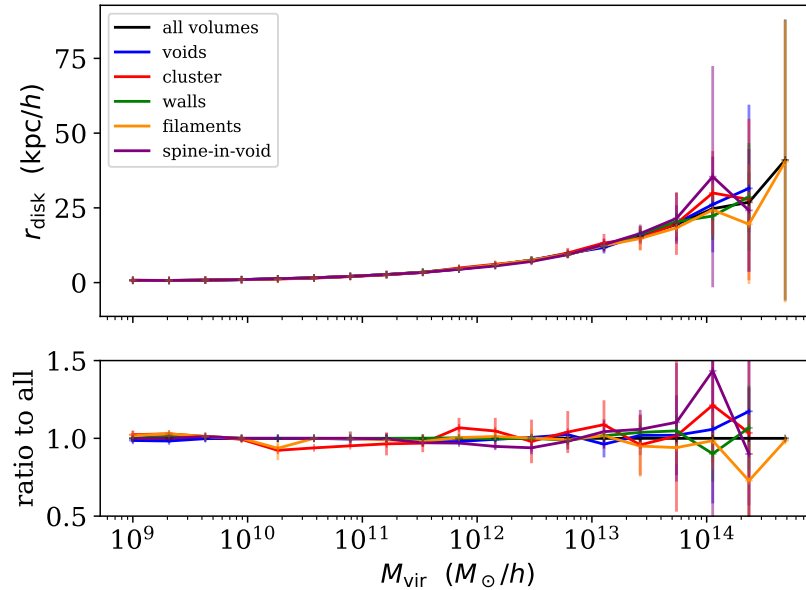


Figure 5.3: The disk scale length of galaxies identified in the Bolshoi simulation characterised by their environment in the large scale structure. The upper panel shows the mean of the full population divided in several bins in the virial mass while errors are estimated using the bootstrap method. The lower panel shows the quotient compared to all galaxies in the simulation.

meaning that it starts with the highest redshift and evolves each halo at this redshift along its descendancy path indicated in the merger-tree. The code does not distinguish between a halo that will host a (satellite) galaxy at  $z = 0$  from haloes that will merge. It evolves all the galaxies in one time snapshot to the next snapshot, and mergers are handled when reported in the merger-tree.

We therefore only consider the information for the first halo in each halo group, and assume that this redshift belongs to the central halo. In the theory of hierarchical structure formation, the most massive structures existing today have typically formed first. This makes the assumption that the central structure formed first (or the oldest structure merged into the central structure) a fair approximation.

The results can be seen in fig. 5.5. Significant differences are found for  $M_{\text{vir}} \lesssim 10^{10} M_{\odot}/h$ , the low mass end of the halo distribution, indicating that void galaxies have a slightly lower formation redshifts by a few percent, while galaxies in dense environments have a slightly higher formation redshift by a few percent. This is qualitatively consistent with what we found with our full merger tree in chapter 4, though for a lower mass range.

### 5.3 Discussion and Conclusion

In this chapter we presented a brief excerpt of the analysis of Jaber et al. (2023) of the hierarchical structures in the cosmic web and how they might influence galaxy properties. The analysis was carried out using similar tools as presented in chapter 3 and used in chapter 4. A major improvement was achieved by using the Bolshoi simulation, which yields several orders of magnitude better resolution, enabling us to make predictions for dwarf galaxies, at the cost of losing well-controlled computational reproducibility. As voids are dominated by dwarf galaxies, this analysis gives useful insights if the trends presented in chapter 4 and Peper & Roukema (2021) also hold true in the low halo mass range. The analysis also probes the different environments



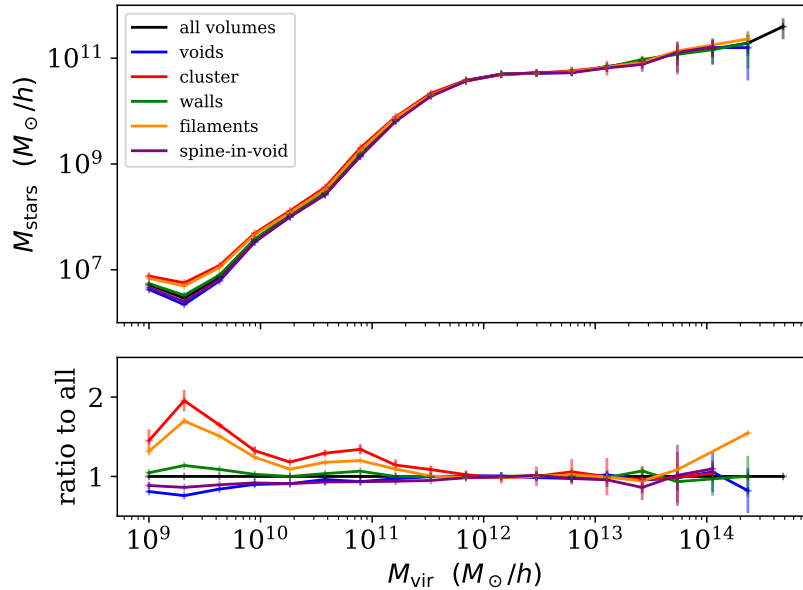


Figure 5.4: The stellar mass of galaxies identified in the Bolshoi simulation characterised by their environment in the large scale structure. The upper panel shows the mean of the full population divided in several bins in the virial mass while errors are estimated using the bootstrap method. The lower panel shows the quotient compared to all galaxies in the simulation.

of the cosmic web in more detail, giving more nuanced insight on the role that the environment plays in galaxy formation.

In this work we found that the differences in galaxy properties only occur in the low mass regime. Despite using different tools, we find similar results to Hellwing et al. (2021), with a threshold below which galaxy properties appear to depend on the environment. The threshold in this work is  $M_{\text{th}} \sim 10^{10} M_{\odot}/h - 10^{11} M_{\odot}/h$ . As in chapter 4, we report a higher spin parameter for void galaxies. While we found a mildly significant dependence in 4, see fig. 4.10, the plot in fig. 5.2 suggests a more significant detection of this trend in the range  $M \gtrsim 10^{10} M_{\odot}/h$ . A direct comparison is difficult, since the methods of analyses differ. The lowest end, with  $M \lesssim 10^{10} M_{\odot}/h$ , in which void galaxies have lower spin parameters, is only measurable in the Bolshoi simulation.

We also find consistency with chapter 4 in seeing a trend for void galaxies to form later, in fig. 5.5. This analysis for the Bolshoi simulation is unfortunately only restricted to a small fraction of the simulated galaxies, the central galaxies per halo, in contrast to the chapter 4 analysis, which is for all galaxies. A followup analysis, estimating the formation epoch of all galaxies based on the data of the merger-trees, might turn out to be feasible and would then yield a more robust result.

We cannot identify any trend in the disk scale length on the environment, in contrast to our earlier work. A credible hypothesis to explain the lower disk scale length found earlier for void galaxies is that this is a consequence of finding lower mass haloes in voids.

As a final result, we report a significantly increased amount of star formation for galaxies in denser environments for  $M \lesssim 10^{11} M_{\odot}/h$ . For the galaxies identified in underdense regions we have a decreased stellar mass ratio below the threshold mass, which is in agreement with previous works, e.g. see (Hoyle et al., 2005; Croton et al., 2005; Moorman et al., 2015). A likely explanation is merger events that trigger bursts in star formation in galaxies in denser environments. While haloes, and galaxies therein, in dense environments should have a rich history of merger events in their past, a galaxy in the low density environments, the most

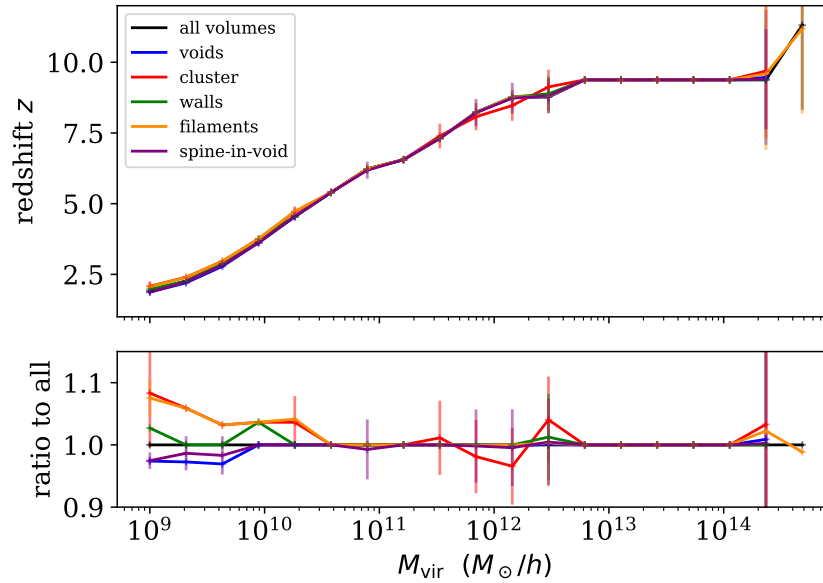


Figure 5.5: The formation redshift of central haloes identified in the Bolshoi simulation characterised by their environment in the large scale structure. The upper panel shows the mean of the full population divided in several bins in the virial mass while errors are estimated using the bootstrap method. The lower panel shows the quotient compared to all galaxies in the simulation.

extreme being a cosmic void, should, in general, pass through fewer merger events. Merger events are tracked in the merger-history tree and thus a follow-up analysis will enable us to verify this interpretation.

The results presented here complement the trends reported in chapter 4 and Peper & Roukema (2021) and underline that the environment should have a measurable effect on galaxy formation. As suggested before, the later formation epoch and the higher spin parameter might be hints that voids are a favourable environment for ultra-diffuse galaxies (UDGs) to form. Moreover, the lower stellar masses for galaxies in lower density environments also favours lower surface brightnesses for void galaxies.

# Chapter 6

## Detecting cosmic voids via maps of geometric optics parameters

### 6.1 Introduction

We discussed the effect of the environment in which a galaxy forms with specific emphasis on the environment of a cosmic void. A complementary aspect of the significance of voids is how they affect light propagation. The work in this chapter aims to investigate the geometric-optics effects on light propagation in a realisation of a matter distribution of a small volume of the Universe, using a higher particle resolution than that of chapter 4. This chapter largely follows the presentation in Peper, Roukema, & Bolejko (2023). The majority of the coding, the running of the code and much of the analysis were done by me.

Curved-spacetime geometric-optics maps derived from a deep photometric survey should contain information about the three-dimensional matter distribution and thus about cosmic voids in the survey, despite projection effects. We use the concepts derived in Sect. 2.3 to investigate four chosen quantities, namely the surface overdensity  $\Sigma$ , the averaged weak-lensing tangential shear  $\overline{\gamma}_{\perp}$ , the Sachs expansion  $\theta$ , and the Sachs shear modulus  $|\sigma|$  to explore to what degree sky-plane geometric-optics maps can reveal the presence of intrinsic three-dimensional voids.

Spectroscopic redshifts to determine the (comoving) three-dimensional structures of cosmic voids require much more telescope resources than photometric surveys alone. While the simplest interpretation of a (single-filter) photometric survey is that it shows only the projected galaxy positions and shapes on the sky, the fact that the Universe is inhomogeneous implies that the photometric map contains information on the three-dimensional distribution of inhomogeneities, with effects that are generically referred to as gravitational lensing. Gravitational lensing theory was developed many decades ago in its generic form of geometric optics (Sachs, 1961; Sasaki, 1993), and gravitational lensing by overdensities was detected with the twin quasar QSO 0957+561 A/B in 1979 (Walsh et al., 1979; Young et al., 1980; Gorenstein et al., 1984, 1988), and with giant luminous arcs (Paczynski, 1987) and an Einstein cross (Adam et al., 1989), providing visually striking evidence favouring general relativity. For an in-depth review, see Bartelmann & Schneider (2001). Here, we argue that geometric-optics parameters that are derived from a deep photometric extragalactic map should contain information that can be used to detect some of the physical, three-dimensional cosmic voids in the map, despite the fact that the voids are projected on the sky plane together with foreground and background voids. By carrying out a full  $N$ -body simulation and analysing it, using an *a priori* reproducible software method, we aim to explore to what degree maps of photometrically derived geometric-optics parameters can reveal intrinsic three-dimensional voids. We consider both the conventional approximation of weak-

lensing parameters and Sachs optical scalars derived directly from the evolving gravitational potential.

We discussed cosmic voids, how to detect them using the watershed mechanism and the cosmic web in Sections 2.2.2 & 3.3. Watershed void finders, such as ZOBOV and SPINE that were used above (e.g. Neyrinck, 2008; Aragón-Calvo et al., 2010b), make no assumptions on the shape of a void and are close to being parameter-free. Watershed finders have become a *de facto* standard for determining the shapes of cosmic voids. Multiple other strategies for detecting voids in either observations or simulations exist. Since voids consist of the absence of luminous matter rather than its presence, this is a challenging task. Void finders trace the underdense regions of the cosmic web. Early routines used the assumption of spherical structures (e.g. Kauffmann & Fairall, 1991b) to detect voids. This was justified from the theoretical description of a void evolving out of a tophat-filtered density fluctuation; ellipsoidal initial density profiles were found to generally evolve to become more spherical (Gunn & Gott, 1972; Lilje & Lahav, 1991; Sheth & van de Weygaert, 2004) (we briefly discuss this toy model in Sect. 3.3).

Watershed mechanisms detect local minima in the density distribution of the cosmic web and identify underdense structures by searching for successively higher density contours, effectively finding the overdense edges of voids. The properties of the resulting voids depend on the spatial number density of the tracer particles used to represent the matter distribution. Nadathur & Hotchkiss (2015a) show that randomly subsampling the density of dark matter particles will tend to bias the void statistics, and suggest the use of halo occupation distribution models instead. To apply a watershed void finder to observational galaxy data, spectroscopic redshifts are needed.

Sánchez et al. (2017) introduce a method of detecting voids from a multi-filter photometric survey by analysing redshift slices whose thickness is based on the photometric redshift uncertainties. The first detector variable that we analyse here results in a roughly comparable method. We detect structures in the surface overdensity, which, under the approximation of a constant mass-to-luminosity ratio, can be inferred from the observed photometric survey.

However, we are primarily interested in other sky-plane variables that can yield information on the large-scale structure of the Universe: the gravitational lensing signal. Due to the nature of dark matter having very weak interactions apart from gravity, we cannot measure the dark matter distribution of the Universe directly from electromagnetic surveys. Photometric galaxy surveys are generally thought to provide a fair proxy for the real projected matter distribution, but with many caveats. In contrast, the gravitational interaction of the dark matter distribution with photons can be measured via lensing effects. A light bundle that transverses a cosmological structure will experience shear and expansion and in particular, cosmic voids should leave an imprint on the shear and expansion. This should make it possible to reconstruct the underdensity field of voids based on the lensing signal, without no dependence on assumptions about baryon cooling or star formation. Large-scale maps of the gravitational lensing signal could thus, in principle, be used to detect cosmic voids. This would provide a method independent of using the projected spatial distribution of galaxies, since the lensing signal depends on the full underlying mass density, no matter whether it is luminous or not.

While in this work we consider lensing parameters that are measurable from source galaxies far beyond the voids that we aim to detect, other observational methods of constructing the lensing signal have been proposed. Lewis & Challinor (2006) argue that since the cosmic microwave background (CMB) is lensed, the lensing potential can be reconstructed based on the observed CMB power spectrum. Another method was proposed by Croft et al. (2018) to use Lyman  $\alpha$  forest observations to obtain lensing signals in the foreground of redshift slices of the forest.

In this work we consider the optimal scenario in which we calculate the detector variables without taking any detector errors into account. In reality, the derivation of the surface overdensity  $\Sigma$ , the averaged weak-lensing tangential shear  $\overline{\gamma}_{\perp}$ , the Sachs expansion  $\theta$ , and the Sachs shear modulus  $|\sigma|$  from observations involves many sources of random and systematic error, so the approach presented here will need further work to take those into account.

In this chapter, we present the software pipeline that was used to create Peper et al. (2023) (which aims to be fully reproducible on any unix-like operating system with sufficient RAM and disk space; Akhlaghi et al. 2021) to generate a cosmological  $N$ -body simulation, to detect galaxies and voids in it, and to ray-trace geometrics-optics parameters. The source package is provided as a frozen record at zenodo.7792910<sup>1</sup> and in live<sup>2</sup> and archived<sup>3</sup> GIT repositories.

In Sect. 6.2.1 we briefly describe our overall pipeline, extending that used in Peper & Roukema (2021). We describe our simulation geometry in Sect. 6.2.2. We first detect intrinsic three-dimensional voids using the watershed algorithm (Sect. 6.2.3). We independently try to detect voids in projection, “photometrically” (in the absence of spectroscopic and photometric redshift information), from either the surface overdensity, conventional weak-lensing or other geometric-optics signals. Our generic void profile search algorithm is defined in Sect. 6.2.3. We compare the sky-plane positions and radii of the photometric voids to those of the intrinsic three-dimensional voids, using Monte Carlo simulations to check if this association is better than random (Sect. 6.2.4). In Sect. 6.2.5 we present our four detector variables, including a modification of our default void profile search algorithm specific to the weak-lensing shear, in Sect. 6.2.5). We present our results in Sect. 6.3, discuss these in Sect. 6.4 and conclude in Sect. 6.5. The version of the source package that can be used to reproduce the results of this chapter is git commit e4f7af0, allowing downloading, configuring, compiling and running the full computational sequence. The specific realisation in this chapter was run on a computer with a Little Endian x86\_64 architecture.

## 6.2 Method

### 6.2.1 Software pipeline

We use a highly reproducible software pipeline, following the Maneage template for reproducibility (Akhlaghi et al., 2021), that generates a realistic distribution of galaxies using a succession of several different cosmological tools. The software pipeline extends the galaxy formation pipeline presented in chapter 4 presented Peper & Roukema (2021). The pipeline includes a full simulation chain, starting with the generation of initial conditions with `MPGRAFIC` and running an  $N$ -body simulation with `RAMSES` (Prunet et al., 2008; Teyssier, 2002). This simulation is processed as in Roukema et al. (1993, 1997), but using more recent software packages: dark matter haloes are detected and their merger-history tree is built with `ROCKSTAR` and `CONSISTENT-TREES` (Behroozi et al., 2013a,b) and semi-analytical galaxy formation recipes are applied with `SAGE` (Croton et al., 2016). We detect voids traced by the resulting spatial distribution of galaxies using a watershed void finder with `REVOLVER` (Nadathur et al., 2019). The coding of our sky-plane void-profile search algorithm (Sections 6.2.3 and Sect. 6.2.5) is original, as described in the paper in which this work is published (Peper et al., 2023). The full details of the analysis are provided in a live git repository<sup>2</sup> and a frozen Zenodo record<sup>1</sup>. We used fixed pseudo-random

<sup>1</sup><https://zenodo.org/record/7792910>

<sup>2</sup><https://codeberg.org/mpeper/lensing>

<sup>3</sup>swh:1:rev:b5dff23ab8ba8c758112d5fd3f737fb6f44cd6fe

seeds in most steps in the pipeline, as indicated in the configuration files. We now primarily focus on new steps that are added to the analysis presented in chapter 4.

## 6.2.2 Simulation geometry

Again, we use a simulation for a standard  $\Lambda$ CDM model (cold dark matter cosmological model with a cosmological constant  $\Lambda$ ) with Hubble constant  $H_0 = 70.0$ , current dark energy parameter  $\Omega_{\Lambda 0} = 0.7$  and current matter density  $\Omega_{m0} = 0.3$ ,  $N_{\text{part}} = 256^3$  particles and a comoving box size  $L_{\text{box}} = 120 \text{ Mpc}/h$ , where  $h := H_0/(100 \text{ km/s/Mpc})$ . This yields a dark matter particle mass of  $m_{\text{DM}} = 0.86 \times 10^{10} M_{\odot}/h$ . We require at least 10 particles to detect a halo. Since our simulated volume is a standard 3-torus ( $T^3$ ) simulation, we detect dark matter haloes, generate a merger-history tree and detect intrinsic voids by interpreting the simulation's spatial section as  $T^3$ .

For computational convenience, for the ‘‘observational’’ steps in which we detect voids in a sky-plane map of a detector variable, we interpret the (projected or ray-traced) simulated volume as the fundamental domain of a 2-torus ( $T^2 := S^1 \times S^1 \times \mathbb{R}$ ), where the two multiply connected directions lie in the sky plane. We informally refer to the fundamental domain as the ‘‘box’’. The foreground and background of the box, at lower and higher redshifts, respectively, are implicitly assumed to be a homogeneous (structure-free), simply connected  $\Lambda$ CDM background, i.e., they are assumed to be transparent and flat, with no effect on gravitational lensing. This simplification helps focus on the primary questions of our analysis; future analyses should include the effects of the full past time cone. We assume that this box is observed at high redshift,  $z' = 0.5$ , corresponding to a large distance from the observer compared to the box size,  $\chi_0 := 1322.0 \text{ Mpc}/h$  in comoving units. We use both an observer-centred Euclidean comoving coordinate system, with the observer at  $(x,y,z) = (0,0,0)$  and the centre of the simulated volume on the  $y$  axis of the  $\Lambda$ CDM simply connected space at  $(0,\chi_0,0)$ , and a simulation-centred system shifted by  $\chi_0$ . To model light rays detected by the observer we convert  $(x,y,z)$  to  $(x = \chi \sin \theta' \cos \varphi', y = \chi \sin \theta' \sin \varphi', z = \chi \cos \theta')$ , where  $\chi$ , the comoving radial distance, together with  $\theta' \in [0,\pi]$  and  $\varphi'$  are spherical coordinates of the spatial part of a flat  $\Lambda$ CDM model, and the simulation's centre is at  $(\chi = \chi_0, \theta' = \pi/2, \varphi' = \pi/2)$ . We compute each of our detector variables on a grid with  $N_{\text{grid}} = 120^2$  ‘‘pixels’’ that we place on the middle plane of the box ( $y = 1322.0 \text{ Mpc}/h$ ), at  $(x,z)$  positions in the grid. We model light rays emitted from an observer-centred spherical surface near the back face of the simulated box ( $T^2$  slice), through to a second observer-centred spherical surface close to the front face of the box. The light rays's spatial paths are assumed to be straight in the non-perturbed space, i.e. with constant  $\theta'$  and  $\varphi'$ . We avoid approximately 5% of the front and back parts of the box to minimise edge effects. Projected variables for a given pixel are computed along the line of sight of a light ray passing from the back spherical surface, through the pixel, to the front spherical surface. In other words, the grid approximately corresponds to what is often referred to as ‘‘the sky plane’’ for small solid angles, although it is (in this construction) a genuinely flat plane in comoving space. For brevity, we will use the term ‘‘sky plane’’ as equivalent to this grid.

For the optical scalar calculations (Sect. 6.2.5), we trace our light rays geometrically under the assumption of a flat  $\Lambda$ CDM model, but calculate the optical scalars with a longitudinal Newtonian gauge approximation of an inhomogeneous model, with the line element

$$ds^2 = a^2 \left[ -(1 + 2\Phi)d\tau^2 + (1 - 2\Phi) \left( d\chi^2 + \chi^2 d\Omega^2 \right) \right], \quad (6.1)$$

where  $\tau$  is conformal time,  $\Phi$  is a potential, and  $d\Omega$  is the solid spherical angle element  $(d\theta')^2 + (\cos \theta' d\varphi')^2$ .

Table 6.1: Parameters used in our two-dimensional void detection algorithm in Eqs (6.6) and (6.7).

	$f_{\text{std}}$	$f_{\text{mean}}$
$\Sigma$	0.50	1.50
$\theta$	0.30	1.30
$\sigma$	0.30	1.10

### 6.2.3 Void detection

#### Intrinsic three-dimensional voids

We detect intrinsic voids traced by the galaxy population using the void finder `REVOLVER`, which is based on the watershed void finder `ZOBOV` (Neyrinck, 2008; Nadathur et al., 2019) discussed in Sect. 3.3. The watershed mechanism in `ZOBOV` uses a Voronoi tessellation to estimate the densities at the particles’ positions, is nearly parameter-free and makes no assumptions on the shape of the void. To characterise the size of a void, we use the effective radius  $R_{\text{eff}}$ , which is based on the sum over the volumes  $V_i$  of all the Voronoi cells that constitute a void, i.e.  $R_{\text{eff}} := \frac{3}{4\pi} (\sum_i V_i)^{1/3}$ . We adopt the geometric centroid of the set of cells that constitute an intrinsic void as the centre of that void. This is called the “barycentre” in the `REVOLVER` code, but is mathematically the barycentre only if the void is assumed to be filled with a uniform density fluid (Peper & Roukema, 2021, Sect. 1).

#### Photometric void detection

We detect voids from variables in the sky plane that are, in principle, observationally measurable in photometric surveys: the surface overdensity  $\Sigma$ , and three geometric-optics related parameters. We propose the following heuristically derived algorithm for detecting a projected void in a map of the surface overdensity  $\Sigma$  (defined below in Sect. 6.2.5) or the Sachs (1961) expansion  $\theta$  or shear  $\sigma$  (optical scalars, defined below in Sect. 6.2.5). Our algorithm for detecting voids from maps of the weak-lensing shear  $\gamma$  is similar, but differs in the ways that are described below in Sect. 6.2.5.

In contrast to the case for overdense extragalactic objects, we expect the (azimuthally averaged) radial density profile of a void in the sky plane, where the radius is  $r := \sqrt{(x - x_0)^2 + (z - z_0)^2}$  in our  $(x, z)$  grid for an object centre  $(x_0, z_0)$ , to have its lowest values in the centre of the void and a sharp maximum at the void’s edge. The Sachs expansion  $\theta$  and shear  $\sigma$  should also have a minimum at the centre of a void and a maximum at the edge. While projection effects for overdense structures are a perennial problem in astronomy (e.g. for determining whether a galaxy group is dynamically real or a chance projection), the projection effects can be expected to be much worse for voids, since voids dominate the volume of the Universe, implying stronger overlaps. In contrast to overdense objects, spectroscopic redshift determination for the rare galaxies in voids is unlikely to be effective in separating a chance projection of voids from a void that is real in three spatial dimensions, and is likely to be a statistically unstable way of dynamically characterising a void. Moreover, voids, in general, are not perfectly spherical objects, making detection via templates unlikely to be easy. Nevertheless, projection along the line of sight should provide a modest effect of symmetrisation, and by appropriately averaging, we hypothesize that detection is feasible.

We define an isotropised (azimuthally averaged) variable  $\bar{X}$ , i.e. the average on a circle in

the  $(x, y \equiv \chi_0, z)$  grid plane, at radius  $r$  and centred on a pixel  $j$ , i.e.

$$\bar{X}_j(r) = (2\pi)^{-1} \int_0^{2\pi} X(r, \varphi) d\varphi, \quad (6.2)$$

where  $\varphi$  is the angle around the circle centred on position  $j$  in the grid and  $X$  is either the surface overdensity  $\Sigma$ , or one of the optical scalars  $\theta$  or  $\sigma$  (for the weak lensing shear  $\gamma$ , see Eq. (6.15) below). To estimate  $\bar{X}_j(r)$ , we sample the grid values at even intervals around a circle of radius  $r$ , with intervals that give at least one value per Mpc/h, we smooth the values with a third-order Savitzky–Golay filter (Savitzky & Golay, 1964), and integrate.

We also define a disc-averaged profile  $\bar{\bar{X}}$  on the disc internal to a given radius (not weighted by the radius) by integrating Eq. (6.2) and appropriately normalising, i.e.

$$\bar{\bar{X}}(r) = \frac{\int_0^r \int_0^{2\pi} X(r', \varphi) d\varphi dr'}{(2\pi)^{-1} \int_0^r \int_0^{2\pi} d\varphi dr'} = \frac{\int_0^r \bar{X}(r') dr'}{r}, \quad (6.3)$$

and a disc-averaged absolute slope,

$$\left| \bar{\bar{X}}' \right|(r_i) = \frac{\sum_{i' < i} \left| d\bar{X}/dr \right|(r_{i'})}{i - 1}, \quad (6.4)$$

where the index  $i$  indicates radial discretisation in estimating  $\bar{X}$  and  $\bar{X}' := d\bar{X}/dr$ .

Apart from the case of the weak-lensing shear  $\gamma$  (Sect. 6.2.5), we expect  $\bar{X}$  (and thus  $\bar{\bar{X}}$ ) to increase monotonically from the centre at  $r = 0$  outwards as  $r$  increases, though the projection against other voids, voids' asphericity, and noise will make this monotonicity difficult to detect. For each pixel  $j$  in our sky plane, we define a heuristic selection criterion  $\eta_X$  motivated by the expected monotonicity as follows.

- (i) Ignore each pixel  $j$  with  $X(r = 0) > X_{\text{median}}$ , where  $X_{\text{median}}$  is the median over all pixels in the sky plane. The motivation is that for any  $X$ , pixels with  $X(r = 0) > X_{\text{median}}$  are unlikely to correspond to the centre of a void. The projected or ray-traced variables  $X$  should have their minima at voids' centres. This step should remove many pixels unlikely to be void centres.
- (ii) For a given pixel  $j$ , for each radial distance  $r_i$  from the pixel, calculate the circular average  $\bar{X}$  as in Eq. (6.2), where for simplicity we omit the subscript  $j$ . We set the interval in  $r_i$  to be smaller than 1 Mpc/h in order to be sensitive to small-scale structure.
- (iii) A persistently positive strong positive slope in  $\bar{X}$  is detected as follows. Find  $i_1$ , the first radial position  $i$ , with respect to pixel  $j$ , where all three of the conditions

$$\bar{X}'(r_i) > \left| \bar{\bar{X}}' \right|(r_i) \quad (6.5)$$

$$\bar{X}(r_i) - \bar{X}(r_{i-1}) > f_{\text{std}} \left\langle \left( \bar{X}(r_{i'}) - \bar{\bar{X}}(r_{i'}) \right)^2 \right\rangle_{i' < i}^{1/2} \quad (6.6)$$

$$\bar{X}(r_i) > f_{\text{mean}} \bar{\bar{X}}(r_i) \quad (6.7)$$

are satisfied over four successive steps  $i - 3, i - 2, i - 1, i$ , where  $\langle \cdot \rangle$  is the mean and  $f_{\text{std}}$  and  $f_{\text{mean}}$  are heuristically chosen fractions. The aim of criteria (6.5) and (6.6) is to find a



range of radii where the slope  $\bar{X}'$  has a stable and significant increase, i.e. where positive second derivatives  $\bar{X}'' > 0$  are numerically persistent. Criterion (6.7) aims to also require the slope  $\bar{X}'$  to be sufficiently positive. The values adopted for  $f_{\text{std}}$  and  $f_{\text{mean}}$  are given in Table 6.1.

- (iv) Find  $i_2$ , the first local maximum in  $\bar{X}$  for  $i > i_1$ , i.e., the first local maximum after the persistently strong positive slope condition that determines  $i_1$ .
- (v) Define an initial void selection criterion  $\eta_X^0(j) := 1/r_{i_2}$ . The radius  $r_{i_2}$  is the estimated radius of the candidate void.
- (vi) Steps 2–5 are carried out for all pixels  $j$  accepted in step 1 (with 3, 4 modified in the case of  $\gamma$ ; see Sect. 6.2.5). In order to cope with the very noisy data, we define a smoothed selection criterion for further use,  $\eta_X(j)$ , as a low-pass triangular filter (weighted mean) of the 25  $\eta_X^0(j)$  values in a  $5 \times 5$  grid of pixels centred on pixel  $j^4$ .

We then find all local minima of the selection criterion  $\eta_X(j)$  over the pixels  $j$  as follows.

- (vii) We select a void centred at pixel  $j$  if it dominates its local region in the sense that  $\eta_X(j) < \eta_X(k)$  where  $k$  indexes pixels in a square grid centred on pixel  $j$  and extending 5 pixels in each of the  $\pm x$  and  $\pm z$  directions. As an extra credibility criterion, selection of a void is only accepted if  $\eta_X(j) < 0.90 \sum_k \eta_X(k) / \sum_k 1$ , where  $k$  indexes all pixels in the map.

This algorithm results in a list of projected voids with centres  $j$  and radii  $r_{i_2}(j)$  that represent the largest locally credible voids.

- (viii) To avoid cases where a single genuine void is misidentified as two slightly offset voids, we check if two or more centres are closer to one another than

$$\min \{R(j_1)/4, R(j_2)/4, 10.0 \text{ Mpc}/h\} . \quad (6.8)$$

In these cases, we merge these voids into a single void. The new centre and radius of the merged void are defined as the mean of the centres and radii of the unmerged voids.

## 6.2.4 Matches to intrinsic voids

To quantify whether the photometric detection of voids – two-dimensional voids – successfully finds the intrinsic three-dimensional voids, we first define a heuristically motivated matching criterion to find the best matches, and then compare the set of best matches to an equivalent set of best matches when the list of two-dimensional void parameters is generated randomly (positions) or randomly shuffled (radii). This aims at answering two different questions: (i) given a detected set of two-dimensional voids, are these better than a random set of two-dimensional voids at revealing true three-dimensional voids? (ii) given a set of intrinsic three-dimensional voids, do the detected two-dimensional voids better match these (numerically) real voids better than a random set of two-dimensional voids would? The former question is interesting for observational detection of three-dimensional voids from photometric or other geometric-optics data; the latter is interesting for using spectroscopically defined three-dimensional voids to motivate searches for gravitational lensing by voids.

---

<sup>4</sup>This step interprets the box as an isolated box, not  $T^2$ , and sets  $\eta_X(j)$  near the borders of the box to a high value to prevent finding minima there.

**Best matches and median sky-plane separation  $\mu_{x,z}$** 

We define the probability of the  $i$ th two-dimensional void being a match to the  $j$ th three-dimensional (watershed) void by first defining the probabilities that the  $x$  and  $z$  positions are close in the  $T^2$  sense and that the radii are logarithmically close. We set a cumulative Gaussian probability that the  $x$  or  $z$  positions for variable  $X \in \{\Sigma, \gamma, \theta, \sigma\}$  are closer to each other than the estimated values,

$$\begin{aligned} P_{x_i,j}^X &= 1 - \operatorname{erf} \frac{d(x_i^X, x_j^X)}{\sqrt{2} \sigma_x} \\ P_{z_i,j}^X &= 1 - \operatorname{erf} \frac{d(z_i^X, z_j^X)}{\sqrt{2} \sigma_z}, \end{aligned} \quad (6.9)$$

where  $\operatorname{erf}$  is the error function,  $d(\dots)$  is the  $T^2$  minimum  $x$  or  $z$  distance, and  $\sigma_x = \sigma_z = 5.0 \text{ Mpc}/h$ . Similarly, we set

$$P_{R_i,j}^X = 1 - \operatorname{erf} \frac{\left| \log_{10} \left( R_i^X / R_j^X \right) \right|}{\sqrt{2} \sigma_{\log_{10} R}}, \quad (6.10)$$

where  $\sigma_{\log_{10} R} = 0.30 \text{ dex}$  (Allen, 1951). These are assumed, for simplicity, to be independent probabilities, giving a heuristic overall probability that the  $i$ th two-dimensional void matches the  $j$ th three-dimensional void

$$P_{i,j}^X = P_{x_i,j}^X P_{z_i,j}^X P_{R_i,j}^X. \quad (6.11)$$

For question (i) (Sect. 6.2.4), given a two-dimensional void  $i$ , we find the three-dimensional void  $j$  with the highest matching probability  $P_{i,j}^X$ , for detector variable  $X$ . This does not exclude the possibility that two different two-dimensional voids best identify with the same three-dimensional void. For a set of  $N_{2D}$  detected two-dimensional voids, this gives us a matched set of  $N_{2D}$  objects, which have both two-dimensional and three-dimensional sky position and radius information, presumed to match.

For each object in this set, we calculate the  $T^2$  distance between the two-dimensional and three-dimensional  $(x,z)$  positions and from the distribution of these values, calculate  $\mu_{x,z}(3D|2D)$ , the median distance for a three-dimensional match given a two-dimensional match. In calculating this median, in cases where a single three-dimensional void is the best match for two or more two-dimensional voids, we only consider the match in which  $P_{i,j}^X$  is maximised.

For question (ii), given a three-dimensional void  $i$ , we find the two-dimensional void  $j$  with the highest matching probability  $P_{i,j}$ . Again, this does not exclude the possibility that two different three-dimensional voids best identify with the same two-dimensional void. In practice, since we find fewer two-dimensional voids to three-dimensional voids, there are necessarily cases where multiple three-dimensional voids identify with a single two-dimensional void. For a set of  $N_{3D}$  detected three-dimensional voids, this gives us a matched set of  $N_{3D}$  objects, which have both two-dimensional and three-dimensional sky position and radius information, presumed to match.

For each object in this set, we calculate the  $T^2$  distance between the two-dimensional and three-dimensional  $(x,z)$  positions and infer  $\mu_{x,z}(2D|3D)$ , the median distance for a two-dimensional match given a three-dimensional match, again using the highest  $P_{i,j}^X$  to reduce non-one-to-one matches.

### Comparison to matches for random two-dimensional voids

We generate a Monte Carlo simulation of two-dimensional voids by choosing  $N_{2D}$  pairs  $(x, z)$  from a uniform random distribution within the  $x$  and  $z$  ranges of the two-dimensional grid. For both questions (i) and (ii) (separately), for each Monte Carlo simulation, we find matched sets using the same algorithm as above.

To answer question (i) we estimate  $\mu_{x,z}(3D|2D)$  for a given detector  $X$ , for both the original matched set and for each of the simulated matched sets. This yields  $P_{x,z}^X(3D|2D)$ , the frequentist probability that the original  $\mu_{x,z}(3D|2D)$  is less than  $\mu_{x,z}(3D|2D)$  from the Monte Carlo simulations. In other words,  $P_{x,z}^X(3D|2D)$  is the probability that, given the two-dimensional voids, the matches with three-dimensional voids in the sky plane are no better than those drawn from a Monte Carlo simulation.

Similarly, for question (ii), the frequency with which the original  $\mu_{x,z}(2D|3D)$  is less than the values of  $\mu_{x,z}(2D|3D)$  from the simulations yields  $P_{x,z}^X(2D|3D)$ , the probability that, given the three-dimensional voids, the matches with two-dimensional voids in the sky plane are no better than those drawn from a Monte Carlo simulation of sky positions.

Cases where three-dimensional voids are concentric or approximately overlap in projection will yield only a single two-dimensional void using our algorithm, and are likely to make estimation of the radii difficult. The range of values of the radii are not as conveniently constrained as the  $(x, z)$  centres of the voids. Rather than choosing an arbitrary range for a Monte Carlo simulation, we use a non-parametric method. We define  $P_R^X(3D|2D)$  as the two-sided probability that the Spearman  $\rho$  rank correlation coefficient (Spearman, 1904) of the matched set of  $N_{2D}$  values  $R_i^X$  and  $R_{j(i)}^X$  is stronger (positive or negative) than what it would be for a set of paired values where one set is randomly permuted.

Similarly, we define  $P_R^X(2D|3D)$  as the two-sided probability that the Spearman  $\rho$  ranking coefficient of the matched set of  $N_{3D}$  values  $R_i^X$  and  $R_{j(i)}^X$  is stronger (positive or negative) than it would be under random permutations.

### 6.2.5 Detector variables $\Sigma, \gamma, \theta, \sigma$

Here we define and describe our detector variables  $X \in \{\Sigma, \gamma, \theta, \sigma\}$ , where here we write the generic forms of these variables for simplicity; the more specific forms are given below. These detector variables can, in principle, be derived from a photometric map, given some minimal assumptions, such as a mass-to-light ratio in the case of the surface overdensity  $\Sigma$ , or statistically isotropic distributions of galaxy shape parameters in the case of the other three parameters. We derive each of these from the particle distribution, not from the galaxy distribution. We include  $\Sigma$  since apart from requiring a mass-to-light ratio assumption, it is the simplest to derive from a photometric map.

#### Surface overdensity $\Sigma$

We calculate the surface overdensity by integrating the overdensity  $\rho - \bar{\rho}$  along the line of sight, neglecting temporal evolution. (Temporal evolution is taken into account with the optical scalar modelling; see Sect. 6.2.5 below.) Densities are constructed for each particle using a Voronoi tessellation followed by linear interpolation. For a flat model, the surface overdensity in direction  $\hat{n}$ , analog to eq.(2.80), is

$$\Sigma(\hat{n}) = \int_{\chi_{\min}}^{\chi_{\max}} (\rho(\hat{\chi}, \Omega) - \bar{\rho}) d\chi, \quad (6.12)$$

where  $\chi_{\min} = \chi(z_O) - 0.95L_{\text{box}}/2$  and  $\chi_{\max} = \chi(z_O) + 0.95L_{\text{box}}/2$ . The 0.95 factor neglects the 5% front and back parts of the box to minimise edge effects (Sect. 6.2.2). Since we expect the surface overdensity  $\Sigma$  to be negative in a void, we aim to detect it in places where it is physically a surface underdensity, i.e., a projected mass deficit.

**Detection strategy with  $\Sigma$**  Voids typically have strong underdensities in their interior, so the two-dimensional projection of a void should still show a strong underdensity in the interior after projection. Thus, we search for local minima in  $\Sigma$ .

The projection of foreground and background voids and their walls (in reality, clusters, filaments and walls) will, to some degree, obscure this search. To the extent that the obscuration can be statistically neglected or removed, the azimuthally averaged radial profile  $\bar{\Sigma}$  (Eq. (6.2)) should show a slow increase in  $\bar{\Sigma}$  from the centre of a projected void outwards until it nears the (projected) wall, when a rapid increase should occur, followed by a drop as  $\bar{\Sigma}$  asymptotes to the mean of the environment surrounding the void. Thus, a local maximum in  $\bar{\Sigma}$  at the wall that surrounds the void should be sought. We expect that larger voids should yield clearer signals.

Some pixels, likely containing galaxy clusters or projections of galaxy filaments, were found to be highly overdense, misleading our algorithm's search for void walls because of these overdense pixels' strong influence on  $\bar{\Sigma}$ . To reduce the influence of these extreme pixels, prior to step 1, we truncate  $\Sigma$  values at the 90th percentile of their distribution.

Substructures of overdensities exist inside of voids, similar to the larger scale overdensities of the cosmic web, but traced by dark matter haloes of much lower mass (Gottlöber et al., 2003). These substructures contribute another obscuring factor that should weaken our proposed detection algorithm (Sect. 6.2.3) using  $\Sigma$ .

### Weak-lensing tangential shear $\bar{\gamma}_{\perp}$

Weak gravitational lensing information is typically extracted from observations by using the distortion of observed images that is induced by cosmological inhomogeneity, with the aim of tracing the spatial distribution of dark matter. We follow the mathematical descriptions of Bartelmann & Schneider (2001); Krause et al. (2013) and Kilbinger (2015), broadly discussed in Sect. 6. For completeness and clarity we give the main equations here again. We derive the parameters of this idealised model from the surface overdensity calculated in our cosmological simulation.

We represent the lens plane, see Fig.2.5 adapted from (Bartelmann & Schneider, 2001, fig. 11), with two orthogonal spatial directions with indices  $a$  and  $b$ ; the direction of propagation of the light bundle as it would arrive at the observer from the source if unlensed, represented as a vector in the lens plane,  $\Theta_S$ ; and the direction at which the light bundle reaches the observer after lensing, again a vector in the lens plane,  $\Theta_O$ . A matrix to convert from the observed directions to the original source directions, the ‘‘deformation matrix’’ (Hossen et al., 2022),  $A$  is defined as the Jacobian as in eq.(2.86). The deformation matrix can be decomposed into the shear  $\gamma$  and the convergence  $\kappa$ , see eq.(2.88) (Bartelmann & Schneider, 2001, eq. (3.11)). In this work we assume that the rotation of the image vanishes and rewrite the deformation matrix as

$$A = \begin{pmatrix} 1 - \kappa - \gamma_1 & \gamma_2 \\ \gamma_2 & 1 - \kappa + \gamma_1 \end{pmatrix}. \quad (6.13)$$

The convergence  $\kappa$  at a generic position in the sky plane can be evaluated, similar to eq.(2.83), as  $\kappa(\hat{n}) = \frac{\Sigma(\hat{n})}{\Sigma_{\text{crit}}}$ , where  $\Sigma_{\text{crit}} = \frac{c^2}{4\pi G} \frac{D_{\text{OS}}}{D_{\text{OL}}D_{\text{LS}}}$  (Bartelmann & Schneider, 2001, eq. (3.7)). The values

$D_{XX}$  are the angular diameter distances between the observer (O), the lens (L) and the source (S). We do not attempt void detection with  $\kappa$ , as the result would be equivalent to using  $\Sigma$ .

For our detection strategy, we use  $\bar{\Sigma}(r, \hat{n})$ , the isotropised (ring averaged) form of  $\Sigma$  (Eq. (6.2)) with respect to a given centre  $\hat{n}$  of a possible void, and subtract it from the surface overdensity averaged within a disc centred on  $\hat{n}$ , yielding

$$\Delta\Sigma(r, \hat{n}) := \tilde{\Sigma}(r, \hat{n}) - \bar{\Sigma}(r, \hat{n}), \quad (6.14)$$

where  $\tilde{\Sigma}(r, \hat{n})$  is defined in Eq. (6.16). As in Krause et al. (2013, eqs (4), (5)) and starting from eq.(2.91) also derived in Kilbinger (2015, eqs (40)–(47)), the mean of the tangential component of the shear internal to a ring at  $r$  can then be evaluated as

$$\bar{\gamma}_{\perp}(r, \hat{n}) = \frac{\Delta\Sigma(r, \hat{n})}{\Sigma_{\text{crit}}}, \quad (6.15)$$

where we leave the weak dependence of  $\Sigma_{\text{crit}}$  on  $r$  and  $\hat{n}$  implicit. The disc average  $\tilde{\Sigma}$  calculated by integrating (6.2) over the radius, using the usual weighting and now leaving the centre  $\hat{n}$  implicit, is

$$\tilde{\Sigma}(r) = \frac{\int_0^r \int_0^{2\pi} \Sigma(r', \varphi) r' d\varphi dr'}{\int_0^r \int_0^{2\pi} r' d\varphi dr'} = \frac{2\pi \int_0^r \bar{\Sigma}(r') r' dr'}{\pi r^2}. \quad (6.16)$$

**Detection strategy with  $\bar{\gamma}_{\perp}$**  By definition,  $\bar{\gamma}_{\perp}(r)$  should be close to zero at  $r = 0$ , the centre of a void, and should decrease to a sharp minimum where  $r$  is the radius of the void's (statistical) wall. At greater radii, both the azimuthally averaged surface overdensity  $\bar{\Sigma}$  and the disc-averaged  $\tilde{\Sigma}$  should approach zero, so  $\bar{\gamma}_{\perp}(r)$  should also increase up to zero. The minimum in  $\bar{\gamma}_{\perp}(r)$  should reveal the edge of the void.

Since this qualitative behaviour of  $\bar{\gamma}_{\perp}(r)$  differs from the other detector variables considered, we modify steps 3 and 4 of the algorithm of Sect. 6.2.3 as follows.

Since  $\bar{\gamma}_{\perp}$  and  $\bar{\gamma}_{\perp}'$  calculated according to (6.2) are noisy, we apply extra smoothing, replacing  $\bar{\gamma}_{\perp}(r_i)$  and  $\bar{\gamma}_{\perp}'(r_i)$  by  $\langle \bar{\gamma}_{\perp}(r_i) \rangle_{\{\max(0, i-3), \dots, i+3\}}$  and  $\langle \bar{\gamma}_{\perp}'(r_i) \rangle_{\{\max(0, i-3), \dots, i+3\}}$ , respectively. This smoothing reduces the role of local fluctuations in the dark matter distribution.

(iii') After this smoothing, we search for the radial distance where  $\bar{\gamma}_{\perp}$  starts dropping sharply, i.e. the index  $i_1$  is the first value  $i$  where  $\bar{\gamma}_{\perp}(r_i) < \bar{\gamma}_{\perp}(r_{i-1})$ .

(iv') The radial distance just past the wall is sought as the radial distance where  $\bar{\gamma}_{\perp}$  increases sharply, i.e. the index  $i_2$  is the first value  $i > i_1$  where  $\bar{\gamma}_{\perp}(r_i) > \bar{\gamma}_{\perp}(r_{i-1})$ .

(iv'.1) In addition, to remove choices of a void centre where the best ‘‘wall’’ found this way has a weak density contrast, we dismiss the candidate detection if  $|\bar{\gamma}_{\perp}| / \max(|\bar{\gamma}_{\perp}|) < 0.1$ . For patterns in  $\bar{\gamma}_{\perp}$  that have almost no significant features, this criterion avoids interpreting a nearly flat curve  $\bar{\gamma}_{\perp}(r_i)$  as a candidate void.

If both  $r_{i_1}$  and  $r_{i_2}$  are detected, then we continue to step 5 as above (Sect. 6.2.3). Even if pixel  $j$  is correctly centred on a void's centre, this algorithm for  $\bar{\gamma}_{\perp}$  can fail to detect  $r_{i_2}$  if the (projected) environment just outside the void's wall includes strong fluctuations. In the case of failure to detect  $r_{i_2}$ , the pixel is considered invalid at step 5 and dropped from further consideration.

**Optical scalars  $\theta$  and  $|\sigma|$** 

Similar to the general derivation in Sect. 6 we calculate optical scalars in this work following Sasaki (1993). In principle, these should model the real Universe more accurately than the weak-lensing approach described above, since fewer assumptions are required. In the Newtonian approximation, the Ricci tensor can be written as

$$R_{00} \approx 8\pi G\rho\omega^2 \quad (6.17)$$

and the Weyl tensor components of interest are

$$C_{A0B0} \approx (2\Phi_{;AB} - \delta_{AB}\Phi_{;C}^C)\omega^2 \quad (6.18)$$

$$= (2\Phi_{;\mu\nu}e_A^\mu e_B^\nu - \delta_{AB}\delta^{CD}\Phi_{;\mu\nu}e_C^\mu e_D^\nu)\omega^2, \quad (6.19)$$

(Sasaki, 1993, eqs (3.22), (3.21)) where  $G$  is the gravitational constant; space and time units are related by  $c = 1$ ;  $\rho$  is density;  $\Phi$  is the gravitational potential;  $\omega = -k_\mu u^\mu = 1 + z_{\text{redsh}}$ , for an observer four-velocity  $u^\mu$ , light propagation one-form  $k_\mu$ , and redshift  $z_{\text{redsh}}$ ;  $\{e_A, e_B\}$  or  $\{e_C, e_D\}$  are a pair of dyad basis vectors; and  $\delta_{AB}$  is the Kronecker delta ( $\delta_{AB} = 1$  if  $A = B$ ,  $\delta_{AB} = 0$  if  $A \neq B$ ). The dyad basis vectors  $e_A, e_B$  span the spacelike 2-plane that is orthogonal to the spatial path of the light ray that points from the observer towards the direction of a cell of the grid. We use the Gram–Schmidt method to construct  $e_A$  and  $e_B$ .

As derived in derived in eq.(2.106) the optical scalars – the expansion  $\theta$  (real) and the shear  $\sigma$  (complex) – are related to each other and the Weyl tensor (Eq. (6.19)) via the coupled pair of differential equations. For clarity we give the expressions used in this work here again

$$\frac{d}{dv}\theta = -R_{00} - 2|\sigma|^2 - \frac{1}{2}\theta^2 \quad (6.20)$$

and

$$\frac{d}{dv}\sigma = -(C_{1010} + iC_{1020}) - \sigma\theta. \quad (6.21)$$

For a visualisation of the effect of  $\theta$  and  $\sigma$  on a light bundle we refer to Sasaki (1993, Fig. 4), where  $\sigma = \sigma_+ + i\sigma_\times$ . The dependence of the optical scalars  $\theta$  and  $\sigma$  to the usual weak-lensing parameters is given in eqs (41)–(43) of Clarkson et al. (2012).

**Detection strategy with  $\theta$  and  $|\sigma|$**  Both the expansion  $\theta$  and the modulus of the shear,

$$|\sigma| = \sqrt{\text{Re}(\sigma)^2 + \text{Im}(\sigma)^2} \quad (6.22)$$

should be closely related to the surface overdensity, since integrations along paths approximately (spatially) orthogonal to the lens plane are performed in all three cases. However, these are not exactly analogous. Not only are these distinct physical quantities, but the overdensity integral is performed parallel to the  $y$  axis, while for each pixel in our two-dimensional grid plane, we estimate  $\theta$  and  $|\sigma|$  along a spatially straight path from the observer through the pixel, i.e. only approximately parallel to the  $y$  axis.

In practice, initial numerical exploration shows that  $\theta$  and  $|\sigma|$  behave qualitatively like  $\Sigma$ , in that they start from a low value at the centre of a void and increase to a sharp maximum at a void boundary. Thus, we use the same search algorithm for finding voids in maps of  $\theta$  and  $|\sigma|$  as indicated above in Sect. 6.2.3, with slightly adjusted parameters (Table 6.1). While qualitatively similar in numerical terms, the physical meanings of these parameters differ. The optical scalars

Table 6.2: Numbers of intrinsic three-dimensional voids detected with REVOLVER,  $N_{3D}$ , and in the two-dimensional grid,  $N_{2D}^\Sigma$ ,  $N_{2D}^\gamma$ ,  $N_{2D}^\theta$ , and  $N_{2D}^\sigma$ , using the surface overdensity  $\Sigma$ , the weak-lensing shear  $\overline{\gamma}_\perp$ , the Sachs expansion  $\theta$ , and the modulus of the Sachs shear  $|\sigma|$ , respectively.

$N_{3D}$	$N_{2D}^\Sigma$	$N_{2D}^\gamma$	$N_{2D}^\theta$	$N_{2D}^\sigma$
46	28	29	34	39

Table 6.3: Probability that the matches between three-dimensional and two-dimensional voids for detector variable  $X$  are no better than those of randomly generated two-dimensional voids,  $P_{x,z}^X(3D|2D)$  when given two-dimensional voids; or  $P_{x,z}^X(2D|3D)$  when given three-dimensional voids; and probability that the Spearman rank correlation coefficient for the radii of matched three-dimensional and two-dimensional voids for detector variable  $X$  could be that of a set of randomly paired values,  $P_R^X(3D|2D)$  when given a two-dimensional void; and  $P_R^X(2D|3D)$  when given a three-dimensional void. See Sect. 6.2.4. Plain-text version available at zenodo.7792910/void\_match\_analysis.dat.

$X$	$P_{x,z}(3D 2D)$	$P_{x,z}(2D 3D)$	$P_R(3D 2D)$	$P_R(2D 3D)$
$\Sigma$	0.017	0.00051	0.94	0.94
$\overline{\gamma}_\perp$	0.00053	$1.0 \times 10^{-5}$	0.77	0.93
$\theta$	0.00027	$1.0 \times 10^{-5}$	0.48	0.16
$ \sigma $	$9.0 \times 10^{-5}$	$1.0 \times 10^{-5}$	0.43	0.37

$\theta$  and  $|\sigma|$ , if derived from observations, represent the underlying matter distribution with no dependence on observed luminosity and without the simplifying assumptions of the weak-lensing approximation. In particular, the weak-lensing shear  $\overline{\gamma}_\perp$  (Eq. (6.15)) is an average defined with respect to a hypothesized void centre, while  $\theta$  and  $|\sigma|$  provide maps prior to assumptions about void centres.

## 6.3 Results

### 6.3.1 Simulation

We performed an *ab initio* simulation and detected voids as described above. As indicated in Table 6.2, we detected  $N_{3D} = 46$  voids in the galaxy population with the watershed mechanism, and smaller numbers of two-dimensional voids using  $\Sigma$ ,  $\overline{\gamma}_\perp$ ,  $\theta$ , and  $|\sigma|$  from the projected density distribution and by ray-tracing through the evolving gravitational potential  $\Phi$ .

Table 6.3 shows the probabilities, defined in Sect. 6.2.4, that quantify the significance of: (i) a detected two-dimensional void revealing the existence of an intrinsic three-dimensional void via its sky plane position or radius,  $P_{x,z}^X(3D|2D)$  or  $P_R^X(3D|2D)$ , respectively, and (ii) an intrinsic three-dimensional void implying that its two-dimensional projection is detectable,  $P_{x,z}^X(2D|3D)$  or  $P_R^X(2D|3D)$ . In each case, these represent the probability that the estimated correspondence between the populations could occur by chance, given prior information on the number of two-dimensional voids (for positions) or non-parametrically (for radii).

Since voids in  $N$ -body simulations are characterised by small numbers of particles, the detection of individual voids, whether in the three-dimensional galaxy distribution or by a two-dimensional detector in variables derived from the particle distribution, is in general numerically sensitive to small changes in machine arithmetic. We performed a small number of independent full-pipeline simulations, retaining the same pseudo-random number seed, to investigate this qualitatively. The re-simulated equivalent of the values listed in Table 6.3 shows moderate vari-

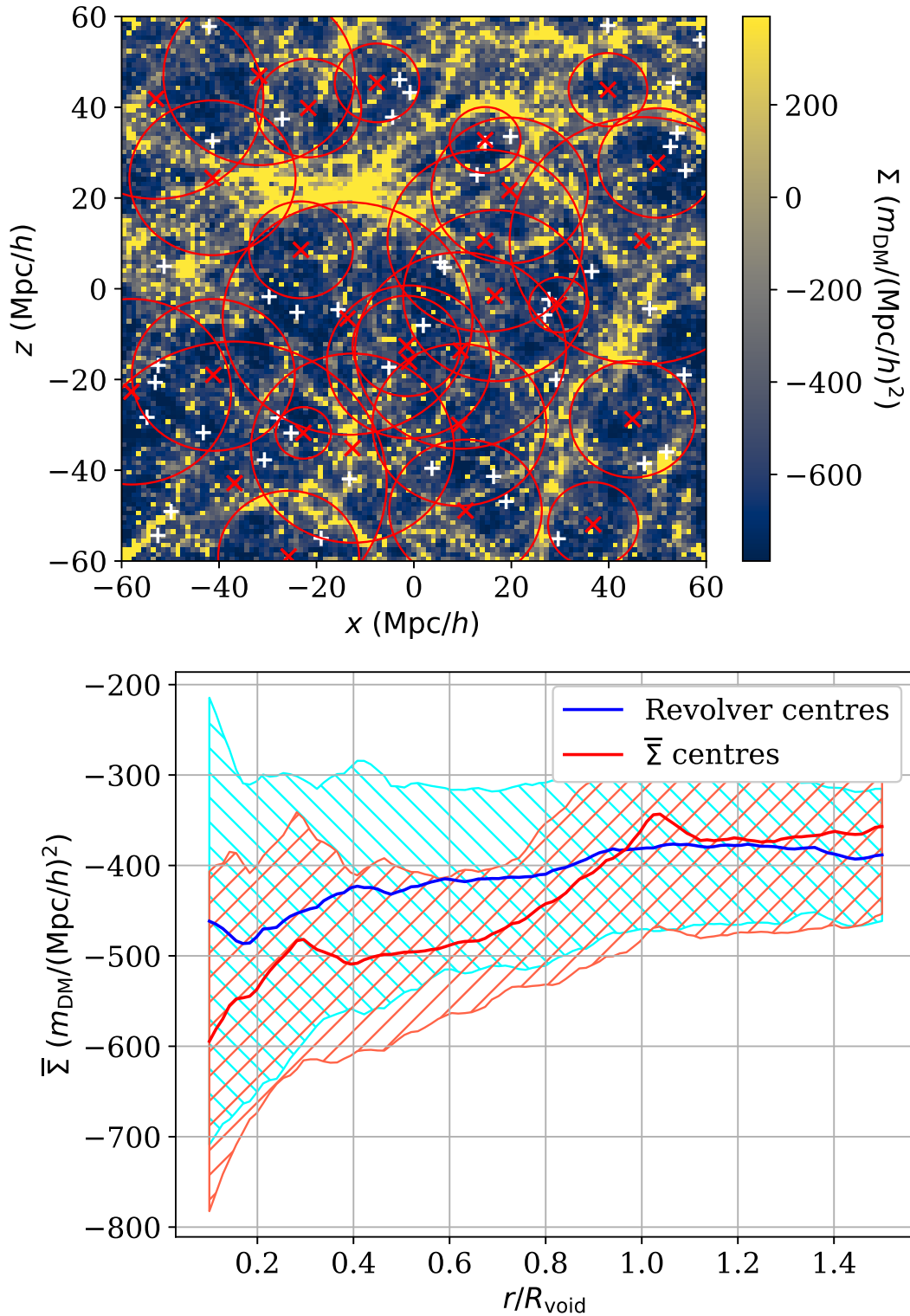


Figure 6.1: *Upper panel*: surface overdensity  $\Sigma$  projected along the line of sight. White + symbols represent the  $x, z$  centres of three-dimensional voids found with `REVOLVER`. Red  $\times$  symbols represent the centres of two-dimensional voids found in the surface overdensity (Sect. 6.2.5); red circles represent the walls of these (circular, by definition) voids. Some of the three-dimensional void centres are projected close to one another in the sky plane; our algorithm is not designed to distinguish these as independent voids. *Lower panel*: radial void profiles of the surface overdensity  $\bar{\Sigma}$  (Eq. (6.2)), normalised to the estimated void radius and then averaged, using the set of all (projected) three-dimensional void centres and radii (mean: blue curve; standard deviation: green “\” hatching; “Revolver centre”) or using the set of all two-dimensional void centres and radii (mean: red curve; standard deviation: red “/” hatching).



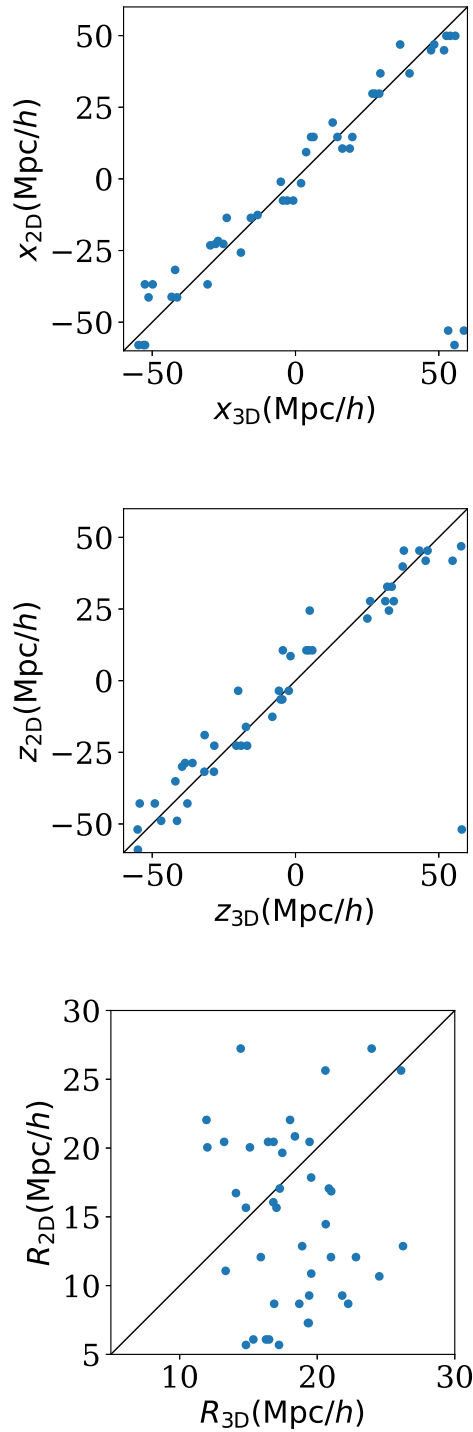


Figure 6.2: *Top to bottom, respectively:* Given a set of intrinsic three-dimensional voids in the galaxy distribution, sky-plane positions  $x$  and  $z$  and radii  $R$  of the voids, and corresponding positions and radii of the two-dimensional voids detected with the surface overdensity  $\Sigma$  that best match these three-dimensional voids. The median  $(x,z)$   $T^2$  distance for the best-matched voids, given a three-dimensional void (Sect. 6.2.4), for detections with  $\Sigma$  is  $7.8 \text{ Mpc}/h$ . Equality is shown by a straight line in all three panels. The radii match poorly, with two-dimensional radii mostly being less than the intrinsic three-dimensional radii. Plain-text data available at [zenodo.7792910/void\\_matches\\_mass\\_def\\_given\\_3D.dat](https://zenodo.org/record/7792910/files/void_matches_mass_def_given_3D.dat).

ation with re-simulation on a given machine, and stronger variation between different machines. We describe our results taking into account our small-scale estimates of their reproducibility, and use the word “robust(ly)” to indicate cross-machine reproducibility.

We find  $P_{x,z}^X(2D|3D)$  values (robustly) indicating significant match distributions in all four cases, with  $P_{x,z}^\Sigma(2D|3D) < 0.001$ , and  $P_{x,z}^X(2D|3D) < 0.0001$  for  $X \in \{\overline{\gamma}_\perp, \theta, |\sigma|\}$ . Thus, we find that given the three-dimensional voids found with the watershed algorithm in the galaxy distribution, the sky plane positions of the two-dimensional voids found using the surface overdensity  $\Sigma$  are significantly closer to the former than they would be if the same number of two-dimensional void positions were chosen randomly. In other words, we have a significant response to question (ii) for  $\Sigma$ . This is reassuring, because it shows that despite the projection effects of multiple voids and their aspherical shapes, the centres of the intrinsic three-dimensional voids can be recovered in the two-dimensional  $\Sigma$  distribution.

Moreover, we find that for the weak-lensing tangential shear  $\overline{\gamma}_\perp$ , and for both the Sachs optical scalar expansion  $\theta$  and shear  $|\sigma|$ , the centres of the two-dimensional voids represent the three-dimensional void centres to high significance. Thus, any of the four parameters should be usable to re-detect the void centres known from the three-dimensional voids.

In contrast, if we start with the two-dimensional photometric map and predict the centres of the three-dimensional voids, we only find (Table 6.3) the weak-lensing tangential shear  $\overline{\gamma}_\perp$ , the Sachs expansion  $\theta$  and the Sachs absolute shear  $|\sigma|$  to significantly and robustly reveal underlying three-dimensional voids, with  $P_{x,z}^X(3D|2D) \ll 0.01$  in all three cases. Comparison with  $P_{x,z}^\Sigma(3D|2D)$  in Table 6.3, for the surface overdensity, shows that discovering a three-dimensional void thanks to its two-dimensional signature is less likely with  $\Sigma$ . In other words, in answering question (i), use of our algorithm with any of the three geometrical optics parameters is more likely to reveal the sky-plane position of the three-dimensional void than using  $\Sigma$ .

These results show that the intrinsic three-dimensional void signal yields detectable void centres with our algorithm in not only the projected (two-dimensional) surface overdensity  $\Sigma$ , inferrable from photometric maps with only a mass-to-light ratio assumption, but also in the two-dimensional maps of weak-lensing and Sachs optical shear parameters. If additional information, such as spectroscopic or photometric redshift information, is available, then combining that information with lensing analyses of the data should lead to tighter constraints on the (partly invisible) underdensity distributions, as opposed to using galaxies’ sky positions and redshifts alone.

Moreover, in the absence of galaxy redshift information, two-dimensional maps should yield constraints on the mass distribution, at least in the case of  $\overline{\gamma}_\perp$  and  $\theta$ . However, while the void centres are detected, the radii are poorly constrained from either three-dimensional or two-dimensional maps.

We examine these results and caveats more closely in the following sections.

### 6.3.2 Surface overdensity $\Sigma$

The upper panel of Fig. 6.1 shows the map of the surface overdensity  $\Sigma$ , together with sky-plane centres of the intrinsic three-dimensional voids of the galaxy distribution and the two-dimensional voids detected via  $\Sigma$  as described in Sect. 6.2.5. The correspondence between these, formalised in Table 6.3, can be inspected qualitatively by judging if a three-dimensional void centre (white +) has a two-dimensional void centre (red  $\times$ ) more close to it than a randomly placed point. Of the  $N_{3D} = 46$  intrinsic galaxy voids, only  $N_{2D}^\Sigma = 28$  two-dimensional voids are detected (Table 6.2). The fact that  $N_{2D}^\Sigma < N_{3D}$  is expected, since we did not design our algorithm to distinguish voids that are nearly concentric when projected to the sky plane.

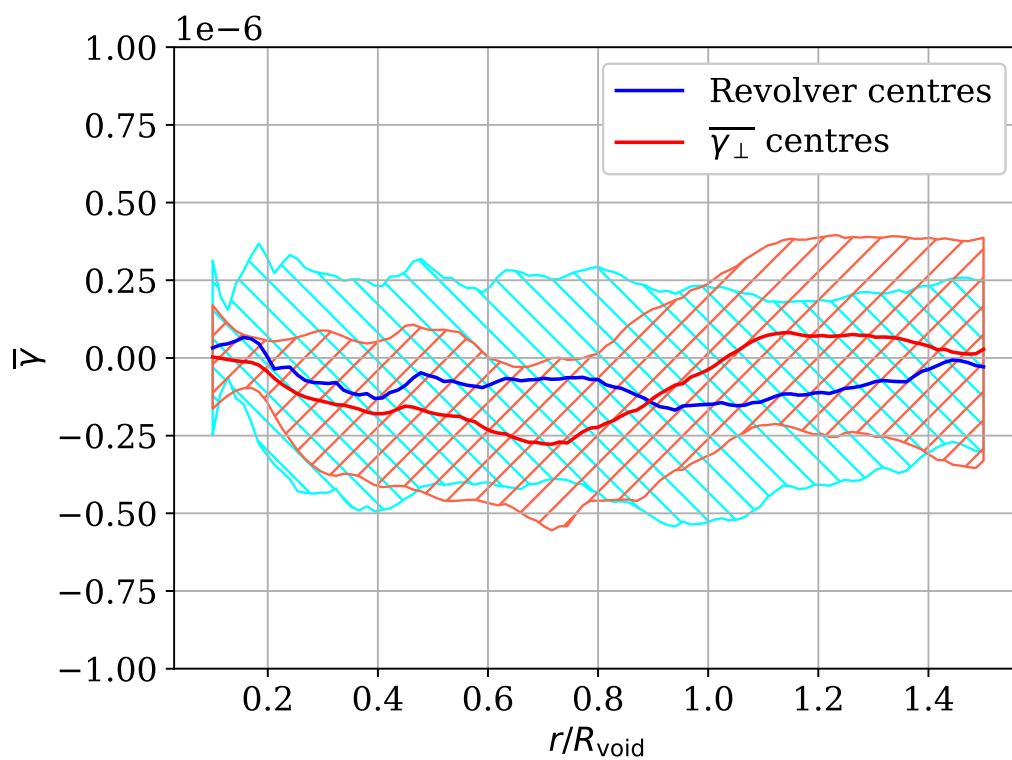


Figure 6.3: Radial void profiles of the weak-lensing shear  $\bar{\gamma}_{\perp}$ , as in the lower panel of Fig. 6.1, for three-dimensional (projected) and two-dimensional ( $\bar{\gamma}_{\perp}$ ) sets of void centres. “1e-6” indicates a factor of  $10^{-6}$  in the vertical scale (and similarly in Figs 6.5 and 6.7 below). A map for  $\bar{\gamma}_{\perp}$  is not shown, since the map of weak-lensing mean tangential shear  $\bar{\gamma}_{\perp}(r, \hat{n})$  is redetermined for each possible void centre  $\hat{n}$ .

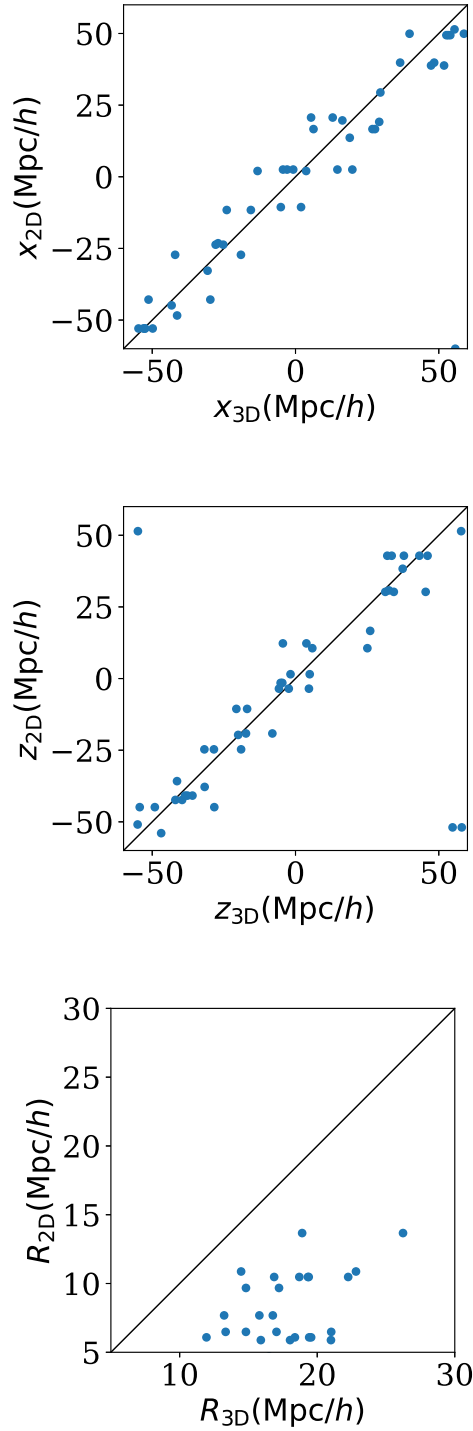


Figure 6.4: *Top to bottom, respectively:* For each intrinsic three-dimensional void, sky-plane positions  $x$  and  $z$  and radii  $R$  of the best-matched two-dimensional void detected with the weak-lensing shear  $\overline{\gamma}_{\perp}$ , as in Fig. 6.2. The median  $(x, z)$   $T^2$  distance for the best-matched voids, given a three-dimensional void (Sect. 6.2.4), for detections with  $\overline{\gamma}_{\perp}$  is  $6.5 \text{ Mpc}/h$ . All two-dimensional radii are lower than those of the three-dimensional voids that they correspond to. Plain-text data available at [zenodo.7792910/void\\_matches\\_gamma\\_given\\_3D.dat](https://zenodo.org/record/7792910/files/void_matches_gamma_given_3D.dat).

The lower panel of Fig. 6.1 shows the  $\bar{\Sigma}$  profiles averaged over all the two-dimensional centres, and, independently, averaged over all the three-dimensional centres (projected by ignoring the  $y$  coordinate). Comparison of these two curves (and their standard deviations, hatched) shows how well we might expect our algorithm to perform. The profiles for the three-dimensional centres are those that would be detected if the algorithm were perfect in recovering the intrinsic voids, leaving aside the difference that the two-dimensional detection uses the full dark matter particle distribution, while the three-dimensional detection is galaxy based. It is clear that projection effects are significant: the mean profile (blue curve) does not show the sharp wall typical of voids. It is also clear that we have found profiles in  $\Sigma$  (red curve) that are stronger in contrast from minimum density to highest wall density than those of the intrinsic voids. This suggests that improving the algorithm further based on the motivation of optimising a typical void-like profile, under the assumption of spherical shapes, would be unlikely to help further: strongly void-like profiles are already well detected.

The top two panels of Fig. 6.2 show the  $x$  and  $z$  coordinates (spanning the sky plane) of corresponding void centres, where the two-dimensional void centres are those found to best match a given three-dimensional void, as described in Sect. 6.2.4. The existence of multiple three-dimensional voids whose best match is a single two-dimensional void is clear in the diagram. We interpret this as illustrating cases where three-dimensional voids are nearly aligned in projection, and thus detected as a single two-dimensional void.

The bottom panel of Fig. 6.2 shows that void radii are very poorly recovered, and generally underestimated. One factor is clearly the difficulty in distinguishing nearly concentric voids. However, it is also likely that substructure is misidentified as void walls, leading to the underestimates. Overall, the bottom panel of Fig. 6.2 shows that the radii of our intrinsic population of three-dimensional voids detected with REVOLVER are reduced by about 5 Mpc/h, in an uncorrelated way with a big scatter, when redetected with  $\Sigma$  as two-dimensional voids.

### 6.3.3 Weak-lensing shear $\bar{\gamma}_{\perp}$

Using  $\bar{\gamma}_{\perp}$ , we find  $N_{2D}^{\gamma} = 29$  two-dimensional voids, i.e., roughly two thirds of the number of intrinsic galaxy voids,  $N_{3D} = 46$  (Table 6.2). Figure 6.3 shows that the mean behaviour of a lensing profile in  $\bar{\gamma}_{\perp}$  using the centres of the intrinsic three-dimensional voids is that  $\bar{\gamma}_{\perp}$  starts near zero, decreases to negative values in the void and appears to (in the mean) reach a minimum at the wall radius found by REVOLVER, before increasing to a maximum at a somewhat greater radius. This is reasonable, given the definition for  $\bar{\gamma}_{\perp}$ . Figure 6.3 shows that the two-dimensional voids also have a (mean)  $\bar{\gamma}_{\perp}$  profile that decreases and then increases to zero, but the increase to zero occurs at lower fractions of the void radius.

Together, these profiles could be interpreted to suggest that applying a systematic correction factor to increase the void radius found when  $\bar{\Sigma}(r, \hat{n}) = \bar{\Sigma}(r, \hat{n})$  (see Eq. (6.14)) might yield radii that better match those of the three-dimensional voids. The lowest panel of Fig. 6.4 is qualitatively consistent with this suggestion, as it shows that the two-dimensional voids that are best matched to the three-dimensional voids have radii that are all smaller than the three-dimensional void radii. However, Table 6.3 shows that correspondence between the radii is insignificant. As in the case of  $\Sigma$ , the projection of nearly concentric intrinsic voids, as well as obscuring effects from more distant overlapping voids, make the use of a single scaling correction for radii poorly motivated, except as a crude statistical correction.

The two upper panels of Fig. 6.4 show what is quantified in Table 6.3: the sky-plane positions are recovered non-randomly to high statistical significance. Moreover, for the reverse question (Table 6.3),  $P_{x,z}^{\gamma}(3D|2D) \lesssim 0.001$  appears to be robust against re-calculation and machine error,

so the use of weak-lensing shear – on its own – to infer the presence of intrinsic three-dimensional galaxy-traced voids appears to be promising.

### 6.3.4 Optical scalars $\theta$ and $|\sigma|$

#### Expansion $\theta$

Figure 6.5 shows a map of the Sachs expansion  $\theta$  and sky-plane centres of both the intrinsic voids and those detected via  $\theta$ . As indicated in Table 6.3, given the three-dimensional voids, the best-matched two-dimensional ( $\theta$ ) voids are recovered to high significance via their sky-plane centres. The top two panels of Fig. 6.6 show the sky-plane matches.

However, we only find  $N_{2D}^{\theta} = 34$  voids using  $\theta$ , many less than the intrinsic voids. As with  $\Sigma$  and  $\overline{\gamma}_{\perp}$ , a likely interpretation is projected concentricity of several voids and obscuration by other cosmic web structure. The lower panel of Fig. 6.5 can be interpreted consistently with this hypothesis: the mean  $\theta$  profile of the full set of intrinsic voids detected with `REVOLVER` is very weak, which would be consistent with both effects. The profile for two-dimensional voids detected with  $\theta$  is very strong, qualitatively resembling a typical void density profile, with a sharp (mean) wall.

The lowest panel of Fig. 6.6 shows that the radii are again poorly correlated. Again, this is consistent with the detections using  $\Sigma$  and  $\overline{\gamma}_{\perp}$ , with the difference that the radii estimated with  $\theta$  expand greatly from the intrinsic voids' range of around 15–25 Mpc/h to around 5–30 Mpc/h. While to some degree these disagreements are likely to be induced by the problems of projection, it might also be possible that radii that are gravitationally realistic in terms of the potential  $\Phi$  differ significantly from those traced by the three-dimensional galaxy distribution. This is a question open for further study.

#### Sachs shear $|\sigma|$

The upper panel of Fig. 6.7 shows a map of the modulus of the Sachs shear,  $|\sigma|$ . Again, Table 6.3 shows that given an intrinsic void, the Sachs shear detects the voids' positions to high significance using our algorithm. The lower panel of Fig. 6.7 shows a qualitatively similar result to the use of the expansion  $\theta$ , in the sense that shear profiles for the full set of three-dimensional voids have a weak mean profile, while those for the voids detected in the two-dimensional map of  $|\sigma|$  show a strong void-like profile. Taking into account the good sky-plane matches and poor radial matches shown in Fig. 6.8, a consistent interpretation is again that the two-dimensional detected profiles are those that bypass both general obscuration and the confusion induced by voids that are nearly concentric in projection.

## 6.4 Discussion

### 6.4.1 Void lensing studies when intrinsic voids are known

With the simulation presented here, we have shown that if intrinsic three-dimensional voids are known, then the effects of geometric-optics parameters should be detectable in the sky plane, enabling the study of the role that gravitational lensing plays in the voids. In other words, we have shown a relation between voids in three-dimensional comoving space with their imprints left on maps of the projected and ray-traced variables. Moreover, the lensing patterns induced by a void should provide feedback to better constrain the model of the void itself. As argued by

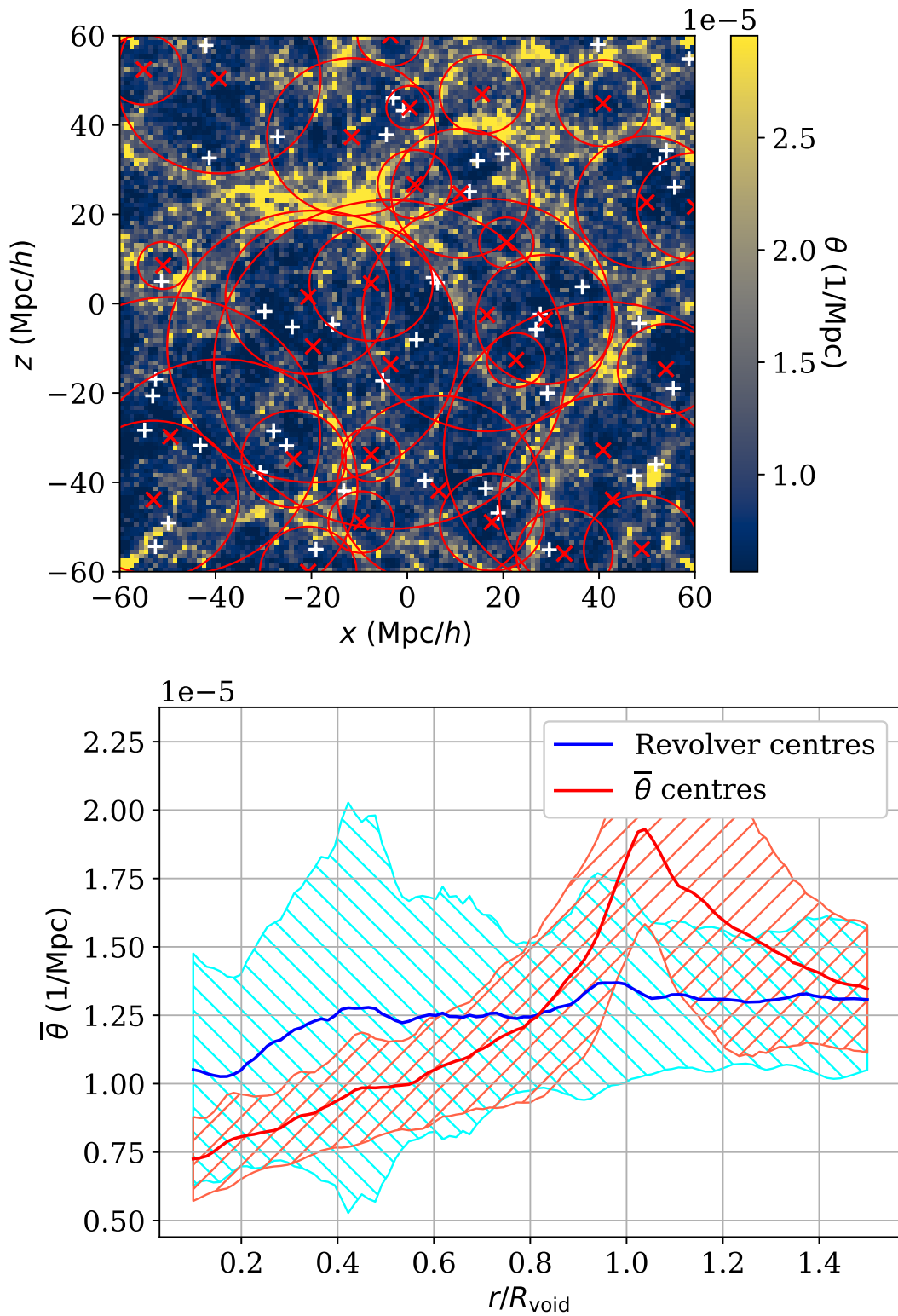


Figure 6.5: *Upper panel*: Sachs expansion  $\theta$ , as for Fig. 6.1, computed using Eqs (6.20) and (6.21), with white + symbols for the  $x, z$  centres of three-dimensional intrinsic galaxy voids and red x symbols for the centres of two-dimensional voids detected with  $\theta$ . *Lower panel*: Radial void profiles of  $\theta$ , as in the lower panel of Fig. 6.1, for three-dimensional (REVOLVER) and two-dimensional ( $\bar{\theta}$ ) sets of void centres.

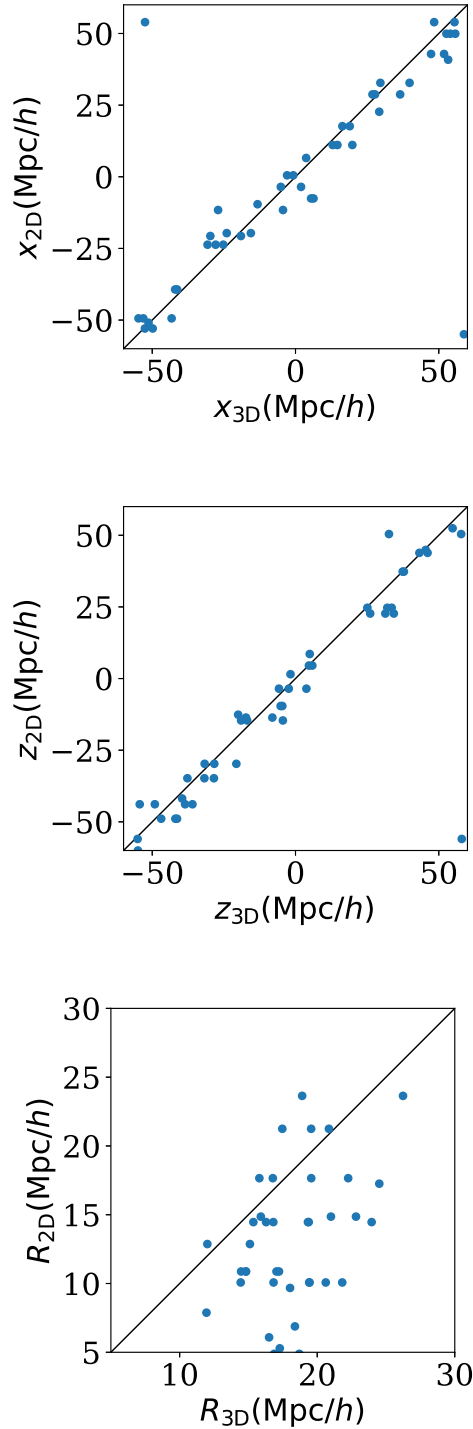


Figure 6.6: *Top to bottom, respectively:* For each intrinsic three-dimensional void, sky-plane positions  $x$  and  $z$  and radii  $R$  of the best-matched two-dimensional void detected with the Sachs expansion  $\theta$ , as in Fig. 6.2. The median  $(x, z)$   $T^2$  distance for the best-matched voids, given a three-dimensional void (Sect. 6.2.4), for detections with  $\theta$  is  $5.8 \text{ Mpc}/h$ . The two-dimensional radii have a much broader distribution than those of the intrinsic three-dimensional voids, with no obvious correlation. Plain-text data available at [zenodo.7792910/void\\_matches\\_exp\\_given\\_3D.dat](https://zenodo.org/record/7792910/files/void_matches_exp_given_3D.dat).



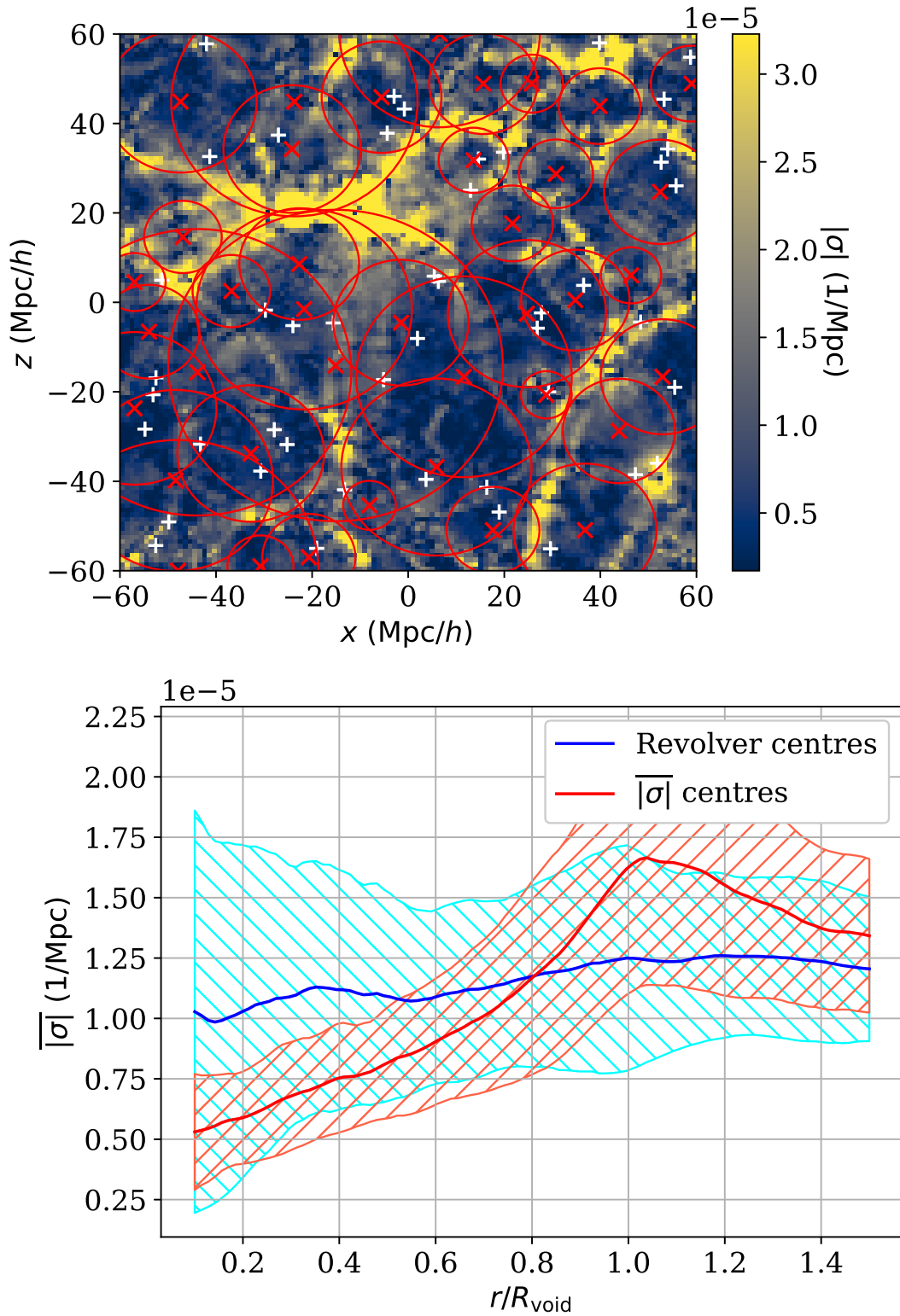


Figure 6.7: *Upper panel*: Sachs shear  $|\sigma|$ , as for Fig. 6.1, computed using Eqs (6.20) and (6.21), with white + symbols for the  $x, z$  centres of three-dimensional intrinsic galaxy voids and red  $\times$  symbols for the centres of two-dimensional voids detected with  $|\sigma|$ . *Lower panel*: Radial void profiles of  $|\sigma|$ , as in the lower panel of Fig. 6.1, for three-dimensional (REVOLVER) and two-dimensional ( $|\sigma|$ ) sets of void centres.

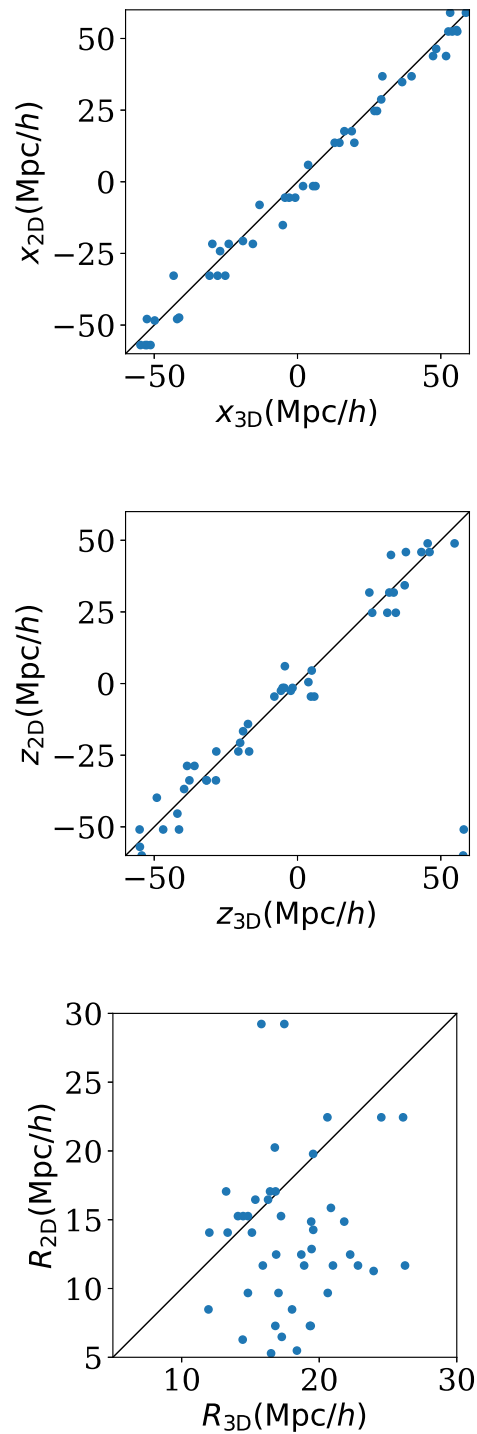


Figure 6.8: *Top to bottom, respectively:* For each intrinsic three-dimensional void, sky-plane positions  $x$  and  $z$  and radii  $R$  of the best-matched two-dimensional void detected with the Sachs shear modulus  $|\sigma|$ , as in Fig. 6.2. The median  $(x, z)$   $T^2$  distance for the best-matched voids, given a three-dimensional void (Sect. 6.2.4), for detections with  $|\sigma|$  is  $4.5 \text{ Mpc}/h$ . The two-dimensional radii again have a broad distribution, as in Fig. 6.6. Plain-text data: zenodo.7792910/void\_matches\_sig\_given\_3D.dat.

Sánchez et al. (2017) using  $\Sigma$  (and photometric redshifts to statistically limit the radial depth of the projection), this would confirm that a galaxy-traced void is a genuine underdensity of the dark matter density field. Other weak gravitational lensing detectors, such as the Lyman  $\alpha$  forest (Croft et al., 2018), could also be compared to foreground galaxy-traced voids to check for consistency.

### 6.4.2 Blind (redshift-free) searches for voids

Without knowledge of spectroscopic or photometric galaxy redshifts, we currently can justify use of the azimuthally averaged tangential weak-lensing shear  $\overline{\gamma}_\perp$  and of the Sachs expansion  $\theta$  or shear  $|\sigma|$  for analysis of a photometric survey with the intention of inferring the presence of three-dimensional voids, since all three of these robustly yield  $P_{x,z}^X(3D|2D) \ll 0.01$  (Table 6.3). Our calculation would appear to be the first time that the use of Sachs expansion maps has been shown to have the ability to reveal underlying voids. Jeffrey et al. (2021) studied the combined use of the usual weak-lensing convergence and shear in Dark Energy Survey (DES) photometry over 4143 deg<sup>2</sup>, which appears to be equivalent to using  $\Sigma$  and  $\overline{\gamma}_\perp$ , to reveal underlying voids, but did not appear to study the Sachs expansion.

Our algorithms can very likely be improved further. For example, combining all four parameters,  $\Sigma$ ,  $\overline{\gamma}_\perp$ ,  $\theta$  and  $|\sigma|$ , could lead to complementary constraints on whether or not a putative void is real or correctly identified. These would only be partially independent from one another, since the four parameters are related to one another, with  $\theta$  and  $|\sigma|$  taking into account the evolution of the gravitational potential. Deriving the weak-lensing parameters for an initial approximation, and then using the Sachs optical scalars for an analysis to higher accuracy could be one viable strategy. Another extension would be to examine individual pairs of the best-matching three-dimensional and two-dimensional voids from the current algorithm presented here to understand how their match could be improved; or alternatively, examine the worst-matching pairs to understand what obstructs the match and search for ways of avoiding the obstruction.

There are several advantages in detecting voids via their sky-plane effects. Some of the fainter galaxies defining the walls of a void may be too faint to be detected in a given survey. The tracing of dark matter by luminous matter is by a long chain of physical effects: baryonic matter has to be associated with the dark matter, and star formation history and feedback effects need to be modelled. Geometric optics bypasses this causal chain, and should lead to inferences made with fewer assumptions.

### 6.4.3 Projected void concentricity and obscuring cosmic web structures

Projection of voids to be nearly concentric is expected in our simulation, since we integrate over the full box size of  $L_{\text{box}} = 120\text{Mpc}/h$  and the largest intrinsic voids detected with the watershed algorithm have radii  $R_{\text{eff}} \sim 30\text{Mpc}/h$ . Our algorithm's only strategy that relates to the problem of projected void concentricity is to prefer larger to smaller radii (step 7 in Sect. 6.2.3). Figures 6.2, 6.4, 6.6, and 6.8 show that despite this, the two-dimensional void radii tend to be lower than the intrinsic radii. This empirical result would tend to favour keeping this step unchanged.

Our algorithm already has many parameters. Extending it to allow successive multiple detections of walls could, in principle, lead to a higher rate of detecting the intrinsic voids. Ideally, this should lead to a statistically significant correlation between the intrinsic and photometric void radii; in this work, our correlations in radii are insignificant (Table 6.3). However, detecting multiple concentric walls would quite likely also lead to false detections.

Strategies for solving the problem of obscuring structures (in the absence of redshift information) are not obvious. Gravitationally dense objects occupy little volume and still suffer from projection effects; voids dominate the volume and thus are strongly affected by projection effects. A Bayesian approach as in Jeffrey et al. (2021) would be worth exploring.

Since our simulation homogenises the foreground and background of the simulated volume, a real observational survey will include stronger levels of both projected void concentricity and obscuring cosmic web structures.

## 6.5 Conclusion

In this work we have studied the two questions of whether voids in the cosmic web yield detectable information in projected variables, the surface overdensity  $\Sigma$ , the azimuthal averaged weak lensing shear  $\overline{\gamma}_\perp$ , the Sachs expansion  $\theta$ , and the Sachs shear  $|\sigma|$ , and vice versa, whether the sky-plane information can be used to infer the existence of the intrinsic three-dimensional voids. We performed this using a cosmological  $N$ -body simulation starting from initial perturbations generated according to a standard initial power spectrum. We carried out the analysis in a fully controlled software environment with full information about the dark matter distribution as well as the luminous matter distribution, which we modelled using galaxies built from a halo merger tree using semi-analytical tools. We detected the intrinsic voids in the three-dimensional comoving spatial distribution of galaxies using a watershed void finder (Sect. 6.2.3). The void detection in the projected plane (Sect. 6.2.3) is based on the assumption that the azimuthally averaged profiles of the four detector variables for the voids have shapes with predictable qualitative behaviour. In the case of the surface overdensity  $\Sigma$  and the two Sachs optical scalars  $\theta$  and  $|\sigma|$ , this expected shape is to start from a minimum at the centre of a void, gradually increase radially outwards, and increase sharply at the void's wall. The weak-lensing shear  $\overline{\gamma}_\perp$  is expected to start from zero, decrease, and increase to zero just past the void's wall. Using a heuristically parametrised algorithm for detecting these profiles, adjusted individually for the four detector variables, we found positions and radii of two-dimensional voids traced by these detectors.

We find roughly similar numbers of two-dimensional voids traced by each of the four different detector variables, and in all cases, fewer voids than in the three-dimensional galaxy-traced distribution, as can be seen in Table 6.2. There are two likely explanations. First, when several intrinsic voids are nearly concentric in projection on the sky, our algorithm only detects one of these, since it is not designed to detect multiple walls. Second, the foreground and background structures of the cosmic web, i.e. walls, filaments, clusters and other voids, obscure the signals associated with any single intrinsic void, making detection difficult. The lower panels of Figs 6.1, 6.3, 6.5, and 6.7 show that the voids detected by us in the projected plane follow the assumed qualitative shapes well, giving confidence that our algorithm works as expected. However, the same panels show that the corresponding mean profiles, using the centres and radial sizes of the three-dimensional intrinsic voids, but the detector variables in the projected plane, are weak.

We interpret these two effects – the detection of fewer two-dimensional voids than those known to exist in the three-dimensional spatial distribution, together with the weak mean profiles of the projected-plane detector variables centred at the intrinsic voids' locations – as consistent with the undetected voids being (statistically) those that are either the most obscured or are concentric with the detected voids.

Given knowledge of the three-dimensional voids' centres, we find (Table 6.3, third column) that the detected two-dimensional voids are significantly closer than random to the three-

dimensional voids' centres in the sky plane, for all four detector variables. In other words, a survey with sufficient spectroscopic or photometric redshift information to detect voids should be usable to infer patterns of gravitational lensing through the voids that should be measurable using either weak-lensing shear or the Sachs optical scalars (answering question (ii) of Sect. 6.2.4 positively).

Conversely, if we only have a photometric survey that is blind, in the sense of having neither spectroscopic nor photometric redshift information, then we have established (Table 6.3, second column) that the two-dimensional voids detected via weak-lensing tangential shear  $\overline{\gamma_{\perp}}$ , Sachs expansion  $\theta$  or Sachs absolute shear  $|\sigma|$  significantly reveal the true underlying three-dimensional void population (question (i) in Sect. 6.2.4). Use of the surface overdensity  $\Sigma$  provides weaker evidence for revealing the sky-plane positions of the underlying void population.

While these results follow from significant correlations of voids' locations in the sky plane, we find no significant correlation for the radii. The bottom panels of Figs 6.2, 6.4, 6.6, and 6.8, show that the two-dimensional void radii tend to be lower than the intrinsic radii. The lack of correlation and the generally lower radii are consistent with the problem of near concentric projection of multiple voids into the sky plane.

While our current results are exploratory, with several caveats as stated above, it does appear that gravitational lensing through individual voids should be observationally detectable. Moreover, weak-lensing tangential shear and Sachs expansion and shear in future blind photometric surveys – such as those provided by the Rubin C. Observatory's Legacy Survey of Space and Time (LSST; Sheldon et al. 2023) – should reveal the existence of intrinsic three-dimensional voids, yielding predictions that will be falsifiable by spectroscopic followup surveys such as those of the 4-metre Multi-Object Spectroscopy Telescope (4MOST; de Jong et al. 2012, 2019; Richard et al. 2019) or the Dark Energy Spectroscopic Instrument (DESI; Levi et al. 2013; Hahn et al. 2022).

# Chapter 7

## Conclusion

In this work we have explored cosmic voids in cosmological dark matter simulations. To do so we introduced and explored the main ingredients of the cosmological standard model, the  $\Lambda$ CDM paradigm, in chapter 2. We studied how the background model evolves over cosmic time and how matter perturbations grow in this model. These perturbations will grow in size and form the walls, filaments and clusters that are seen in the cosmic web, see e.g. figs. 2.4 and 5.1. Matter will clump together and eventually collapse into virialised dark matter haloes; these structures will yield the gravitational wells in which baryonic matter can cool down and form galaxies. We describe the basics of the numerical tools that are used to model these processes in this work in chapter 3, i.e. starting from generating initial velocity perturbations and position displacements from a regular grid and evolving a dark-matter-only simulation, identifying halo structures and building a merger-history tree to finally populating these merger-trees with galaxies using semi-analytical recipes and detecting voids in the density distribution.

### 7.1 Galaxy formation in voids

The contents of chapter 4 present our publication investigating galaxy formation in voids with special emphasis on the position of a galaxy inside a void. We hypothesise that a void, due to its repulsive net gravitational force should hinder halo virialisation. A relativistic treatment of a void, and the negative spatial curvature that it locally induces, should similarly show to an effective net repulsive force, making it even more unlikely for a halo to virialise, though the  $N$ -body simulation code we use does not account for curvature effects. We establish the term “*elaphrocentre*” to denote the hill of the gravitational potential in a cosmic void. The expected effect of the repulsive nature of the void should be strongest in the elaphrocentre. We present a fully reproducible pipeline to model galaxy formation in a pure dark matter distribution together with the generation of a void catalogue from the same dark matter distribution and analyse these. Moreover, we ask if the unique environment of the elaphrocentre might favour the formation of large, diffuse galaxies with low surface brightness. With this goal, we investigate key quantities including the spin parameter and the virial radius of the dark matter halo. We also investigate the disk scale length of the galaxy and the formation epoch of the galaxy, which we define as the first time snapshot at which the galaxy has a stellar mass above zero. In addition, we use the data provided by SAGE to estimate the matter infall into each galaxy, assuming that the matter infall into void galaxies is a more extended process over time.

We do not find statistically significant differences in the infall rates of galaxies found in a void compared to the non-void population. A possible reason is that the assumed exponential decay rate, see eq. (4.2), is an overstrong simplification for galaxies experiencing merger events

and does not take into account the possibility of almost instantaneous episodes of matter infall.

The halo and galaxy properties yield more promising results, hinting that the position of a galaxy in the cosmic web might have measurable effects on the galaxies. Considering the full population of galaxies (“all mass scales” in Table 4.2), we find that void galaxies have significantly smaller disk scale lengths than non-void galaxies and an (insignificant) hint of a higher spin parameter (which is not detectable via these global median values). As seen in upper part of the same table, these trends also hold for galaxies in the mass interval  $M_{\text{vir}} = 10^{11} M_{\odot}/h - 10^{13} M_{\odot}/h$ , which should be a more robust result due to the exclusion of haloes with low numbers of particles. Statistical properties of haloes detected with low particle numbers in an  $N$ -body simulation will tend to be sensitive to the uncertainties in accurate dynamical characterisation of the haloes.

We investigate these trends further for void galaxies based on their position in the void (see figs 4.8–4.13) by evaluating their position with respect to the proportional distance from the elaphrocentre and  $f_{\mathcal{H}\cap\mathcal{V}}$ . The fraction-in-void,  $f_{\mathcal{H}\cap\mathcal{V}}$ , that we introduce here measures the fraction of dark matter particles that are in the host halo of a galaxy and that are also identified as lying in a void:  $f_{\mathcal{H}\cap\mathcal{V}}$  is unity for a halo fully located in a void, decreasing to zero for a halo closer to the densest nodes of the cosmic web. In general, we find more significant trends for galaxy properties as a function of  $f_{\mathcal{H}\cap\mathcal{V}}$  in comparison to their dependence on the elaphrocentric distance. One likely contributing fact is that since voids are not perfectly spherical (in particular, the small voids that we identify in the dark matter distribution tend to have more irregular shapes), a single void-centric distance is likely to be inaccurate in terms of characterising the degree to which a galaxy lies in a void. We conclude that  $f_{\mathcal{H}\cap\mathcal{V}}$  is a better measure for the “voidness” of a galaxy than the galaxy’s radial position with respect to the elaphrocentre.

The slopes indicated in the captions of figs 4.8 and 4.10, for the disk scale length and spin parameter as a function of  $f_{\mathcal{H}\cap\mathcal{V}}$ , show qualitatively equivalent results to those in Table 4.2, but with reversed statistical significance. The spin parameter is significantly higher for galaxies with higher fraction-in-void values  $f_{\mathcal{H}\cap\mathcal{V}}$ , but the disk size is only marginally smaller.

As seen in Table 4.4, we do not measure any significant difference between the three different centres discussed in the work, the elaphrocentre, the geometric centroid, and the circumcentre, which are native outputs of REVOLVER. As the void boundaries are set by the density distribution and thus are independent of the centre, this comparison only makes sense with respect to the relative radial distance to the void’s centre. We find nearly no galaxies with  $r/R_{\text{eff}} \lesssim 0.5$ , where differences should show up most strongly, which we suspect is the explanation for the absence of any significant dependence on the choice of void centre.

Among the many possible extensions to this study of galaxy properties in voids, one possible improvement would be the replacement of our simulation by a relativistic  $N$ -body simulation (Macpherson et al., 2017; Adamek et al., 2016; Barrera-Hinojosa & Li, 2020), which should, in principle, better account for the negative curvature inside a void.

The results of chapter 5 are broadly consistent with the finding that void galaxies are significantly different to galaxies in denser environments. The methods of the two approaches are similar enough for approximate comparison of the results, although there are differences, including a significant improvement in the resolution of masses in the Bolshoi simulation, differing methods of characterising a galaxy as being located in a void, differing statistical approaches, and better computational reproducibility in the case of our own  $N$ -body simulation.

We confirm the higher spin parameter for void galaxies of host halo mass  $M_{\text{vir}} \gtrsim 10^{10} M_{\odot}/h$ , although void galaxies with lower mass haloes have lower spin parameters than non-void galaxies. We also confirm later formation epochs of void galaxies. We do not confirm the smaller disk scale lengths; a possible explanation is that in the chapter 4 analysis, smaller void disks are a

proportional effect in relation to lower host halo masses. Interestingly, in the Bolshoi simulation analysis, we see that the void and non-void galaxy populations in high mass haloes behave similarly; the differences only occur below  $M_{\text{vir}} \sim 10^{10} M_{\odot}/h - 10^{11} M_{\odot}/h$ .

These results strongly invite observational testing of the statistical properties of void galaxies, although that is difficult for many reasons. Their number density is low; they themselves are typically less luminous than non-void galaxies; the numbers of galaxies that are fully located in voids are much fewer than those near overdense structures; and quantifying galaxies' identities as void galaxies is difficult. Large samples of void galaxies will be needed to statistically analyse the effects of voids on the galaxies forming inside them observationally, and observational surveys such as that of Beygu et al. (2016) should be strongly encouraged.

The difficulty in characterisation of galaxy voidness is highlighted by the fact that watershed void finders are space filling, which holds true for both ZOBOV and SPINEWEB. This behaviour is seen in Table 5.1, where large fractions of the simulated volume are allocated to the voids. The assumption that walls and filaments are only of side length of one voxel ( $0.488 \text{ Mpc}/h$ ) in the Bolshoi simulation analysis is an oversimplification that can be improved in future work. Some galaxies at the edges of a void are likely to be misclassified. The high fractions of void galaxies in chapters 4 and 5 suggest that we identify too many galaxies as belonging to voids. An analysis of the properties in relation to their position in a void, similarly to figs. 4.8–4.13, would be useful followup for understanding the galaxies studied in chapter 5.

The lower stellar masses found for low-mass galaxies in void environments (see fig. 5.4) hints that luminosities and colours of low mass void galaxies should differ from those galaxies found in denser environments. The observations of Hoyle et al. (2005); Patiri et al. (2006) and Kreckel et al. (2011), who find that void galaxies are bluer, could potentially offer a falsification of our models, since lower stellar masses would tend to indicate less star formation, and redder colours. However, this inference is highly qualitative. The results we present in this thesis are not sufficient to infer the colours of galaxies, as modelling these requires several further steps that are planned for followup work, but not yet completed.

A straightforward approach will be to add a stellar population synthesis code, e.g. Fioc & Rocca-Volmerange (2019), that will build upon the mass infall, mass outflow and star formation history modelled by SAGE to calculate the spectral energy distribution of each synthetic galaxy. This approach is only suitable for a small simulation, as presented in chapter 4, as we firstly need to produce the full matter infall and star formation history for each galaxy and its progenitors, and secondly need to generate the spectral energy distributions for all the galaxies in the sample. This is a computationally heavy process in terms of computing time.

Given that we find the several consistent trends between our simulation and the Bolshoi simulation, it is justified to aim at seeing if void versus non-void galaxy differences in colour and surface density can be detected in a smaller simulation in a fully controlled and portable software environment. Combing colour and an estimate of the surface density, we also will be able to answer the question of whether voids are a favourable environment for LSBG formation. As argued in Sect. 4.5, the later formation epoch and the higher spin parameter of void galaxies support the hypothesis that void galaxies are more likely to be LSBGs.

## 7.2 Geometric optics through voids

In chapter 6 we have described a novel approach to detect structures, namely voids, in the projected signal of geometric-optics measurements. We establish a heuristic algorithm to detect voids in the surface overdensity  $\Sigma$ , the averaged weak lensing shear  $\overline{\gamma}_{\perp}$  and the two Sachs optical scalars  $\theta$  and  $\sigma$ . We again use a cosmological simulation to generate the lensing signal



for these four detector variables and compare the detected voids to the intrinsic population of voids found in the galaxy distribution using the watershed method of `REVOLVER`. Unsurprisingly, we find fewer voids in the projected quantities (Table 6.2), most likely due to the difficulty in distinguishing voids that are nearly concentric in projection on the sky plane. Our proposed algorithm does not detect multiple void walls.

Firstly, we find that given a three-dimensional void, we can expect to see a void-like structure also in the projected detector variables. Secondly, we find that given the sky-plane geometric-optics information alone, the centres of voids estimated in  $\overline{\gamma}_\perp$ ,  $\theta$  and  $|\sigma|$  using our algorithm each significantly reveal the existence of the intrinsic three-dimensional void centres (Table 6.3). Figures 6.1, 6.3, 6.5, and 6.7 illustrate the correspondence in voids centres and show the radial profiles of voids for our detector variables.

However, the estimates of void radii are very poorly matched, for all four detector variables. As for the difficulty in detecting all the three-dimensional voids, we attribute the radius misestimates to similar causes. One problem is that our method cannot distinguish void walls that are nearly aligned in projection. A second problem is that the cosmic web is very complex, with many filaments, walls and clusters, which in projection will tend to obscure the signal that an isolated void should generate.

These preliminary results appear to be promising. Further development of the algorithm to check for its use on more realistic observational models to detect voids in the sky plane would justify its application to observational data, such as the reconstructed surface overdensity (Jeffrey et al., 2021). A void finder of this sort is only sensitive to the underlying dark matter distribution and, in principle, only needs two-dimensional a photometric survey. In contrast, the watershed void finders used in this work are used observationally to detect voids defined by luminous galaxies in three-dimensional (real or redshift) space.

Here we see the bridge between the different components of this thesis. We show that cosmic voids should have significant effects on galaxy formation. These effects depend, to some degree, on the position in a void. Detecting voids in the dark matter distribution directly thus might yield physically more accurate characterisation of cosmic voids, only dependent on the gravitational signal found in the geometric optics quantities. This in turn will enable better observational analysis of characterising which galaxies should be identified as void galaxies.

# Bibliography

- Abel, T., Hahn, O., & Kaehler, R. 2012, MNRAS, 427, 61, [arXiv:1111.3944]
- Adam, G., Bacon, R., Courtes, G., et al. 1989, A&A, 208, L15
- Adamek, J., Daverio, D., Durrer, R., & Kunz, M. 2016, JCAP, 7, 053, [arXiv:1604.06065]
- Akhlaghi, M., Infante-Sainz, R., Roukema, B. F., et al. 2021, Comp. in Sci. Eng., 23, 82, [arXiv:2006.03018]
- Allen, C. W. 1951, The Observatory, 71, 157
- Alpher, R. A. & Herman, R. 1948a, Nature, 162, 774
- Alpher, R. A. & Herman, R. C. 1948b, Physical Review, 74, 1737
- Aragón-Calvo, M. A., Platen, E., van de Weygaert, R., & Szalay, A. S. 2010a, ApJ, 723, 364, [arXiv:0809.5104]
- Aragón-Calvo, M. A., Platen, E., van de Weygaert, R., & Szalay, A. S. 2010b, ApJ, 723, 364, [arXiv:0809.5104]
- Aragon-Calvo, M. A. & Szalay, A. S. 2013, MNRAS, 428, 3409, [arXiv:1203.0248]
- Barnes, J. & Hut, P. 1986, Nature, 324, 446
- Barrera-Hinojosa, C. & Li, B. 2020, JCAP, 2020, 007
- Bartelmann, M. & Schneider, P. 2001, Phys.Rep., 340, 291, [arXiv:astro-ph/9912508]
- Baugh, C. M. 2006, Reports on Progress in Physics, 69, 3101, [arXiv:astro-ph/0610031]
- Behroozi, P. S., Wechsler, R. H., & Wu, H.-Y. 2013a, ApJ, 762, 109, [arXiv:1110.4372]
- Behroozi, P. S., Wechsler, R. H., Wu, H.-Y., et al. 2013b, ApJ, 763, 18, [arXiv:1110.4370]
- Bentivegna, E. & Bruni, M. 2016, Physical Review Letters, 116, 251302, [arXiv:1511.05124]
- Bernardeau, F., van de Weygaert, R., Hivon, E., & Bouchet, F. R. 1997, MNRAS, 290, 566, [arXiv:astro-ph/9609027]
- Bertschinger, E. 2001, ApJS, 137, 1, [arXiv:astro-ph/0103301]
- Beygu, B., Kreckel, K., van der Hulst, J. M., et al. 2016, MNRAS, 458, 394, [arXiv:1601.08228]

- Birkhoff, G. D. & Langer, R. E. 1923, *Relativity and modern physics* (Cambridge, Mass., USA: Harvard University Press)
- Blas, D., Lesgourgues, J., & Tram, T. 2011, *Journal of Cosmology and Astroparticle Physics*, 7, 034
- Bos, E. G. P., van de Weygaert, R., Dolag, K., & Pettorino, V. 2012, *MNRAS*, 426, 440, [arXiv:1205.4238]
- Bothun, G. D., Impey, C. D., Malin, D. F., & Mould, J. R. 1987, *AJ*, 94, 23
- Bruzual A., G. 1983, *ApJ*, 273, 105
- Buchert, T., Coley, A. A., Kleinert, H., Roukema, B. F., & Wiltshire, D. L. 2016, *International Journal of Modern Physics D*, 25, 1630007, [arXiv:1512.03313]
- Buchert, T., Nayet, C., & Wiegand, A. 2013, *Physical Review D*, 87, 123503, [arXiv:1303.6193]
- Buchert, T. & Ostermann, M. 2012, *Physical Review D*, 86, 023520, [arXiv:1203.6263]
- Bullock, J. S., Dekel, A., Kolatt, T. S., et al. 2001, *ApJ*, 555, 240, [arXiv:astro-ph/0011001]
- Butcher, H. R. 1987, *Nature*, 328, 127
- Cautun, M., van de Weygaert, R., Jones, B. J. T., & Frenk, C. S. 2015, in *IAU Symposium, Vol. 308, The Zeldovich Universe: Genesis and Growth of the Cosmic Web*, ed. R. van de Weygaert, S. Shandarin, E. Saar, & J. Einasto, [arXiv:1501.01306]
- Chan, T. K., Kereš, D., Wetzel, A., et al. 2018, *MNRAS*, 478, 906, [arXiv:1711.04788]
- Clarkson, C., Ellis, G. F. R., Faltenbacher, A., et al. 2012, *MNRAS*, 426, 1121, [arXiv:1109.2484]
- COBE. 1992, COBE DMR data, [https://lambda.gsfc.nasa.gov/product/cobe/dmr\\_image.cfm](https://lambda.gsfc.nasa.gov/product/cobe/dmr_image.cfm), (archive)
- Colberg, J. M., Pearce, F., Foster, C., et al. 2008, *MNRAS*, 387, 933, [arXiv:0803.0918]
- Cooley, J. W. & Tuckey, J. W. 1965, *Math. Comp.*, 19, 297
- Cooray, A. & Sheth, R. 2002, *Phys.Rep.*, 372, 1, [arXiv:astro-ph/0206508]
- Couchman, H. M. P. 1991, *ApJL*, 368, L23
- Croft, R. A. C., Romeo, A., & Metcalf, R. B. 2018, *MNRAS*, 477, 1814, [arXiv:1706.07870]
- Croton, D. J., Farrar, G. R., Norberg, P., et al. 2005, *MNRAS*, 356, 1155, [arXiv:astro-ph/0407537]
- Croton, D. J., Springel, V., White, S. D. M., et al. 2006, *MNRAS*, 365, 11, [arXiv:astro-ph/0508046]
- Croton, D. J., Stevens, A. R. H., Tonini, C., et al. 2016, *ApJS*, 222, 22, [arXiv:1601.04709]

- Davis, M., Efstathiou, G., Frenk, C. S., & White, S. D. M. 1985, *ApJ*, 292, 371
- de Jong, R. S., Agertz, O., Agudo Berbel, A., et al. 2019, *The Messenger*, 175, 3, [arXiv:1903.02464]
- de Jong, R. S., Bellido-Tirado, O., Chiappini, C., et al. 2012, in *Society of Photo-Optical Instrumentation Engineers (SPIE) Conference Series*, Vol. 8446, *Ground-based and Airborne Instrumentation for Astronomy IV*, ed. I. S. McLean, S. K. Ramsay, & H. Takami, 84460T, [arXiv:1206.6885]
- de Lapparent, V., Geller, M. J., & Huchra, J. P. 1986, *ApJL*, 302, L1
- Dekel, A. & Rees, M. J. 1994, *ApJL*, 422, L1, [arXiv:astro-ph/9308029]
- Di Cintio, A., Brook, C. B., Dutton, A. A., et al. 2017, *MNRAS*, 466, L1, [arXiv:1608.01327]
- Di Paolo, C. & Salucci, P. 2020, arXiv e-prints, [arXiv:2005.03520]
- Domínguez-Gómez, J., Lisenfeld, U., Pérez, I., et al. 2022, *A&A*, 658, A124, [arXiv:2111.06844]
- D’Onghia, E. 2008, in *IAU Symposium*, Vol. 245, *Formation and Evolution of Galaxy Bulges*, ed. M. Bureau, E. Athanassoula, & B. Barbuy, 51–54
- Einasto, J., Hütsi, G., Saar, E., et al. 2011a, *A&A*, 531, A75, [arXiv:1012.3550]
- Einasto, J., Suhhonenko, I., Hütsi, G., et al. 2011b, *A&A*, 534, A128, [arXiv:1105.2464]
- Einstein, A. 1915, *Sitzungsberichte der Königlich Preussischen Akademie der Wissenschaften*, 778
- Einstein, A. 1917, *Sitzungsberichte der Königlich Preussischen Akademie der Wissenschaften (Berlin)*, Seite 142-152., 142
- Eke, V. R., Baugh, C. M., Cole, S., et al. 2004a, *MNRAS*, 348, 866, [arXiv:astro-ph/0402567]
- Eke, V. R., Frenk, C. S., Baugh, C. M., et al. 2004b, *MNRAS*, 355, 769, [arXiv:astro-ph/0402566]
- Ellis, G. F. R. 1984, in *General Relativity and Gravitation*, ed. B. Bertotti, F. de Felice, & A. Pascolini, 215–288
- Fioc, M. & Rocca-Volmerange, B. 2019, *A&A*, 623, A143, [arXiv:1902.07929]
- Fixsen, D. J. 2009, *ApJ*, 707, 916, [arXiv:0911.1955]
- Fliche, H.-H. & Triay, R. 2010, *JCAP*, 2010, 022, [arXiv:gr-qc/0607090]
- Florez, J., Berlind, A. A., Kannappan, S. J., et al. 2021, *ApJ*, 906, 97, [arXiv:2011.08276]
- Fort, B., Mellier, Y., & Dantel-Fort, M. 1997, *A&A*, 321, 353
- Friedmann, A. 1922, *Zeitschrift für Physik*, 10, 377

- Frigo, M. & Johnson, S. G. 2012, FFTW: Fastest Fourier Transform in the West, Astrophysics Source Code Library, record ascl:1201.015, [arXiv:1201.015]
- Fukugita, M., Yamashita, K., Takahara, F., & Yoshii, Y. 1990, ApJL, 361, L1
- Gorbunov, D. S. & Rubakov, V. A. 2011, Introduction to the theory of the early universe: Hot big bang theory (World Scientific)
- Gorenstein, M. V., Cohen, N. L., Shapiro, I. I., et al. 1988, ApJ, 334, 42
- Gorenstein, M. V., Shapiro, I. I., Rogers, A. E. E., et al. 1984, ApJ, 287, 538
- Gottlöber, S., Łokas, E. L., Klypin, A., & Hoffman, Y. 2003, MNRAS, 344, 715, [arXiv:astro-ph/0305393]
- Gregory, S. A. & Thompson, L. A. 1978, ApJ, 222, 784
- Gunn, J. E. & Gott, III, J. R. 1972, ApJ, 176, 1
- Hahn, C., Wilson, M. J., Ruiz-Macias, O., et al. 2022, arXiv e-prints, arXiv:2208.08512, [arXiv:2208.08512]
- Hellwing, W. A., Cautun, M., van de Weygaert, R., & Jones, B. T. 2021, Physical Review D, 103, 063517, [arXiv:2011.08840]
- Hockney, R. & Eastwood, J. 1988, Computer Simulation Using Particles (Taylor & Francis)
- Hoffleit, D. 1994, in Astronomical Society of the Pacific Conference Series, Vol. 60, The MK Process at 50 Years: A Powerful Tool for Astrophysical Insight, ed. C. J. Corbally, R. O. Gray, & R. F. Garrison, 215
- Hoffman, Y., Silk, J., & Wyse, R. F. G. 1992, ApJL, 388, L13
- Hossen, M. R., Ema, S. A., Bolejko, K., & Lewis, G. F. 2022, MNRAS, 513, 5575, [arXiv:2205.00458]
- Hoyle, F., Rojas, R. R., Vogeley, M. S., & Brinkmann, J. 2005, ApJ, 620, 618, [arXiv:astro-ph/0309728]
- Hoyle, F. & Vogeley, M. S. 2002, ApJ, 566, 641, [arXiv:astro-ph/0109357]
- Hoyle, F. & Vogeley, M. S. 2004, ApJ, 607, 751, [arXiv:astro-ph/0312533]
- Hubble, E. 1929, Proceedings of the National Academy of Sciences, 15, 168
- Icke, V. 1984, MNRAS, 206, 1P
- Jõeveer, M., Einasto, J., & Tago, E. 1978, MNRAS, 185, 357
- Jaber, M., Peper, M., Hellwing, W. A., Aragon-Calvo, M. A., & Valenzuela, O. 2023, in preparation
- Jeffrey, N., Gatti, M., Chang, C., et al. 2021, MNRAS, 505, 4626, [arXiv:2105.13539]
- Jiang, F., Dekel, A., Freundlich, J., et al. 2019, MNRAS, 487, 5272, [arXiv:1811.10607]

- Junais, Boissier, S., Epinat, B., et al. 2020, *A&A*, 637, A21, [arXiv:2003.09492]
- Kauffmann, G., Colberg, J. M., Diaferio, A., & White, S. D. M. 1999a, *MNRAS*, 303, 188, [arXiv:astro-ph/9805283]
- Kauffmann, G., Colberg, J. M., Diaferio, A., & White, S. D. M. 1999b, *MNRAS*, 307, 529, [arXiv:astro-ph/9809168]
- Kauffmann, G. & Fairall, A. P. 1991a, *MNRAS*, 248, 313
- Kauffmann, G. & Fairall, A. P. 1991b, *MNRAS*, 248, 313
- Kauffmann, G., White, S. D. M., & Guiderdoni, B. 1993, *MNRAS*, 264, 201
- Khokhlov, A. 1998, *Journal of Computational Physics*, 143, 519, [arXiv:astro-ph/9701194]
- Kilbinger, M. 2015, *Reports on Progress in Physics*, 78, 086901, [arXiv:1411.0115]
- Kim, J. H. 2015, in *American Astronomical Society Meeting Abstracts*, Vol. 225, American Astronomical Society Meeting Abstracts #225, 250.12
- Klypin, A. A., Trujillo-Gomez, S., & Primack, J. 2011, *ApJ*, 740, 102, [arXiv:1002.3660]
- Knebe, A., Knollmann, S. R., Muldrew, S. I., et al. 2011, *MNRAS*, 415, 2293, [arXiv:1104.0949]
- Kolb, E. W. & Turner, M. S. 1990, *The Early Universe* (Westview Press)
- Krause, E., Chang, T.-C., Doré, O., & Umetsu, K. 2013, *ApJL*, 762, L20, [arXiv:1210.2446]
- Kravtsov, A. V. 2013, *ApJ*, 764, L31, [arXiv:1212.2980]
- Kreckel, K., Platen, E., Aragón-Calvo, M. A., et al. 2012, *AJ*, 144, 16, [arXiv:1204.5185]
- Kreckel, K., Platen, E., Aragón-Calvo, M. A., et al. 2011, *AJ*, 141, 4, [arXiv:1008.4616]
- Lacey, C. & Cole, S. 1993, *MNRAS*, 262, 627
- Landau, L. & E.M.Lifschitz. 2009, *Lehrbuch der Theoretischen Physik Band II* (Harri Deutsch)
- Lemaître, G. 1927, *Annales de la Société Scientifique de Bruxelles*, 47, 49
- Levi, M., Bebek, C., Beers, T., et al. 2013, *ArXiv e-prints*, [arXiv:1308.0847]
- Lewis, A. & Challinor, A. 2006, *Phys.Rep.*, 429, 1, [arXiv:astro-ph/0601594]
- Li, B., Zhao, G.-B., & Koyama, K. 2012, *MNRAS*, 421, 3481, [arXiv:1111.2602]
- Lilje, P. B. & Lahav, O. 1991, *ApJ*, 374, 29
- Lindholm, T. 1999, *N-body algorithms*, <https://web.archive.org/web/20190214150157/http://www.cs.hut.fi/~ctl/NBody.pdf>, [Accessed: 30.03.2023]
- Liu, Y., Gao, L., Bose, S., et al. 2023, *arXiv e-prints*, [arXiv:2303.15894]

- Luminet, J. & Roukema, B. F. 1999, in NATO ASIC Proc. 541: Theoretical and Observational Cosmology. Publisher: Dordrecht: Kluwer, ed. M. Lachièze-Rey, 117, [arXiv:astro-ph/9901364]
- Macpherson, H. J., Lasky, P. D., & Price, D. J. 2017, *Physical Review D*, 95, 064028, [arXiv:1611.05447]
- Mao, Q., Berlind, A. A., Scherrer, R. J., et al. 2017, *ApJ*, 835, 161, [arXiv:1602.02771]
- Maury, A. C. & Pickering, E. C. 1897, *Annals of Harvard College Observatory*, 28, 1
- McKellar, A. 1941, *Publications of the Dominion Astrophysical Observatory Victoria*, 7, 251
- Mkleine & other Wikipedia contributors. 2023, *Schnelle Fourier-Transformation*, oldid=3988130
- Mo, H. J., Mao, S., & White, S. D. M. 1998, *MNRAS*, 295, 319, [arXiv:astro-ph/9707093]
- Moorman, C. M., Vogeley, M. S., Hoyle, F., et al. 2015, *ApJ*, 810, 108, [arXiv:1508.04199]
- Morell, O., Kallander, D., & Butcher, H. R. 1992, *A&A*, 259, 543
- Mukhanov, V. 2005, *Physical Foundations of Cosmology* (Cambridge: Cambridge Univ. Press)
- Müller, V., Arbabi-Bidgoli, S., Einasto, J., & Tucker, D. 2000, *MNRAS*, 318, 280, [arXiv:astro-ph/0005063]
- Nadathur, S., Carter, P. M., Percival, W. J., Winther, H. A., & Bautista, J. E. 2019, *Physical Review D*, 100, 023504, [arXiv:1904.01030]
- Nadathur, S. & Hotchkiss, S. 2014, *MNRAS*, 440, 1248, [arXiv:1310.2791]
- Nadathur, S. & Hotchkiss, S. 2015a, *MNRAS*, 454, 2228, [arXiv:1504.06510]
- Nadathur, S. & Hotchkiss, S. 2015b, *MNRAS*, 454, 889, [arXiv:1507.00197]
- Nadathur, S., Hotchkiss, S., & Crittenden, R. 2017, *MNRAS*, 467, 4067, [arXiv:1610.08382]
- Narlikar, J. V. 1994, *American Journal of Physics*, 62, 903
- Neyrinck, M. C. 2008, *MNRAS*, 386, 2101, [arXiv:0712.3049]
- Okamoto, T. & Nagashima, M. 2001, *ApJ*, 547, 109, [arXiv:astro-ph/0004320]
- Ostrowski, J. J. 2020, *Acta Physica Polonica Supplement*, 13, 177, [arXiv:1912.12683]
- Paczynski, B. 1987, *Nature*, 325, 572
- Pan, D. C., Vogeley, M. S., Hoyle, F., Choi, Y.-Y., & Park, C. 2012, *MNRAS*, 421, 926, [arXiv:1103.4156]
- Patiri, S. G., Prada, F., Holtzman, J., Klypin, A., & Betancort-Rijo, J. 2006, *MNRAS*, 372, 1710, [arXiv:astro-ph/0605703]
- Peebles, P. J. E. 1969, *ApJ*, 155, 393

- Penzias, A. A. & Wilson, R. W. 1965, *ApJ*, 142, 419
- Peper, M. & Roukema, B. F. 2021, *MNRAS*, [arXiv:2010.03742]
- Peper, M., Roukema, B. F., & Bolejko, K. 2019, *Proceedings of the International Astronomical Union*, 14, 279
- Peper, M., Roukema, B. F., & Bolejko, K. 2023, submitted, [arXiv:2304.00591]
- Perlmutter, S., Aldering, G., Goldhaber, G., et al. 1999, *ApJ*, 517, 565, [arXiv:astro-ph/9812133]
- Pisani, A., Lavaux, G., Sutter, P. M., & Wandelt, B. D. 2014, *MNRAS*, 443, 3238, [arXiv:1306.3052]
- Pisani, A., Sutter, P. M., Hamaus, N., et al. 2015a, *Physical Review D*, 92, 083531, [arXiv:1503.07690]
- Pisani, A., Sutter, P. M., & Wandelt, B. D. 2015b, *ArXiv e-prints*, [arXiv:1506.07982]
- Planck Collaboration, Aghanim, N., Akrami, Y., et al. 2020, *A&A*, 641, A6, [arXiv:1807.06209]
- Press, W. H. & Schechter, P. 1974, *ApJ*, 187, 425
- Prunet, S., Pichon, C., Aubert, D., et al. 2008, *ApJS*, 178, 179, [arXiv:0804.3536]
- Pustilnik, S. A., Kniazev, A. Y., Perepelitsyna, Y. A., & Egorova, E. S. 2020, *MNRAS*, 493, 830, [arXiv:1912.06857]
- Richard, J., Kneib, J. P., Blake, C., et al. 2019, *The Messenger*, 175, 50, [arXiv:1903.02474]
- Riess, A. G., Filippenko, A. V., Challis, P., et al. 1998, *AJ*, 116, 1009, [arXiv:astro-ph/9805201]
- Robertson, H. P. 1929, *Proceedings of the National Academy of Science*, 15, 822
- Rong, Y., Guo, Q., Gao, L., et al. 2017, *MNRAS*, 470, 4231, [arXiv:1703.06147]
- Rosenbaum, S. D., Krusch, E., Bomans, D. J., & Dettmar, R. J. 2009, *A&A*, 504, 807, [arXiv:0908.4023]
- Rougier, N. P., Hinsen, K., Alexandre, F., et al. 2017, *PeerJ Comp. Sci.*, 3, e142, [arXiv:1707.04393]
- Roukema, B. F. 1993, PhD thesis, Mount Stromlo & Siding Spring Observatoires, Australian National University, <https://zenodo.org/record/4294185>
- Roukema, B. F. 2018, *A&A*, 610, A51, [arXiv:1706.06179]
- Roukema, B. F., Bajtlik, S., Biesiada, M., Szaniewska, A., & Jurkiewicz, H. 2007, *A&A*, 463, 861, [arXiv:astro-ph/0602159]
- Roukema, B. F. & Ostrowski, J. J. 2019, *JCAP*, 2019, 049, [arXiv:1902.09064]



- Roukema, B. F., Peterson, B. A., Quinn, P. J., & Rocca-Volmerange, B. 1997, *MNRAS*, 292, 835, [arXiv:astro-ph/9707294]
- Roukema, B. F., Quinn, P. J., & Peterson, B. A. 1993, in *Astronomical Society of the Pacific Conference Series*, Vol. 51, *Observational Cosmology: an International Symposium*, Milano, Italy, 21–25 September 1992, ed. G. L. Chincarini, A. Iovino, T. Maccacaro, & D. Maccagni, 298
- Roukema, B. F. & Yoshii, Y. 1993, *ApJL*, 418, L1
- Sachs, R. 1961, *Proceedings of the Royal Society of London Series A*, 264, 309
- Sánchez, C., Clampitt, J., Kovacs, A., et al. 2017, *MNRAS*, 465, 746, [arXiv:1605.03982]
- Sandage, A. & Binggeli, B. 1984, *AJ*, 89, 919
- Sasaki, M. 1993, *Progress of Theoretical Physics*, 90, 753, <https://academic.oup.com/ptp/article-pdf/90/4/753/6866845/90-4-753.pdf>
- Savitzky, A. & Golay, M. J. E. 1964, *Analytical Chemistry*, 36, 1627
- Schaap, W. E. 2007, PhD thesis, University of Groningen, Netherlands
- Schechter, P. 1976, *ApJ*, 203, 297
- Schmidt, B. P., Suntzeff, N. B., Phillips, M. M., et al. 1998, *ApJ*, 507, 46, [arXiv:astro-ph/9805200]
- Schombert, J., Maciel, T., & McGaugh, S. 2011, *Advances in Astronomy*, 2011, 143698, [arXiv:1109.2360]
- Schombert, J. & McGaugh, S. 2014a, *PASA*, 31, e036, [arXiv:1407.6778]
- Schombert, J., McGaugh, S., & Maciel, T. 2013, *AJ*, 146, 41, [arXiv:1306.4278]
- Schombert, J. M. & McGaugh, S. 2014b, *PASA*, 31, e011, [arXiv:1401.0238]
- Schwarz, D. J. 2008, *9 Particle Cosmology*, ed. H. Schopper (Berlin: Springer), 360–402
- Seigar, M. S. 2008, *PASP*, 120, 945, [arXiv:0807.1124]
- Sen, P. K. 1968, *J. Amer. Stat. Assoc.*, 63, 1379
- Shandarin, S. F. 2011, *JCAP*, 2011, 015, [arXiv:1011.1924]
- Sheldon, E. S., Becker, M. R., Jarvis, M., Armstrong, R., & The LSST Dark Energy Science Collaboration. 2023, arXiv e-prints, [arXiv:2303.03947]
- Sheth, R. K. & van de Weygaert, R. 2004, *MNRAS*, 350, 517, [arXiv:astro-ph/0311260]
- Spearman, C. E. 1904, *The American Journal of Psychology*, 15, 72
- Springel, V. 2005, *MNRAS*, 364, 1105, [arXiv:astro-ph/0505010]
- Sutherland, R. S. & Dopita, M. A. 1993, *ApJS*, 88, 253

- Sutter, P. M., Lavaux, G., Hamaus, N., et al. 2015, *Astronomy and Computing*, 9, 1, [arXiv:1406.1191]
- Sutter, P. M., Lavaux, G., Wandelt, B. D., et al. 2014, *MNRAS*, 442, 3127, [arXiv:1310.7155]
- Suzuki, N., Rubin, D., Lidman, C., et al. 2012, *ApJ*, 746, 85, [arXiv:1105.3470]
- Synge, J. L. 1964 (Amsterdam: North-Holland)
- Szomoru, A., van Gorkom, J. H., Gregg, M. D., & Strauss, M. A. 1996, *AJ*, 111, 2150, [arXiv:astro-ph/9511128]
- Teyssier, R. 2002, *A&A*, 385, 337, [arXiv:astro-ph/0111367]
- Theil, H. 1950, *Nederl. Akad. Wetensch., Proc.*, 53, 386
- van de Weygaert, R., Kreckel, K., Platen, E., et al. 2011, *Astrophysics and Space Science Proceedings*, 27, 17, [arXiv:1101.4187]
- van de Weygaert, R. & Sheth, R. 2004, in *Astrophysics and Space Science Library*, Vol. 301, *Astrophysics and Space Science Library*, ed. M. Plionis (Springer), 223–226
- van Dokkum, P. G., Abraham, R., Merritt, A., et al. 2015, *ApJL*, 798, L45, [arXiv:1410.8141]
- Vigeneron, Q. & Buchert, T. 2019, *Classical and Quantum Gravity*, 36, 175006, [arXiv:1902.08441]
- Vigeneron, Q. & Roukema, B. F. 2023, *Physical Review D*, 107, 063545, [arXiv:2201.09102]
- Walker, A. G. 1937, *Proceedings of the London Mathematical Society*, 42, 90
- Walsh, D., Carswell, R. F., & Weymann, R. J. 1979, *Nature*, 279, 381
- Weistrop, D., Hintzen, P., Liu, C., et al. 1995, *AJ*, 109, 981
- Wiltshire, D. L. 2007, *New Journal of Physics*, 9, 377, [arXiv:gr-qc/0702082]
- Yoshii, Y. & Peterson, B. A. 1995, *ApJ*, 444, 15
- Young, P., Gunn, J. E., Kristian, J., Oke, J. B., & Westphal, J. A. 1980, *ApJ*, 241, 507
- Zeldovich, I. B. & Grishchuk, L. P. 1984, *MNRAS*, 207, 23P
- Zhu, Q., Xu, D., Gaspari, M., et al. 2018, *MNRAS*, 480, L18, [arXiv:1805.09341]
- Zjupa, J. & Springel, V. 2017, *MNRAS*, 466, 1625, [arXiv:1608.01323]